UNIVERSIDAD COMPLUTENSE DE MADRID
FACULTAD DE CIENCIAS FÍSICAS
Departamento de Física Atómica, Molecular y Nuclear

ULTRA-FAST TIMING STUDY OF EXOTIC NEUTRON-RICH FE ISOTOPES

ESTUDIO DE COINCIDENCIAS ULTRA-RÁPIDAS DE ISÓTOPOS EXÓTICOS DE FE RICOS EN NEUTRONES

MEMORIA PARA OPTAR AL GRADO DE DOCTOR
PRESENTADA POR

Bruno Olaizola Mampaso

Bajo la dirección de los doctores

Luis Mario Fraile Prieto
Henryk Mach

Madrid, 2014

Universidad Complutense de Madrid
Facultad de Ciencias Físicas
Dpto. de Física Atómica, Molecular y Nuclear

Ultra-fast timing study of exotic neutron-rich Fe isotopes

Bruno Olaizola Mampaso

Phd thesis directors:
Dr. Luis Mario Fraile Prieto
Dr. Henryk Mach

Madrid, 2013

Ultra-fast timing study of exotic neutron-rich Fe isotopes

Bruno Olaizola Mampaso

25th June 2013

Director	Co-director
Luis Mario Fraile	Henryk Mach

Dpto. Física Atómica, Molecular y Nuclear
Universidad Complutense de Madrid

Dedicatoria

Agradcimientos

Contents

Summary

The cornerstone of nuclear structure, as we know it from stable nuclei, is the existence of magic numbers. The most stable nuclei arise for completely occupied shells, *closed shells*, and give rise to the magic numbers. At the valley of stability their values are 8, 20, 28, 50, 82 and 126.

The steady development of the production, separation and identification of exotic nuclei, together with the improvement of the detection techniques, makes it possible to experimentally explore nuclei further away from the valley of stability. These exotic nuclei with nucleon numbers supposed to be magic do not always have the properties one would expect. As extra nucleons are added (or removed) from stable nuclei, the single particle energies are modified and strong quadrupole correlations appear, which may neutralize the spherical mean-field shell gaps.

The investigation of the *evolution of shell structure* far off stability has become a major subject in Nuclear Physics. Research in this field has strong implications also in nuclear astrophysics, because exotic nuclei have a crucial role in the processes of stellar nucleosynthesis leading to the formation of the nuclei present in the Universe.

The IS474 experiment was performed at the ISOLDE Facility, CERN, where $^{59-66}$Mn isotopes were created and their β-decay studied. In this PhD Thesis we focused on the study of the neutron-rich iron isotopes (odd-A ^{63,65}Fe and even-A ^{66}Fe) by means of gamma and Advanced Time-Delayed spectroscopy.

Theoretical description

In the harmonic oscillator potential $N = 40$ is a magic number and, indeed, the excitation energy of the $E(2_1^+)$ state in ^{68}Ni lies over 2 MeV. However, in the nuclear framework it is weakened by the spin-orbit interaction, which lowers the orbitals with the highest j in the next major oscillator shell, which in the present case is the $g_{9/2}$ orbital. The $g_{9/2}$ orbital is a primary reason for a strong collectivity in the neutron-rich nuclei of Fe and Cr around $N = 40$. As protons are added to the $f_{7/2}$

orbital, the spin-orbit splitting of the negative parity pf neutron orbitals increase due the strongly attractive neutron-proton tensor interaction [1]. Therefore, as the neutron pf orbits are filled, the excitation to the intruder positive parity orbital $g_{9/2}$ becomes more and more accessible.

However, the shell model calculations using only the pfg ($1p_{3/2}$, $1p_{1/2}$ $0f_{5/2}$ and $0g_{9/2}$) neutron valence space failed to correctly describe the collectivity at $N = 40$ [2, 3], and specifically the low energy of the 573 keV 2_1^+ state in ^{66}Fe [4]. As pointed out in [5], a proper description of the strong quadrupole collectivity in this region requires also an inclusion of the neutron $1d_{5/2}$ orbital. Recently Lenzi *et al.* [6] have developed shell-model calculations in a large valence space that encompasses the pf shell for protons and the $1p_{3/2}$, $1p_{1/2}$ $0f_{5/2}$, $0g_{9/2}$ and $1d_{5/2}$ orbitals for neutrons, by using an effective interaction based on G matrix and with the monopole part empirically tuned to reproduce the experimental single-particle energies. With this approach a very good agreement with the available experimental data was obtained, not only for excitation energies but also for transition rates. A strong quadrupole deformation, coming close to the rotational regime, is predicted for Cr isotopes. The onset of collectivity in Fe isotopes is shown to develop at $N = 40$ (^{66}Fe), with multiparticle-multihole configurations playing a key role in the ground state wave functions, and as many as four neutrons present in the intruder $g_{9/2}$ and $d_{5/2}$ orbitals coming from the upper oscillator shell.

The $N = 40$ nucleus ^{68}Ni ($Z = 28$) shows some of the characteristics of a doubly magic nucleus. It has a large $E(2_1^+)$ energy of more than 2 MeV [7] and a small value of $B(E2; 0_1^+ \rightarrow 2_1^+) = 265\ e^2fm^4$ [8] corresponding to 3.2 W.u. However, mass measurements have showed that the shell gap at $N = 40$ is weak for ^{68}Ni [9] and imply that the small $B(E2)$ value does not indicate a sub-shell gap. One should note that neutrons from the valence $\nu p_{1/2}$ orbital, which is completely filled in a spherical $N = 40$ system, cannot couple together to form a $J = 2$ state, which explains the high energy of the 2_1^+ state in ^{68}Ni.

As protons are removed from the $f_{7/2}$ orbital, the energies of the 2_1^+ states drop sharply and the $B(E2)$ values increase. By removing only two protons from ^{68}Ni the energy of the 2_1^+ state drops from 2033 keV to only 573 keV in ^{66}Fe [4]. By removing two more protons the energy decreases even further to 420 keV in ^{64}Cr, which is in the middle of the proton shell (Z=24). This is the lowest-lying 2_1^+ level experimentally reported so far in the region [10]. It is in consonance with theoretical calculations [6], which also predict a large value for the $B(E2; 2^+ \rightarrow 0^+)$ to occur in ^{64}Cr. Recently this value was measured at NSCL by the Coulex method to be 21(5) W.u. [11].

In comparison to ^{66}Fe, the 2_1^+ energy is even lower in ^{68}Fe [12], at 517 keV. This behaviour suggests a rapid development of collectivity in the heavier neutron rich

Fe isotopes where the $\nu g_{9/2}$ orbit plays an important role (see for example Ref. [3]). This is consistent with a decreasing excitation energy of the $9/2^+$ isomers in the odd Fe isotopes. Precise experimental information on the Fe isotopes is crucial for the understanding of the nuclear structure in the region and mapping the onset of collectivity. Of particular interest are the transition rates, which provide stringent tests of theoretical models.

Our present study includes the γ- and fast timing spectroscopy of the levels in ^{63,65,66}Fe populated in the β-decay of thei Mn isobars. Since the radioactive source was collected in a saturated mode, equilibrium was established among all decay products from the decay of Mn isotopes, which allowed to include in the analysis the decays of the daughter products. The Advanced Time Delayed $\beta\gamma\gamma$(t) method [13, 14] was employed to measure level lifetimes in the subnanosecond range.

The Advanced Time Delayed $\beta\gamma\gamma$(t) method

One of the best available probes we have to know the insight of the nuclear structure are the excited level half lives, as they provide with essential information about the transition matrix elements for comparison with theoretical nuclear models. The Advanced Time Delayed (ATD) $\beta\gamma\gamma$(t) method is the best suited to measure half lives between a few picoseconds and several nanoseconds by using triple coincidences $\beta\gamma\gamma$. The ATD method was invented by Henryk Mach in 1986 in the TRISTAN facility at Brookhaven National Laboratory. Later it was further developed and published by H. Mach, M. Moszynski and R. Gill [13, 14, 15].

As other delayed coincidence methods, it is based in the time distribution since the population of an excited state and its de-excitation. The population of the studied level follows the β-decay of the parent nucleus, so the emission of the β-particle must be detected by an appropriate detector. The main difference of the ATD method compared to other delayed coincidence methods is the use of a thin plastic scintillator $\triangle$E, usually a NE111A coupled to a Photonis XP20D0 photomultiplier tube (PMT). By using a very thing detector, it is ensured that all the energetic β-particles deposit a similar amount of energies, thus giving a similar time response.

This level will be de-excited by a γ-ray, which must also be recorded by a suitable detector. The time distribution between these two events (measured with a Time-to-Amplitude-Converter, TAC) will give us the half life of the excited level. As the measured half lives are in the picoseconds range, very fast crystals are needed. The common choice are $LaBr_3$(Ce) crystals (truncated cone shape) coupled to Photonis XP20D0 PMTs. These crystals further improve the energy resolution

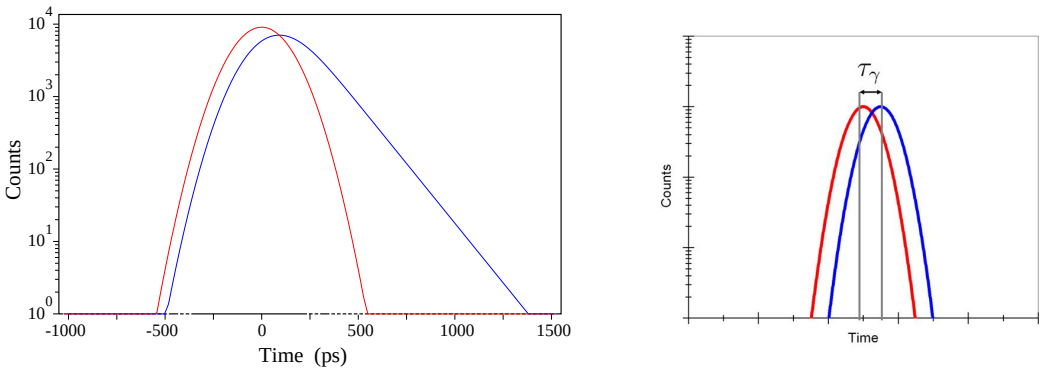

Figure 1: *Left:* Deconvolution technique. *Right:* Centroid shift technique

compared to BaF_2 crystals and have a comparable timing resolution.

When the decay pattern is not simple enough to perform $\beta\gamma$ coincidences, a third detector may be used with very high energy resolution to select a specific gamma cascade, thus the $\beta\gamma\gamma$(t) coincidences. HPGe detectors are chosen for its excellent energy resolution and their high peak-to-background ratio.

When the level half life is long enough to appear as a slope on the delayed part of the time distribution (see left Fig. 1), it can be obtained directly by fitting the slope. The whole spectrum is fitted to a convoluted function:

$$F(t_j) = \gamma \int_A^{+\infty} e^{-\delta(t_j - t)^2} e^{-\lambda t} dt \tag{1}$$

where γ is a normalization factor, δ is a parameter related to the width of the Gaussian prompt distribution and A is the centroid of the Gaussian which is related, but not necessarily equal to, the position of the prompt.

In the case of shorter half lives, the centroid shift technique is used. This technique, specially, relies on the precise calibrations of the timing detector for the β, Compton and full-energy peak events, as each of them will trigger a different time response in the scintillators. The experimental time distribution obtained in the limit $\tau \to 0$ is called *prompt time distribution*. Assuming that the time distribution of prompt mono-energetic events in a given detector is Gaussian (which is a good approximation down to three orders of magnitude) the centroid position of this distribution will be determined only by its energy (for a given experimental conditions). For another gamma of the same energy but de-exciting a non-prompt level ($5 < \tau < 60$ ps) the centroid of its time distribution will be shifted by the

mean-life of the parent level (see right Fig. 1).

Technical details

The experiment IS474 was performed on August 2010 at ISOLDE in CERN, Geneva, by the Fast Timing Collaboration. The list of participants was: B. Olaizola, L.M. Fraile, H. Mach, J.A. Briz, J. Cal-Gonzalez, D. Ghita, W. Kurcewicz, S. Lesher, D. Pauwels, E. Picado and D. Radulov.

The first large scale and, currently, world leading ISOL facility is ISOLDE, at CERN. Schematically, it consist of a device that accelerates protons, a heavy target where they impact and produces the desired isotopes, an ion source that ionizes them and a mass separator that selects the isotopes by their mass to charge ratio. Among its most notable characteristics that made the facility ideal for this experiment are: the precise optics that focuses the radioactive beam almost to a point (key feature in fast timing analysis), the high precision of the isobaric separation and chemical differentiation, as well as the low energy but high intensity of the delivered beams, fundamental for the study of beta decay.

The experimental setup consisted of 5 detector arranged in close geometry. A very fast ΔE NE111A plastic, two fast $LaBr_3$(Ce) crystals of truncated cone shape and two HPGe detectors of 60% relative efficiency. The electronic setup consisted of two main sections, a timing part and another for energy signals. Fig. 2 shows a simplified diagram of the experiment electronic setup. The diagram only shows one HPGe detector and one $LaBr_3$(Ce).

The data were collected using a digital system which consisted of four Digital Gamma Finder (DGF) Pixie-4 modules Revision C made by XIA [16]. Ten parameters were collected in an independent ungated mode without external triggers. Out of the five energy pulses from individual detectors, signals from the two HPGe detectors were directly fetched to the module inputs, while the three dynode signals from the β and γ scintillator detectors were too fast to be directly processed by the XIA modules. Instead they were preamplified, amplified and reshaped with a Linear Gate and Stretcher before they were fetched to the Pixie-4 cards.

For a precise timing information four analog time-delayed $\beta\gamma(t)$ coincidence systems were set, each started by signals from the β-detector and stopped by a fast signal from one of the γ detectors. The analog outputs from the TAC units were directly fed to the Pixie-4 modules. The acquisition system has also collected the time of arrival of the proton pulse on the target.

In order to sort the coincident events recorded during the experiment, a whole set of programmes was written. They made use of the PIXIE time stamp on each

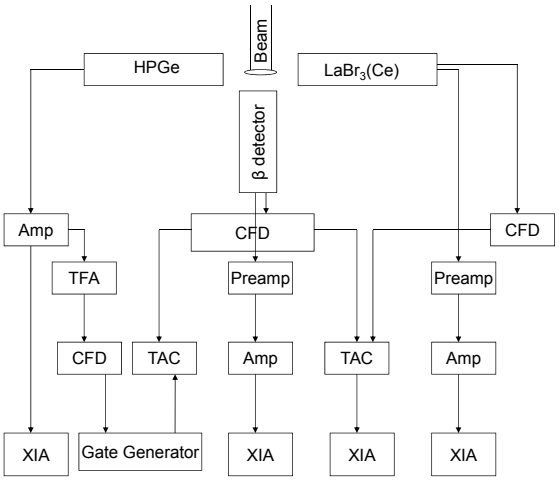

Figure 2: Simplified diagram of the IS474 electronics setup. During the experiment run there were two HPGe and two $LaBr_3$ detectors, but only one of each is included in the diagram.

collected parameter so different combinations of coincident detectors could be arranged. Spectra of the sorted data were later projected after gates were imposed on time or energy.

Calibrations

The ATD method relies on very precise time-response calibrations. These calibrations are common to all the nuclei studied in this work.

The energy calibrations of the HPGe detectors were made to the precision of ± 0.1 keV using the sources of ^{152}Eu, ^{24}Na, ^{88}Rb and ^{140}Ba. During the whole measurement the energy shifts remained within the ± 0.1 keV limit. The same sources provided relative efficiency calibrations of the HPGe detectors in the energy range from 120 keV to 2.7 MeV. At lower energies relative efficiency calibrations were provided by the decay of ^{63}Co to ^{63}Ni observed in the same ISOLDE experiment. The $LaBr_3$(Ce) crystals were coupled to Photonis XP20D0 PMTs, a very fast phototube but highly non-linear. Their energy calibration was done using the same radioactive sources, but fitted to a fourth polynomial order function. Their stability through the experiment run was checked and no significant drifts were observed.

The TACs connected to the HPGe detectors (slow-TACs) were calibrated using

an ORTEC 462 Time Calibrator module, with a calibration of 240 ps per channel. After the experiment it was found that this module did not work properly on the shortest range of 10 ns, so the calibration of the TACs connected to the $LaBr_3$(Ce) crystals (fast-TACs) was done using the known half life of the 2083 keV level in ^{140}Cs, which was precisely measured to be 3.474(10) ns [17]. This gave a calibration of 1.8 ps per channel.

Even with all the precautions taken to minimize the plastic scintillator time response (choosing a ΔE plastic, optimizing the electronics), there is still a dependence with the deposited energy and the Q_β of the β-particle. This is known as the *β-walk*. We have used standard procedures to make this walk-curve flat to within a few ps. This procedure is performed for each studied nucleus and source independently.

The time response of scintillator crystals depends on the energy of the incident photon and, in the case of Compton events, the energy deposited inside the crystal. At the same energy, the time response is different for a Compton and a full-energy event. To correct the contribution to the time response of the Compton event under the full-energy peak, a different time-response curve is needed for each kind of event.

The black curve in Fig. 3 shows the time response for Compton events as a function of the deposited energy. This curve is very smooth, but it presents a very steep slope, as well. This is due to the high working voltage and the high light-yield of the $LaBr_3$(Ce). An event by event procedure was performed to flatten out the time response, see the black red curve in Fig. 3.

^{65}Fe results

The ^{65}Mn half life have been precisely measured ($T_{1/2}$=91.9(9) ms), confirming previous results. The ^{65}Fe level scheme now includes 87 γ-transitions and 41 excited states (up to 4.4 MeV) and an upper limit for the direct β-feeding to the ground state has been given for the first time, see Fig. 4 for the lower lying level scheme. A new value of P_n = 7.9(1.2)% was obtained, which does not agree with previous value of 21.0(5)% [18]. Moreover, it has been observed for the first time that the βn branch populates excited states in ^{64}Fe.

The energy of the $9/2^+$ β-decaying isomer has been precisely determined at 393.7 keV. Gamma transitions populating and de-exciting the 397.6 keV isomer have been directly or indirectly observed.

Employing the ATD method, the half lives of 4 excited levels have been measured and upper limits have been set for a few more. The measured transition rates allowed to make spin/parity assignments to the low energy levels. The proposed

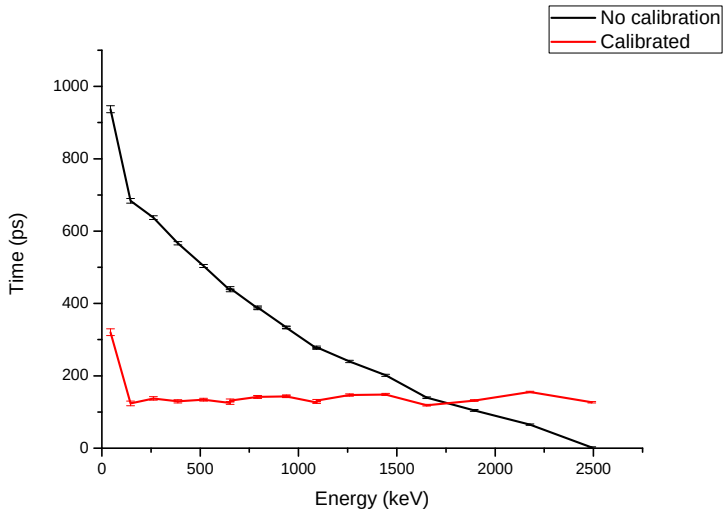

Figure 3: Time response of the $LaBr_3(Ce)$ crystals as a function of the Compton energy in 24Na. Before the procedure the difference in the centroid of the time distribution was almost 1 ns in the 200 keV to 2 MeV range, when after the procedure it is under 50 ps.

assignments suggest that some of the first excited states arise from the coupling of the unpaired neutron with the collective 2^+ and 4^+ states. During the analysis the $1/2^-$ (ground state), $3/2^-$, $5/2^-$ and $7/2^-$ were identified, but not the $9/2^-$ spin state. The arrangement of these levels have been corroborated by shell model calculations using the LNPS effective interaction.

Positive parity states have also been observed at low energies ($9/2^+$ at 393.7 keV, $5/2^+$ at 397.6 keV and $7/2^+$ at 609.5 keV), with the observation supported by the calculations. They show the importance of the positive parity orbitals across the N = 40 subshell gap.

^{63}Fe results

The ^{63}Fe proposed level scheme confirms the results from the Fast Timing Collaboration preliminary run [19]. It also expands the level scheme to a total of 73 γ transitions and 31 levels, see Fig. 5. Additionally 13 γ-rays have been assigned to the ^{63}Mn decay, but were not placed in the level scheme. An upper limit of $< 7\%$, compatible with zero, has been set for the direct β-feeding to the ground state. For the first time a neutron delayed emission branch has been observed and a value of $P_n = 2.0(2)\%$ was measured. In a very similar way to the ^{65}Mn βn decay, the ^{63}Mn

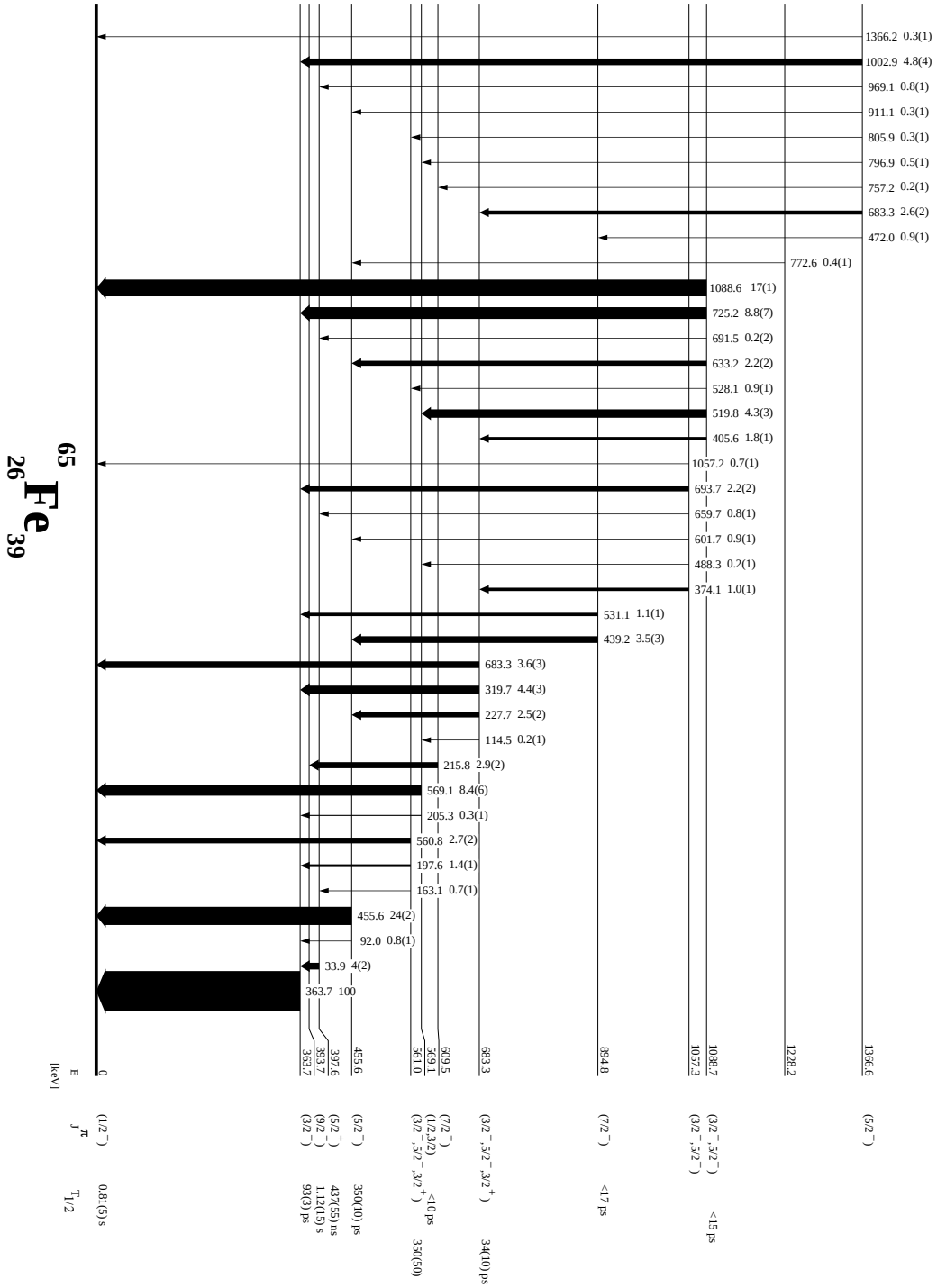

Figure 4: Lower energies ^{65}Fe level scheme populated in the β-decay of ^{65}Mn. Measured half lives and tentatively assigned spin-parities are shown next to each level. All results are from this work except for the half-lives of the β-decaying states.

βn decay populates excited states in ^{62}Fe.

We have identified a level at 475.0 keV, which is proposed to be the $9/2^+$ β-decaying isomer. If confirmed, the systematic of the $9/2^+$ states in odd-Fe isotopes would be described as a perfect decreasing parabola, with its minimum at ^{65}Fe and then increasing again for ^{67}Fe. This would be a solid verification of the strong influeance of the $g_{9/2}$ orbital as neutrons are added.

By making use of the deconvolution technique the half lives of the first two excited states were measured. By using these results the spin-parity sequence could be proposed. It follows the same order as in ^{65}Fe, $1/2^-$ $3/2^-$ $5/2^-$. No suitable candidate has been found so far for the $7/2^-$ or $9/2^-$ states.

^{66}Fe results

Our new ^{66}Fe level scheme confirms most of the γ transitions previously observed [20] and expands it to include a total of 24 γ-rays and 16 excited levels (see Fig. 6), plus two other high energy gammas assigned to the ^{66}Mn decay but not placed in the level scheme. The observed direct β-feeding to the ground state (46(12)%) is in good agreement with recently reported values. A more precise value of $P_n = 3.8(7)\%$ has been measured for the beta delayed neutron emission branch. Moreover, the populated excited states in ^{65}Fe have been firmly observed.

Employing the centroid shift technique, from the ATD $\beta\gamma\gamma$(t) method, the half lives of two levels (including the 2_1^+ state) have been measured and two more upper limits have been established. The measured value $B(E2; 2_1^+ \rightarrow 0_1^+) = 15(3)$ W.u. is in agreement with previously reported results [21] and it indicates a high collectivity in the nucleus, but also points out that the onset of collectivity may be not in ^{66}Fe, as was recently calculated, but in ^{64}Fe.

Detailed shell model calculations using the LNPS effective interaction have been performed, providing information on the ^{66}Mn β-decay and ^{66}Fe excited level configuration. These calculations reveal the multinucleon-multihole character of the 2_1^+ state.

Making use of these calculations and the measured transition rates a spin-parity has been proposed for several levels. The previous tentative identification of the 4_1^+ state is confirmed [22] and we propose the assignment of spin-parity of 1_1^+ to the 2874.3 keV state.

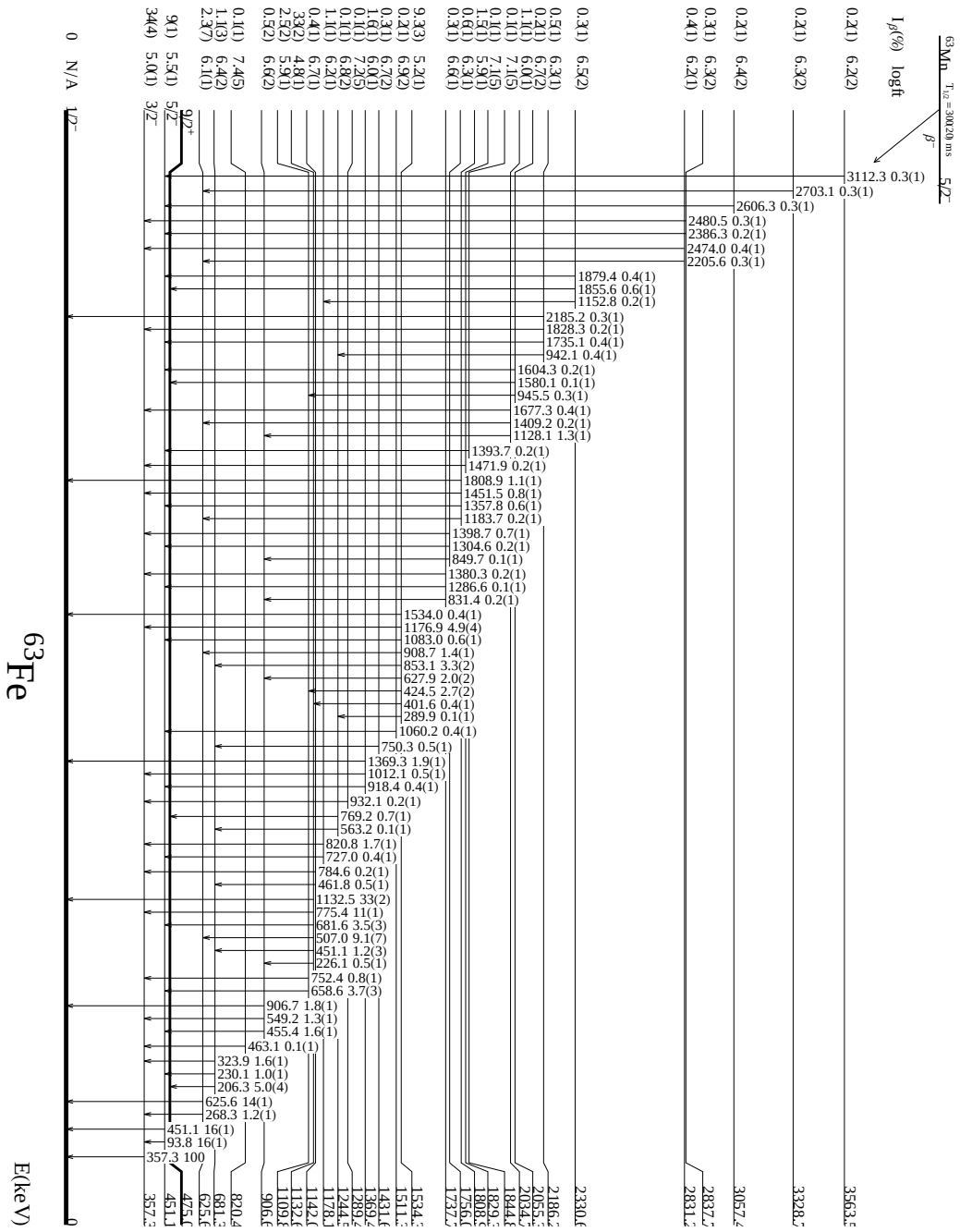

Figure 5: ^{63}Fe level scheme populated in the β-decay of ^{63}Mn from this work.

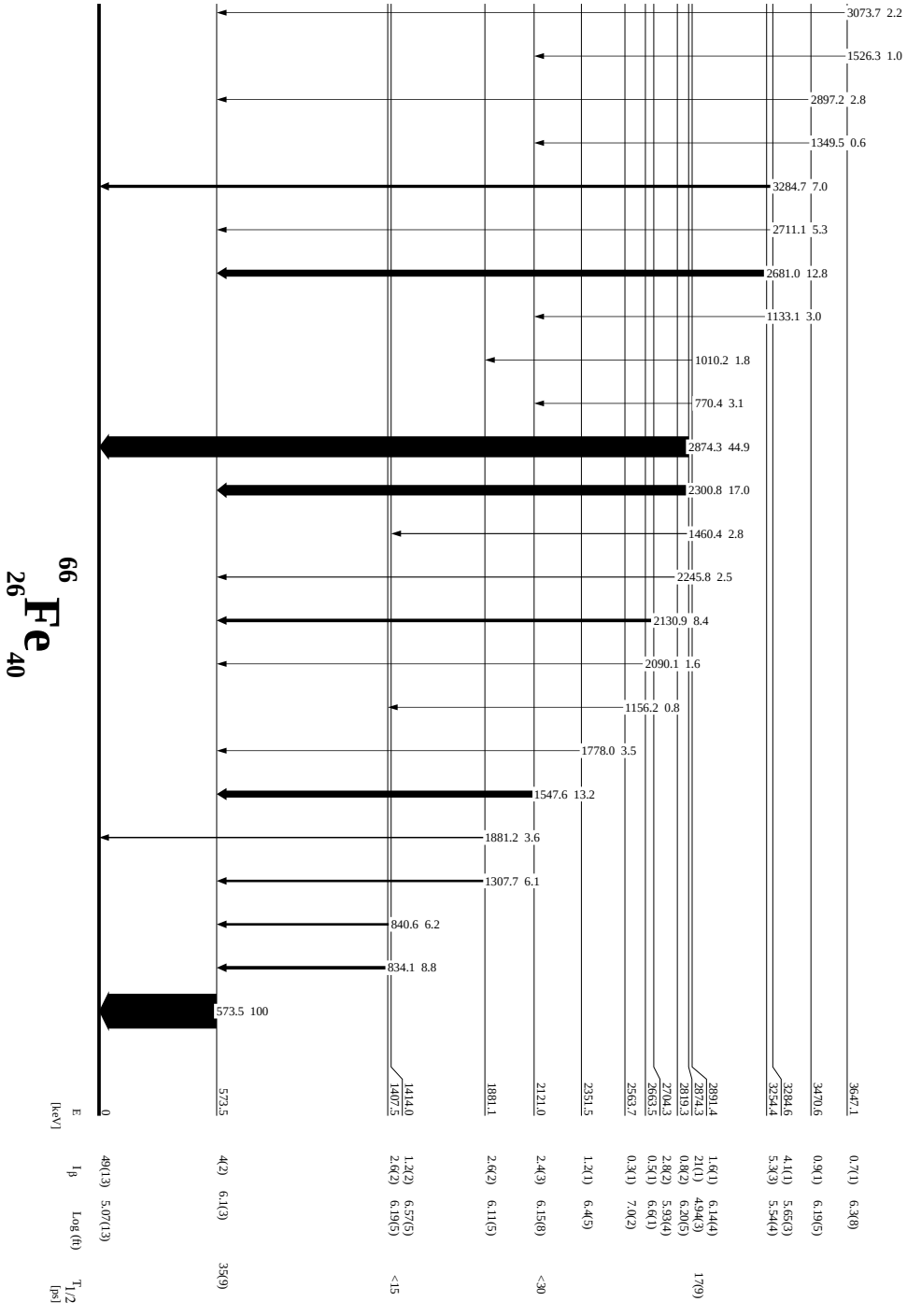

Figure 6: ^{66}Fe level scheme populated in the β-decay of ^{66}Mn from this work.

Conclusions and future work

This work has characterized the low energy level structure of the ^{63,65,66}Fe populated following the β-decay of their Mn isobars. The results presented on ^{63}Fe confirm the previous work and further expands the level scheme with several new gammas and levels. For the first time a detailed study of the ^{65}Fe has been performed. Many new transitions and levels have been observed and 4 level lifetimes have been measured. Finally, the known level scheme of ^{66}Fe was confirmed and a B(E2$_1$) value was determined which is slightly lower than, although consistent with, the previous results. The new experimental results on ^{65}Fe and ^{66}Fe have been compared to shell model calculations and found in a good agreement. The model calculations provide a deeper understanding of the observed nuclear structure in the nuclei. The results obtained in the analysis of the ^{65}Fe have been submitted to the *Physical Review C* journal for publication. The articles on the other two nuclides are in preparation.

As the work for the nearest future, we will focus on the preparation of the publications on the ^{63}Fe and ^{66}Fe results. Moreover, during the same experiment data were collected on a few more Mn isotopes, so the analysis of the beta decay of lighter Mn isotopes can yield new results which will help to understand the systematic of the neutron rich Iron nuclei.

Resumen en castellano

Uno de los pilares fundamentales de la estructura nuclear, tal y como la conocemos de los núcleos estables, es la existencia de números mágicos. Los núcleos más estables surgen de orbitales completamente llenos, *orbitales cerrados*, y dan lugar a los nágicos. En el valle de estabilidad dichos números son 8, 20, 28, 50, 82 y 126.

La constante evolución en la producción, separación e identificación de núcleos exóticos, junto a una mejora en las técnicas de detección, hace posible el estudio experimental de núcleos lejos del valle de estabilidad. Estos núcleos exóticos con número supuéstamente mágicos no siempre tiene las propiedades que uno esperaría. Al ir añadiendo o sustrayendo nucleones de un núcleo estable, la energías de partícula independiente se modifican y fuertes correlaciones octupolares aparecen, las cuales pueden neutralizar los saltos de capa del campo medio esférico.

La investigación de la evolución de la estructura de capas lejos de la estabilidad se ha convertido en uno de los temas mas importantes en Física Nuclear. Investigaciones en este área tienen grandes implicaciones en astrofísica nuclear, ya que los núcleos exóticos juegan un papel crucial en los procesos de nucleosíntesis estelar que dan lugar a la formación de los núcleos presentes en el Universo.

El experimento IS474 se realizó en las instalaciones ISOLDE, CERN, donde se crearon isótopos de $^{59-66}$Mn y su desintegración β estudiada. Esta tesis doctoral se centra en el estudio de isótopos ricos en neutrones (los impares ^{63,65}Fe y el par ^{66}Fe) empleando espectroscopía gamma y estudios de coincidencias retardadas avanzadas.

Descripción teórica

En el potencial de oscilador armónico, $N = 40$ es un número mágico y, de hecho, la energía de excitación del estado $E(2_1^+)$ en el ^{68}Ni se encuentra por encima de 2 MeV. Sin embargo, el salto de capa $N = 40$ se debilita por la interacción espín-órbita, la cual baja los orbitales con el j más alto en la siguiente capa de oscilador, que en este caso se trata del orbital $g_{9/2}$. El orbital $g_{9/2}$ es una de las principales razones de

la fuerte colectividad en los isótopos ricos en neutrones de Fe y Cr cerca de N=40. Al añadir protones al orbital $f_{7/2}$, el desacoplo del espín-órbita de los órbitales de neutrones de paridad negativa pf se incrementa debido al fuerte tensor de la interacción de atracción neutrón-protón [1]. Por lo tanto, al ir llenando los órbitales pf de neutrones, la excitación de partículas a los estados intrusos de paridad positiva del orbital $g_{9/2}$ se vuelven más y mas accesibles.

Sin embargo los cálculos de modelo de capas usando tan solo el espacio de valencia de neutrones pfg ($1p_{3/2}$, $1p_{1/2}$ $0f_{5/2}$ y $0g_{9/2}$) fallan al intentar describir correctamente la colectividad cerca de $N = 40$ [2, 3], y específicamente la baja energía del estado 573 keV 2_1^+ en el ^{66}Fe [4]. Tal y como ya se apuntaba en [5], un descripción adecuada de la fuerte colectividad octupolar en la región requiere también la inclusión del orbital $\nu 1d_{5/2}$. Recientemente Lenzi *et al.* [6] han desarrollado cálculos de modelo de capas en un gran espacio de valencias que engloba tanto la capa pf para protones como los orbitales $1p_{3/2}$, $1p_{1/2}$ $0f_{5/2}$, $0g_{9/2}$ and $1d_{5/2}$ para neutrones, empleando una interacción efectiva basada en la matriz-G y con al parte de monopolo empíricamente ajustada para reproducir las energías de partícula independiente. De esta manera se logra una gran concordancia con los datos experimentales disponibles, no solo para las energías de excitación, si no también para las probabilidades de transición. Se predice una fuerte deformación cuadrupolar, cercana al régimen rotacional, para los isótopos de Cr. En el caso de los isótopos de hierro la colectividad se comienza a desarrollarse en $N = 40$ (^{66}Fe), donde las configuraciones de multipartícula-multiagujero juegan un papel fundamental en las funciones de onda del estado fundamental, con hasta 4 neutrones presentes en los orbitales intrusos $g_{9/2}$ y $d_{5/2}$ de la capa superior.

El núcleo de ^{68}Ni ($Z = 28$, $N = 40$) muestran algunas de las características de un núcleo doblemente mágico. Tiene una gran energía de excitación de más de 2 MeV para su estado $E(2_1^+)$ [7] y un reducido valor $B(E2; 0_1^+ \rightarrow 2_1^+) = 265\ e^2fm^4$ [8] que corresponde a 3.2 W.u. Sin embargo, estudios de masa muestran que el salto de capa en $N = 40$ es débil para el ^{68}Ni [9] e implican que un pequeño valor $B(E2)$ no indica un salto de sub-capa. Debería recalcarse que los neutrones de valencia del orbital $\nu p_{1/2}$, el cual esta completamente lleno en $N = 40$ para un sistema esférico, no pueden acoplarse para formar un estado $J = 2$, lo que explica la gran energía del estado 2_1^+ en el ^{68}Ni.

Al sustraer protones del orbital $f_{7/2}$, las energías de los estados 2_1^+ caen abruptamente y los valores $B(E2)$ se incrementan. Con tan solo quitar dos protones del ^{68}Ni la energía del estado 2_1^+ baja de 2033 keV a tan solo 573 keV en el ^{66}Fe [4]. Quitando otros dos protones la energía disminuye aun más hasta 420 keV en el ^{64}Cr,, el cual se encuentra en mitad de la capa de protones (Z=24). Este es el estado 2_1^+ de energía más bajo observado experimentalmente hasta el momento en la región [10]. Esto está en consonancia con los cálculos teóricos [6], los cuales tam-

bién predicen un gran valor $B(E2; 2^+ \rightarrow 0^+)$ para el ^{64}Cr. Recientemente este valor se midió experimentalmente en el NSCL mediante método Coulex con un valor de 21(5) W.u. [11].

En comparación al ^{66}Fe,la energía del estado 2_1^+ es incluso menor para el ^{68}Fe [12], de 517 keV. Este comportamiento sugiere un rápido desarrollo de la colectividad en isótopos de Fe ricos en neutrones más pesados, donde el orbital $\nu g_{9/2}$ juega un papel crucial (ver, por ejemplo, Ref. [3]).

Esto es consistente con una disminución en la energía de excitación de los isómeros $9/2^+$ en los isotopos impares de Fe. Información experimental precisa sobre los isótopos de Fe es crucial para entender la estructura nuclear en la región y explorar la colectividad en la región. De especial interés son las probabilidades de transición, las cuales producen una rigurosa información con la que comparar los modelos teóricos.

El presente estudio incluye la estpectroscopía gamma y de coincidencias ultrarápidas de los niveles en ^{63,65,66}Fe poblados en la desintegración β de sus correspondientes isóbaros de Mn. Puesto que los datos se recolectaron en modo de saturación, se estableció un equilibrio a lo largo de toda la cadena de desintegración de los isótpos de Mn lo cual permitió incluir en el análisis los productos de desintegración. Se empleó el método *Advanced Time Delayed* $\beta\gamma\gamma$(t) [13, 14] para medir la vida media de los estados excitados en el rango de los sub-nanosegundos.

El método *Advanced Time Delayed* $\beta\gamma\gamma$(t)

Uno de los mejores métodos de los que disponemos para caracterizar la estructura nuclear es la vida media de los estados excitados, ya que proporcionan una información sobre los elementos de matriz de transición para poder compararlo con los modelos nucleares teóricos.

El método *Advanced Time Delayed* $\beta\gamma\gamma$(t) es el mejor disponible para la medición de vidas meidas en el rango de unos pocos picosegundos a varios nanosegundos mediante el uso de triples coincidencias $\beta\gamma\gamma$. El método ATD fue inventado por Henryk Mach en 1986 en la instalación TRISTAN, en el Brookhaven National Laboratory. Más adelante fue desarrollado y publicado por H. Mach, M. Moszynski y R. Gill [13, 14, 15].

Al igual que otros métodos de coincidencias retardadas, se basa en la distribución temporal desde la población de un estado excitado y su desexcitación. La población del nivel estudiado sigue a la desintegración β del nucleo padre, por lo que la emisión de dicha partícula β debe ser detectada por un detector apropiado. La gran diferencia del método ATD comparado con otros es el uso de un centellador

plástico delgado $\triangle$E, normalmente un NE111A acoplado a un tubo fotomultiplicador (PMT por sus siglas en inglés) Photonis XP20D0. Al usar un detector tan fino, se asegura que todas las partículas β depositen una cantidad similar de energía, por tanto dando una respuesta temporal muy similar.

Este nivel se desexcitará mediante la emisión de un rayo gamma, el cual también debe detectarse mediante un detector adecuado. La distribución temporal entre estos dos eventos (medida con un Convertidor-Tiempo-Amplitud, TAC por sus siglas en inglés) nos dará la semivida del estado excitado. Como las vidas medias medidas están en el rango de los picosegundos, se precisan de cristales centelladores muy rápidos. La elección más común son cristales de $LaBr_3$(Ce) con forma de cono truncado acoplados a PMTs Photonis XP20D0. Estos cristales mejoran la energía de resolución que tiene los cristales de BaF_2 con una resolución temporal similar.

Cuando la patrón de desintegración no es lo suficientemente sencillo como para realizar coincidencias $\beta\gamma$, un tercer detector con una gran resolución en energía puede emplearse, de ahí las coincidencias $\beta\gamma\gamma$(t). Se emplean detectores de Germanio Hiperpuro (HPGe por sus siglas en inglés) por su incomparable resolución en energía y su ratio pico a fondo.

Cuando la vida media es lo suficientemente larga como para aparecer como una pendiente en al parte retardad de la distribución temporal (ver figura izquierda 7), esta se puede obtener directamente ajustando dicha pendiente. Todo el espectro se ajusto a la función convolucionada:

$$F(t_j) = \gamma \int_A^{+\infty} e^{-\delta(t_j - t)^2} e^{-\lambda t} dt \tag{2}$$

donde γ es un factor de normalización, δ es un parámetro relacionado con el ancho de la distribución instantánea Gaussiana y A es el centroide de dicha Gaussiana que está relacionado, pero no es necesariamente igual, a la posición de la distribución instantánea.

En el caso de vidas medias más cortas, se emplea la técnica de desplazamiento del centroide. Esta técnica, especialmente, depende de precisas calibraciones de los detectores temporales para los eventos β, Compton y picos de energía total, ya que cada uno producirá un respuesta temporal distinta en el centellador. La distribución temporal obtenida experimentalmente en el límite $\tau \to 0$ se conoce como *distribución temporal instantánea*. Asumiendo que la distribución instantánea de eventos monoenergéticos para un detector dado es Gaussiana (una buena aproximación hasta tres órdenes de magnitud) la posición del centroide de dicha distribución vendrá determinado tan solo por su energía (para unas condiciones experimentales dadas). Otra gamma de la misma energía pero que desexcite un nivel con un vida media en el

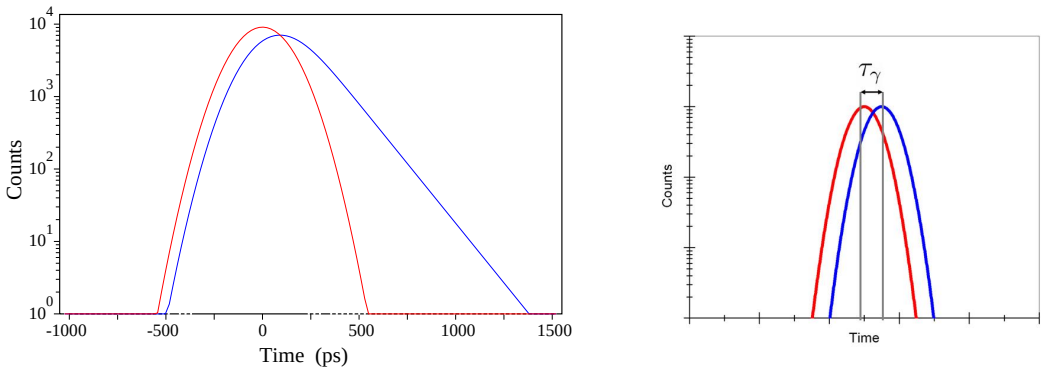

Figura 7: *Left:* Técnica de deconvolución. *Right:* Técnica de desplazamiento del centroide.

rango $5 < T_{1/2} < 60$ ps tendrá su centroide desplazado por la semivida del nivel padre (ver figura derecha 7).

Detalles técnicos

El experimento IS474 se realizó en Agosto del 2010 en la instalación ISOLDE en el CERN, por la colaboración *Fast Timing*. La lista de participantes fue: B. Olaizola, L.M. Fraile, H. Mach, J.A. Briz, J. Cal-Gonzalez, D. Ghita, W. Kurcewicz, S. Lesher, D. Pauwels, E. Picado and D. Radulov.

La primera instalación ISOL a gran escala, y actualmente la mas avanzada, es ISOLDE, en el CERN. Esquemáticamente consiste en un dispositivo que acelera protones, un blanco pesado donde impactan y se producen los isótopos a estudiar, un fuente de iones que los ioniza y un separador de masas que los selecciona por su ratio masa-carga. Entre las características que hacen esta instalación la más apta para el experimento son: la precisión de su óptica que enfoca el haz radioactivo hasta casi un grosor puntual (algo clave en los experimentos de coincidencias ultra-rápidas), la gran precisión de su separación isobárica y diferenciación química, así como la baja energía pero alta intensidad de los haces que distribuye, algo fundamental en los estudios de desintegración β.

El montaje experimental consistió en 5 detectores dispuestos en una geometría cerrada. Un plástico centellador muy rápido ΔE NE111A, dos cristales $LaBr_3(Ce)$ en forma de cono truncado y dos detectores HPGe de eficiencia relativa 60 %. El montaje de la electrónica disponía de dos secciones principales, una parte para análisis de tiempos y otra para las señales de energía. La figura 8 muestra un diagrama

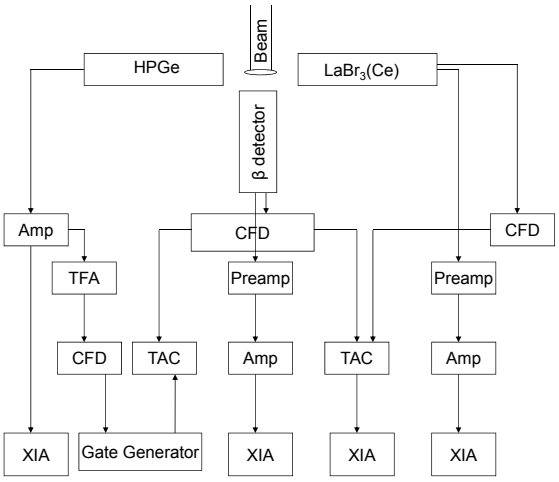

Figura 8: Diagrama simplificado de la electrónica del experimento IS474.

simplificado de la electrónica del experimento. En el diagrama tan solo se muestra un detector HPGe y un cristal $LaBr_3(Ce)$ de los 5 usados.

Los datos se grabaron empleando un sistema de adquisición de datos digital que consistía en cuatro *Digital Gamma Finder (DGF) Pixie-4 modules Revision C* de la casa XIA [16]. Se recolectaron diez parámetros en modo independiente sin disparador externo. De las 5 señales de cada detector individual, las señales de los dos detectores HPGe se conectaron directamente a los módulos DGF, mientras que las señales de los tres dínodos de los centelladores β y γ eran demasiado rápidas para ser procesadas directamente por los módulos XIA. En vez de eso, primero fueron pre-amplificadas, amplificadas y reformadas con un *Linear Gate and Stretcher* antes de ser conectadas a las tarjetas PIXIE-4.

Para poder recolectar un información temporal precisa, se disponía de 4 sistemas analógicos de coincidencias retardadas $\beta\gamma(t)$, cada uno iniciado por la señal del detector β y detenido por una señal rápida de uno de los detectores γ. Las señales de salida de las unidades TAC se conectaron directamente a los módulos PIXIE-4. El sistema de adquisición también recolectaba el tiempo de impacto de los pulsos de protones en el blanco.

Para poder construir los eventos coincidentes entre distintos experimentos, se escribió un conjunto de programas informáticos. Dichos programas emplean el sello temporal que el sistema XIA asigna a cada evento para buscar las coincidencias entre las distintas combinaciones de detectores. Se proyectaron espectros de los datos procesados imponiendo ventanas en la energía y el tiempo de los eventos.

Calibraciones de los detectores

El método ATD requiere de calibraciones muy precisas. Estas calibraciones son comunes a todos los núcleos estudiados, y por lo tanto se emplearon durante todo el análisis.

Las calibraciones en energía de los detectores HPGe se llevaron a cabo hasta la precisión de ± 0.1 keV empleando fuentes de ^{152}Eu, ^{24}Na, ^{88}Rb y ^{140}Ba. Durante todo el experimento los desplazamientos en energía permanecieron en el límite de ± 0.1 keV. Las mismas fuentes se emplearon en la calibración de eficiencia relativa en el rango de energía desde 120 keV hasta los 2.7 MeV. Para energías más bajas se empleó la desintegración de ^{63}Co a ^{63}Ni, medidas durante el experimento. Los cristales $LaBr_3$(Ce) estaban acoplados a PMTs XP20D0, un fototubo muy rápido pero altamente no-linear. La calibración en energía fue realizada empleando las mismas muestras radioactivas, pero se ajustó a un polinomio de cuarto orden. Se comprobó su estabilidad a lo largo del experimento y no se observaron desviaciones en la energía significativas.

Los TACs conectados a los detectores HPGe (referidos como *slow-TACs*) fueron calibrados usando un módulo ORTEC 462 Time Calibrator, resultando en una calibración de 240 ps por canal. Tras el experimento se descubrió que este módulo no funcionaba correctamente para su rango temporal más corto de 10 ns. Por lo tanto la calibración de los TACs conectados a los cristales $LaBr_3$(Ce) (referidos como *fast-TACs*) se realizó empleando la vida media del nivel 2083 keV en el ^{140}Cs, la cual se ha mediado de manera muy precisa, 3.474(10) ns [17]. El resultado fue una calibración de 1.8 ps por canal.

Incluso con todas las precauciones tomadas para minimizar la respuesta temporal del centellador plástico, este aun tiene una cierta dependencia con la energía depositada por la partícula β. Este efecto es conocido como β-*walk*. Se emplearon procedimientos estándar para que la curva fuese plana en rango de unos pocos picosegundos. Esto se realizó para cada núcleo y fuente de calibración de manera independiente.

La respuesta temporal de los cristales centelladores depende de la energía del fotón incidente y, en el caso de los eventos Compton, de la energía depositada dentro del cristal. Para una energía dada, la respuesta temporal del detector es distinta para eventos Compton y foto-eléctricos. Por lo tanto, para poder corregir la contribución de los eventos Compton que se hayan bajo el pico de energía total, se requiere una curva de respuesta temporal distinta para cada tipo de evento.

La curva negra en la figura 9 muestra la respuesta temporal para eventos Compton en función de la energía depositada. La curva tiene una tendencia muy suave, pero su pendiente es demasiado pronunciada, afectando a la resolución temporal del

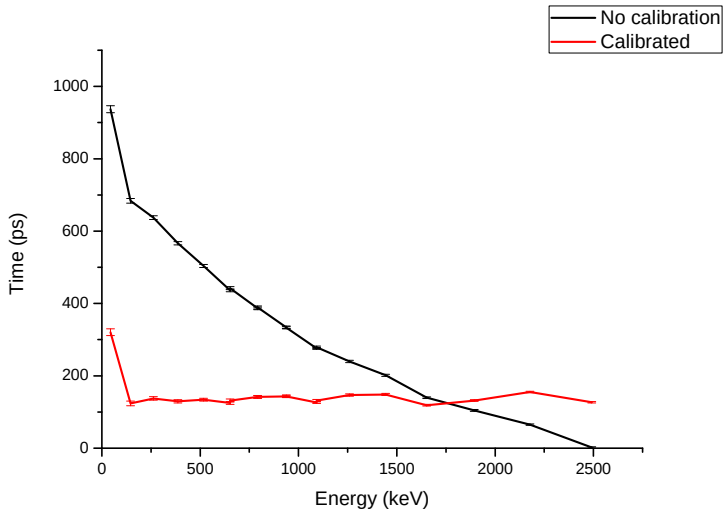

Figura 9: Respuesta temporal de un cristal $LaBr_3(Ce)$ en función de la energía Compton de gammas de una muestra de 24Na. Antes del procedimiento (curva negra) la diferencia en la respuesta temporal era de casi 1 ns entre 200 keV y 2 MeV, mientras que tras el procedimiento aplicado (curva roja) la diferencia se encuentra por debajo de 50 ps.

detector. Este efecto se debe al alto voltaje de trabajo y a la alta producción de luz del cristal de $LaBr_3(Ce)$. Se realizó un procedimiento estándar evento a evento para que la respuesta temporal fuese lo más plana posible, como muestra la curva roja en la figura 9.

Resultados del ^{65}Fe

La vida media del ^{65}Mn se ha medido con gran exactitud ($T_{1/2}$=91.9(9) ms), confirmando resultados previos. El esquema de niveles del ^{65}Fe ahora incluye 87 transiciones y 41 estados excitados (hasta una energía de 4.4 MeV) y un límite superior la población β directa del estado fundamental se ha obtenido por primera vez. La figura 10 muestra el esquema de niveles observado a bajas energías. Un nuevo valor de $P_n = 7{,}9(12)\,\%$ se ha medido, que no concuerda con el valor anterior de $21{,}0(5)\,\%$ [18]. Es más, por primera vez se ha observado que la rama de desintegración βn puebla estados excitados en el ^{64}Fe.

La energía del isómero β $9/2^+$ se ha determinado con precisión a 393.7 keV. Transiciones populando y desexcitando el isómero 397.6 keV han sido observadas direcatemente o indirectamente.

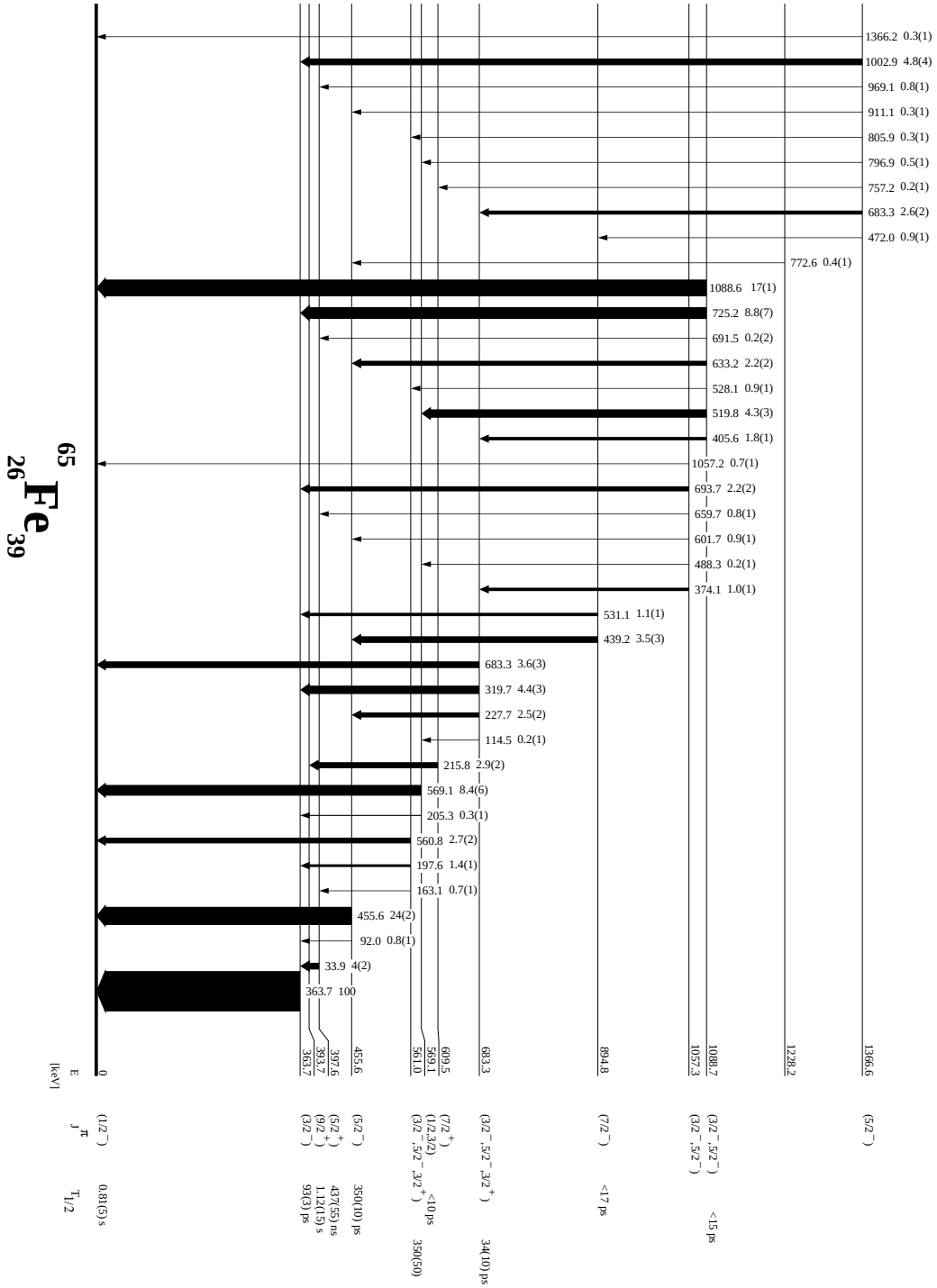

Figura 10: Esquema de niveles a bajas energías del ^{65}Fe poblado en la desintegración β del ^{65}Mn. Todos los resultados mostrados se han obtenido durante este trabajo excepto de la vida media del estado fundamental y del isómero $9/2^+$.

Empleando el método ATD, se ha medido la vida media de 4 estados excitados y se han observado límites superiores para varios más. Las probabilidades de transición nos han permitido asignar espín-paridad a los níveles de baja energía. El espín propuesto sugiere que algunos de los primeros estados excitados surgen del acoplamiento del neutrón desapareado con los estados colectivos 2^+ and 4^+. Durante el análisis se identificaron el the $1/2^-$ (estado fundamental), $3/2^-$, $5/2^-$ and $7/2^-$, pero no así el $9/2^-$. La ordenación de estos niveles ha sido corroborada por calculos del modelo de capas empleando la interacción efectiva LNPS [6].

También se han observado estados de paridad positiva a baja energía ($9/2^+$ a 393.7 keV, $5/2^+$ a 397.6 keV y $7/2^+$ a 609.5 keV). Dichas observaciones se confirman por los cálculos. Estos niveles muestran la importancia de los orbitales de paridad positiva cerca del salto de sub-capa N=40.

Resultado del ^{63}Fe

El esquema de niveles que proponemos para el ^{63}Fe confirma los resultados de la prueba preliminar realizada por la colaboración Fast Timing para este experimento [19]. También expande este esquema a un total de 73 transiciones y 31 niveles (ver figura 11). También se observaron 13 rayos γ que se asignaron a la desintegración del ^{63}Mn pero no se situaron en el esquema de niveles. Un límite superior, compatible con cero, se ha observado para la población directa del estado fundamental. Por primera vez se ha observado la emisión retardad de nuetrones y se ha medido un valor $P_n = 2{,}0(2)\,\%$. De manera similar a la desintegración βn del ^{65}Mn, el ^{63}Mn puebla estados excitados en el ^{62}Fe.

Hemos observado un nivel a 475.0 keV, el cual proponemos tentativamente como un isómero β $9/2^+$. Si se confirma, la sistemática de los estados $9/2^+$ en los isótopos impares de Fe describiría una parábola decreciente perfecta, alcanzando el mínimo en el ^{65}Fe y después incrementándose otra vez para el ^{67}Fe. Esto sería una sólida verificación de la importante influencia del orbital $g_{9/2}$ al añadir neutrones.

Empleando la técnica de deconvolución se midió la vida media de los dos primeros estados excitados. Usando estos resultados se propone la secuencia de espín-paridad para los niveles a baja energía. Esta sigue la misma secuencia que en el ^{65}Fe, $1/2^-$ $3/2^-$ $5/2^-$. No se han encontrado candidatos adecuados para los estados $7/2^-$ or $9/2^-$

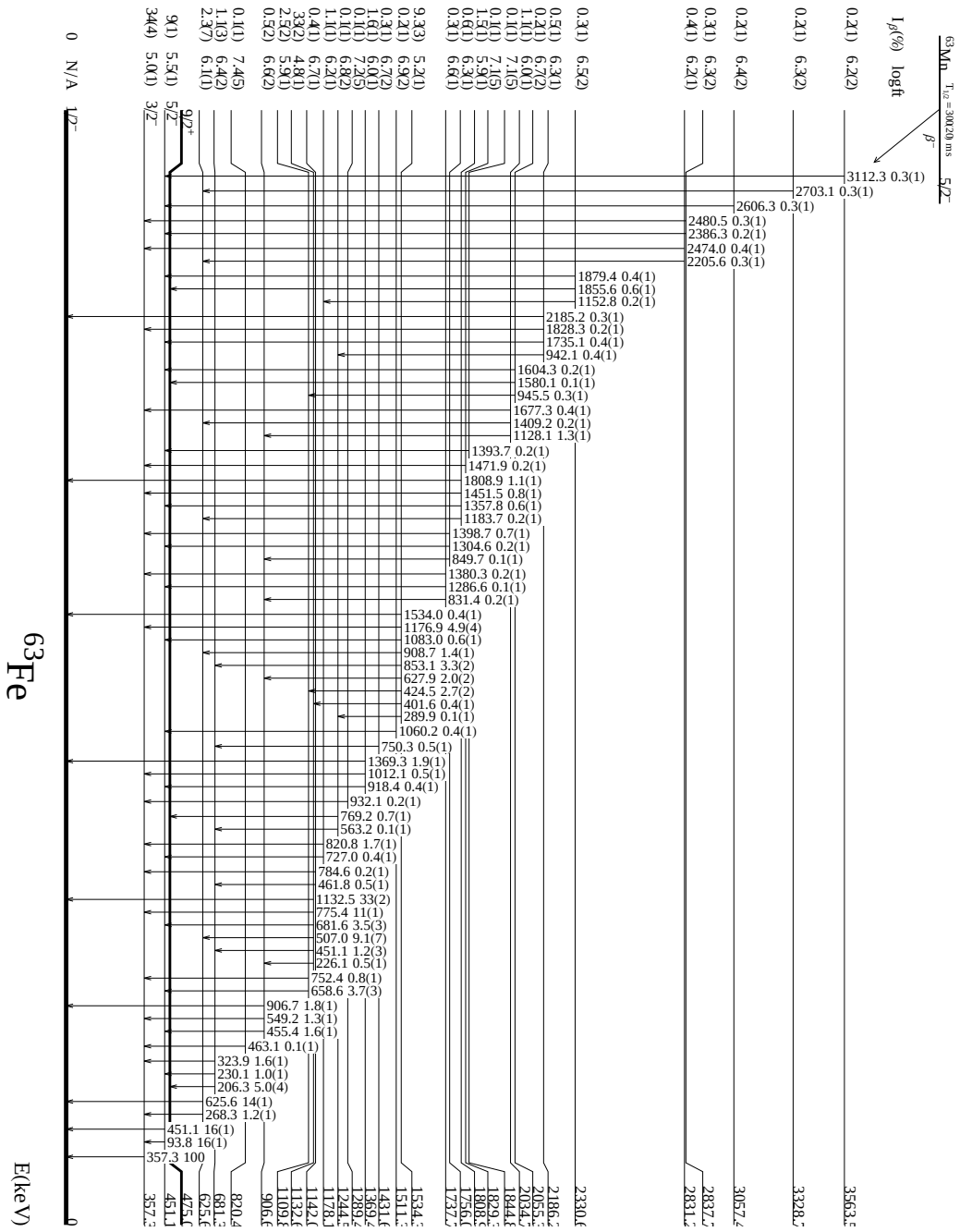

Figura 11: Esquema de niveles del ^{63}Fe poblado en la desintegración β del ^{63}Mn.

Resultados del ^{66}Fe

Nuestro nuevo esquema de niveles para el ^{66}Fe confirma la mayoría de las transiciones γ observadas anteriormente [20] y lo amplía hasta un total de 24 rayos γ y 16 estados excitados (ver figura 12), además de otros dos rayos γ de alta energía que pertenecen a la desintegración del ^{66}Mn pero no se colocaron en el esquema de niveles. La población β directa del estado fundamental (46(12) %) coincide con trabajos recientes. Se ha medido un valor más preciso de $P_n = 3{,}8(7)$ % para la emisión retardada de neutrones. Lo que es más, la población de estados excitados en el ^{65}Fe se ha observado claramente.

Empleando la técnica de desplazamiento del centroide, del método ATD $\beta\gamma\gamma$(t), se ha medido la vida media de dos niveles (incluyendo el estado 2_1^+) y se han establecido límites superiores para otras dos. Nuestro valor $B(E2; 2_1^+ \rightarrow 0_1^+) = 15(3)$ W.u. coincide con el obtenido en trabajos anteriores [21] e indica el caracter colectivo de este núcleo, pero también apunta a que el máximo de colectividad puede no ser el ^{66}Fe, como se había calculado, si no el ^{64}Fe para los isótopos de Fe.

Se realizaron detallados cálculos de modelo de capas empleando la interacción efectiva LNPS, proporcionando información sobre la desintegración β y la configuración de los estados excitados en el ^{66}Fe. Estos cálculos revelaron el caracter multinucleón-multiagujero del estado 2_1^+.

Haciendo uso de estos cálculos y de las probabilidades de transición medidas, se propuso asignaciones de espín-paridad para varios niveles. Se confirma la identificación tentativa anterior del estado 4_1^+ [22] y proponemos la asignación de espín-paridad 1_1^+ para el estado 2874.3 keV.

Conclusiones y trabajo futuro

Este trabajo ha caracterizado la estructura de niveles a baja energía de los núcleos ^{63,65,66}Fe poblada en la desintegración β de sus isobares de Mn. Los resultados presentado para el ^{63}Fe confirman el trabajo anterior y amplían el esquema con varias transiciones y niveles nuevos. Por primera vez se ha realizado un estudio detallado sobre el ^{65}Fe. SE han observado muchas transiciones y niveles nuevos y se han medido la vida media de 4 niveles. Finalmente, el esquema de niveles conocido del ^{66}Fe se ha confirmado y se ha determinado un valor B($E2_1$) el cual es ligeramente inferior, aunque consistente con, resultados anteriores. Los nuevos resultados experimentales sobre el ^{65}Fe y el ^{66}Fe se han comparado con cálculos de modelo de capas y se encontraron en buena concordancia. Los cálculos del modelo de capas proporcionaron un entendimiento más profundo de la estructura nuclear observada durante el

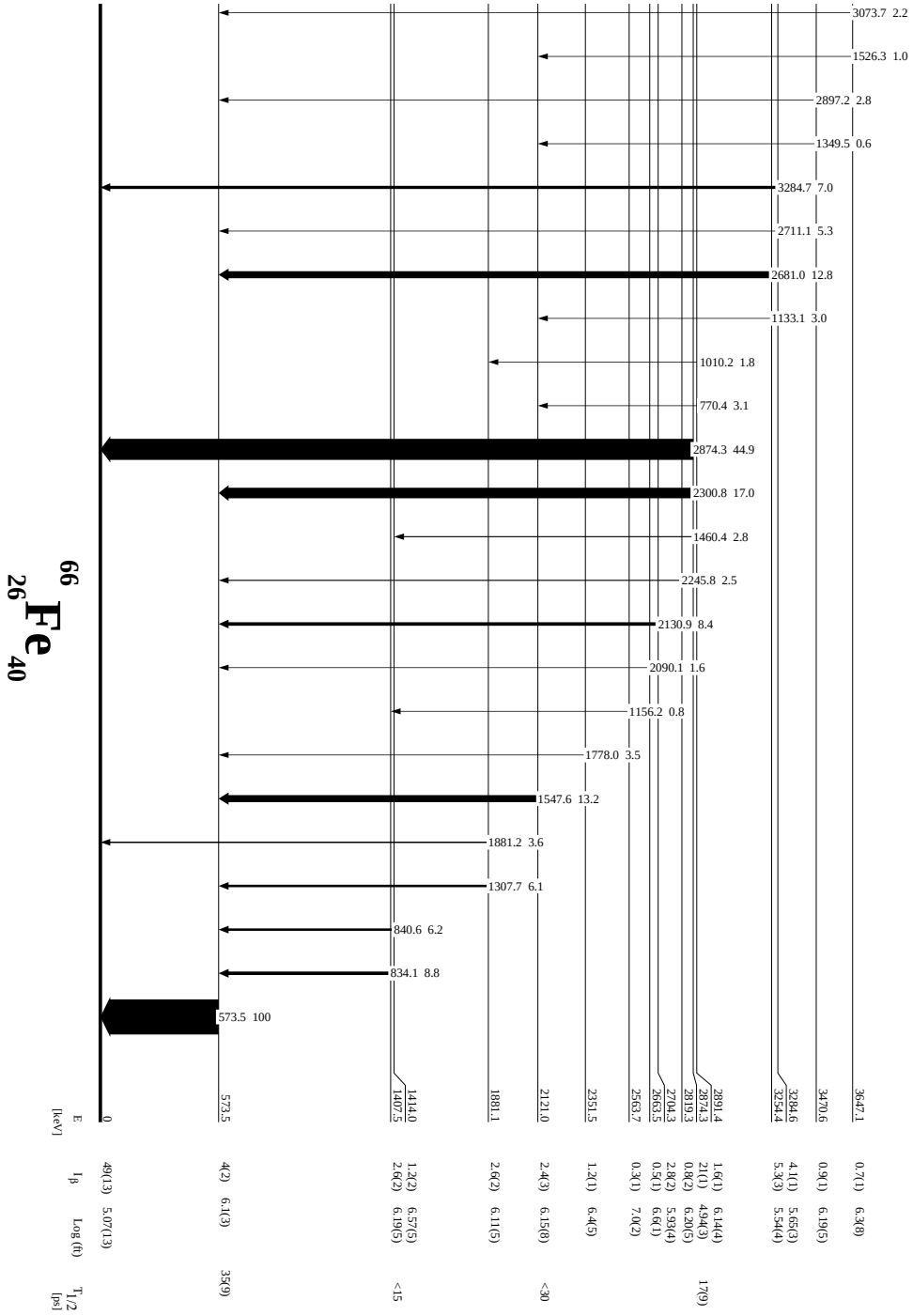

Figura 12: Esquema de niveles del ^{66}Fe poblado en la desintegración β del ^{66}Mn medido en este trabajo.

experimento. Los resultados obtenidos durante el análisis del ^{65}Fe se han enviado a la revista *Physical Review C* para su publicación. Los artículos sobre los otros dos núcleos se encuentran en preparación.

Como trabajo para un futuro cercano, nos centraremos en la publicación de los resultados sobre el ^{63}Fe y el ^{66}Fe. Lo que es más, durante este mismo experimento se recolectaron datos sobre más isótopos de Mn. Como trabajo futuro el análisis de la desintegración β de núcleos más ligeros de Mn puede proporcionar valiosa información para entender la evolución sistemática de los núcleos ricos en neutrones de hierro.

Outline of this thesis

The steady development of the production, separation and identification of exotic nuclei, together with the improvement of the detection techniques, makes it possible to experimentally explore nuclei further and further away from the valley of stability. These nuclei far from stability may exhibit significantly different structure than stable nuclei. Their investigation has strong impact in our understanding of nuclear physics and allows models to be confronted with new observations.

The cornerstone of nuclear structure, as we know it from stable nuclei, is the existence of magic numbers. In the framework of the nuclear shell model, each nucleon (neutron or proton) is moving in the mean potential created by its interactions with the rest of the nucleons. This potential leads to the existence of nuclear shells, the quantum energy levels where nucleons reside. The most stable nuclei arise for completely occupied shells, *closed shells*, and give rise to the magic numbers. At the valley of stability their values are 8, 20, 28, 50, 82 and 126.

Experimental studies over the years have shown that this picture blurs far from stability. Exotic nuclei with nucleon numbers supposed to be magic do not always have the expected properties. As extra nucleons are added (or removed) from stable nuclei, the single particle energies are modified and strong quadrupole correlations appear, which may neutralize the spherical mean-field shell gaps. The quadrupole correlations make deformed intruder configurations energetically favourable, to the extent of making them even the ground states, thus inverting the normal orbital sequence. Therefore, since nucleons occupy different shells than their stable counterparts, the known magic numbers may disappear to give way to new ones. This inversion was first observed in the $N = 8$ nucleus ^{11}Be [23] and has been thoroughly investigated in several regions of the table of nuclides, for example in the *Island of Inversion* around ^{32}Mg, at the neutron shell closure $N = 20$ [24]. These structural changes may be due to the modification of the strength of the spin-orbit coupling [25] and the strong proton-neutron interaction in the neutron rich nuclei [1].

The investigation of the *evolution of shell structure* far off stability has become a major subject in Nuclear Physics. Research in this field has strong implications also in nuclear astrophysics, because exotic nuclei have a crucial role in the processes of

stellar nucleosynthesis leading to the formation of the nuclei present in the Universe.

In this PhD Thesis we investigate the structure of several exotic, neutron-rich iron isotopes (odd ^{63,65}Fe and even ^{66}Fe) by means of gamma and advanced time-delayed spectroscopy. The nuclei were produced in the β^--decay of neutron rich Mn isotopes delivered by the ISOLDE Facility at CERN.

The interplay of spherical and collective configurations is of special interest in the neutron-rich nuclei below $Z = 28$ and $N = 40$. In the harmonic oscillator potential $N = 40$ is a magic number. Indeed, the excitation energy of the $E(2_1^+)$ state in ^{68}Ni is very high, above 2 MeV, and the $B(E2)$ transition rate is the lowest in the region. However, in the nuclear framework the $N = 40$ is weakened by the spin-orbit interaction, which lowers the orbitals with the highest j in the next major oscillator shell, the $g_{9/2}$ orbital in the present case.

The $g_{9/2}$ orbital, near the negative parity $f_{5/2}$, $p_{3/2}$, $p_{1/2}$ shell (pf-shell) with much smaller j-value, is the primary reason for a strong collectivity in the neutron-rich nuclei of Fe and Cr around $N = 40$. The neutron $g_{9/2}$ orbital is believed to be the one driving the shape changes in this mass region, also leading to the appearance of isomers in this region of the nuclear chart, with half lives spanning several orders of magnitude. Moreover, the filling of the proton $f_{7/2}$ orbital, moving from Cr to Fe and then Ni, modifies the relative energies of negative parity pf neutron orbitals due the strongly attractive neutron-proton tensor interaction.

Recently Lenzi *et al.* [6] have developed shell-model calculations in a large valence space that encompasses the pf shell for protons and the $1p_{3/2}$, $1p_{1/2}$ $0f_{5/2}$, $0g_{9/2}$ and $1d_{5/2}$ orbitals for neutrons. With this approach a very good agreement with the available experimental data is obtained, not only for excitation energies but also for transition rates. A strong quadrupole deformation, coming close to the rotational regime, is predicted for Cr isotopes. The onset of collectivity in Fe isotopes is shown to develop at $N = 40$ (^{66}Fe), with multiparticle-multihole configurations playing a key role in the ground state wave functions, and as many as four neutrons present in the intruder $g_{9/2}$ and $d_{5/2}$ orbitals coming from the upper oscillator shell.

Precise experimental information on the Fe isotopes is crucial for the understanding of the nuclear structure in the region and mapping the onset of collectivity. Of particular interest are the transition rates, which provide stringent tests of theoretical models. This is the aim of this Thesis for the odd ^{63,65}Fe and even ^{66}Fe isotopes. The first Chapter provides a general introduction to the shell model and the region of interest. Chapter 2 describes the Advanced Time-Delayed $\beta\gamma\gamma$ method, employed in this thesis. Chapter 3 addresses the experimental tools employed, while Chapter 4 describes the general calibrations required by the ATD method. Chapters 5, 6 and 7 describe the data analysis and results of the investigation of ^{63,65}Fe and ^{66}Fe respectively. The conclusions and outlook are presented in Chapter 8.

Chapter 1

Theoretical description

The development of the Radioactive Ion Beams (RIB) facilities made possible the experimental study of nuclei far from the valley of stability. These nuclei may exhibit significantly different structure than their stable counterpart. The investigation of this exotic isotopes allows us a deeper understanding of nuclear physics and the models we use to describe ti.

In the nuclear shell model, each neutron or proton (nucleon) is moving in a mean field potential created by its interactions with the other of the nucleons. From this potential arise the nuclear shells, the quantum energy levels where nucleons reside. The stable nuclei arise for completely occupied shells, *closed shells*, and give rise to the magic numbers. If both the amount of neutron and protons is a magic number, the nucleus is called *doubly magic* and its ground state is strongly bound. At the valley of stability their values are 8, 20, 28, 50, 82 and 126.

But experimental studies shows that the magic number properties do not hold far away from the valley of stability. Very neutron or proton rich isotopes supposed to be magic do not always have the expected properties. As extra nucleons are added (or removed) from stable nuclei, the single particle energies are modified and strong quadrupole correlations appear, which may neutralize the spherical mean-field shell gaps. The quadrupole correlations make deformed intruder configurations energetically favourable, to the extent of making them even the ground states, thus inverting the stable orbital sequence. Therefore, since nucleons occupy different shells than their stable counterparts, the known magic numbers may banish and arise new ones. This inversion of configurations was first observed in the $N = 8$ nucleus ^{11}Be [23] and has been thoroughly investigated in several regions of the table of nuclides, for example in the *Island of Inversion* around ^{32}Mg, at the neutron shell closure $N = 20$ [24]. These structural changes may be due to the modification of the strength of the spin-orbit coupling [25], and the strong proton-neutron interaction

in the nuclei with strong excess of neutrons [1].

1.1 Shell model

It is a common feature of the fermionic systems to create a shell structure in which the fermions are organized in shells of increasing energy. Maybe the best known example of such shell structure are the electrons around the atoms nucleus. In the atomic shell model, these shells are defined by the quantum numbers that emerge from the Coulomb potential created by the protons in the nucleus. Each of the shells contain a number of orbitals (energy levels) and each orbital can be filled with a definite number of electrons (according to the *Pauli exclusion principle*). The chemistry properties of the atoms are determined by electrons in the non-completely filled shell.

1.1.1 Single particle

This same model can be applied to the atomic nucleus. The nuclear shell model was first developed independently by Eugene Paul Wigner, Maria Goeppert-Mayer and J. Hans D. Jensen in 1949. It follows the same principle as the atomic shell model, but there are some major differences when both are compared. In the atomic shell, the Coulomb potential is created by point-like external source (the nucleus) and not by the electrons themselves. In the nucleus the potential is created by the interaction between each nucleon to each other. Furthermore, instead of having just one type of particle (the electron) in the nucleons there are two different fermions (protons and neutrons) filling two independent shells, as each particle type will follow Pauli's principle independently.

This inner nuclear potential that binds nucleons together can be expressed as the combination of the nuclear and Coulomb interaction:

$$\mathcal{H} = \sum_i \frac{\vec{p^2}_i}{2m_i} + \sum_{j,i\leq j} V_{nuc}(|\vec{x}_i - \vec{x}_j|) + \sum_{j,i\leq j} \frac{e^2}{|\vec{x}_i - \vec{x}_j|} \tag{1.1}$$

The last term is the Coulomb potential which arise from the proton charge, and will only be applied to them and banishes for neutrons. From now on, whenever this term appears, will only be referred to protons.

To simplify this Hamiltonian, we can apply the *mean field theory*. In this theory, each nucleon evolves in a mean field created by all the other nucleons. This

simplified Hamiltonian of the j^{th} nucleon can be written as:

$$\mathcal{H}_j = \frac{\vec{p^2}_j}{2m_i} + \sum_{i \leq j} V_{nuc}(|\vec{x}_i - \vec{x}_j|) + \sum_{i \leq j} \frac{e^2}{|\vec{x}_i - \vec{x}_j|} \tag{1.2}$$

and the total Hamiltonian of the nucleus could be expressed as the sum of each individual one:

$$\mathcal{H} = \sum_{j \text{ (neutrons)}}^{N} \mathcal{H}_j^{\nu} + \sum_{k \text{ (protons)}}^{Z} \mathcal{H}_k^{\pi} \tag{1.3}$$

This is a simplification, as the field created by the other nucleons depends on the j^{th} nucleon (in its position, for instance). This feed-back effect is ignored in this approximation.

The term V_{nuc} arises from the nuclear force, a residual interaction of the strong force. This force is attractive at distances of a few femtometers, but decreases rapidly with distance and is the main responsible of the bound state of nuclei. There are many expressions that describes the V_{nuc} potential, such as Yukawa or Wood-Saxon potential, but in first approximation it can be described as the sum of many square wells (one for each nucleon). Each well will have a range proportional to the nucleus radius, $R \sim 1.25A^{1/3}$ fm. For large A nucleus the depth of the well will be almost constant, $V_0 = 50$ MeV. When we sum many of these wells, the potential smooths and approximates to a parabola. In this simple approximation the nuclear potential can be written as:

$$V_{nuc} \approx -V_0 \left(1 - \frac{r^2}{R_0^2}\right) \tag{1.4}$$

If we assume that the proton charge is evenly distributed in a spherical nucleus, the Coulomb term is just that of the potential inside of a sphere of radius R_0 with an uniform charge $(Z-1)e$, where Z is the atomic number which denotes the number of protons.

$$V_{coulomb} = \frac{(Z-1)e^2}{R_0} \left(\frac{3}{2} - \frac{r^2}{2R_0^2}\right) \tag{1.5}$$

Thus, the mean field effective potential under the approximations described above is:

$$V_{eff} = r^2 \left(\frac{V_0}{R_0^2} - \frac{(Z-1)e^2}{2R_0^3} \right) - V_0 + \frac{3}{2}\frac{(Z-1)e^2}{R_0} \tag{1.6}$$

The Coulomb term makes the proton well slightly shallower and wider than for neutrons, due to the charge repulsion, and will be denoted as V_0'.

The harmonic oscillator frequencies in the potential are given by $\omega^2 = \frac{2}{\mu}\left(\frac{V_0}{R_0^2} - \frac{(Z-1)e^2}{2R_0^3}\right)$. In 3 dimensions, the eigenvalues of such potential are:

$$E_N = \hbar\omega \left(N + \frac{3}{2} \right) - V_0 \ (V_0' \text{ for protons}) \tag{1.7}$$

The harmonic oscillator quantum number N can be expressed as a function of the radial and orbital quantum numbers $N = 2(n-1)+l$. Since $l = 0,\ 1,\ ...,\ n-1$, the degeneration of the eigenvalues is $(N+1)(N+2)$ if the spin is included (two particles per state). These crude approximation correctly predicts the three first magic numbers (2,8 and 20), but there are discrepancies for the higher ones.

1.1.2 Spin-orbit interaction

To solve some of these discrepancies, the spin-orbit interaction must be taken into account. The potential of this interaction can be described as $\hbar^{-2}V_{so}(r)\vec{l}\cdot\vec{s}$, where $\vec{l}$ and $\vec{s}$ are the angular momentum and spin of a given nucleon. This potential is an additional term to the mean field potential described above.

If $\vec{j}$ is the total angular momentum of the nucleon, the spin orbit product can be calculated:

$$\vec{l}\cdot\vec{s} = \frac{1}{2}\left(\vec{j^2} - \vec{l^2} - \vec{s^2}\right) = \frac{\hbar^2}{2}\left(j(j+1) - l(l+1) - \frac{3}{4}\right) \tag{1.8}$$

The spin of the nucleon $s = \frac{1}{2}$ has already been taken into account, and gives as possibles values of the angular momentum $j = l \pm \frac{1}{2}$. Substituting in previous equation:

$$\vec{l}\cdot\vec{s} = \begin{cases} l\frac{\hbar^2}{2} & \text{for } j = l + \frac{1}{2} \\ -(l+1)\frac{\hbar^2}{2} & \text{for } j = l - \frac{1}{2} \end{cases} \tag{1.9}$$

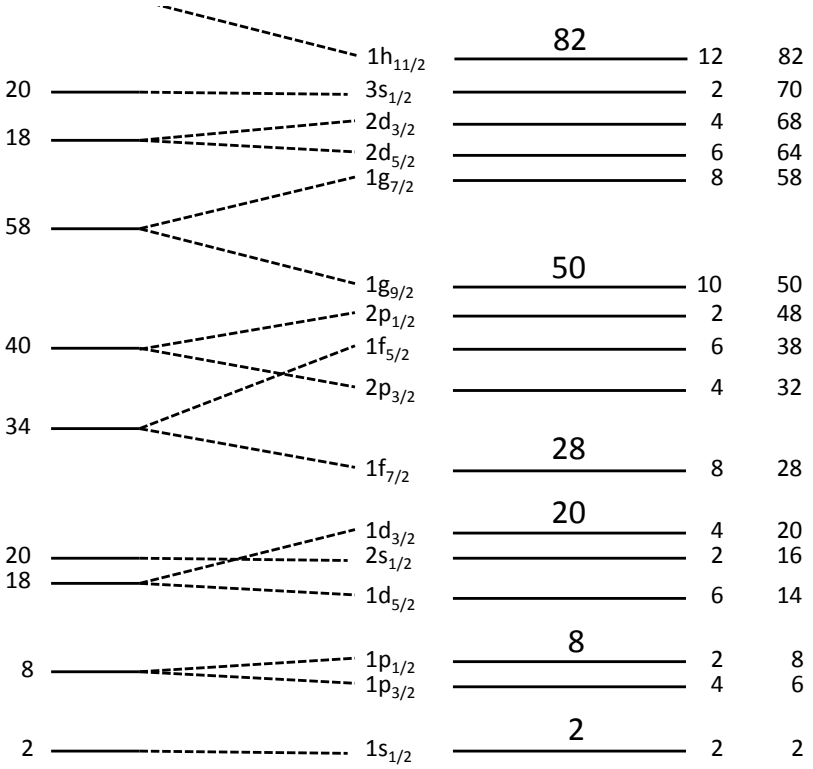

Figure 1.1: Orbitals sequence predicted by the shell model for spherical nuclei, including the spin-orbit coupling.

This result indicates that when the spin and the angular momentum are aligned $\left(j = l + \frac{1}{2}\right)$ this term is attractive and thus the state is more strongly bound. On the other hand, if the spin and the angular momentum are anti-parallel $\left(j = l - \frac{1}{2}\right)$, the potential will be repulsive and the system will be less bound, thus rising the energy of the orbital.

Thus, the spin-orbit coupling splits the energy levels. This split is directly proportional to the angular momentum l: $\Delta E = \frac{\hbar^2}{2}(2l + 1)$. This splitting also predicts correctly the higher magic numbers 2, 8, 20, 28, 50, 82... Fig. 1.1 shows the orbital sequence predicted for a spherical nucleus.

In spite of the many approximations and simplifications, this model can predict many properties of the nuclei near the Valley of Stability, such as the spin-parity of the ground state or the magnetic dipole and electric quadrupolar moments.

For instance, in the ground state of even-even nuclei, all the nucleons will be paired, thus having a total spin-parity of 0^+, as experiments have confirmed. In the case of an odd-A nucleus, the model predicts that it will be composed by an inert even-even core, and their ground state properties are given by the unpaired nucleon.

For this reason the model is known as the *single particle model*.

As we move away towards more exotic nuclei, some of this predictions start to fail. When there is a large abundance of one of the nucleons, neutrons for example, nuclei may not be spherical and the approximations made are no longer valid. In these cases the predicted orbital sequence may change, and the observed spin for the nuclei ground state are not those proposed by the shell model.

1.1.3 Deformed nuclei

The fact that the Shell Model fails to predict the ground state of some nuclei suggested that some of them may be deformed and the spherical approximation is no longer valid for them. S. G. Nilsson proposed in 1955 [26] a non-spherical potential for an anisotropic harmonic oscillator Hamiltonian $\mathcal{H}_0$:

$$\mathcal{H}_0 = -\frac{\hbar^2}{2m}\nabla^2 + \frac{1}{2}m\left(\omega_x^2 x^2 + \omega_y^2 y^2 + \omega_z^2 z^2\right) \tag{1.10}$$

and the total Hamiltonian of the nucleons will be given by:

$$\mathcal{H} = \mathcal{H}_0 + C(\vec{l}\cdot\vec{s}) + Dl^2 \tag{1.11}$$

$\vec{l}\cdot\vec{s}$ is the spin-orbital coupling described in the previous section, with $C = -2\hbar\omega_0\kappa$ giving the strength of the force. When nucleon moves away from the centre of the nucleus, the attracting force increases, which is the same as saying that the potential well deepens. To reproduce this effect, the l^2 (with $D = -\hbar\omega_0\kappa\mu$) term is introduced thus shifting the levels with higher l-values to lower energy. The κ and μ parameters are different for each shell and they are set to fit the experimental results.

If we assume axial symmetry along the z-axis, we can write:

$$\omega_x^2 = \omega_y^2 = \bar{\omega}^2\left(1 + \frac{2}{3}\epsilon_2\right) \tag{1.12}$$

$$\omega_z^2 = \bar{\omega}^2\left(1 - \frac{4}{3}\epsilon_2\right) \tag{1.13}$$

where ϵ_2 is the deformation parameter and $\bar{\omega}$ the system frequency. ϵ_2 was introduced by Nilsson and in first order is related to β_2 as $\beta_2 \approx 1.05\epsilon_2$. If volume conservation is imposed, the relation between frequencies is given by $\omega_x\omega_y\omega_z = \bar{\omega}_0^3$, where ω_0 is the frequency at no deformation (for a spherical oscillator). If we write the frequency as a function of the deformation parameter:

$$\omega_0(\epsilon) = \bar{\omega}_0 \left(1 - \frac{4}{3}\epsilon_2^2 - \frac{16}{27}\epsilon_2^3\right) - \frac{1}{6} \tag{1.14}$$

Fig. 1.2 shows the predicted orbital sequence as a function of the deformation parameter (positive values correspond to prolate shape and negative to oblate, see Fig. 1.3).

1.2 The neutron rich N=40 region

The magic numbers predicted in the spherical shell model points to energy gaps between the orbitals, giving as a result very stable nuclei. Double magic nuclei (those with a magic number of both protons and neutrons) are characterized by a high energy 2^+ first excited state with a very low B(E2). This predictions work very well along the Valley of Stability, but as neutrons are added to the nucleus its ground state may become deformed. This may lead to an inversion in the orbital sequence, making deformed intruder orbitals energetically favourable, eventually becoming the ground states. In such cases the magic numbers may change or even disappear, as nucleons occupy different shells than their stable counterpart. Such inversion of configurations was first observed in the $N = 8$ nucleus ^{11}Be [23] and has been thoroughly investigated in the *Island of Inversion* around the $N = 20$ nucleus ^{32}Mg, where deformed ground states emerge [24].

1.2.1 ^{68}Ni

^{68}Ni has 28 protons (Z=28 is a well established magic number) and 40 neutrons. When it was first studied by Broda and collaborators [7], they observed a high energy 2_1^+ state at over 2 MeV. They interpreted this energy as the characteristic signature of a double magic nuclei, and thus proposed that the N=40 sub-shell gap could be large enough for the arising of a new magic number 40 in the region.

The transition rate $0_1^+ \rightarrow 2_1^+$ was measured in Coulomb excitation and a low value of B(E2)=3.2(7) W.U. was found [8]. If N=40 is a shell closure, this

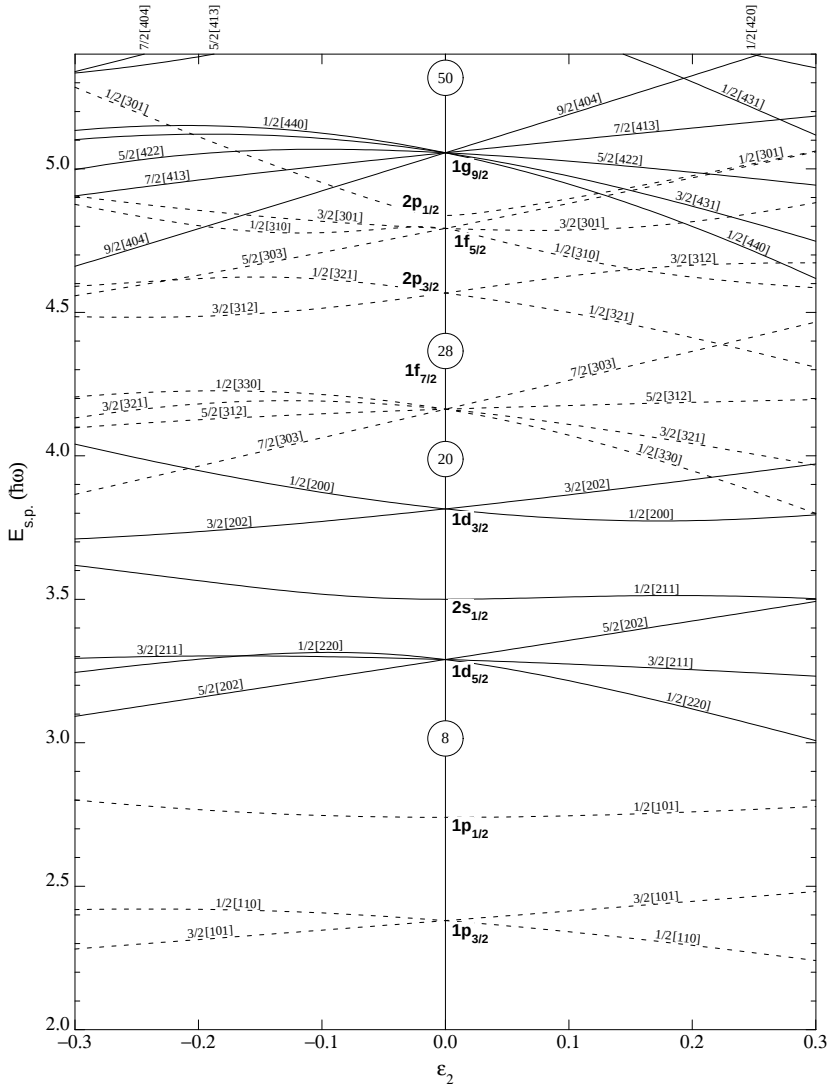

Figure 1.2: Nilsson diagram showing the orbital sequence as a function of the deformation parameter. Solid lines represent positive parity orbitals while negative parity is represented by dashed lines. At $\epsilon_2 = 0$ this diagram coincides with the spherical approximation shown in Fig. 1.1.

Figure 1.3: If the deformation parameter β_2 is negative the shape is called oblate (left). When β_2 is positive is called prolate (right).

value should be much lower, as the lowest 2^+ state would be produce by a 2p-2h configuration, which strictly has a limit of B(E2)=0 [5].

C. Guènaut *et al.* performed mass measurement with the ISOLTRAP ion trap in nickel, copper and gallium isotopes around the N=40 Z=28 region. They found no behaviour resembling that of the already established magic numbers. They did not found a shell or sub-shell closure from the pairing gap energy, but they suggested that a competing midshell stabilization effect might be present between N=40 and N=39, with some fine structure between them.

The possibility of a new magic number had been already demonstrated for Z=40 by the well known structure of ^{90}Zr [27]. On the other hand, Lister *et al.* [28] already studied the ^{80}Zr N=Z=40 and found it extremely deformed and no trace of a shell closure signature.

It has been argued that the high energy of the 2_1^+ state in ^{68}Ni is due to the fact that the two neutrons in the $p_{1/2}$ shell (which is filled in a N=40 spherical nucleus) cannot be coupled to form a 2^+ state. Due to the different parity of pf and $g_{9/2}$ orbits, the 2_1^+ state in ^{68}Ni cannot have a 1p-1h neutron component [29]. It will require the excitation of more than one particle to form a positive parity state, thus explaining the high energy.

1.2.2 The area below ^{68}Ni

In nuclei below ^{68}Ni the 2_1^+ states energy drops abruptly and their $B\,(E2)$ values increase, as can be seen in the systematics of the $E\,(2^+)$ and $B\,(E2)$ in the region presented in Fig. 1.4. These nuclei are characterized by an open proton shell that favours the development of quadrupole correlations.

Two protons below ^{68}Ni, the energy of the 2_1^+ state drops from 2033 keV to

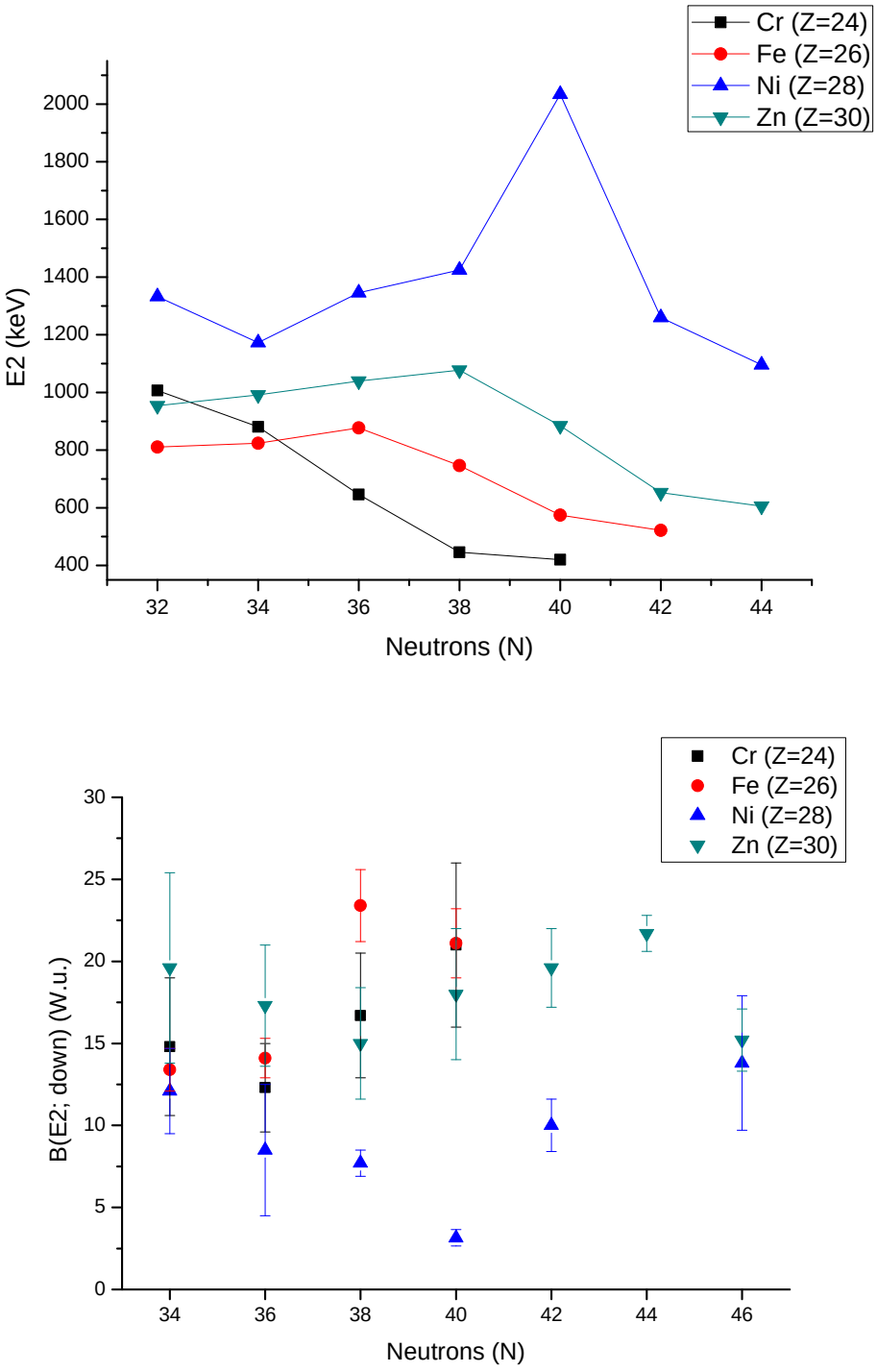

Figure 1.4: $E\left(2_1^+\right)$ evolution (top) and $B\left(E2\right)$ systematics (bottom) in the ^{68}Ni region. Data extracted from the Pritychenko *et al.* evaluation [30].

only 573 keV in ^{66}Fe [4]. This energy is even lower for ^{68}Fe with the 2_1^+ state at 517 keV[12], but higher for ^{64}Fe (746.4 keV [31]). The fact that as the number of neutrons increases the 2_1^+ state energy is lowered, suggests a rapid development of collectivity in the neutron rich Fe isotopes. Lunardi *et al.* [3] suggests that the $\nu g_{9/2}$ orbit plays an important role. The $\nu d_{5/2}$ orbital is also a key player in generating deformation by the quadrupole interaction with the $\nu g_{9/2}$, within the same major oscillator shell.

Another two protons below, the ^{64}Cr, which is in the middle of the proton shell (Z=24), has the lowest-lying 2_1^+ level experimentally reported at 420 keV and the onset of collectivity in the region [10]. This nucleus also has the largest value for the $B\left(E2; 2^+ \rightarrow 0^+\right)$, which has been recently measured at NSCL using the Coulex method to be $B\left(E2; 2^+ \rightarrow 0^+\right) = 21(5)$ *W.u.* [11]. Theoretical calculations by Lunardi *et al.* predict a strong quadrupole deformation, coming close to the rotational regime. The authors compare this situation with the $N = 20$ *Island of Inversion* around ^{32}Mg, and suggests that a similar situation can develop around ^{64}Cr.

1.2.3 The fp shell and the g and d intruders

The collectivity in this neutron rich region around $N = 40$ can be explained by the intruder $g_{9/2}$ orbital. The spin-orbit coupling splits the g orbital according to the spin in two configurations: the aligned $g_{9/2}$ is lowered towards the pf shell while the anti-aligned $g_{7/2}$ is raised up. This effect causes the $N = 40$ gap between the pf shell and the $g_{9/2}$ orbital to shrink. Moreover, as protons are added to the $f_{7/2}$ orbital, the relative energies of negative parity pf neutron orbitals ($p_{3/2}$, $p_{1/2}$ and $f_{5/2}$) also change due the strongly attractive neutron-proton tensor interaction [1]. Therefore, as the pf orbit is being filled, the excitation to the intruder positive parity orbital $g_{9/2}$ becomes more and more relevant.

The intruder $g_{9/2}$ orbital can be observed in the $9/2^+$ isomers of the odd nuclei in the region. These isotopes appear when there is an unpaired neutron in the $g_{9/2}^+$ orbital with no allowed transition to the $f_{5/2}^-$ or $p_{1/2}^-$. Fig. 1.5 shows the evolution of the $9/2^+$ isomers in the odd Fe isotopic chain. It is clear how it rapidly drops as neutrons are added, indicating how the fp-$g_{9/2}$ gap closes as we move away from stability. ^{57}Fe, ^{59}Fe and ^{61}Fe values were taken from [32], [33] and [34] respectively. For ^{63}Fe Lunardi *et al.* [3] claim to have observed gammas populating a $9/2^+$ isomer, but its energy could not be deduced. In an ISOLTRAP experiment a $9/2^+$ β-decaying isomer was identified in ^{65}Fe, but its energy could not be precisely measured [35]. The situation with ^{67}Fe is not clear, but a μs delayed component has been observed. It has been assigned to the first excited state by Grzywacz and

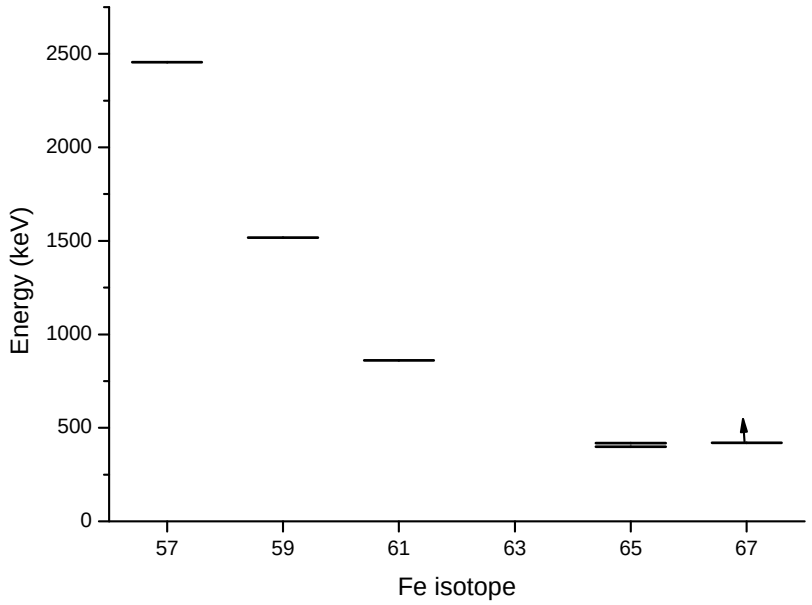

Figure 1.5: Evolution of the $9/2^+$ isomers in the odd neutron rich Fe isotopes. See text for details about the isomer energies.

collaborators [34] while Kameda *et al.* assigned it to the 366.8 keV level [36] (the second excited state). Daugas and collaborators claim that an isomer is situated above 420 keV (lower limit) and feeds the lower levels through unseen gammas [37]. Even if all authors agree in its positive parity and that it arises from the $\nu g_{9/2}$ orbital, its spin has not been definitely assigned and 5/2, 7/2 and 9/2 spins are possible.

Calculations using the fpg space can predict Ni excited levels with some succes, but such calculations fail when applied to Fe and Cr isotopes. Caurier and collaborators performed and compared calculations for Fe isotopes using fpg and $fpgd$ shell spaces [5]. fpg calculations were able to reproduce the 2_1^+ energy of Fe isotopes up to N=36, but overestimated the energy for more neutron rich isotopes. While the $d_{5/2}$ orbital was added, the 2_1^+ energy where nicely reproduced up to N=40.

This results were later corroborated by Ljungvall *et al.* [38]. They also compared calculations using fp, fpg and $fpgd$ spaces. Their conclusion was the need to include the $d_{5/2}$ orbital in the calculations to reproduce the 2_1^+ energy and B(E2) of Fe isotopes above N=36. There is experimental observation of a sudden increase in

collectivity from ^{62}Fe (N=36) to ^{64}Fe, when the $g_{9/2}$ and $d_{5/2}$ orbitals become crucial in the calculations, further corroborating the key role of these orbits in the region.

Lenzi, Nowacki, Poves and Sieja developed the LNPS interaction, based on a G-matrix obtained from a nucleon-nucleon interaction with the monopole part corrected to fit the experimental results [6]. The calculations also operated in the $fpgd$ space, using ^{48}Ca as a core. They concluded that when protons are removed from the $f_{7/2}$ shell, the attractive spin-orbit monopole with the $\nu f_{5/2}$ is weakened, which change the relative energy of the fp orbitals. This effect increases as neutrons are added, shrinking the gap and promoting neutrons to the $g_{9/2}$ orbital. As more protons are removed, neutrons are further promoted to occupy the $d_{5/2}$ orbital, leading to an increase in quadropole moments and thus deformation. They obtained the onset of deformation would be ^{64}Cr, bearing many similarities to the N=20 *Island of Inversion* and predicted a new one around this isotope.

1.3 Experimental motivation

The experimental information in Fe isotopes is of paramount importance for the understanding of the nuclear structure and the mapping of the onset of collectivity in the region. For this reason we performed an experiment using the Advance Time Delayed Method $\beta\gamma\gamma$(t) [13, 14, 15]. Neutron rich Fe isotopes were populated in the β decay of Mn ions. The use of the ATD method allows us to obtain simultaneously a detailed level scheme and level lifetimes of both odd and even nuclei.

The use of this method in the region can provide us with precise energies of the 2^+ and 4^+ states as well as the transition rates from the even nuclei. This elements are key to characterize the development of collectivity as neutrons are added to Fe isotopes.

Important information can be obtained from the odd nuclei as well. Identification of $9/2^+$ isomers can fill the gaps in the $g_{9/2}$ evolution in the region, which has been demonstrated fundamental in understanding the behaviour of nuclei below ^{68}Ni.

Chapter 2

The Advanced Time Delayed $\beta\gamma\gamma$(t) method

One of the best available probes we have to know the insight of the nuclear structure are the excited level half lives, as they provide with essential information about the transition matrix elements for comparison with theoretical nuclear models. The experimentally accessible range of nuclear lifetimes covers over 45 orders of magnitude. The micro and nanosecond range can be measured with delayed coincidence methods using HPGe detectors, while in the femto and picosecond range the recoil distance method and Doppler shift attenuation method can be employed. The Advanced Time Delayed (ATD) $\beta\gamma\gamma$(t) method is the best suited to measure half lives between a few picoseconds and several nanoseconds by using triple coincidences $\beta\gamma\gamma$.

The ATD method was invented by Henryk Mach in 1986 in the TRISTAN facility at Brookhaven National Laboratory. Later it was further developed and published by H. Mach, M. Moszynski an R. Gill [13, 14, 15]. As other delayed coincidence methods, it is based in the time distribution since the population of an excited state and its de-excitation. The population of the studied level follows the β-decay of the parent nucleus, so the emission of the β-particle must be detected by an appropriate detector. This level will be de-excited by a γ-ray, which must also be recorded by a suitable detector. The time distribution between these two events (measured with a Time-to-Amplitude-Converter, TAC) will give us the half life of the excited level. When the decay pattern is not simple enough to perform $\beta\gamma$ coincidences, a third detector may be used with very high energy resolution to select a specific gamma cascade, thus the $\beta\gamma\gamma$(t) coincidences.

What follows is a description of the ATD $\beta\gamma\gamma$(t) method, the information mainly extracted from [13, 14, 15, 39, 40] and the author personal experience while

analysing data using this method.

2.1 Experimental setup

The ATD method is based in triple coincidences between a β-particle and two γ-rays. To measure picoseconds lifetimes, two of them must be very fast. A thin and fast plastic detector will measure the β particles while a scintillator crystal with good timing resolution is used for the γ-rays. The second γ-ray is detected by the HPGe detector, characterised by its good energy resolution. This way this method combines good energy resolution with good timing properties.

Fig. 2.1 shows an overly simplified version of the standard electronic setup of an ATD experiment. There are two TACs, both started by the plastic scintillator. The so called *fast-TAC* measures the time difference with the fast timing crystal scintillator (thus called fast because it will be able to measure the shortest half lives), while the *slow-TAC* is stopped by the HPGe detector (which will be used to measure longer half lives). The amplified signals of these three detector will be recorded as the energy of the events detected. While the half life is usually obtained from the fast-TAC, the HPGe detector is used to select a specific gamma cascade within the level scheme, thus acting as a filter. For a much more detailed experimental setup specific to the IS474 experiment see Sec. 3.2.

2.1.1 Detector selection

The curve describing the relative time differences from recording events of the same type (β, Compton or full-energy gamma) but different energy is called the *walk-curve*, which is specific for each pair of electronic-detector. As the delayed coincidence methods involve two timing detectors, this correction is very complicated, moreover in the case of β particles due to its continuous energy spectrum. Hence,the main difference of the ATD method compared to other delayed coincidence methods is the use of a thin plastic scintillator $\triangle$E. By using a very thing detector, it is ensured that all the energetic β-particles deposit a similar amount of energies, thus giving a similar time response.

The scintillator plastic commonly used in ATD experiments is a NE111A coupled to a Photonis XP20D0 photomultiplier tube (PMT). As mentioned above, it is $\triangle$E type by using a 3 mm thickness plastic, which not only ensures a constant time response, but also a volume small enough so the γ-ray detection efficiency is negligible. With a typical diameter of 1.3 cm and situated about 5 mm away from the source, it covers a solid angle of $20 - 25\%$ of 4π. To shield it from conversion

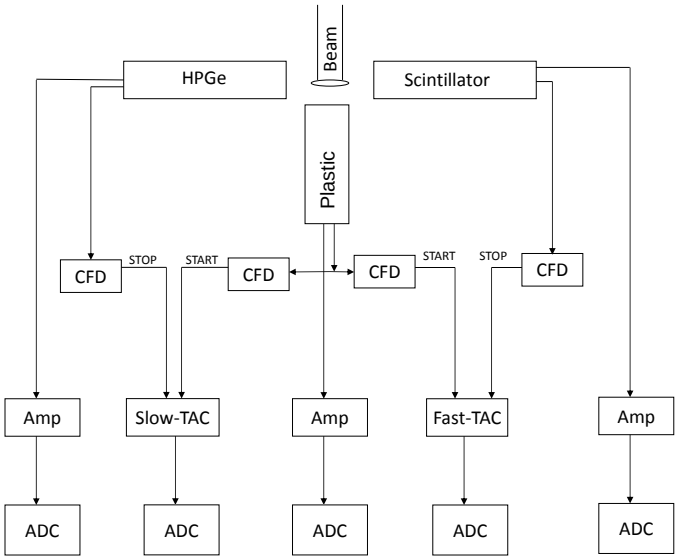

Figure 2.1: An oversimplified scheme of the standard electronic setup for an ATD experiment.

electrons of up to 500 keV an aluminium foil is situated between the radioactive source and the detector.

When the method was first developed, the chosen fast timing crystal was the BaF_2 with a truncated cone shape called Studvik design, which has a timing resolution similar to that of a plastic scintillator, but with much better energy resolution [41]. Since then, new inorganic scintillators have been developed and the common choice nowadays for fast timing experiments are the $LaBr_3$(Ce) crystals coupled to Photonis XP20D0 PMTs. This crystals further increase the energy resolution of the BaF_2 crystals and have a comparable timing resolution.

The optimal shape for $LaBr_3$(Ce) is a truncated cone of 45 mm height, 43 mm diameter at the bottom and 32 mm diameter at the entrance window (see Fig. 2.2 for a scheme). A smaller crystal would have better timing resolution at the cost of a much lower detection efficiency, and, vice versa, larger crystals would have better efficiency at the cost of worse timing resolution. So the volume is a compromise between timing and efficiency while the truncated cone shape improves the light collection.

The crystals are encapsulated in a thin aluminium enclosure to stop electrons and the lateral faces are covered by several layers of lead to avoid backscatter gammas from other detectors or the aluminium frame. Thanks to the truncated cone shape the crystals can be positioned very close to the radioactive source, covering a

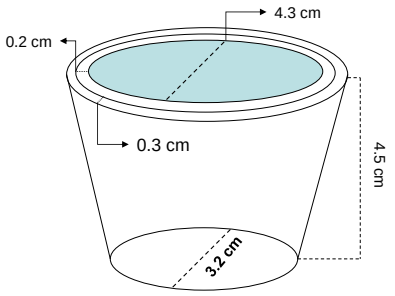

Figure 2.2: Scheme of the $LaBr_3(Ce)$ truncated cone with aluminium encapsulation. This image is courtesy of E. Picado.

solid angle near $\sim 7\%$ of 4π.

HPGe detectors are chosen for its incomparable energy resolution and their peak-to-background ratio. But to achieve this energy resolution it is necessary a 2 μs shaping time. This limits the source intensity in order to avoid signal pile up which would distort the measurement. They are positioned about 5 cm away from the source (see Fig. 3.9 for picture on the dispositions of the detectors during the IS474 experiment).

The system efficiency is designed for measurements of sources with an intensity up to 50.000 Bq (of which the system would detect 15-20 kBq) for about ten days. This ensure that enough data is collected so the statistic is good enough to achieve the desired timing resolution and satisfactory results.

2.1.2 Detector arrangement

There are two standard configurations for the detector arrangement in the ATD method experiments: the saturated beam and the moving tape.

Saturated beam In this configuration an isobar beam of the selected mass is continuously deposited at the deposition point creating a saturated radioactive source.

The experimental chamber, where the ions are deposited, is an aluminium tube of 2 cm of diameter, 1.5 mm thickness lateral walls and a front end with a thin wall of about 0.3 mm. The radioactive source size is given by the beam quality, which, in the ISOL technology case, are very compact beams. If needed, a lead collimator can be introduced in the aluminium tube to further shrink the beam dispersion. The diameter of the collimator (of about 5 mm) is slightly smaller than the beam particle, to minimize the changes in the source position, even at the cost of beam intensity. The beam size and position are fundamental for the fast timing experiments, as each millimetre deviation means $3.\bar{3}$ ps time resolution broadening (approximately the time it takes a photon to travel one millimetre), within the time precision of the ATD method.

The β plastic detector sees the source through the thin aluminium wall. A small gap is left between the detector and the deposition point in order to protect it from possible accidental movements of the beam line. It also allows to place calibration sources in the same point where the beam is deposited, thus reproducing for the off-line calibrations similar conditions than the on-line measurements.

The scintillator crystals are positioned above and below the β-plastic detector and as close as possible to the radioactive source in order to increase the efficiency. The truncated cone shape helps the compact close geometry arrangement of the detectors. γ rays are collimated to the centre of the crystals through an opening in their lead shielding. This lead shielding not only minimize backscatter Compton from other detectors, it also decrease the number of Compton events, as they are more likely to happen when the gamma impacts near the crystal walls. An aluminium foil stops the β-particles emitted by the source or scattered by the other detectors, but it is thin enough to allow γ-rays through without significant loose of energy.

Moving tape If any of the isotopes in the decay chain of the selected mass or possible contaminants have a long half life (usually half lives of several hours and above), they can accumulate in the experimental chamber and build up an activity such that saturates the system. To avoid this, the beam is deposited in an aluminized Mylar tape at about 50 cm away from the detectors. After a suitable collection time the tape is cycled moving the deposited ions to the detectors station, with a time-step calculated to maximize the studied parent nucleus activity. The detector station is basically the same as described in the saturation beam configuration, but usually there is only room to use one HPGe detector instead of two.

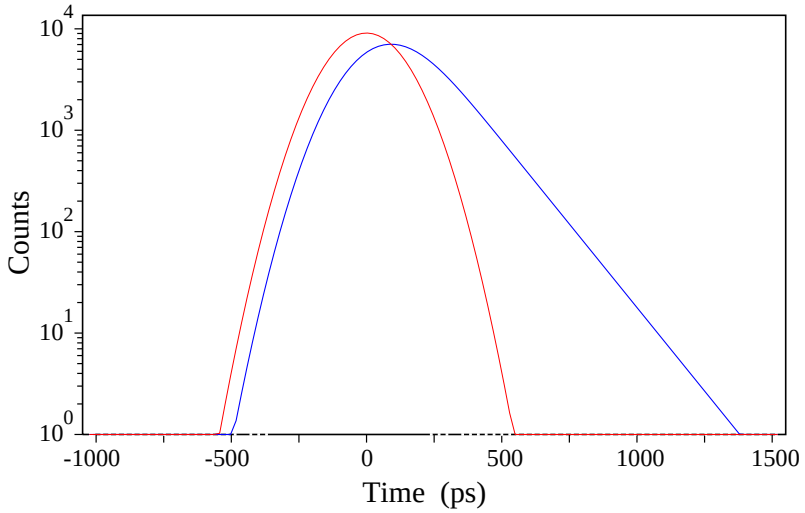

Figure 2.3: The red line shows a prompt distribution while the blue shows a convoluted time distribution with a slope in the delayed part.

2.2 Techniques of data evaluation

Neutron rich nuclei are characterized by having large Q_β values, up to 15 MeV, and by populating excited levels in the 2-4 MeV range. In a typical β disintegration some high energy levels are populated that de-excite to the ground state through gamma cascades that do not involve a large number of transitions. Is in this cases when the ATD $\beta\gamma\gamma$(t) method is most useful.

The following procedures are the two different techniques used in the ATD method to extract level half lives. Each works for a different time range, but both of them rely on the precise calibrations described in Sec. 4.2.

2.2.1 Convolution technique

When the level half life is long enough to appear as a slope on the delayed part of the time distribution (see Fig. 2.3), it can be obtained directly by fitting the slope. The delayed part can be fitted to an exponential decay or, more accurately, the whole spectrum can be fitted using a convoluted function. This technique makes a least square fit via an iterating method where the exponential decay and prompt time distribution are unfolded from the time spectrum obtained during the experiment.

The delayed time spectrum can be expressed as:

$$F(t_j) = \mathrm{N} \int_0^{+\infty} P(t_j - t) f(t) dt \tag{2.1}$$

where the number of events observed in time t_j are due to events at time t, that have been shifted by the time jitter of the detector. N is the total number of counts in the time spectrum, $P(t_j)$ is the function that characterizes the prompt time distribution and $f(t) = e^{-\lambda t}$ for $t > 0$ with λ being the decay constant of the level $\left(\lambda = \frac{\ln(2)}{T_{1/2}}\right)$.

Even if the prompt time spectrum should be determined by the obtained experimental distribution, it can be approximated to a Gaussian function. Then, the time distribution can be expressed analytically as:

$$F(t_j) = \gamma \int_A^{+\infty} e^{-\delta(t_j - t)^2} e^{-\lambda t} dt \tag{2.2}$$

$$F(t_j) = -\frac{\sqrt{\pi}\gamma}{2\sqrt{\delta}} \cdot e^{-\lambda t - A + \frac{\lambda^2}{4\delta}} \cdot \mathrm{erf}\left(\frac{2\delta(t_j - t) - \lambda}{2\sqrt{\delta}}\right)\Bigg|_{t=A}^{t=+\infty} \tag{2.3}$$

where γ is a normalization factor, δ is a parameter related to the width of the Gaussian prompt distribution and A is the centroid of the Gaussian which is related, but not necessarily equal to, the position of the prompt. $erf(t)$ is the Gauss error function, a non-elementary function of sigmoid shape.

This technique works for half lives of over 60 ps and abundant statistics. For distributions with low number of counts or half lives above few nanoseconds, a χ^2 fit underestimates the half life and the fit should be done using Poisson statistics. This problem can be avoided if there is the possibility to measure the half life through several gammas. The different time spectra are added together, thus increasing the total statistics. Another alternative is compressing the time spectrum. This way the number of counts per channel is also increased, at the cost of having less points to fit. The fitting is repeated for different compression factors and the obtained half life is slightly larger with each compression level, until a stable value is reached.

Depending on the electronic setup, the experimental prompt distribution may show asymmetries, even an apparent slope in the delayed part. In cases where these apparent slope is comparable to the half life measured, the Gaussian approximation

is invalid. Another secondary effect are small tails three orders of magnitude below the main distribution, and they can appear at either side. They emerge due to pile-up effects and should be excluded in centroid calculation and convolution fit, even if its effect, when included, would be minor and they can be corrected or incorporated in the systematic errors.

2.2.2 Centroid shift technique

In the case of shorter half lives, below a general limit of 60 ps limit (more precisely 1/3 of the FWHM of the crystal timing resolution) and down to 5-10 ps (depending on the amount of statistic and the experimental conditions) the centroid shift technique is used. This technique, specially, relies on the precise calibrations of the timing detector for the β, Compton and full-energy peak events, as each of them will trigger a different time response in the scintillators.

The experimental time distribution obtained in the limit $\tau \to 0$ is called *prompt time distribution*. Assuming that the time distribution of prompt mono-energetic events in a given detector is Gaussian (which is a good approximation down to three orders of magnitude) the centroid position of this distribution will be determined only by its energy (for a given experimental conditions). Another gamma of the same energy but de-exciting a non-prompt level ($5 < \tau < 60$ ps) the centroid of its time distribution will be shifted by the mean-life of the parent level (see Fig. 2.4).

Depending on the level structure, one of the following analysis is performed in the centroid shift technique.

Sequential transitions

We have two gamma transitions, γ_1 and γ_2 from the simple level scheme shown in Fig. 2.5. If we select γ_1 in the HPGe detector and γ_2 in the scintillator crystal, the plastic detector would necesarily have detected a β_2 decay to level 2, as it is the only β feeding level 2, whose de-excitation we have observed with the inorganic detector. With this setting, the time distribution T_1 recorded will be

$$T_1 = \tau_0^{(2)} + \tau_2 \tag{2.4}$$

where τ_2 is the mean life of level 2 and $\tau_0^{(2)}$ is the prompt time response in the scintillator by a gamma of the same energy as γ_2. The level 1 lifetime (τ_1) would not contribute to the time distribution, as the fast-TAC gives the time difference

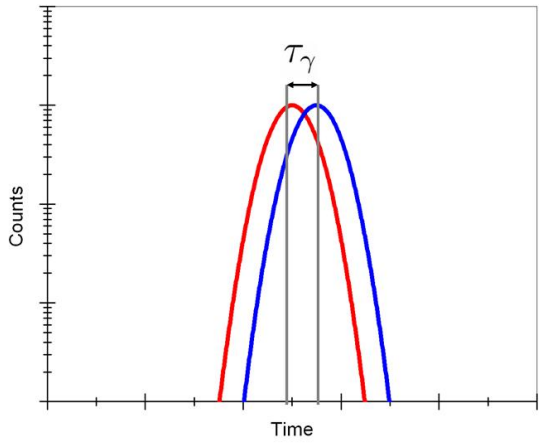

Figure 2.4: The parallel, sequential and absolute transitions analysis are encompassed in the centroid shift technique, which relies on measuring the shift of the studied γ time distribution (blue) from the prompt reference calibration (red).

Scintillator	HPGe	Time
γ_1	γ_2	$\tau_1 + \tau_2 + \tau_0^{(1)}$
γ_2	γ_1	$\tau_2 + \tau_0^{(2)}$
γ_1	γ_4	$\tau_1 + \tau_3 + \tau_4 + \tau_0^{(1)}$
γ_1	γ_5	$\tau_1 + \tau_4 + \tau_0^{(1)}$
γ_4	$\gamma_{(1,2,3)}$	$\tau_4 + \tau_0^{(4)}$
γ_1	γ_6	$\tau_1 + \tau_6 + \tau_0^{(1)}$

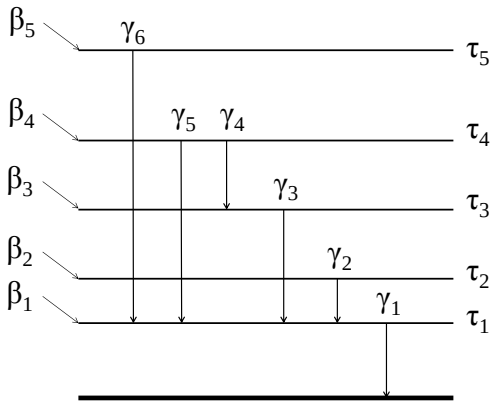

Figure 2.5: Very simple level scheme populated by β-decay to illustrate the centroid shift technique. Gates combinations between the fast timing scintillator crystal and the HPGe with the time distribution obtained are given in the table next to it.

between the plastic and the crystal scintillator and in this case the event detected by the HPGe will necessarily arrive at a later time.

If we take the inverse gate selection, γ_2 in the HPGe and γ_1 in the scintillator crystal, the TAC would record the mean lives of levels 1 and 2 plus the prompt time response $\tau_0^{(1)}$ for a gamma of energy γ_1.

$$T_2 = \tau_0^{(1)} + \tau_1 + \tau_2 \tag{2.5}$$

The centroid shift between these two time distributions give us:

$$T_2 - T_1 = \tau_1 + \tau_0^{(1)} - \tau_0^{(2)} \tag{2.6}$$

If γ_1 and γ_2 have similar energies, their prompt time responses should be very similar, thus approximating $\tau_0^{(1)} - \tau_0^{(2)} \approx 0$. In this circumstance we obtain directly the mean life of level 1 as:

$$\tau_1 = T_2 - T_1 \tag{2.7}$$

This kind of analysis can be applied, in principle, to longer gamma cascades, not only limited to two transitions. But in practice, when the number of gammas is bigger, the complexity of the analysis grows considerably and the chances that the full-energy peaks overlap in the scintillator spectrum are very high.

Parallel transitions

When we want to measure the mean life of a level whose depopulating gammas are not in a direct cascade as in the previous example, we can make use of parallel transitions. If in the level scheme shown in Fig. 2.5 we select γ_4 in the HPGe detector and γ_1 in the scintillator crystal, the plastic detector would have necessarily detected β_4 and the time response T_4 measured by the TAC between β_4 and γ_1 will be:

$$T_4 = \tau_0^{(1)} + \tau_1 + \tau_3 + \tau_4 \tag{2.8}$$

Now, if instead of choosing γ_4 in the HPGe, we choose its parallel transition γ_5, the time response T_5 will be:

$$T_5 = \tau_0^{(1)} + \tau_1 + \tau_4 \tag{2.9}$$

As this gamma cascade does not go through level 3 (γ_5 goes directly from level 4 to level 1), its lifetime will not contribute to the time distribution. This way, the centroid shift between T_4 and T_5 distributions will give as τ_3:

$$\tau_3 = T_4 - T_5 \tag{2.10}$$

The main advantage of the parallel transitions over the sequential ones is that, as we chose the same transition γ_1 both times in the scintillator crystal, the prompt time response will be the same and they will cancel out when we calculate the centroid shift. With this technique it is not necessary to use the *prompt calibration curve*, avoiding complications and sources of errors during the analysis.

Absolute comparison

The parallel and sequential transitions described above are rather ideal situations which will not happen very often in real experiments. In most cases the level scheme will be much more complex, with several gammas contributing to the time distributions or the higher energy transitions will not have enough statistics to accurately calculate the time centroid distribution in $\beta\gamma\gamma(t)$ coincidences. In this cases the ATD method employs the absolute comparison technique, which relies on the *prompt calibration curve*. This calibration can be obtained in up to three different ways.

The prompt position for a given energy can be measured from the time distribution of a gamma depopulating an excited state which half life is precisely known. For example, we precisely know the mean life of level 2, τ_2, in Fig. 2.5. In this case, we could measure the prompt response of the detector, $\tau_0^{(2)}$, for a γ_2 energy, by selecting γ_2 in the scintillator and γ_1 obtaining:

$$T = \tau_0^{(2)} + \tau_2 \tag{2.11}$$

as we know τ_2, the time response is just:

$$\tau_0^{(2)} = T - \tau_2 \tag{2.12}$$

By using several gammas with known lifetimes, we can construct the *prompt calibration curve*, covering a wide energy range. As usually it is a very smooth curve,

if we wish to measure the half life of a level using a gamma for which we do not have a prompt reference with the exact same energy, it can be interpolated from the points in the curve.

If one of the gammas presents a clear slope in the delayed time distribution and its level is not populated by higher energy gammas (γ_5 in level 4, for example) its half life can be obtained using the convolution analysis (see Sec. 2.2.1). Knowing its mean life the prompt response can be obtained from the time response:

$$\tau_0^{(5)} = T - \tau_4 \tag{2.13}$$

The third method is based on a characteristic of some nuclei in which a large number of transitions feed a low-lying state which then de-excites to the ground state (a simple example would be level 1 in Fig. 2.5, which is fed by γ_2, γ_3, γ_5 and γ_6). If we select any of the higher energy feeding transitions γ_i in the HPGe detector, we will see γ_1 in the fast timing crystal. All these gammas selected in the HPGe detector will provide the same time response:

$$T_i = \tau_0^{(1)} + \tau_1 + \tau_i \tag{2.14}$$

Nuclear levels at high energy are characterized by femtosecond half lives. If we have several levels which de-excite only by transition above 2 MeV, it is safe to assume that they do not have lifetimes above 1 ps, and much more that not all of them have such a long half life. In this circumstances, for a group of transitions with energy above 2 MeV, that provide the same time response T_i and that is the lowest for all the gammas feeding the low-lying level, we can set $\tau_i = 0$ (it is below the precision of the ATD method, so it can be considered prompt) and know the value of $\tau_0^{(1)} + \tau_1$.

In the example shown in Fig. 2.5, we would take γ_6 in the HPGe and γ_1 in the scintillator. The time response T_6 would be given by:

$$T_6 = \tau_0^{(1)} + \tau_1 + \tau_6 \tag{2.15}$$

Now assuming that level 6 is high and γ_6 energy is larger than 2 MeV, it would be safe to approximate $\tau_6 \approx 0$:

$$T_6 = \tau_0^{(1)} + \tau_1 \tag{2.16}$$

Now we could measure the mean lives of levels 2, 3 and 4. For example, for the level 2 lifetime, we could use Eq. 2.6 and 2.16

$$T_2 - T_6 = \tau_2 + \tau_0^{(1)} + \tau_1 - (\tau_0^{(1)} + \tau_1) = \tau_2 \tag{2.17}$$

Independently of the way we obtain it, once we have characterized the time response of the scintillator crystal, we can, hipothetically, measure any half life in a given level scheme. In practice the energy resolution of the timing detector is a limitation, as even with the help of the HPGe coincidences most peaks can have contributions from similar energy transitions. Also, when working in $\beta\gamma\gamma$ coincidences, the statistics may be so low that centroid position can not be accurately determined.

2.3 Concluding remarks

The Advance Time Delayed $\beta\gamma\gamma$(t) method allows the measurement of half lives in a range from a few picoseconds to the tens of nanoseconds. The lower limit of the method is caused by statistics, the time resolution of the scintillator crystals and the uncertainties in the calibrations, while only the electronic hardware and the TAC range set and upper limit. In ideal cases, half lives below the picosecond have been measured, but the statistics to do so are out of reach for the actual on-line measurements.

The method is most reliable when applied to simple level schemes, for which most of the different techniques described above could be used, but for most nuclei only the use of a carefully calibrated prompt reference curve would allow the measurement of lifetimes. When possible, the different techniques of the method allows us to measure the same half life in several independent ways, serving as a verification of the goodness of the results.

Since its introduction, this method has been applied at several facilities and in a wide number of regions of the nuclear chart, providing valuable data in the nuclear structure and systematic evolution of numerous nuclei. The method next step is the FATIMA experiment, which will be built for FAIR at GSI. It will be composed by a large array of $LaBr_3$(Ce) crystals and HPGe detectors that will cover almost a 4π solid angle. The electronic involved will stretch the ATD method to a new limit and the consequent analysis of such complex experiment will represent a formidable challenge in the years to come.

Chapter 3

Technical details

One of the most interesting properties for nuclear structure are the reduced probabilities of transitions, which depend on several characteristics, as energy of the gamma, branching ratio or the half life of the excited state. In order to measure many different properties of exotic nucleus at the same time, the Advance Time Delayed method relies on the characteristic of different detectors and very precise electronics.

The experimental study of the properties of exotic nuclei requires the use of large and complex facilities as well as delicate and precise detectors and electronics. These exotic radioactive nuclei are not found in nature, so they must be created in laboratories. One of the methods to create such nuclei relies on the impact of high energy protons onto heavy targets, where different nuclear reactions occur, creating all kinds of different isotopes. The amount of the desired isotope created inside the target is only a tiny fraction of the total, so it must be separated from the rest of the by-products. If the amount of contaminants is high enough, the data which is being looking for may be buried under huge amount of random or undesired events, difficulting the analysis or even rendering the collected data useless. For these reasons, beam purity and production yield are some of the main concerns when choosing the facility for the experiment.

The experiment IS474 was performed on August 2010 at ISOLDE in CERN, Geneva, by the Fast Timing Collaboration. The list of participants was: B. Olaizola, L.M. Fraile, H. Mach, J.A. Briz, J. Cal-Gonzalez, D. Ghita, W. Kurcewicz, S. Lesher, D. Pauwels, E. Picado and D. Radulov.

3.1 ISOLDE

The Isotope Separators On-Line (ISOL), mass separators or electromagnetic separators make use of the fact that charged particles are deflected when they travel through a magnetic field and the angle of that deflection depends on their charge-to-mass ratio. If all the atoms are singly ionized (thus having the exact same charge), the bend of the curve they will describe when entering the magnetic field will depend only on their masses. By placing a thin slit inside the magnetic field, only a given mass will have the exact bent trajectory to go through, while stopping all the others and preventing them to contaminate the experimental area.

The first large scale and, currently, world leading ISOL facility is ISOLDE, at CERN, in the Franco-Swiss border near Geneva. Schematically, it consist on a device that accelerates protons, a heavy target where they impact and produces the desired isotopes, an ion source that ionizes them and a mass separator that select the isotopes by their mass to charge ratio (see Fig. 3.8). Among its most notable characteristics that made the facility ideal for this experiment are: the precise optics that focus the radioactive beam almost to a point (key feature in fast timing analysis), the high precision of the isobaric separation and chemical differentiation, as well as the low energy but high intensity of the delivered beams, fundamental for the study of beta decay.

When not cited otherwise, all the information in this section (Sec. 3.1) was obtained from Ref. [42], a paper by E. Kugler describing the ISOLDE facility, .

3.1.1 Linac-2

The protons that will impact on the ISOLDE target begin their journey at the linear accelerator known as Linac 2. Even if not a part of the ISOLDE facility, it plays a crucial role in its operation, as it is where the protons are produced and injected in Proton Synchroton Booster (PS-Booster or PSB). The 50 MeV injected proton pulses are 200 μs length, for a total maximum intensity of 180 mA [43].

The protons are generated in a hydrogen plasmatron ion source with a 90 kV extraction potential, which can generate a current of up to 300 mA. The main accelerator is a Drift Tube Linac of standard Alvarez design. The three accelerating tanks (see them in Fig. 3.1), accelerating the beam up to 10.3, 30.5 and 50 MeV respectively, have in common the radio-frequency (202.56 MHz) and add up for a total length of 33.3 meters [44].

The 180 mA current generates very intense space charge forces, so very precise beam optics are required. Pulsed electromagnetic quadrupoles placed inside the

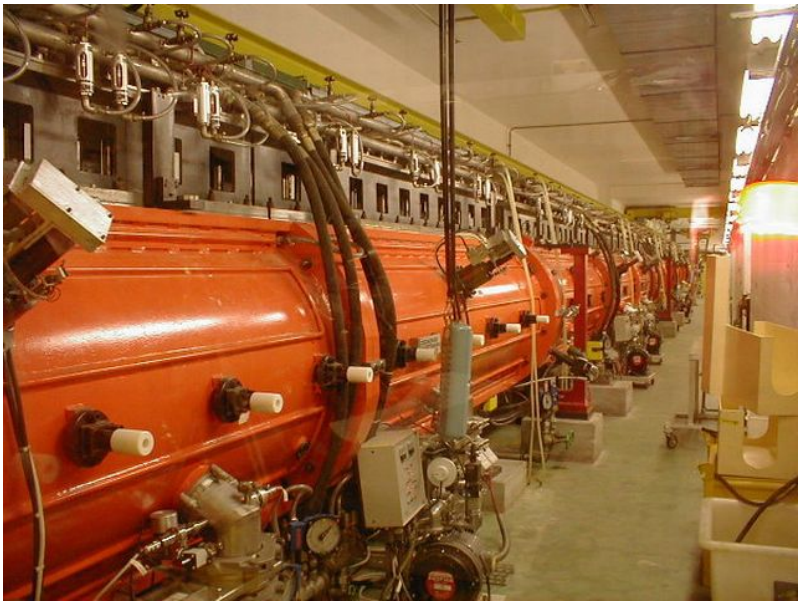

Figure 3.1: Picture of the Linac-2 acceleration tanks, which accelerate the protons to inject them into to the PS-Booster.

drift tubes focus the beam to minimize emittance below 50% of the accepted limit [45].

At the end of the accelerating tanks, a line of over 100 m transports the beam up to the connection point to the PS-Booster line. At the junction with the PSB, additional magnets are installed in order to minimize the dispersion and convert the beam to a more ordered FODO structure. First, a bending magnet generates horizontal dispersion. A second bending magnet deflects the beam in opposite direction. Finally, there are measurement lines for emittance and beam energy and a number of quadrupoles to match the the beam into the PSB [46].

In recent years, it has been brought into consideration to increase the intensity delivered by Linac 2, but the space charge tune shift at 50 MeV, in the PSB injections, limits the maximum total intensity. The only way to surpass this limitation is by increasing the linac energy, which can only be achieved by building a new machine. Linac 4 has already been commissioned and it is expected to deliver low-current long-pulse hydrogen beams at 160 MeV by the end of 2017 [47].

3.1.2 PSBooster and its proton cycle

The second step in the proton acceleration is the Proton Synchrotron Booster (PS-Booster or PSB), even if, again, it is not part of ISOLDE itself. It receives the

protons from the Linac 2 (Linac 4 in the future) at 50 MeV and accelerate them to 600 MeV, 1.0 or 1.4 GeV before delivering them to the different facilities (see Fig. 3.2). It consists of 4 superimposed rings for 25 metres of diameter and has 32 dipoles and 48 quadrupoles, each a stack of 4 magnets for each of the 4 rings [48]. It delivers pulses of up $3.6 \cdot 10^{13}$ protons, with a length of 2.4 μseconds, every 1.2 seconds with an average intensity of 1.5-2 μA [49].

There are several clients for the proton delivered by the PSB every 1.2 second. The pulses are organized in a super-cycle to periodically distribute the bunches to the different facilities. Traditionally, the super-cycles were 12 or 14 pulses long, delivering approximately every other one to ISOLDE. More important, this supercycles were very stable and its structure did not change often over time.

With the recent addition of the LHC to the client list of the PSB, the scenario has changed completely. Now the total length of the super-cycles is not fixed, varying in a wide range from 30 up to 50 cycles. During the IS474 experiment the supercycle length oscillated from 33 to 38 pulses. ISOLDE no longer receives every other pulse, but a much more random sequence, from consecutive protons to gaps of up to 3 or even 4 pulses apart. Now this supercycles structure changes very often, every hour or even more often.

The CERN master timing system emits a signal each time it receives a pulse, which can be recorded during experiments to later reconstruct the supercycle. This information allows to measure isotopes half lives, as there is a time frame reference since the creation of each isotope. But a problem arises when ISOLDE receives a proton pulse while the DAQ system has dead time (during write out, for example). In this case one proton pulse would not be recorded and the isotopes created in that impact would be considered at least 1.2 seconds (actually the time difference with the previous pulse) "older" than they really are. When the supercycle was simple and did not suffered changes often, it was easy to notice missing proton pulses (by comparing with previous and subsequent pulses, for instance). But now that it changes so often, it is too much effort to reconstruct it for a very small gain (estimations suggest that the data lost is below 3%).

3.1.3 Target

From the PSB the protons come through the transfer line into the ISOLDE facility itself, where they can be directed to either target (there is on for the HRS separator and another for the GPS, explained in detail in the next section), where several types of fission, fragmentation and spallation nuclear reactions will occur. By varying several factors, as the beam energy, chemical composition or thickness of the target, a wide range of isotopes can be produced at ISOLDE. Currently, the facility is

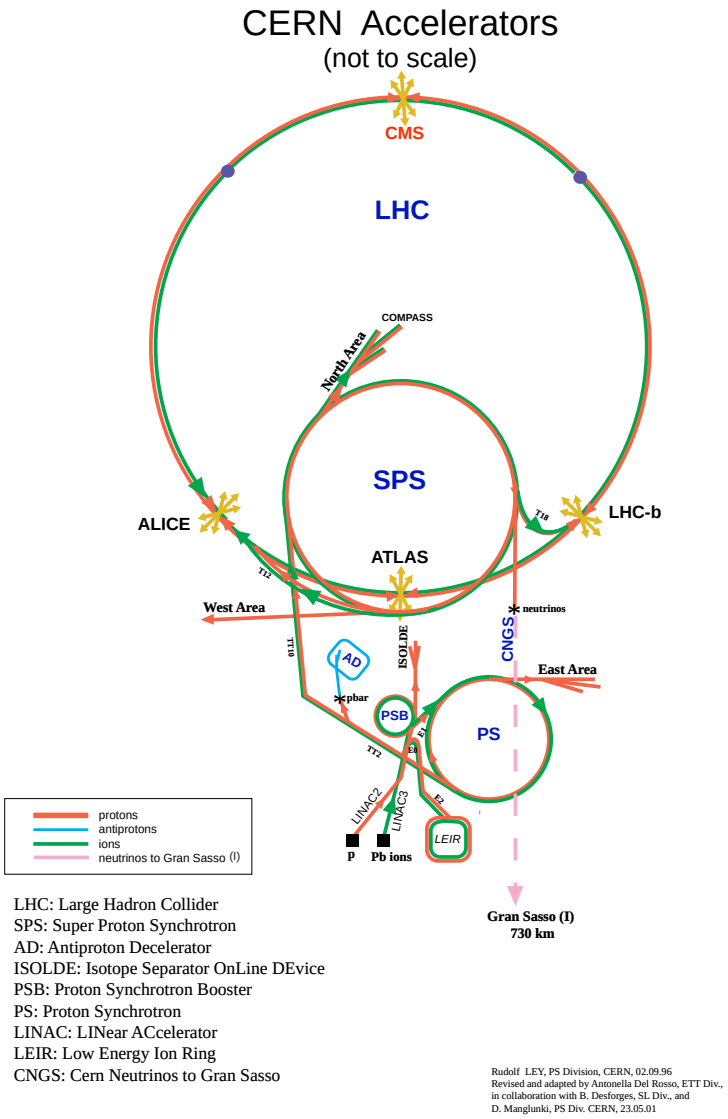

Figure 3.2: Map of the different accelerators at CERN, Geneva. At the bottom we can see the Linac 2 that supplies the protons to the PS-Booster, which accelerates the protons to 1.4 GeV and then inject them to ISOLDE (just below the big LHC ring in the image).

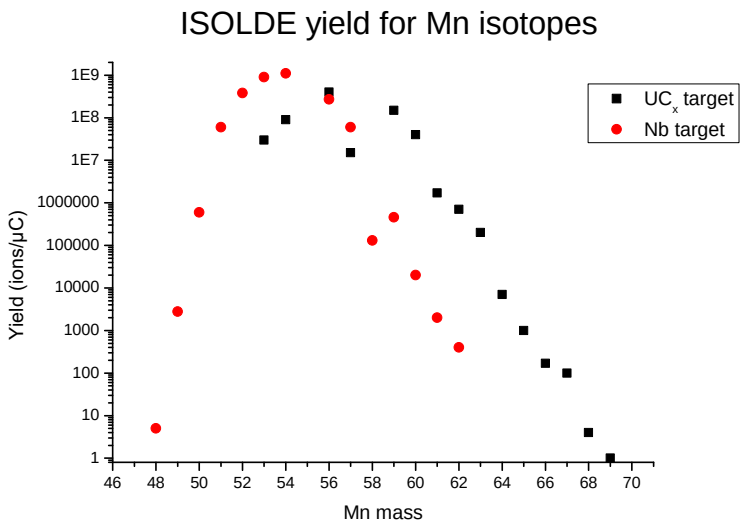

Figure 3.3: Comparison of the Mn isotope yield for 50 g/cm^2 Nb (red) and 51 g/cm^2 UC_x (black) targets. Protons injected from the PSB at 1 GeV. All data taken from [51].

able to create more than 1000 isotopes of over 70 different chemical elements, with intensities ranging from 1 to more than 10^{10} ions per second [50].

The target must be carefully chosen, so the cross section of the desired nuclear reaction (the one that will create most abundantly the isotope that will be studied) is enhanced, while for nearby nucleus and possible contaminants is as suppressed as possible. As the isotopes are created inside the target, its fast extraction is also of critical consideration, specially for short lived nuclei, since otherwise they would decay before arriving to the experimental area. For these reasons, the most common target materials are oxide or metallic carbides, which present a very high fusion temperature, thermal stability and vapour pressure at high temperatures

The specific yield for Mn isotopes at ISOLDE is shown in Fig. 3.3, which were measured in [51]. For isotopes closer to the stability, as ^{59}Mn, the production is slightly higher for Nb than UC_x targets, but as we move away from the Valley of Stability, the isotope production is much higher for the uranium target. The IS474 experiment was interested in the more exotic isotopes, so it was decided to use a 51 (g/cm^2) UC_x (UC_2/graphite) target.

Isotope	Target	α	t_r (s)	t_f (s)	t_s (s)
Mn	UC_x	0.6	0.1	0.6	12

Table 3.1: Release parameters for $^{62-68}$Mn isotopes in a UC_x target at 2100°C. Data taken from [55].

Target release

The isotopes are created inside a thick target and they have to diffuse out of it. It is a complex process as there is a large variety of boundary conditions, diffusion and effusion at variable temperature in complex three dimensional volumes, for which most of the coefficients are unknown. The release can be fitted to a semi-empirical formula, expressed as the ion-beam intensity as function of time after proton impact. This curve was proposed by Lettry *et al.* in [52]:

$$P\left(t, \lambda_r, \lambda_f, \lambda_s, \alpha\right) = \frac{1}{\text{Norm}} \left(1 - e^{-\lambda_r \cdot t}\right) \left[\alpha \cdot e^{-\lambda_f \cdot t} + (1-\alpha) \cdot e^{-\lambda_s \cdot t}\right] \tag{3.1}$$

Each parameter, except α is a decay constant, so some times they are given as time constants, following the equation $\lambda = \frac{\log(2)}{t}$. t_r governs the rise time, t_f the fall time of the fast component, t_s the fall time of the slow component and α is the proportion between the weight of the fast and slow components [53]. To properly describe the intensity of the beam, equation (3.1) must be convoluted by the decay of the isotope, because when the half life is in the miliseconds range a significant proportion of isotopes may have decayed away before reaching the experimental area.

It has been noted that this parametrisation of the release curve does not exactly describe the actual curve [54], but it is sufficient to determine yields and release efficiencies.

There are databases with these parameters for specific isotopes and targets [55], but those numbers vary with the operation conditions (proton energy, temperature of the target matrix) or with target synthesising due to ageing. Table 3.1 shows the parameters for the Mn isotopes studied in this thesis.

Fig. 3.4 shows the curve P(t) corrected by the half life of ^{65}Mn compared to the actual activity recorded during the experiment (a gate in the 363.7 keV photopeak was set to get a cleaner spectrum). It is clear that the actual release of Mn isotopes from the target is much slower than the calculated with the parameters extracted from the database (see Tab. 3.1).

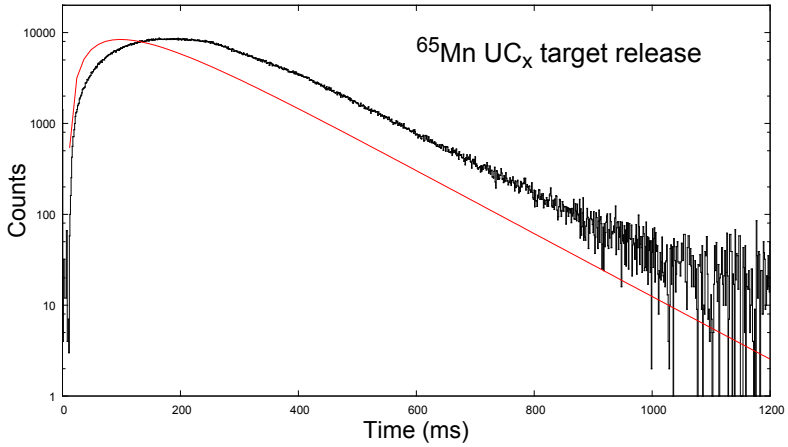

Figure 3.4: In black the activity of the ^{65}Mn, cleaned with a gate in the 363.7 keV line in ^{65}Fe. In red the predicted activity by equation (3.1), with the parameters from table 3.1 and corrected by the half life of ^{65}Mn. It can be clearly see how the actual release is much slower. Not so clear, but if looked closely, it can be appreciated how the slope of the decay changes at 400 ms, when the beam gate is close and ions stop arriving.

Radioprotection

Radioprotection is a main issue at ISOLDE and more so in the target area, where not only radiation levels are very high during operation, but also there is a potential risk of accidental release of radioactive particles. The target area and radioactive handling bay are completely separated from the control room and experimental hall, where the experiments are run.

This whole zone is built 8 m underground and is surrounded by steel and concrete blocks. It has a special ventilation system to prevent radioactive airborne leaks and that it is kept confined to ensure that most of the activity has decayed away before releasing [56].

Targets radioactivity remains above human safety level for a long time after their useful life has expired. To prevent stopping the facility for long periods of time to let spent targets to cool off, all handling inside the target area is done by robots. Moving, changing and storing of targets is done by industrial robots, which moves in rails. These robots do not contain any semiconductor or radioactivity sensitive circuit, so they can work in such environment. All the electronic controlling the robots is installed on the other side of the concrete walls, were the radiation levels are safe for humans standards.

3.1.4 RILIS

One of the main problems of the ISOL facilities is the isobaric contamination. Isobars are nuclei with the same total number of nucleons, but different ratio of protons and neutrons, so their mass difference is very small and may be bellow the mass separation power of the magnets. This difference in the number of protons make the isobars chemically different, each with a different number of electrons and ionization energies. The Resonance Ionization Laser Ion Source (RILIS) make use of the photo-ionization technique [57] to select a specific chemical species, providing a rapid and effective Z-selective ionization process which delivers a pure Radioactive Ion Beam (RIB).

Just as the nucleus present discrete excited states of energy, the electrons of the atom have orbitals of different discrete energy up to the limit where they detach and left the atom. The radiation of a pulsed laser tuned to the consecutive transitions of such electronic states can ionize the atom. The probability, and thus the efficiency of the laser, to photo-ionize an atom is given by the thermal population of the atomic ground state, the transition cross-sections and the laser beam intensities used in the excitations, as well as the spontaneous decay times of the excited states. This value, in the appropriate conditions and for certain chemical species, can go above 10% [58].

At RILIS atoms are ionized by the repetition of a pulsed laser with a frequency rate of over 10 kHz inside a hot cavity. This cavity plays an important role, as it has to confine the ions for a certain time in a compact volume where they can be irradiated by the laser before they drift to the extraction region. This confinement is made by the natural emission of electrons by high temperature metallic surface, which produces a negative potential well, preventing the ions to hit the wall an capture an electron, loosing its negative charge. To minimize this effect, materials with low electron work function can be used, specifically RILIS uses niobium and tantalum cavities [59]. The heating of the cavity creates a gradient that pushes the ions towards the exit, see Fig. 3.5.

As mentioned before, to provide the adequate ion confinement of the ions, the temperature in the cavity must be very high. This can cause thermal ionization of some atoms, particularly if the ionization potential is low. Thus, in isobars with low ionization potential, perfect selectivity is not achieved, as was the case with gallium during this experiment.

In Fig. 3.6 the RILIS operation is illustrated in an schematic way. The lasers consists of copper vapour lasers (CVL), dye lasers, non-linear crystals and optical elements to focus the laser beams. The three CVLs are shot simultaneously in order to give two beams with power around 70 W. The dye lasers and the amplifiers can

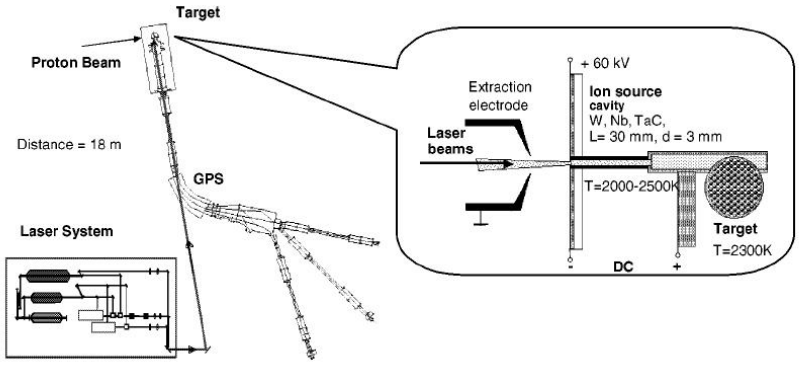

Figure 3.5: Schematic layout of the RILIS ion source at the ISOLDE facility, with the hot cavity and the General Purpose Separator. Image taken from Ref. [59].

be pumped by the CVLs. Varying the dye solutions RILIS can cover a spectral range of $540 - 850\ nm$ [59].

RILIS was first used to ionized Mn in [61] (in that experiment the ^{65}Mn isotope was seen for the first time). Mn atoms present a very complicated atomic spectrum with many multiplets and with a considerable amount of levels above the first ionization limit, at 7.44 eV. The most efficient setup is a three step ionization (see Fig. 3.7), first excited by a laser of $\lambda_1 = 279.8\ nm$, then another of $\lambda_2 = 628.3\ nm$ and finally ionized by a laser of $\lambda_3 = 510.68\ nm$. This needs a temperature above $2300\ ^\circ C$ and has an efficiency below $< 19\%$ [62].

It was clear during the experiment that huge amount of Ga was present in the experimental area. Gallium has a first ionization energy of only 5.999 eV [63], so just by thermal collision with the ion source surface, it was easily ionized. With a mass close to the Mn isotopes, the mass separator was unable to resolve the two of them, but the large difference in half lives allowed us to differentiate them by a proper setting of time gates (for example see Fig. 7.1).

3.1.5 Mass separators and beam line

Once ionized by RILIS, the isotopes are extracted into the beam line by a 60 kV potential gap between the target and the front-end of the line. This gap is enclosed in a metallic airtight cage, which defines the ground potential in the separators. Dry air is continuously flowing through the gap in order to prevent sparks and avoid the formation of nitric acid due to the passage of high energy particles. Lastly, this gap is in an underpresure state, which would prevent the leak of radioactive material in case of accidental breakage.

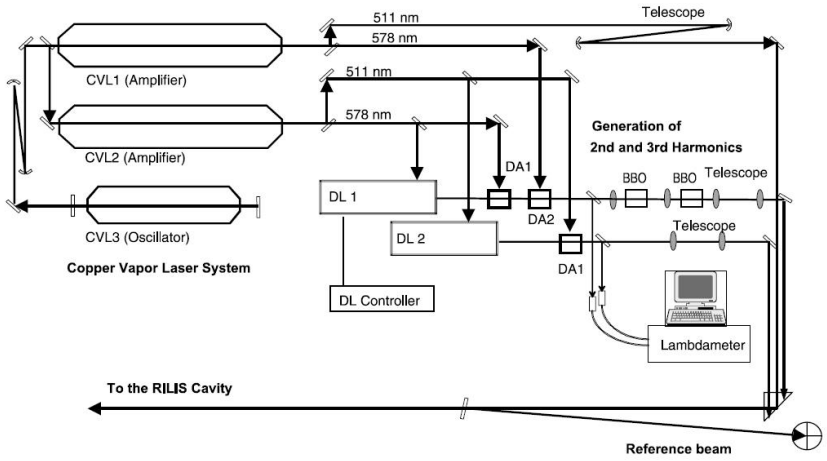

Figure 3.6: Simplified scheme of the RILIS set up. CVL1-3 are copper vapour lasers, DL1-2 are dyed lasers, DA1-2 are dye amplifiers. Image taken from Ref. [60].

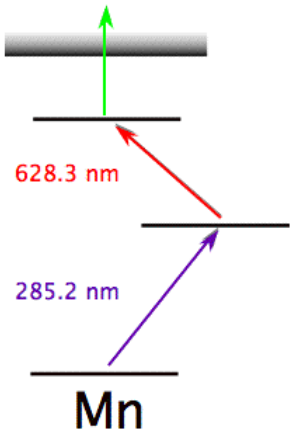

Figure 3.7: Three steps ionization of the Mn atom.

The ion beam impacting on the target has an intensity of about 2 μA, which causes an intense ionization of the air around the target. This ionization can break down the potential gap of 60 kV, so in order to avoid this, the voltage is turned off just before the proton impact and is not turned on until 7 to 8 ms after the impact.

When the proton pulse impinges the target, all kind of isotopes are created, and some are immediately ejected from the target. To avoid the ions going into the beam line, ISOLDE has the so called beam gates, electrostatical deflectors of about 4.5 kV [64] that deflect away the ions. After a certain period of time, the beam gate is open, allowing the passage of ions through the beam line.

If checked, the activity of the studied isotope will increase since the opening of the beam gate as more ions are extracted from the target and arrive to the experimental area. After some time, most of the ions will have left the target or will have decayed away, which can be observed as a decrease in the activity. At that time, any ion leaving the isotope is a potential contaminant, so the beam gate is closed to minimize presence of other isobars in the experimental area. Fig. 3.4 is a good example of how the activity first grows and then decays, even how the slope of the decay changes after the beam gates closes after 400 ms.

ISOLDE has two independent mass separators, each with a different target. Both of them receive the protons from the PSB and, after separating the ions by their mass, they deliver the beam to the common central beam line, so every experiment (permanent or temporary) can make use of either of those separators (see a schematic layout of the ISOLDE facility in Fig. 3.8). This junction in the central beam line consists in a parallel plate condenser, which, by increasing one polarization or the other, will accept the beam from one of the separators. After this switch-yard, the beam distribution systems distributes the beam to a specific experiment. As there is no mechanical components, fast switching in possible, but only one beam can be in the beam line at a time. Only the mass separators have magnetic components, the rest of the guiding beam line is made of electrostatic elements in order to make the beam transport independent of mass, as it will only depend on the charge of the particle, and all the atoms are once ionized.

The smaller separator is the General Purpose Separator (GPS), which has a double focusing 70° magnet with a bending radius of 1.5 m. Calculations show it has a mass resolving power of 2400. It has a switch-yard that allows it to select three ion beams with a mass range of $\pm 15\%$ (0 for central, up to -15% for the low mass and up to $+15\%$ for the high mass line) and to transport them simultaneously to three different experiments. This switch-yard is built up of two pairs of electrostatic cylinder shaped deflector plates, one to each side of the central line. This lateral lines serve mainly for collecting ions or smaller experimental setups, as solid state physics, for example.

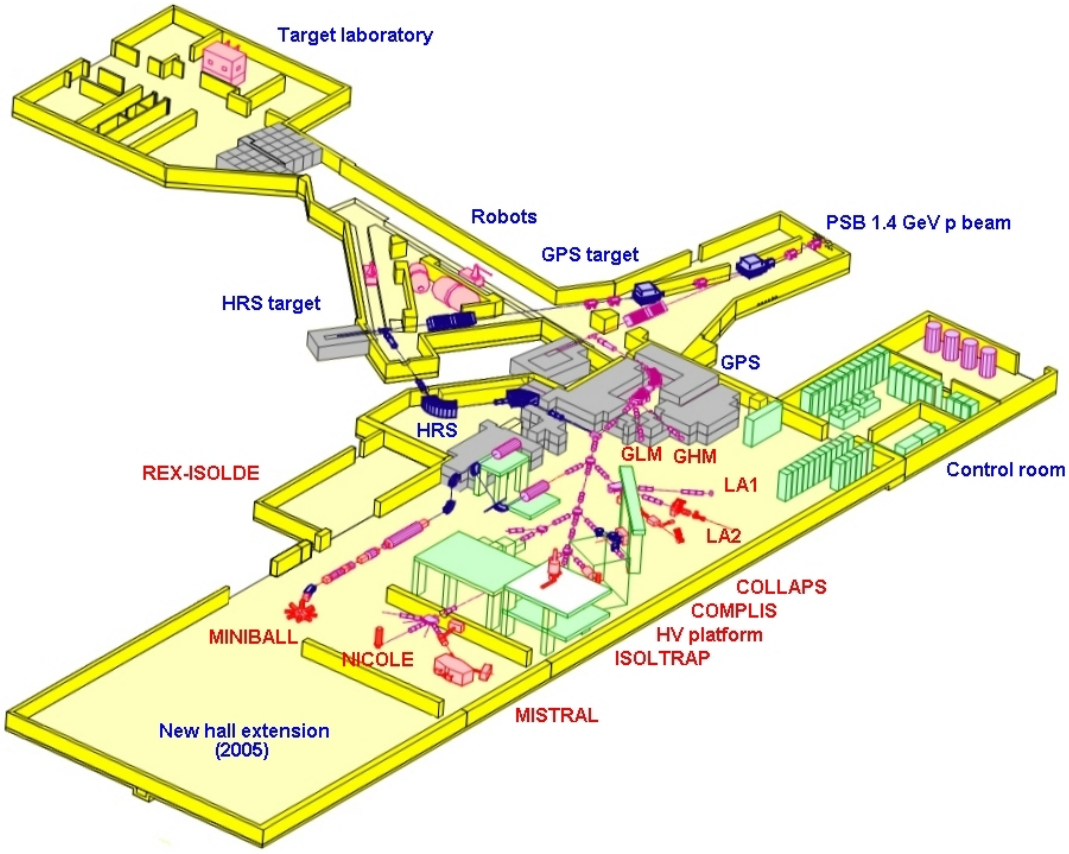

Figure 3.8: Schematic layout of the ISOLDE facility. 1.4 GeV protons come into the facility and are directed to either one of the two targets (HRS or GPS). After ionizing and selecting a specific isotope, the ions are conducted through the beam line to the permanent experiments, like ISOLTRAP or MINIBALL, or to the experimental areas LA1 and LA2, where temporary experiments are set. Image taken from the ISOLDE web page [65].

The second more powerful separator is the High Resolution Separator (HRS). It comprises a two stages magnetic analysis (the first of 90° and the second of 60°), electrostatic quadrupole lenses and a number of magnetic and electrostatic elements for correction of higher order image aberrations. The two magnets bend the beam in opposite directions, so there is no need for an intermediate focus before the second magnet. Nominally it has a mass resolving power of $M/\Delta M = 7000$, but in practice its limit is near $M/\Delta M \approx 5000$.

Nuclear structure experiments in general, and fast timing in particular, rely on a sufficient amount of statistics of good quality. As beam time is always a constraint when running experiment on big facilities, a high enough intensity is the only way to achieve the desired amount of data. To accomplish this, it is indispensable that as many ions as possible that diffuse out of the target reach the experimental area. In every bend, focusing point, mass selection segment or just due to Coulombian repulsion of the particles, a fraction of the beam is lost. In order to monitor the beam intensity in each section, a number of Faraday cups, moving wire scanners and wire grids are set all along the beam line. With these diagnosis tools, the user can try to optimize the quadrupoles intensity in the beam line and, by doing so, maximize the intensity of the beam at the experimental area.

3.2 Experimental setup

3.2.1 Experiment detectors

Five detectors were used in the experiment in a close geometry configuration. In front of the beam was a fast plastic scintillator NE111A, in the horizontal plain two High Purity Germanium (HPGe) detectors and in the vertical plane two $LaBr_3$ fast scintillator crystals. Fig. 3.9 shows the disposition of the five detectors, as close as possible to the beam deposition point to maximize the solid angle covered.

NE111A plastic As the β energy spectrum is continuous, energy resolution is not a concern when choosing a plastic detector, but its timing resolution and efficiency. For this reason the NE111A [66] organic plastic detector was chosen as the β detector for its very fast rise time. The EJ-232 (the current commercial equivalent plastic detector to NE111A) has reported rise time of $\tau = 0.35$ ns [67]. It was placed just in front of the aluminium stopper, with a separation of only a few millimetres to maximize the efficiency. There is no need that the β particle deposits all its energy, only a fraction is enough to trigger the detector and start a coincidence in the TACs. For this reason it is considered that the detector has an intrinsic efficiency of 100%, but only covers about a solid angle of 30%. It has 1.3 cm diameter and 3 mm

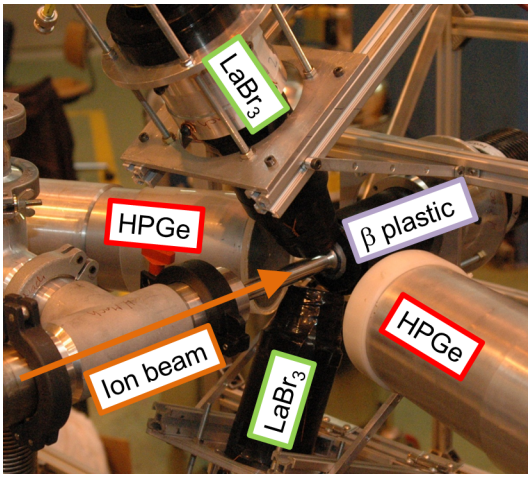

Figure 3.9: Close picture of the 5 detectors set-up used in the IS474 collaboration experiment.

thickness, for a total volume of around 400 mm^3 and it was coupled to a Photonis XP20D0 photomultiplier. The β detector must be as thin as possible to ensure that all the β particles deposit a similar amount of energy, and thus minimize any contribution from the time walk of the plastic scintillator. As explained in Sec. 4.2.2, the time response as a function of the energy deposited by the β particle was not uniform and some corrections were needed.

$LaBr_3$ crystals The traditional choice for timing crystals was the BaF_2 scintillator, one of the fastest crystals but with a poor energy resolution. In the last decade the $LaBr_3$ were developed with a time resolution of 107(4) ps at ^{60}Co energies for 1 inch crystal [68] (the time resolution is worse for 1.5 inches crystals), comparable to that of a BaF_2 but with a much better energy resolution as low as 3% at 662 keV [69]. To maximize their timing properties they need to be relatively small and to enhance their light collection the shape needs to be optimized. In this experiment we used a new generation of $LaBr_3$(Ce) crystals with truncated cone shape. The crystals had 38.1 mm height, 38.1 mm diameter at the bottom and 25.4 mm diameter at the entrance window. The crystals were coupled to Photonis XP20D0 PMTs, optimized for fast timing. The XP20D0 were operated at $HV = 1020V$. This leads to a good gain at the expense of energy linearity and in a particular long time walk. The PMTs were protected from magnetic fields with μ-metal shielding, as these fields greatly affect electron gain and linearity of the PMTs. The energy resolution improvement of $LaBr_3$(Ce), compared to previous crystals such as BaF_2, has a positive impact in timing measurement as well. The peak-to-Compton ratio underneath is greatly reduced, therefore minimizing the corrections needed (see Sec.

4.2).

HPGe detectors Even with the large improvement that the $LaBr_3$ crystals brought to energy resolution in crystal scintillators, it is not enough to resolve the high number of gamma peaks that an odd nucleus such as ^{65}Fe would present. In order to select a specific gamma cascade the energy resolution of a HPGe is required. Two HPGe detectors from the LPSC, France, laboratory were used in the experiment. *Xavier* (labelled as Ge-1 in this experiment) is P type ORTEC GEM60200 with a 60% efficiency, 1.95 keV FWHM at 1.33 MeV and a 70:1 peak-to-Compton ratio [70]. *André* (Ge-2) is N type ORTEC GMX60200-S with a 60% efficiency, 2.3 keV FWHM at 1.33 MeV and a 56:1 peak-to-Compton ratio [71]. Due to the the slow charge collection and the variable shape of their signals, HPGe detectors have poor timing resolution (one of the best timing resolution reported is 8 ns by Mihailescu *et al.* [72]). With this timing resolution they are not suitable to measure half lives in the picosecond range, but they were connected to TACs to measure the half lives of isomers in the range of nano to microseconds.

3.2.2 Electronics of the experiment

For the electronic setup NIM standard (Nuclear Instrument Module [73]) modules were used. This standard was established in 1964 for the nuclear and high energy physics experiments, with the goal to promote the interchangeability of instrumentation modules. It is a modular system, formed by bins (or modules) and crates, were the bins are plugged. Each module has a specific function and dimensions of 8.75 inches tall by 1.35 inches width (2.7 inches for double modules). The crate supplies a constant voltage for the modules, that are connected between them by cables in the back part of the crates. Under every crate there is an additional slot to introduce a tray with several fans. Each module have holes in the top and bottom faces, so the air can flow though them. Several crates can be put into a rack, one on top of the other. As each of them have a tray with fans, a column of air can flow through all the modules, cooling them and maintaining a constant temperature.

The electronic setup consists of two main sections, a timing part and another for energy signals. In the timing section very fast (short rise time, in the order of a few nanoseconds) but with worse shaping signals are used. On the other hand, the energy part does not need so fast signals (their rise times are in the order of hundreds of nanoseconds) but their shape is much better defined.

Fig. 3.10 shows a simplified diagram of the IS474 electronic setup. The diagram only shows one HPGe detector and one $LaBr_3$(Ce), but the experiment was run with two of each. The electronic for the other detectors was exactly the same,

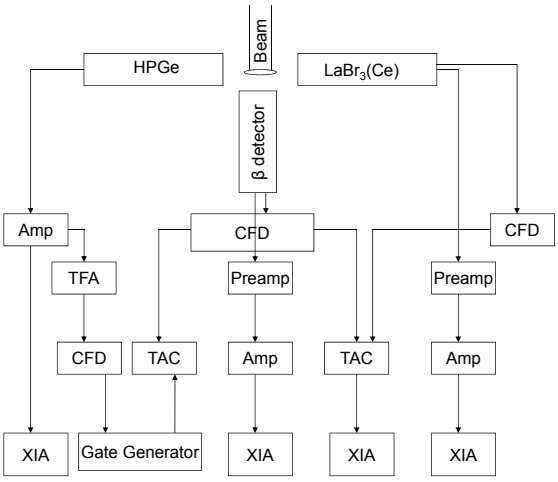

Figure 3.10: Simplified diagram of the IS474 electronics setup. During the experiment run there were two HPGe and two $LaBr_3$ detectors, but only one of each is included in the diagram to keep it simple. The electronics for the other detectors are identical.

so only one of each is included in the diagram for simplicity.

β plastic detector The β plastic detector was coupled to Photonis XP2020 PMT, whose base has two outputs. The signal from the last dynode is much more linear than that of the anode, so it is used for the energy deposited by the β particle. It first goes to an ORTEC 113 Preamplifier, which integrates the signal, slightly amplifies it and acts as a noise filter. The next step is an ORTEC 572A amplifier, which has a built-in pile-up rejector, great gain range and a very fast base line restorer. From there, the dynode signals goes through an ORTEC 542 Linear Gate Stretcher, which will only allow the signal to proceed if there is a coincidence from any of the TACs. The final step is the PIXIE4 module.

The anode signal has gone through an additional dynode step, so it is more amplified and, more important, it is negative, the only polarization that the constant faction discriminators (CFD) accept. It goes through a 10 ns cable to an ORTEC 935 Quad CFD, where it receives an additional 2.5 ns delay, which is supposed to deliver a walk-free signal (for details, see Sec. 4.2.2). The triggered signal of the CFD goes to an ORTEC 567 TAC/SCA, where it will act as the START. Time-to-Amplitude-Converters(TACs) work in coincidence, when the START signal arrives, it starts rising a voltage, linearly proportional to the time elapsed, until the STOP signal

arrives. The output of the TAC is a signal whose amplitude is that of the increased voltage. The START signal for all the TACs is the plastic detector, while the STOP is the gamma detector associated with each TAC. The TAC output signal goes to the PIXIE DAQ while the SCA output signal goes to a 418A Universal Coincidence module, which acts as the gate for the Linear Gate Stretcher mentioned before.

$LaBr_3$ scintillator detector The electronic setup for the $LaBr_3$ is very similar to the β plastic detector. The dynode signal is used for the energy and it is first pre-amplified by an ORTEC 113 Preamplifier. A 10 ns cable connects it to a Tennelec TC 247 Dual Amplifier (it accepts both scintillators dynode signals) and from there to the ORTEC 542 Linear Gate Stretcher. If there is a positive coincidence, the signal is allowed to continue to the PIXIE DAQ, where it is recorded.

The timing part goes from the anode through a 10 ns cable to the same Quad CFD as the β plastic where they have a 3 ns delay. A 16 ns cable connects them to the TACs, where they act as STOPs for the coincidence started by the β detector signal. As their timing range was set to 50 nano-secs, they were marked as fast-TACs.

HPGe detector The signal from a semiconductor detector is very weak, so the HPGe detector has already a preamplifier integrated. It has two identical output signals, but typically one is used for timing and the other for energy. This second one can go directly to the DAQ, where it is recorded as the energy and the second one goes to an ORTEC 863 QUAD Time filter Amplifier. The timing signals from the HPGe detectors need of additional shaping and amplification. From there the timing signal goes to Canberra 454 Quad CFD, suffers a delay before continuing to an ORTEC GG8020 Octal Gate and Delay Generator. This module only allows the signal to proceed if it receives a coincidence from the SCA back output of the β-$LaBr_3$ TACs (this is is, the β plastic has detected a particle and there is a β-HPGe coincidence). From there it goes to an ORTEC 567 TAC/SCA, where it acts as the STOP input signal (the β was the START). The TAC output signal goes to the PIXIE DAQ where it is recorded as the Slow-TAC. As their timing range was 2 μ-secs they were labelled as slow-TACs.

3.2.3 Digital Gamma Finder PIXIE-4

The data acquisition system was a XIA crate with 4 synchronized Digital Gamma Finder (DGF) PIXIE-4 Rev. C cards from XIA LLC [16]. It is a digital system designed for high resolution gamma spectroscopy with HPGe detectors, specially well suited to work with 4-fold clover detectors. This system is compatible with other

types of scintillator/PMT detectors and any other kind of semiconductor detectors, provided the processing of the signals in the module is modified (and sometimes preprocessing is required). It works as a waveform digitalizer, acquiring data at rates of 75 mega samples per second (or 75 MHz) using 14-bit ADCs [74].

For slow signals the optimal input signal for this system is directly the output of a preamplifier integrator, with no need of further processing. The systems allows to measure the amplitude of the incoming signal and analyse the pulse shape simultaneously for each channel. Fig. 3.11 shows the schematic of the integrated electronic of a XIA card.

The XIA crate can accommodate 4 modules, each of them with 4 input channels. This allows the use of up to 16 different input, but during the experiment only 10 were used:

- Module 1
  - Channel 0: PSBooster proton impact signal
  - Channel 1: HPGe-1 energy
  - Channel 2: HPGe-2 energy
- Module 2
  - Channel 0: $LaBr_3$-1 energy
  - Channel 1: $LaBr_3$-1 fast-TAC
  - Channel 2: $LaBr_3$-2 energy
  - Channel 3: $LaBr_3$-2 fast-TAC
- Module 3
  - Either the module or the slot was not functional, but a module must be inserted into the crate in order for the acquisition system to write out to the PC correctly.
- Module 4
  - Channel 0: β plastic energy
  - Channel 1: HPGe-1 slow-TAC
  - Channel 2: HPGe-2 slow-TAC

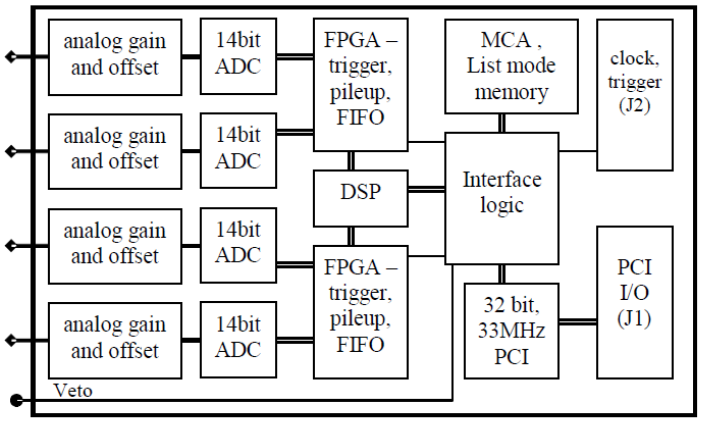

Figure 3.11: Diagram of the electronics of a PIXIE-4 XIA card. Each card has four input channels and can record the amplitude and process the signal shape. Image taken from [74].

Analog signal conditioning The input of each data channels is represented in Fig. 3.11 by the *analog gain and offset* box. Its main function is to convert the input signal to the range of the Analog to Digital Converter (ADC), which has a maximum amplitude of 2 V. For this purpose, it fixes the gain so the signals are within the voltage range of the DAC and sets the dynamic range.

Analog to Digital Converter The next component is the 14-bit ADC, which converts the analog signal into a digital one. It simply realizes a linear conversion from the input voltage signal to a 16 bit digital word. $2^{16} = 65536$, so V=0 correspond to 0 value and $V = 2$ will correspond to 65535.

Real time processing unit The real time processing units are represented by the Field-Programmable Gate Array (FPGA) boxes in Fig. 3.11.

First it applies a filter to shape the signal, transforming it to trapezoidal one, making the analysis of the pulse height less sensible to the variations of the signal shape.

In the next step a pile-up inspector will check if there is a second pulse to close too the first one that may distort the height of the first pulse. If such thing happens, both pulses are discarded. It is an effective method as long as the time difference between the two signals is longer than the rising time of the input signal.

After a signal has been detected and have passed the pile-up filter, it triggers a

communication with the DSP module to allow the storage of data. After that there is a FIFO memory, which is continuously filled with information about the ADC pulse shape and only stops to avoid over-writing of valid events.

Digital Signal Procesor This component receives the information from the previous module, reconstructs the real pulse height, assigns it a temporal value, prepares the data to send them to the PC and sends another signal to the MCA spectra. All the information about the event and the MCA spectra is sent to the PC through a PCI interface. The MCA spectra are histograms that only contains information about the number of events and their energy recorded in each module. The other information is recorded in list-mode, in which the information is recorded event by event, each of them containing its energy and a time-stamp.

3.3 Sorting software

When running an ATD experiment, a large amount of data is generated, but only a small fraction will contain useful information. To separate the desired timing data from randoms and background events and extract a lifetime value, several levels of sorting are necessary.

In the first step of the sorting process, the so called "presorting", all the files of the a same mass are merged together and classified according to the detector that recorded the event or the coincidence pattern. As explained below, PIXIE arranges the data in blocks of 32 buffers for each module. This method has advantages in order to minimize the dead time due to the write out of the system, but it is not manageable when comes to analyse the data. In the proper sorting, the data is projected following some defined conditions.

3.3.1 PIXIE data writing structure

The first step in writing appropriate sorting software for the data analysis is to fully understand the way the PIXIE DAQ structures the writing of the recorded data .

First of all the PIXIE DAQ is composed by 4 module slots, each of them with 4 channels. Each module has 32 memory buffers and each buffer can store up to 744 events (how PIXIE defines an event will be explained later). Each time any module fills one buffer with 744 events, all the modules will close their current buffer and start storing information on the next one, no matter how many recorded events they storage, even if it was empty. During the experiment, the energy of the HPGe detector and the proton pulses signals were fed to the first module. Due to the

higher efficiency of the HPGe over the scintillator crystals at high energies and the fact that their energy-signals were not run with a hardware coincidence condition, every single time the first buffer to store 744 events was the one from this module. So, in practice, every time the first module buffer was full, the buffers of the other three modules (still half empty) were closed and started new ones.

Once every module has closed 32 buffers (as explained before, in practice only the first module buffers were full) the system writes out the data to the PC hard drive. It writes first the 32 buffers of the first module consecutively, then the 32 buffers of the second module and so on. Due to this sequential reading/writing, the systems requires the 4 modules to be plugged to the crate, as it cannot skip any before proceeding to the next. For this reason we had to plug a non-working module in the third slot of the crate with no input signal attached, which recorded no events at all.

The system was set to write in each file 64.000 buffers, which, for the usual activity of a few thousand β particles detected per second, meant a new file every hour. This way if, for any reason, the file became corrupt, only a small fraction of the data would be lost. All the data recorded from PIXIE is sent to the PC as unformatted binary data in 16-bit words. This unformatted structure of the data implies that the words must be read in a very specific order, since skipping just one word could make the whole data incomprehensible.

Files do not have any kind of preamble or file header, they start directly with a buffer header for the first buffer of the first module. Each buffer header is composed of 6 words, as explained in Tab. 3.2. The total number of words in a buffer refers to the total number of events words plus the total number of event headers, but not the six words from the buffer header. This means that this number was zero for the empty buffers of the third module of this experiment. It is important to consider the extremely unlikely possibility (other than for malfunctioning reasons) of a empty buffer, as it is easy to overlook this possibility that would cause errors in the reading programme.

The second word refers to the module number, numbered from 0 to 3 from left to right in the crate slots. Even if the modules are always read out in order, this number can be used as a check.

The format descriptor is a number that indicates what information is being recorded. This experiment was run in mode compression 3, indicated by number 259. It only records energy and time, the minimum required, thus reading and writing faster than if more unneeded information was recorded as well.

The last three words records the beginning of the buffer with the PIXIE clock. As they are only 16 bit long, that mean that each one of them can hold up to 65536 ticks. PIXIE clock has a frequency of 75 MHz, which means that each tick is $13.\bar{3}$

Word	Variable	Description
0	BUF-NDATA	Number of words in this buffer
1	BUF-MODNUM	Module number
2	BUF-FORMAT	Format descriptor = RunTask + 0x2000
3	BUF-TIMEHI	Run start time, high word
4	BUF-TIMEMI	Run start time, middle word
5	BUF-TIMELO	Run start time, low word

Table 3.2: Order and meaning of the 6 words of the each buffer header.

ns and that a whole 16 bit word is ≈ 0.874 ms. The standard experiment spans through several days, so obviously more time is required. Each time the low time word reaches its maximum value, that is 65535, the medium time word is increased by one. When the medium time word reaches itself the maximum value of 65535, it is the high time word which increases by one, and the medium and low words go back to 0. By composing the time with three 16 bit words the clock can run for over 43 days before overflowing.

The PIXIE DAQ system is capable of recoding coincidences for detectors plugged within the same module with a time window of ± 8.107 μs or 608 PIXIE clock ticks. In the IS474 experiment it implies that HPGe detectors coincidences were recorded as a single event, because both of them were connected to the first module. There cannot be an event containing coincidences from a HPGe and a β detector, for they were in different modules. Since each module has 4 channels, in a single PIXIE event can be up to 4 different input signals.

Due to the fact that the number of words from an event is variable, the total length of a buffer is not fixed (even if it was known that the buffer was filled with the maximum 744 events) and the need for the first word defined in table 3.2, with the total number of words in the buffer. For this reason, the only way to read this list mode data is by keeping track of the number of words already processed so when the program has read BUF-NDATA words, it knows a new buffer will begin.

Each event starts with an event header, composed by three words (see Tab. 3.3). The last two words (called high and low) are equivalent to the medium and low time words from the buffer header. To reconstruct the time for the beginning of the event, the high word from the buffer header, the high (acting as medium in spit of the name) and low word from the event header must be used. The main problem is that PIXIE is assuming that the high word from the buffer header does not change for the whole buffer duration, which is not always true. This can be checked if the total time is always increasing (as the events are written sequentially), and if it ever decreases, it only needs a +1 in the high time word.

Word	Variable	Description
0	EVT-PATTERN	Hit pattern. Bit [15..0] = [gate pattern : hit pattern : status : read pattern]
1	EVT-TIMEHI	Event time, high word
2	EVT-TIMELO	Event time, low word

Table 3.3: Each event begins with a three words header.

Word	Variable	Description
1	CHAN-TRIGTIME	Fast trigger time
2	CHAN-ENERGY	Energy

Table 3.4: The proper experimental data itself are those two words, containing the energy of the event and the time stamp.

The first word in the event header is called the event pattern and is a complex way to describe how many detectors are involved in the coincidence and it is done down to the bit level. The 16 bit word is subdivided in 4 smaller words of 4 bits each. The first four bits indicate which channels have recorded information, with 1 if they have or 0 if they have not. For example 0110 would indicate that the first and fourth channel have no data but there was a coincidence between the second and third. The other 12 bits of the word are not relevant for this type of experiment.

After the event header comes the event information itself, called channel header. Given the fact that each individual module has 4 input channels, up to 4 different input signals can belong to a single PIXIE event. The system always writes the coincident events in order, from first channel to fourth, but only the ones which actually recorded data. In compression mode 3 (the one used in this experiment) only time and energy are recorded (see Tab. 3.4). The energy word contains the amplitude of the signal converted to a digital number by the ADC, which is not necessarily an energy, it can be time, as with the TACs cards. The time word, this time called fast trigger time, is nothing else then the low time word. To construct the time stamp of a event, one must use the high word from the buffer header, the medium (called high) from the event header and the low (called fast trigger) from the channel header. As explained before, the high and medium word can increase between the moment they were recorded and the moment the event was recorded, but this is easily checked, as time should always increase.

3.3.2 Presorting

In the presorting step, the main goal is to rearrange the data so it is organized by detectors instead of modules. To achieve this, a number of programmes were developed in FORTRAN77, partly based on previous work by Henryk Mach. Each programme was aimed to select the events recorded in one specific detector or coincidences between a set of them, but all followed the same structure.

An input file tells the programme the names of the output files we wish to create and the location of the data files we want to merge together. In other versions of the programme the input file would also contain information about the proton pulse pattern sent from the PSBooster to ISOLDE (for more information about this, see Sec. 3.1.2).

The presorting programme may be subdivided in three main parts. The first part reads the data files and loads a buffer from each module onto the RAM memory of the PC. The second part, which is not always called, is a subroutine that looks for coincidences between detectors in different modules. The last part writes each event in a different output file according to which detector recorded it.

If we are interested just in single events, not in coincidences, each event will contain 4 parameters. Two of them will be related to the proton supercycle, which was not reconstructed in this experiment, so this two words were not used (but a fixed number was written nevertheless, for consistency with the following sorting programme). The other two parameters were the energy of the events and the time since last proton pulse impact (proton time from now on). PIXIE adds a time stamp, but it is referred to the system clock, which is started at the beginning of the experiment. The time, expressed like this, is not used. Instead, we are interested in the proton time, which is a much more suitable time reference, as it gives us a time frame since the creation of the isotopes. To construct this time, the programme looks for a proton pulse (channel 0 first module). When it finds one, it sets it as the time reference, and then looks for the next one. All the events found between those two protons have their time stamp changed to the time difference between their actual time stamp and the first proton time. PIXIE clock works with steps of $13.\bar{3}$ ns, while the isotopes half lives spans from dozens of ms to a few seconds (longer half lives rapidly reach saturation and may be treated as constant background). Moreover, the proton pulse cycles is a multiple of 1.2 seconds, so the proton time is expressed in milliseconds instead of $13.\bar{3}$ ns ticks, as it is a much more suitable time unit.

The coincidences may contain from 5 to 9 parameters, depending whether they are double or triple coincidences and which detectors are involved. Typically, the parameters will be the energies of the detectors, the TACs associated to these de-

tectors and the proton time. The time differences between detectors in a coincidence usually are below a microseconds and the proton time is measured in milliseconds (as explained above), so just one time is required for the multiple events. The most common coincidences used are: HPGe-HPGe, β-HPGe, β-HPGe-HPGe, β-$LaBr_3$ or β-$LaBr_3$-HPGe. As mentioned in Sec. 3.2.3, the system can only automatically construct coincidences for detectors within the same module. From the list given before, only the two HPGe detectors were connected to the same XIA module, so all the other coincidences were built off-line.

Every coincidence of interest that was made offline had a β event as a start. All the buffers from the modules are started at the same time and, when any of them is filled, all are closed and new ones opened. Thus, the subroutine loads parallel buffers from each module, looks in the appropriate one for a β event and sets its time stamp as the beginning of the coincidence. Then it will look in the other buffers for an event of other detector that is within the coincidence time window (typically a little over 1 μs). If working with triple coincidences, it would go to another buffer and look for another one. For $LaBr_3$ detectors, their TACs where always connected next to them in the modules, so it was not necessary for the subroutine to look for them, they were always recorded consecutively. For HPGe detectors this was not the case, so an additional loop was necessary in order to look for them.

In order to verify the working of the subroutine, it was run to look for HPGe-HPGe coincidences and compared them to the ones recorded online by the DAQ system. The PIXIE coincidence time window is not as strict as expected. By default it is set at 8.107 μsecs or 608 PIXIE clock tics, but it still found a non negligible number of counts after the window should be closed, see Fig. 3.12. After discarding the counts outside the time window, the difference in the number of coincidences found by the PIXIE system and the subroutine was below 0.1% (see the green plot in Fig. 3.12). The differences are nearly zero for the true coincidences, while the number increase with the time difference between the coincident gammas (random coincidences).

As mentioned before, the constructed coincidences were HPGe-HPGe, β-HPGe, β-$LaBr_3$ and β-$LaBr_3$-HPGe. Since each detector had a different energy calibration and each TAC a slightly different time calibration, for each coincidence type there were all possible detectors combination, so, in the end, the programme produced a large number of output files.

3.3.3 Sorting

Once this pre-sorted files have been created the sorting procedures can be applied. For this porpouse we used programs written by Henryk Mach. This second pro-

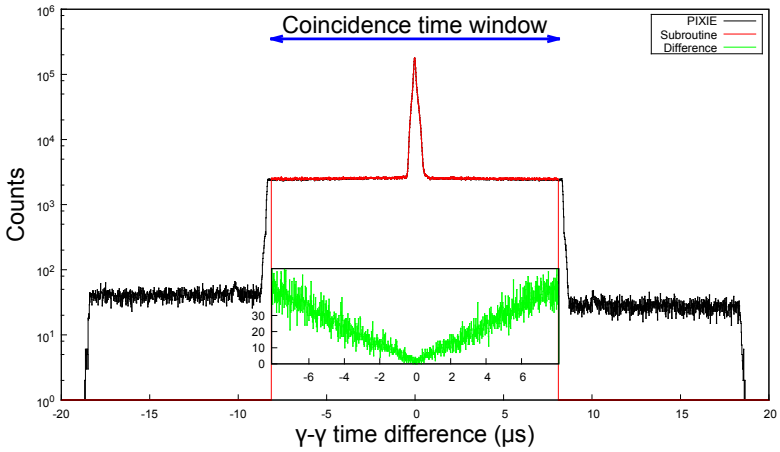

Figure 3.12: Time difference of the HPGe-HPGe coincidences recorded by PIXIE (black) and the subroutine written for the analysis (red). In the edges of the random plateau it is clear how there are additional coincidences after the time window should be closed. The green plot shows the difference of coincidences found by the subroutine and PIXIE within the coincidence window.

gramme needs an input file that gives the number of parameters per event, provides labels for each of them and up to three levels of gates. For example, in triple coincidences $\beta\gamma\gamma$(t), typically the parameters would be:

- β energy
- HPGe energy
- TAC β-HPGe
- $LaBr_3$ energy
- TAC β-$LaBr_3$
- Proton time

In the first level of gates, general conditions can be set for each parameter, that will apply to all subsequent gate sets. A typical example would be a gate in the β energy. This level of gates may or may not have subtraction of random/background events.

The second level of gates is dynamic, another gate with the same width must be subtracted and only applies to one parameter. In the previous example, it could

apply the HPGe energy. Dynamic means that several gates can be defined (one for each energy peak, for example) and each one will be applied at a time.

The third level of gates is dynamic as well but does not accept subtraction, only applies to an individual parameter and needs to be correlated to another gate in the second level. Following the example, it would be the $LaBr_3$ energy, and a peak in coincidence with the HPGe peak would be selected.

The final result will be an histogram of 32768 channels. To finish the previous example, the programme would project onto the β-$LaBr_3$ TAC. This gives the time difference between β particles with an energy set by level 1 and gamma detected in the $LaBr_3$ which energy is set in the level 3 and which is in coincidence with another gamma of the energy set by level 2 detected by the HPGe.

The programme also accepts running with 1 or 2 level gates or even none, thus producing an ungated spectrum.

3.4 Concluding remarks

This chapter covers three main topics.

In the first part a general overview of the ISOLDE facility was given. Emphasis was put in the isotope creation process, from the proton acceleration in the LINAC-2 and PSB to their impact at the heavy target, and their mass separation, the key element in the facility which truly allows the measurement of the most exotic nuclei.

The second part described the specific elements of the IS474 experiment. Even if the setup was standard for ATD experiments, it was the first one to run exclusively in digital DAQ system and one of the first to only use $LaBr_3$(Ce) crystals coupled to the XP20D0 PMT. This gave rise to several new challenges, as the correction of the steep time walk curve (described in Sec. 4.2) or the need to develop new analysis software.

The last part of this chapter covers these new programme developed for the data analysis. A great number of programmes were already written by Henryk Mach for previous analysis, but they were aimed for analog DAQ system. Thus, new programmes were written to sort the data from the PIXIE system. The new subroutine is flexible enough to search several different detector combinations. This way, several different coincidence data set were constructed for the data analysis:

1. HPGe-HPGe to construct the level schemes
2. β-HPGe(-HPGe) to clean HPGe energy spectra or measure nuclear or isomeric half lives

3. β-$LaBr_3$(Ce)-HPGe to measure short half lives with the centroid shift technique

4. β-$LaBr_3$(Ce) to measure longer lifetimes with the convolution technique by the slope of their time distributions

The set programmes have been designed so it can be used in the analysis of future experiments with minimal changes. It can sort data generated with PIXIE but with different

Chapter 4

Calibrations

This chapter describes the calibration procedures common to the analysis of every nucleus in the experiment.

On one hand the energy an efficiency calibrations of the HPGe gamma detectors is carefully characterized, as the construction of the nuclear level scheme and unambiguous identification of gamma transitions is key in the timing analysis. $LaBr_3$(Ce) crystals coupled to XP20D0 PMTs are non-linear at higher energies, so their energy calibration is non-trivial and in most cases one has to rely in the HPGe energy spectra to identify the peaks in the $LaBr_3$(Ce) ones.

On the other hand the timing calibrations procedures are crucial for the ATD method, which is able to measure half lives below 10 ps in optimal conditions [13, 14]. When using the centroid method to measure such short half lives, multiple effects must be taken into account. The time response of the scintillator crystals is energy-dependent of the gamma and in its nature (it is not the same for a Compton than for a full-energy peak). Moreover, even if a ΔE plastic detector was chosen so every β-particle deposits the same energy, in fact there is a dependence with the β particle energy distribution that must be calibrated as well.

4.1 Energy calibration

An essential condition to measure lifetimes is that the level scheme of the studied nucleus in well understood. In this experiment we relied in two HPGe detectors to construct such level schemes, so their correct precision was of paramount importance. The timing analysis itself is done with the $LaBR_3$(Ce) crystals, but their energy resolution does not allow to resolve most of the peaks. We used fine calibrated HPGe detectors to determine the gamma peaks and then be able to identify them

in the $LaBr_3$(Ce) energy spectra.

4.1.1 $LaBr_3$ energy calibration and stability

The Photonis XP20D0 photomultiplier tube (PMT) was designed to match the light output of the $LaBr_3$(Ce) at the cost of a strong non-linearity at high energies. Newer Hamamatsu R9779 PMT are best suited for fast timing with $LaBr_3$(Ce), but at the time of the experiment their properties had not been tested to the extend they are now [75]. To best describe this lack of linearity, several sources were used in the calibration, to cover the widest energy range possible. ^{24}Na, ^{88}Rb, ^{140}Ba and ^{152}Eu gammas were included (see Tab. 4.1, except for ^{63}Co, which was only used for the efficiency) for an energy range of 160 keV to 2.7 MeV.

PIXIE-4 DAQ uses 16-bit words for a total of 64k channels. That produced too broad $LaBr_3$ energy peaks, so the scintillator crystal spectra were compressed by a factor of 4 (or even more, sometimes). Due its strong non-linearity, it was decided to fit the energy calibration to a fourth order polynomial. This fit produced an offset of several hundred of keV, that strongly distorted the calibration, especially at lower energies. For this reason, it was decided to fix the offset to zero. The result of the fit for both detectors can be seen in Fig. 4.1 and the resulting parameters are:

- $LaBr_3$-1: $\mathrm{E(keV)} = 0.16(3)\cdot\mathrm{chan} + 5.3(16)\cdot10^{-4}\cdot\mathrm{chan}^2 - 2.7(7)\cdot10^{-7}\cdot\mathrm{chan}^3 + 5.2(12)\cdot10^{-11}\cdot\mathrm{chan}^4$

- $LaBr_3$-2: $\mathrm{E(keV)} = 0.41(3)\cdot\mathrm{chan} + 2.8(19)\cdot10^{-4}\cdot\mathrm{chan}^2 - 1.5(10)\cdot10^{-7}\cdot\mathrm{chan}^3 + 3.6(17)\cdot10^{-11}\cdot\mathrm{chan}^4$

The resulting calibration gives inaccurate energies, near 2% off but much larger for very low energies, as expected for the energy resolution reported for this crystals. This calibration was enough to identify peaks in a $LaBr_3$ energy spectrum, given that they were previously known from a HPGe spectrum.

Changes on temperature or small fluctuations on the power supply are known to cause changes in the gain of the electronic systems. This may lead to drifts in the energy or timing calibration of the detectors and thus the importance to monitor its stability. Fig. 4.2 shows the position of the 363.7 keV peak (the most intense in the ^{65}Mn decay) for each file recorded by the DAQ (approximately one hour duration). As can be seen there is a random fluctuation, but it is below $\pm$ 0.2 keV, lower than the energy resolution of a $LaBr_3$(Ce) at that energy. With no apparent shift observed, no correction was done to the $LaBr_3$(Ce) crystals.

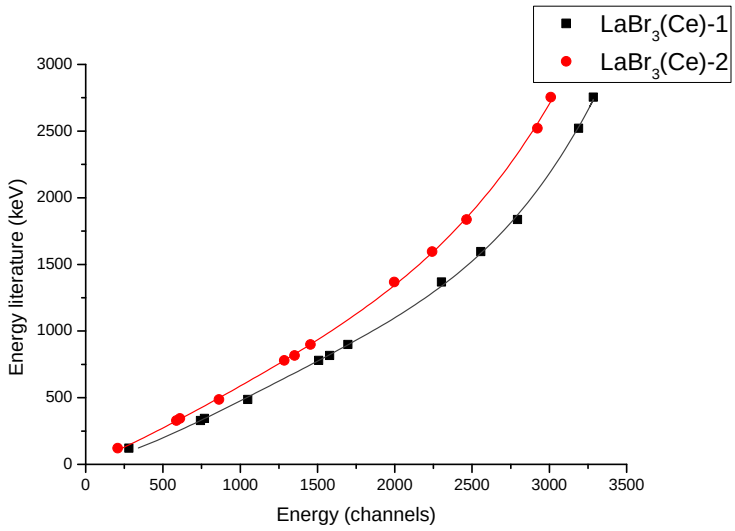

Figure 4.1: Comparison of the energy calibration of both $LaBr_3$ detectors. The fit was done to a 4^{th} order polynomial, due its clear non-linearity.

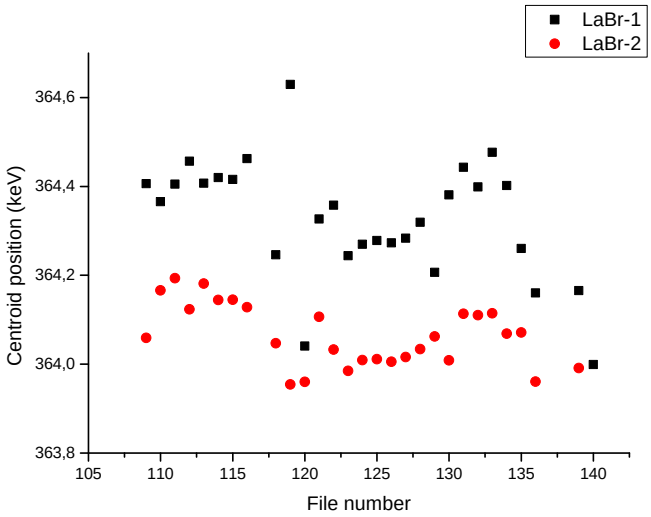

Figure 4.2: Centroid position of 363.7 keV peak in $LaBr_3$ detectors during the A=65 mass measurement. The oscillation is within 0.5 keV, whereas the resolution of the detectors at that energy is about 10 keV, so they can be considered very stable. $LaBr_3$-1 was shifted 0.5 keV so both detectors could be plotted in the same figure.

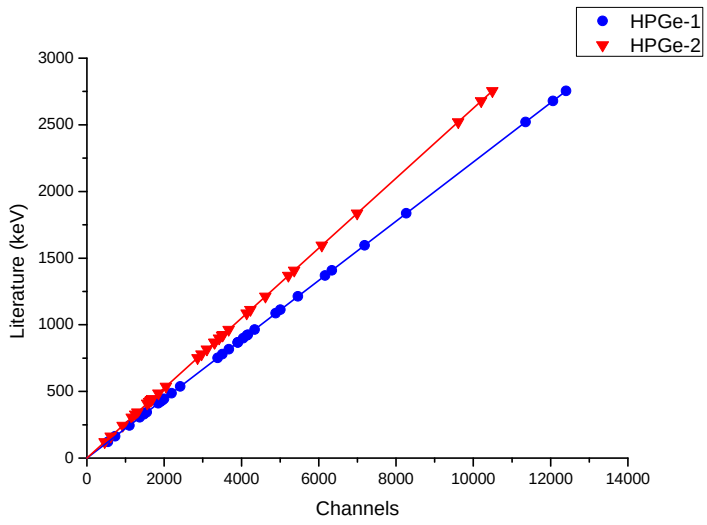

Figure 4.3: Energy calibrations of the HPGe detectors. It was done using ^{24}Na, ^{88}Rb, ^{140}Ba and ^{152}Eu sources.

4.1.2 HPGe energy calibration and stability

The gamma and level energies and intensities informations were obtained from the HPGe, so a carefull energy calibration was performed for the semiconductor detectors. The same sources used for the energy calibration of the $LaBr_3$(Ce) detectors were used now. Fig. 4.3 shows how linear the detectors are, so the fit was done to a straight line. The resulting parameters are:

- HPGe-1: $E(keV) = 0.222020(5) \cdot chan + 0.40(3)$
- HPGe-2: $E(keV) = 0.262370(9) \cdot chan + 0.74(5)$

To check the quality of the HPGe detector energy calibration, it was compared to the literature energies of several transitions. Fig. 4.4 shows the difference between the recorded and tabulated energies. The average difference is -0.01(10) keV, which indicates that there is an almost equal deviation above and below zero. If we take the absolute value of the difference between literature and experiment, the average is 0.1(1) keV.

The same procedure followed for the $LaBr_3$ crystals was used to check the stability of the HPGe detectors. As can be seen in Fig. 4.5, during the A=65 mass run the drift of the 363.7 keV peak was below 0.1 keV, the energy resolution of HPGe detectors at that energy.

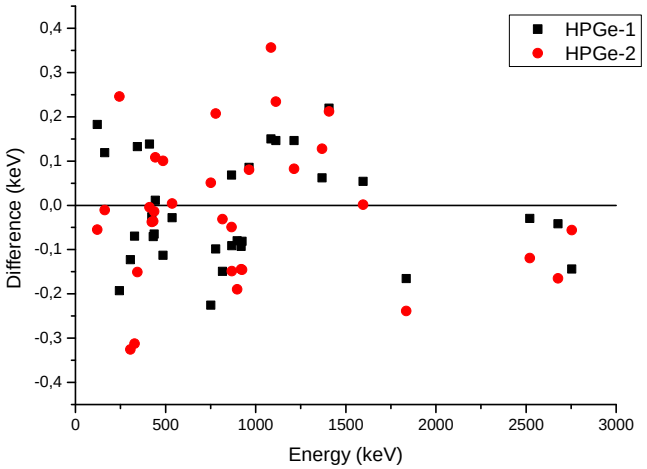

Figure 4.4: Difference between the measured energies and the tabulated in the literature. The random distribution and their close value to zero are a good indicator of the high quality of the energy calibration.

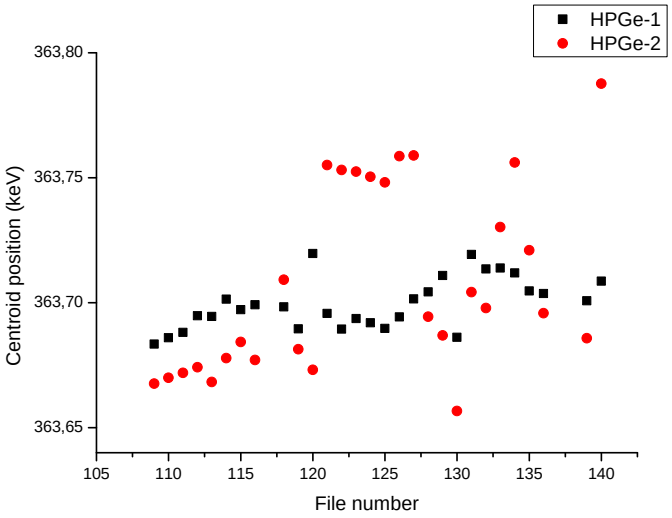

Figure 4.5: Stability of the 363.7 keV peak in the HPGe detectors during the A=65 measurement. The energy oscillation is around ±0.05 keV..

4.1.3 HPGe efficiency

The relative efficiency of the HPGe detectors was measured using several radioactive sources: ^{24}Na, ^{88}Rb, ^{140}Ba and ^{152}Eu (a list of the gammas is in Tab. 4.1. With these sources, an energy range from 121 keV up to 2.7 MeV was covered. This sources covered very well the intermediate region, with plenty of gammas around 1 MeV and down to 500 keV and provide a reasonable number of points for higher energies (even if they have larger error bars and are not as reliable). But there is a lack of points below 120 keV. That region is precisely where the HPGe detector present a bend in their efficiency, with a steep drop. In order to characterizes this low energy region, an analysis of the ^{63}Co peaks was made, as it is a well studied nucleus with an intense transition of 87.13 keV [76].

As the analysis only requires relative efficiencies and not an absolute calibration, in a first step only the peaks from the ^{152}Eu were analysed. To expand the energy range the other radioactive sources were included in the calibration. Every gamma in a given source was analysed, and for the ones within the ^{152}Eu energy range its distance to the interpolated efficiency curve calculated. As every point of each source would give a slightly different result, every source was vertically displaced an intensity-weighted average to match the ^{152}Eu source (including the ^{63}Co points). In Fig. 4.6 all the displaced points from every source can be seen.

Fig. 4.6 (specially for HPGe-1) clearly shows the bending in efficiency below 150 keV. There are several equations in the literature to fit this kind of curves (specifically for HPGe effiency curves [78, 79, 80, 81]) but none of them probed to be accurate enough and usually gave too large errors. It was decided to fit the two regions of the curves (before and after the bending) independently, using a second order polynomial (after taking the logarithms of both energy and efficiency). Fig. 4.6 shows the fitted curves for both detectors. The parameters of the fitted curve are:

- HPGe-1 :
  - Low energies: log(efficiency) = -14 + 16 · log(E) - 3.8 · log^2(E)
  - Medium energies: log(efficiency) = 4.3 + 0.21 · log(E) - 0.15 · log^2(E)
- HPGe-2 :
  - Low energies: log(effi) = -2.3 + 6.8 · log(E) -1.7 · log^2(E)
  - Medium energies: log(effi) = 5.1 - 0.20 · log(E) - 0.097 · log^2(E)

The transition from low to medium energies is not exact, but neither critical. Both parabolas have an intersection point, and even if their behaviour is not exactly

Isotope	Energy (keV)	Intesity (%)
^{152}Gd	344.2	26.6(5)
^{152}Gd	411.1	2.237(25)
^{152}Gd	778.9	12.96(14
^{152}Sm	121.8	28.67(15)
^{152}Sm	244.7	7.61(4)
^{152}Sm	443.9	3.158(27)
^{152}Sm	867.3	4.26(3)
^{152}Sm	964.0	14.65(7)
^{152}Sm	1112.1	13.69(7)
^{152}Sm	1408.0	21.07(1)
^{24}Na	1368.6	99.994(15)
^{24}Na	2754.3	99.855(5)
^{88}Sr	898.3	14.68(13)
^{88}Sr	1836.0	22.73(15)
^{88}Sr	2677.9	2.123(21)
^{140}Ba	162.66	6.22(9)
^{140}Ba	304.9	4.29(6)
^{140}Ba	423.7	3.15(5)
^{140}Ba	537.3	24.39(22)
^{140}La	328.7	20.3(3)
^{140}La	487.0	45.5(6)
^{140}La	815.8	23.28(19)
^{140}La	925.2	6.9(1)
^{140}La	1596.2	95.40(8)
^{140}La	2521.4	3.5(4)
^{63}Co	87.13	49(3)
^{63}Co	981.7	2.11(15)

Table 4.1: Table that sumarizes all the gammas used in the efficiency calibration of the HPGe detectors. Energies and intensities taken from NSR database [77], except the ^{63}Co values, taken from [76].

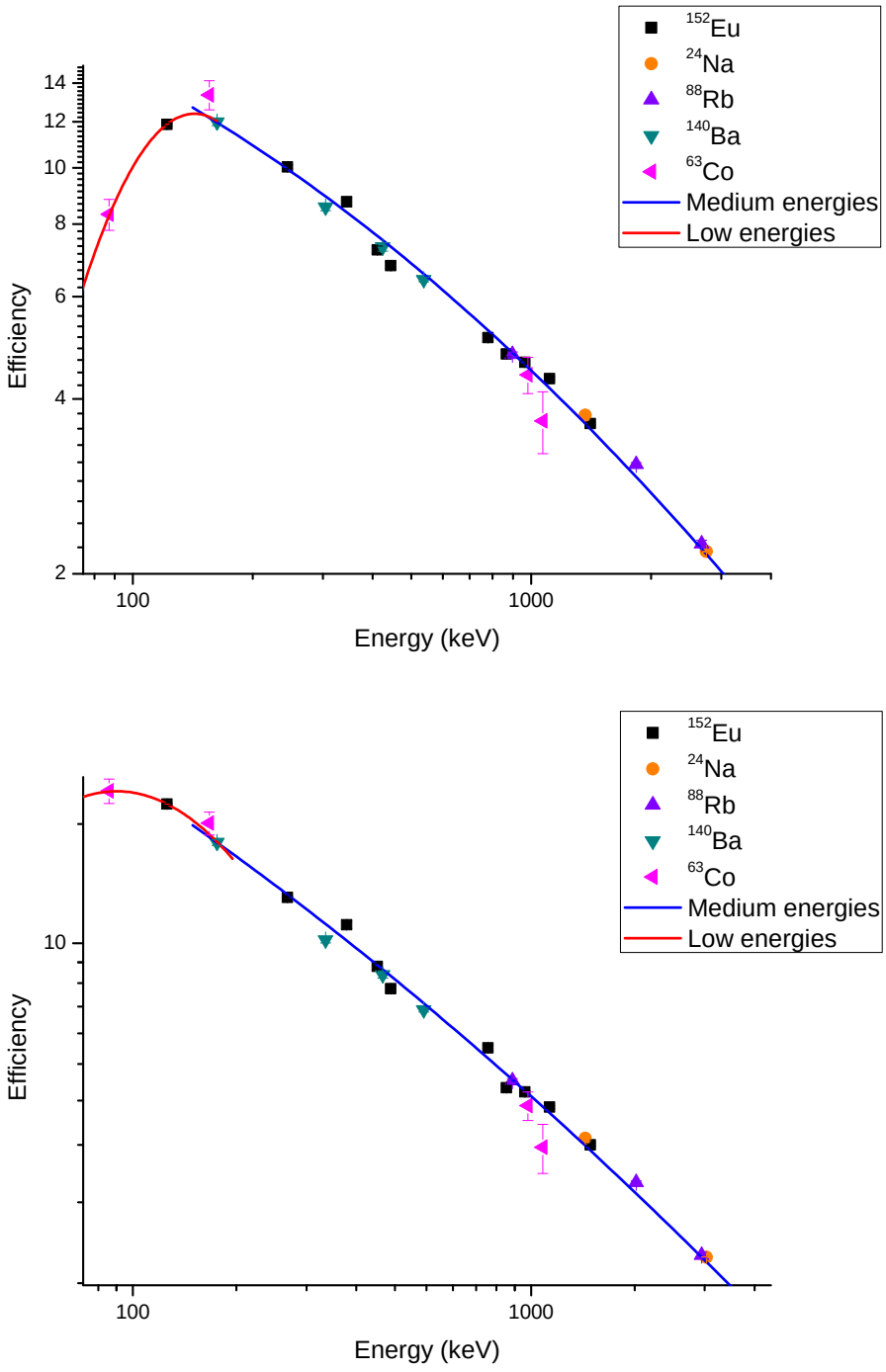

Figure 4.6: Relative efficiency calibration curves of the HPGe-1 (upper) and HPGe-2 (lower) detectors.

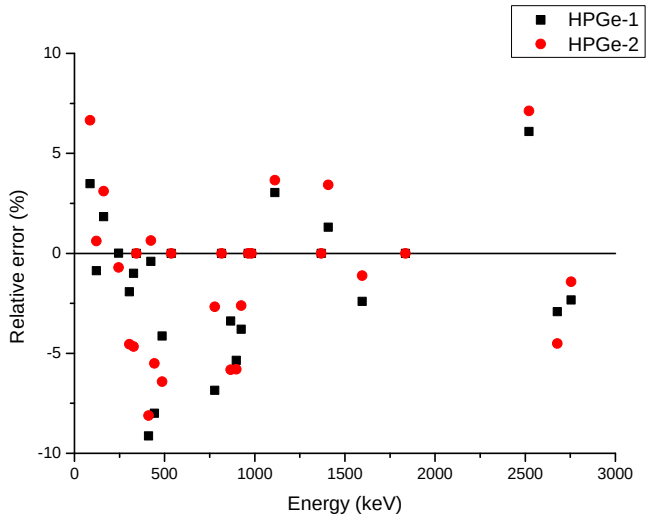

Figure 4.7: Difference between the intensities in the literature and the ones obtained for the calibration sources. Every source has been normalized independently to its most intense peak.

the same and their derivatives do not perfectly match at that point, their values around 170 keV are close enough so that the results are pretty much the same if one curve or the other is used in that energy range.

To verify the goodness of the fit and estimate a possible systematic error in the efficiency, the relative errors for the intensities of the calibration sources were calculated. As the efficiency curve is relative and not absolute, the most intense transition in every nuclei was used as reference and the intensity of every other gamma was normalized using the value from literature. The plot in Fig. 4.7 shows those relative error for both detectors. Except for the low energy regions, the distribution seems random and with a similar behaviour for both detectors, as shows that the average value of the errors is $-1(2)\%$, compatible with zero.

The average of the absolute value of the deviations is 4% for detector 1 and 5% for detector 2. Calculating a weighted average using the relative error from the literature intensities, thus giving more weight to the better known transitions and lessening those of the peaks with higher uncertainties. In this way the weighted error are 2.4% for HPGe-1 and 1.4% for HPGe-2 (the normalization peaks were not taken into account in these calculus, as they have an error of 0 and it makes not sense to include them). In both cases they are reasonable deviations, within the expected intensity error for this experiment.

4.2 Timing calibration

As mentioned before, careful time calibrations and corrections are of paramount importance to achieve the picoseconds precision with the ATD method. When measuring psicoseconds lifetimes, a number of effects can induce systematics errors. The electronic modules used to determine fine time differences, the TAC in particular, hasve an intrinsic time resolution. The time response of the plastic detector to the β-particles, even if it is a correction of second order, must be calibrated. The time response of the crystals is not the same for a Compton event than that of a full energy peak, so they different contributions to the time distribution must be taken into account.

4.2.1 TAC calibrations

The 4 TACs of the experiment were calibrated using an ORTEC 462 Time Calibrator. This module emits START and STOP signals with a very precise frequency ($\pm$0.005% [82]) with adjustable period and range. When the calibrator is connected, the TAC spectra presents several consecutive equidistant sharp peaks. The period of the calibrator divided by the distance in channels between those peaks gives the time calibration of the TAC.

For the slow-TACs (β-HPGe), the calibrator was set for a range of 5.12 μ-secs and a period of 0.64 μ-secs, which yielded the following calibration:

- SlowTAC-1: 241.4(2) ps/chan
- SlowTAC-2: 240.5(2) ps/chan

The same calibrator was used for the fast-TACs (β-$LaBr_3$) but with a period of 10 ns. This produced time spectra which apparently were correct, but, when checked with known half lives, probed to be wrong. The half life of the 2083.26(3)keV level in ^{140}Cs was precisely measured to be 3.474(10) ns [17], but the fits result in half lives of over 4 ns. The calibrator was not working for that specific period, so its results for the fast TACs were discarded. The fit to the half life of the 2083.26(3)keV level in ^{140}Cs (shown in Fig. 4.8) was used for calibration. The resulting calibrations were:

- FastTAC-1: 1.813(33) ps/chan
- FastTAC-2: 1.777(41) ps/chan

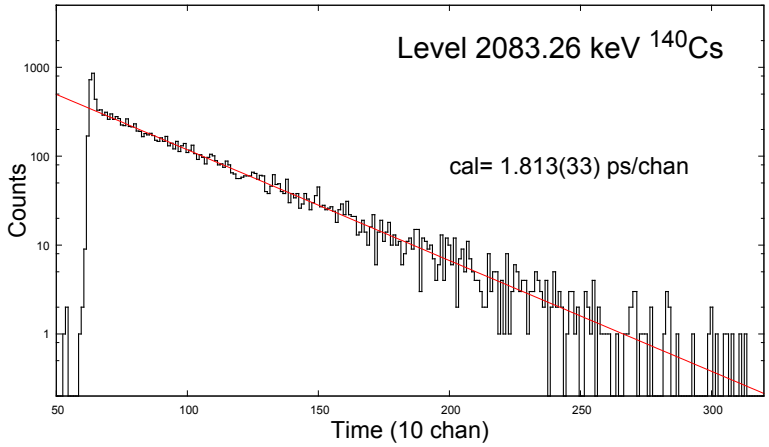

Figure 4.8: Exponential decay fit to the half life of the 2083.26(3)keV level in ^{140}Cs for the fast TAC-1. Knowing the half life, the calibration was 1.813(33) ps/chan.

4.2.2 β-walk

The NE111A plastic detector time response depends on the energy deposited by the β particle. In order to minimize this effect, a very thin plastic of only 3 mm was used, so every particle deposited a similar amount of energy. Fig. 4.9 (bottom) shows an example of a β energy spectrum, shown in channels as the detector was not calibrated. As expected for β-decay, the β particles reaching the plastic detector follow a continuous energy distribution whose end-point is related by the Q_β value of the decay to the populated levels.

Since the detector is very thin, only a fraction of the incident energy is deposited in the plastic. But no all the β particles are impinging in the detector perpendicularly, so the effective thickness can be much longer. Furthermore, once inside the plastic the β particle can suffer a different number of collisions. All these effect contribute to produce a β-energy spectrum as seen in Fig. 4.9 (top).

Even with all the precautions taken to minimize the plastic time response, there is still a dependence with the deposited energy and the Q_β of the β-particle. This is known as the *β-walk* and is a second order contribution to the system time response that can be corrected.

In triple coincidences $\beta\gamma\gamma$, the β energy spectrum was divided into several gates and projected on to the TAC. Fig. 4.9 (top) shows the result after setting gates on the 363.7 keV in ^{65}Fe. It is clear that there is a dependence of the time response with the β energy. To correct this effect the TACs were displaced event by event as a function of the β energy, to give a constant response. Fig. 4.9 (middle)

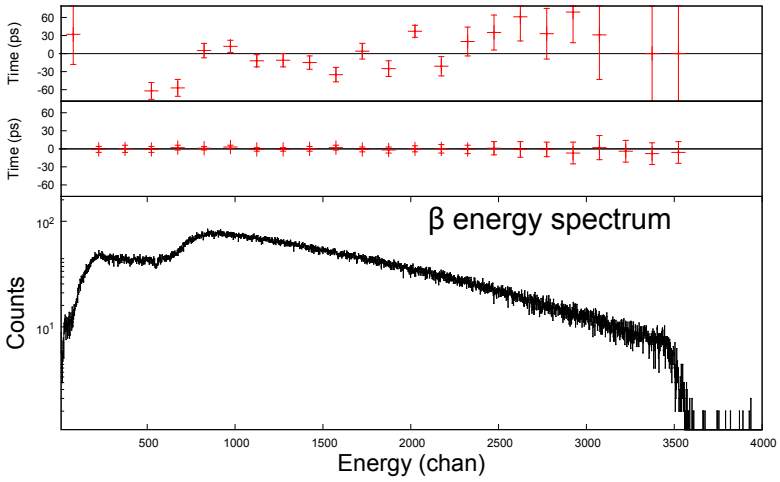

Figure 4.9: Example of a β energy spectrum. It was taken in coincidences with the HPGe detectors during the A=65 mass run. On top can be seen the time response of the plastic detector before the β-walk correction and in the middle the same response after the calibration.

shows the same time response after the correction of the β-walk. Now it is constant for almost every energy. At lower and higher energies the correction did not work so well, so they were discarded, but they only represented a very small fraction of the total statistic.

As every β decay has a very different Q_β and energy distribution, this correction must be made independently for each nucleus or calibration source studied.

4.2.3 Compton-walk

The time response of scintillator crystals depends on the energy of the incident photon and, in the case of Compton events, the energy deposited inside the crystal. At the same energy, the time response is different for Compton and full-energy events, so a different response curve is needed for each kind of event in order to correct the contribution of the Compton events under the full-energy peak.

When we select an energy gate in a peak the time distribution obtained from this gate will have two components, one from the full-energy peak and the other from the Compton events of higher energy transitions. When measuring the intensity of a transition in an HPGe, for example, the nearby Compton can be subtracted as it is safe to assume it has the same behaviour of that underneath the peak. But when measuring lifetimes this is not possible, as the Compton events next to the full-energy peak do not have the same time response as those underneath it. For

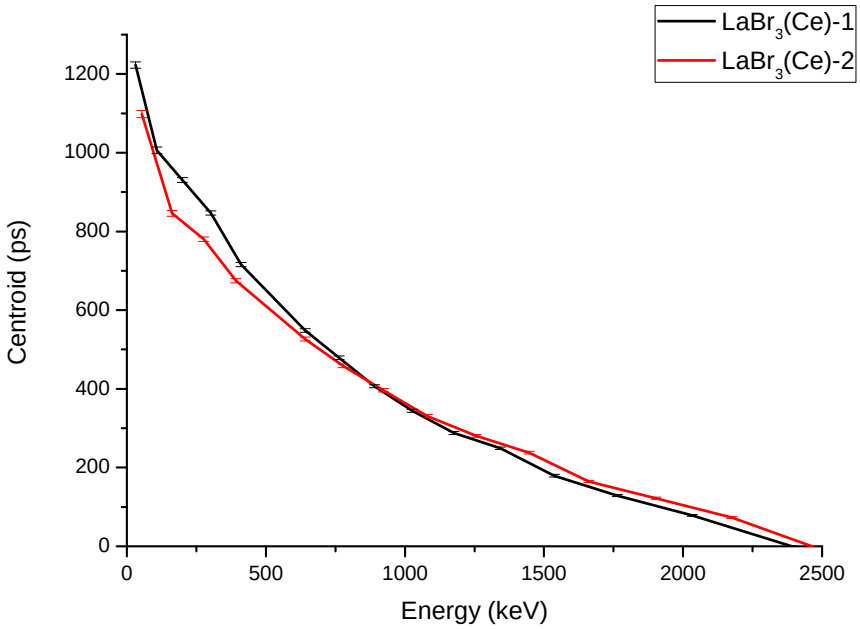

Figure 4.10: Compton walk curve for both $LaBr_3(Ce)$ crystals. Both detectors present a very smooth curve, but too steep, worsening time resolution.

this reason is needed the *Compton-walk* curve, so we can measure the relative time difference of the Compton events at different energies.

The curve was made using the ^{24}Na calibration source. A gate was set in the 1368 keV HPGe peak and projected on to its $LaBr_3$ coincidences. The resulting projection was a spectrum with the 2.7 MeV photopeak and its long Compton background. This Compton was divided in 15 gates of around 200 channels each and projected on to the TAC.

The results for both detectors are shown in figure 4.10, in which the curves were shifted so the end point was zero. Both detectors show a very smooth curve (the small bump in the anihilation peak 511 keV was removed) but they present a very steep slope, as well. This is due to the high working voltage and the high light-yield of the $LaBr_3(Ce)$.

This steep slope of the time response affects negatively the time resolution of the crystals. During this experiment, an energy resolution of 2.5% at 898.03 keV (^{88}Rb decay) was observed for the $LaBr_3(Ce)$ crystals. When setting an energy gate in these detectors, the gate may be a few tens of keV wide. When the time response curve is so steep, the time difference between both ends of such a broad gate can

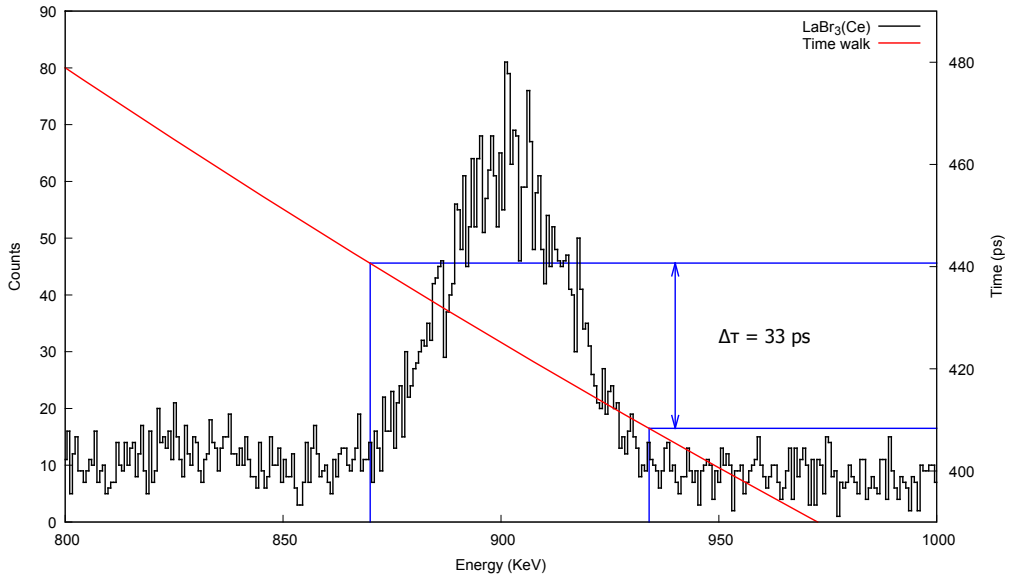

Figure 4.11: Time walk over the $LaBr_3(Ce)$ energy spectrum. It can be seen how the time response of the detector changes over 30 ps from the lower energy point of the full-energy peak to the higher energy.

be of 20-30 ps instead of the usual 2 or 3 ps (see Fig. 4.11). This causes a broader time spectra, worsening the time resolution of the detector.

To minimize this effect, a correction is performed in two steps. The Compton walk curve of each detector was independently fitted to a 4^{th} order polynomial, which yielded a fair result (lower order were not able to reproduce the curve). In this first step, the TACs were displaced as a function of the energy, event by event, by an integer amount shift $= 5000 - (\text{int} + Ax + Bx^2 + Cx^3 + Dx^4)$, where x is the uncompressed energy in channels. This way it should yield a very flat walk curve around channel 5000. Fig. 4.12 shows the result of this first correction. The time difference now in the analysed energy range is under 60 ps, compared to the ~ 1.2 ns before the recalibration, but still it is not smooth enough, so a second one was performed.

In the second step another shift was made to the TACs, but this time in a similar way to the one made to the β-shift. The Compton continuum produced by the 2.7 MeV transition in ^{24}Na was taken, segmented (using the same energy gates as before) and calculated its distance to channel 5000, to shift every TAC event within that energy range by that amount. The high non linearity of the $LaBr_3$ makes the energy window width quite different from one to the other, but they range from 100 keV in the lower ones to 200 keV in the higher ones. Fig. 4.13 shows the result after

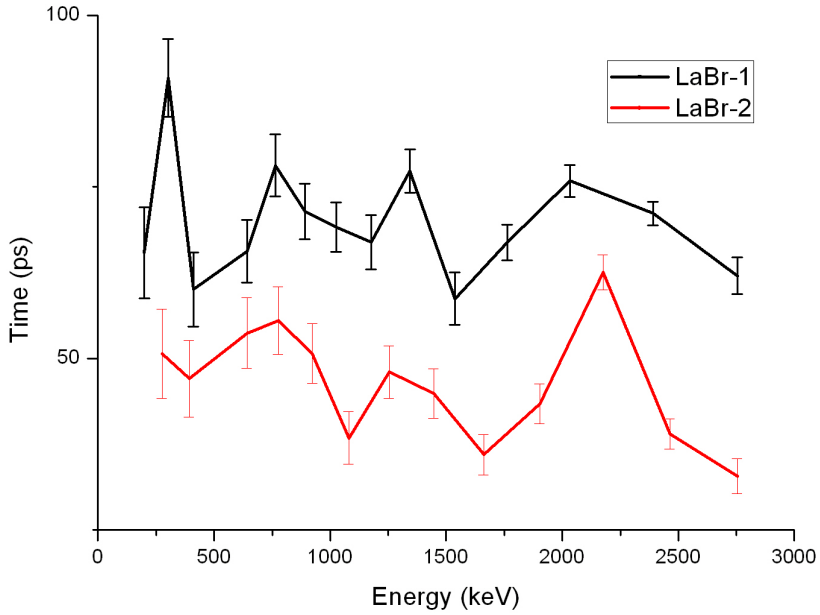

Figure 4.12: Compton walk curve from 2.7 MeV peak in ^{24}Na after the 4^{th} polynomial order correction. Even if it is clear that the curve is not as steep as before, the dispersion of the points around a flat line is still too large.

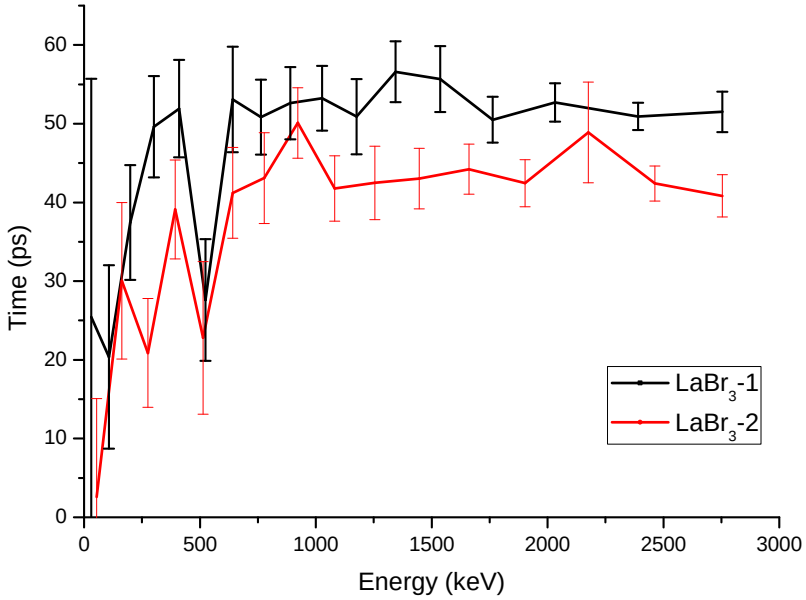

Figure 4.13: Compton walk curve from 2.7 MeV peak in ^{24}Na after the the second correction. Above 511 keV the time response is really flat, but below it is clear that it did not worked that well, mainly because the fit to the polinomy was not that precise at lower energies.

the second correction. There is still some deviation from a flat line of the points, but it is much smaller than in the previous step (an average of around 5 ps versus the previous 15 ps). The large negative bump near the 511 keV energy is due that this point was not taken when fitting the time response (as it cannot be reproduced) and thus is over-subtracted.

The Compton walk curve is different depending on the energy of the incident gamma, thus for each photopeak studied, a different Compton walk curve should be corrected. This is a minor correction, well below the precision of the current experiment. For this reason, this calibration was performed to all the masses run in the experiment using the curve obtained from the ^{24}Na source.

4.2.4 Prompt curve

As mentioned above, the time response of a scintillator crystal is different for a Compton than for a true full-energy event, so it is necessary to make a different

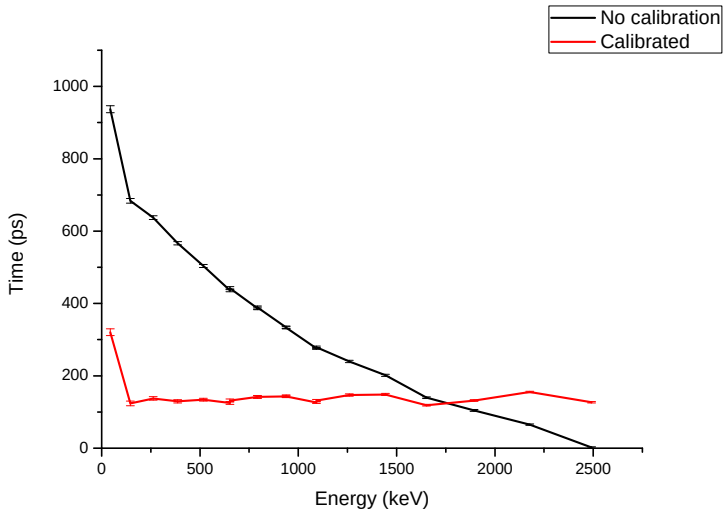

Figure 4.14: Time response of the $LaBr_3(Ce)$ crystals as a function of the gamma energy. Before the correction the difference in the centroid of the time distribution was almost 1 ns in the 200 keV to 2 MeV range, when after the correction it is under 50 ps.

calibration for prompt full-energy peaks. The sensitivity of the ATD Method is near a few picosecond, so any transition which half life is lower than 1 ps is considered prompt. For this calibrations, when the half life is close but not below 1 ps, the centroids are shifted by the mean life so they fit in the prompt curve. Tab. 4.2 summarizes the transitions used for this calibration.

Each time the mass or the calibration sources is changed, the position of the new radioactive source is not exactly the same as the previous one and, furthermore, any of the detectors may have been displaced from its original position. Each millimetre shift in the relative radioactive source-detector position means $3.\overline{3}$ ps time difference, within the time precision of the ATD method. Every nucleus presents the same time response (after correcting the different β-walk curves) but each will be shifted a constant time due to this geometrical effect.

It must be noted that, even if the absolute position of the prompt curve changes from one measurement to another, its characteristic shape is the same for a given experimental conditions (all nuclei measured during the same experiment will give parallel curves). For this reason this curve can be used as a relative prompt calibration curve, and time distributions can be shifted until they match a point from a calibration source or the interpolated line between two of them. This characteristic is what allow us to measure most of the mean lives in an experiment but it is aswell the largest source of uncertainty when using the centroid shift technique, specially

Isotope	Energy (keV)	Intesity (%)	Half life (ps)
^{24}Mg	1368.6	99.994(15)	1.33
^{24}Mg	2754.3	99.855(5)	0.022
^{88}Sr	898.3	14.68(13)	0.78
^{88}Sr	1836.0	22.73(15)	0.148
^{140}Ce	328.7	20.3(3)	1.3
^{140}Ce	432.5	2.9(3)	1.3
^{140}Ce	751.6	4.3(4)	0.15
^{140}Ce	815.8	23.28(19)	1.3
^{140}Ce	925.2	6.9(1)	0.9
^{140}Ce	1596.2	95.40(8)	0.1

Table 4.2: Sumary of all gammas used in the promt walk calibration of the $LaBr_3$ detectors. ^{24}Mg and ^{88}Sr values from [77], ^{140}Ce half lives from [83].

when the walk-curve is very steep.

Firstly the transitions of the ^{140}Ba source (^{140}Ba$\rightarrow$ ^{140}La $\rightarrow$ ^{140}Ce) were analysed. The other two sources, ^{24}Na and ^{88}Rb, each present two transitions prompt or near prompt, one of them within the energy range of the ^{140}Ba and the other outside. Both pair of points were shifted until the lower energy transition was in the interpolation of the ^{140}Ba prompt curve. This way the energy range was from 328.7 keV up to 2754.3 MeV.

Fig. 4.15 shows the prompt response curve of both crystals as the difference of the time response of a photopeak respect to Compton of its same energy. As can be seen, below 511 keV the photo-electric events are faster (thus negative in the plot), but for intermediate energies above the electron mass they are slower. Depending on the crystal, for higher energies of around 2 MeV the photopeaks become slower again.

4.3 Concluding remarks

This chapter has described the careful calibrations performed for the analysis of the data collected in the IS474 experiment.

Special emphasis has been put in the relative efficiency calibration of the HPGe detectors, as is with this curves with will be used to measure the intensity of the gammas and the transitions rates, one of the most useful probes we have to understand the nuclear structure.

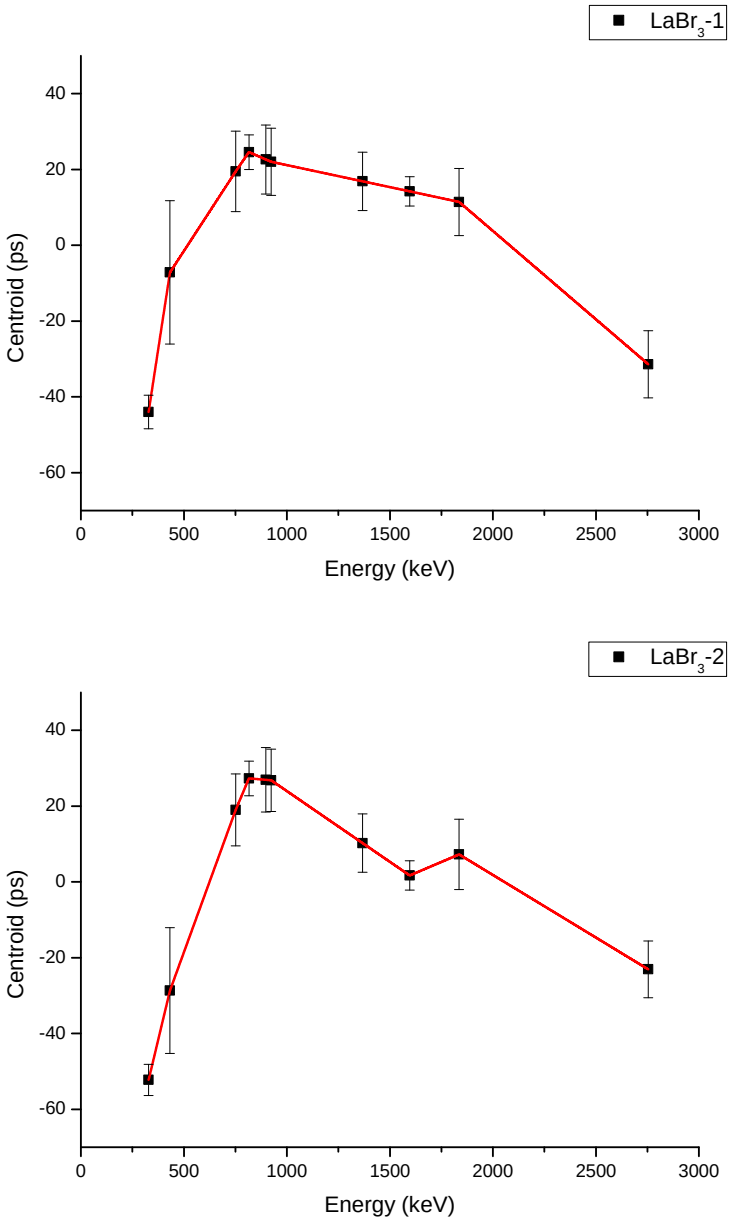

Figure 4.15: Prompt time response as a function of the γ energy of $LaBr_3$(Ce)-1 (up) and $LaBr_3$(Ce)-2 (bottom), as the difference with their respective Compton walk curve.

The other key element in the reduced transition measurements are the level lifetimes. The ATD method is powerful tool to measure half lives in the picosecond range, but it needs of careful timing calibrations. The steep time walk curve of the timing detectors was a new challenge for our group. The correction applied to flatten the curve was not as sucesful as expected, with a small improvement in time resolution.

All these calibrations will be applied to the future analysis of the data collected on the other masses during the experiment.

Chapter 5

^{65}Fe analysis

There was almost no information on the ^{65}Mn β decay to ^{65}Fe and very little information on the nuclear structure of this iron isotope. We have studied the low energy structure of the ^{65}Fe nucleus populated in the ^{65}Mn β decay by means of γ- and fast-timing spectroscopy.

A new level scheme was constructed including over 35 new levels and over 80 new transitions, including the direct β population to the ground state and a P_n value for the neutron delayed emission branch. Moreover, the first evidence of that this β-n branch populates excited levels in ^{64}Fe was observed.

The two isomers previously observed were identified. An improved value of the γ-decaying lifetime was measured and for the first time the precise energy value of β-decaying was deduced.

We were able to measure some of the lower energy level lifetimes in the sub-nanosecond range, which were used to calculate B(XL). By comparing the level scheme with shell model calculations that use the LNPS interaction tentative spin-parity were assigned to some of the levels.

5.1 Information on ^{65}Fe from previous studies

Prior to this study, there was scarce information on the β-decay of ^{65}Mn and on the levels in ^{65}Fe. The half-life of the ^{65}Mn ground state has been measured several times and the adopted value [84] is 92(1) ms. A $P_n = 21.0(5)$ % for the β-n branch of ^{65}Mn was reported by Hannawald and collaborators [18], who concluded that all the delayed neutron intensity directly feeds the ground state of ^{64}Fe.

The first information on the excited states in ^{65}Fe came from the study of

Grzywacz *et al*, [34] who reported a 430(130) ns isomer at the excitation energy of 364 keV de-excited by a 364 keV γ ray to the ground state. Later Daugas *et al.* [85, 37] established that the isomer is in fact at the energy of 396.8 keV as it feeds the 363.3(5) keV level by a previously unobserved 33.5(5) keV transition. They have made a new measurement of isomer half-life as $T_{1/2} = 420(13)\ ns$. They assigned the 33.5 transition as E1 [86]. A tentative and partial level scheme of ^{65}Fe following the β-decay of ^{65}Mn was proposed by Gaudefroy *et al.* [87]. They have identified ten transitions in the β decay of ^{65}Mn and placed five of them in a tentative level scheme. Since no $\gamma - \gamma$ coincidences were observed two new levels at the excitation energy of 455 and 1089 keV were proposed based on the energy matching. The 455 keV level was proposed to be de-excited by the 455 and 92 keV transitions, while the 1089 level by the 752 and 1089 keV lines. The 397 keV level was not observed in β decay, while the β feeding was proposed to be <10%, 47%, 13% and 15% to the ground, 364, 455, and 1089 keV states, respectively.

A second isomer in ^{65}Fe was identified in mass excess measurements using Penning trap mass spectrometry. The excitation energy of this β^- decaying state was first reported at 402(5) keV [88] and then corrected to 402(10) keV [35]. Its half-life was estimated to be longer than 150 ms. Precise γ-spectroscopic measurements established that the two β-decaying states in ^{65}Fe populate two sets of mutually independent level schemes in ^{65}Co [89]. The half-lives of the β-decaying states were measured as $T_{1/2} = 1.12(15)$ s for the 402(10) keV $(9/2^+)$ isomer and $T_{1/2} = 0.81(5)$ s for the $(1/2^-)$ ground state [89].

Studies of the multinucleon transfer reactions on a ^{238}U target [3] revealed two transitions in ^{65}Fe with energies of 771.6(7) and 1118.2(10) keV. It was suggested that they form a high spin yrast cascade with the sequence started by the less intense γ-ray, 1118.2 $\rightarrow$ 771.6 with the proposed spin sequence $17/2^+ \rightarrow 13/2^+ \rightarrow 9/2^+$. These transitions are not expected to be observed in the β-decay of ^{65}Mn.

5.2 Experimental details

The activity of ^{65}Mn was produced at the ISOLDE facility at CERN by bombardment of a 51 g/cm^2 UC_2/graphite target with 1.4 GeV protons from the PS-Booster. The reaction products diffused out of the target matrix, were ionized by the selective resonant ionization laser ion source RILIS [90] and extracted with a differential potential [42]. The $A = 65$ ions were then mass separated by the General Purpose Separator (GPS) and deposited onto a thin aluminum foil in the center of the experimental setup. The proton beam from the PS-Booster is pulsed with pulses separated in time by multiples of 1.2 s. During the brief interaction of protons on the target the ions released at that time were deflected away. The full function of the

separator was restored about 8 ms after the proton pulse, and then the separated beam was collected again at the detector station. After a predefined period of time of 400 ms the beam is deflected again (by closing the so-called beam-gate) in order to block the collection of long-lived activities released from the target and the collected sample was allowed to decay out. In our experiment the ions were deposited on the collection foil creating a saturated source that included short- and long-lived decay products from the decay of ^{65}Mn and its daughters. The strongly produced long-lived ($T_{1/2}$ = 15.2(2) min) ^{65}Ga was also present in the data as a contaminant by the surface-ionization capability of the ion source.

The measurement station included five detectors positioned in close geometry around the beam deposition point (see Fig. 5.1). The fast timing β-detector was a 3 mm thick NE111A plastic scintillator placed directly behind the radioactive source. The γ-ray detectors included two fast-response $LaBr_3$(Ce) scintillators in the shape of truncated cones (38.1 mm in height, 38.1 mm diameter at the bottom and 25.4 mm diameter at the entrance window), which were coupled to the Photonis XP20D0 photomultipliers, as well as two HPGe detectors with relative efficiencies of 60%. The experimental set-up and data collection was optimized for the application of the Advanced Time-Delayed $\beta\gamma\gamma$(t) method described in [13, 14, 15], so only a few details are given below.

The data were collected using a digital system which consisted of four Digital Gamma Finder (DGF) Pixie-4 modules Revision C made by XIA [16]. Ten parameters were collected in an independent ungated mode without external triggers. Out of the five energy pulses from individual detectors, signals from the two HPGe detectors were directly fetched to the module inputs, while the three dynode signals from the β and γ scintillator detectors were too fast to be directly processed by the XIA modules. Instead they were preamplified, amplified and reshaped with a Linear Gate and Stretcher before they were fetched to the Pixie-4 cards.

For a precise timing information we had set four analog time-delayed $\beta\gamma(t)$ coincidence systems each started by signals from the β-detector and stopped by a fast signal from one of the γ detectors. The time range was set to 50 ns for coincidences between scintillator detectors and 2 μs for the β-HPGe coincidences. The analog outputs from the Time-to-Amplitude Conversion units were directly fed to the Pixie-4 modules. The acquisition system has also collected the time of arrival of the proton pulse on the target.

Coincident events between detectors were sorted off-line using the PIXIE time stamp on each collected parameter. Since the two HPGe detectors were connected to the same XIA card coincident events between their signals were automatically identified on-line within a total time resolving window of $\pm$8 μs. More restrictive time windows were selected in the off-line analysis where one could inspect the

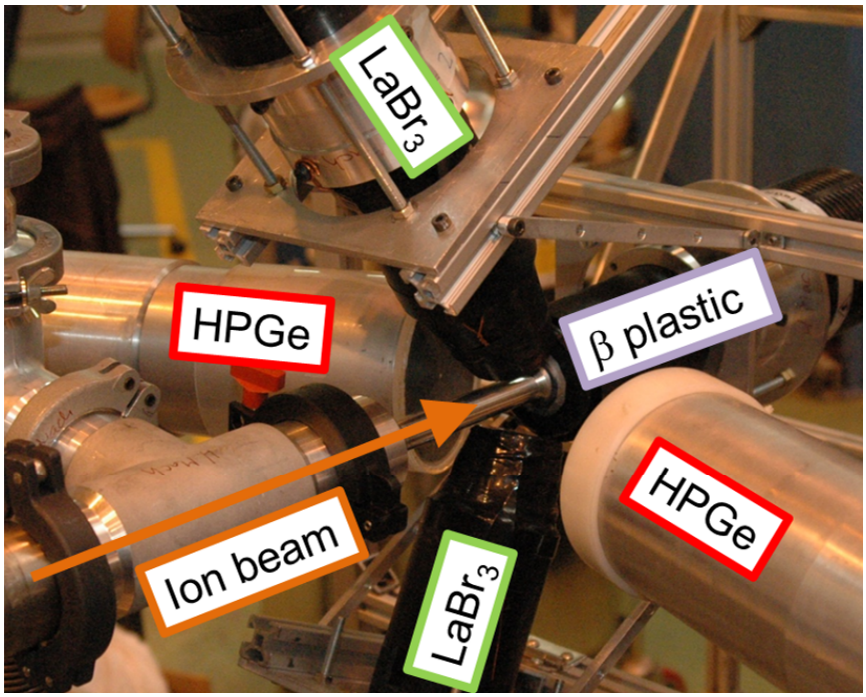

Figure 5.1: Five detectors in the compact set-up used for the measurements on ^{65}Mn decay. The front HPGe detector is slightly moved back for the picture in order not to block the view of other detectors.

coincidence peak and flat spectrum of random events.

The energy calibrations of the HPGe detectors were made to the precision of ±0.1 keV using the sources of ^{152}Eu, ^{24}Na, ^{88}Rb and ^{140}Ba. During the whole measurement the energy shifts remained within the ±0.1 keV limit. The same sources provided relative efficiency calibrations of the HPGe detectors in the energy range from 120 keV to 2.7 MeV. At lower energies relative efficiency calibrations were provided by the decay of ^{63}Co to ^{63}Ni observed in the same ISOLDE experiment.

Time response calibrations of the scintillator detectors

The lifetime measurements in the nanosecond and subnanosecond ranges were performed using the $\beta\gamma\gamma$(t) method [13, 14, 15]. The time-delayed $\beta\gamma(t)$ coincidences were started by a signal from the β-detector and stopped by one of the $LaBr_3$(Ce) γ detectors. An additional coincidence with the HPGe detector was used to select the desired γ decay branch. A comparison of the $\gamma\gamma$ coincidences using HPGe-HPGe and HPGe-$LaBr_3$(Ce) detectors allowed to reveal the exact composition of the $LaBr_3$(Ce) coincident spectra characterized by worse energy resolution. The time response calibration of the fast timing detectors were performed using the β-decay sources of ^{140}Ba/^{140}La, ^{88}Rb and ^{24}Na. The shape of the semi-prompt $\beta\gamma(t)$ time spectra was verified to be close to symmetric Gaussians over the range of γ-ray energies of interest. We have corrected for the β walk-curve non-linearity using our standard procedures. The residual differences from a flat constant response were on the average less than 5 ps.

The time responses of the fast timing $LaBr_3$(Ce) γ detectors were carefully calibrated to a 10 picoseconds precision separately for the Compton and the Full-Energy-Peak (FEP) γ events recorded in the crystals. The procedure started with the construction of an "Approximate Prompt Curve" (APC) using the Compton events for transitions following the decay of the ^{24}Na source, and then using this curve to extract "Residual Differences" (RD) between the FEP events and the APC curve using different sources. Our procedure is very similar to the one described in detail in Ref. [15]. The Residual Differences for the Compton and FEP events are shown in Fig. 5.2, which is equivalent to figure Fig. 4 in Ref. [15]. We note here, that the time response of a Compton event is not the same as that of FEP of the same energy, for the discussion of the issue see [15].

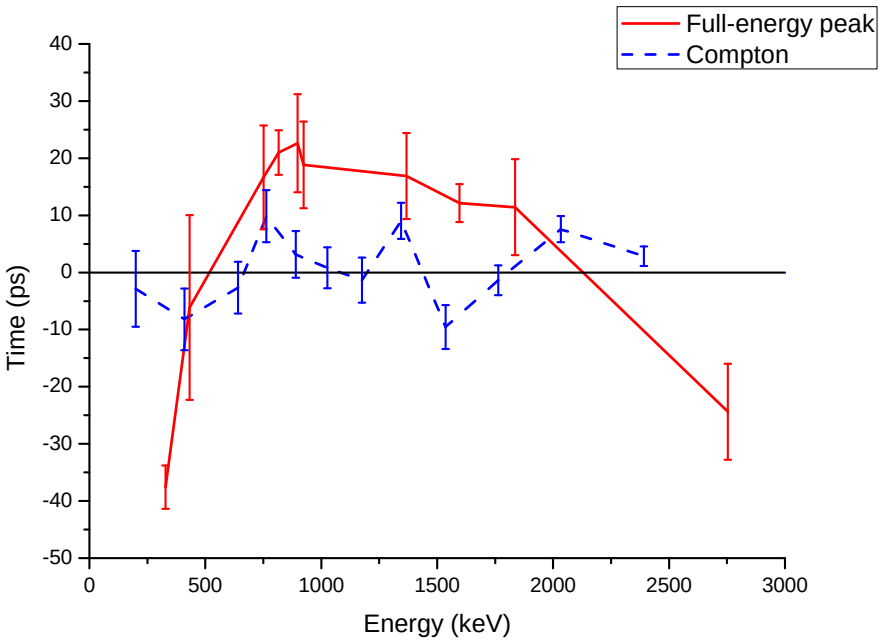

Figure 5.2: Residual Difference curves showing relative time response for $LaBr_3(Ce)$-1 detector as a function of energy for the FEP (solid line) and Compton events (dashed line).

5.3 Results

The identification of γ-rays belonging to the β decay of ^{65}Mn was made using three lines of evidence. First, a two-parameter data set, which included the energies of events recorded in the HPGe detector and the time elapsed between the event and the last proton pulse, was analyzed. The short-lived activity of ^{65}Mn was enhanced in the off-line sorting by selecting a time window from 10 to 450 ms after the proton pulse. Longer-lived components, including those arising from the ^{65}Ga contaminant, have been subtracted. The subtracted spectrum was obtained by selecting an equivalent time window above 800 ms, which contained virtually no ^{65}Mn activity.

Figures 5.4 and 5.3 show an energy spectrum recorded in a HPGe detector sorted from the two-parameter data set involving HPGe events and the time elapsed between the event and the last proton pulse. Time gate was set on the proton time spectrum in order to enhance the ^{65}Mn activity and longer lived activities were subtracted. For a better display, the higher energy spectrum was further compressed. Figure 5.5 shows an equivalent energy spectrum observed for one of the $LaBr_3$(Ce) detectors, which was characterized by 3.3(1)% energy resolution at 898.0 keV in ^{88}Sr.

Next, using the same data set gates were set on the full energy peaks in the HPGe spectrum and projected on the proton time spectrum. The γ-rays were identified as belonging to the Mn decay if their time spectrum was consistent with the decay half-life of 92 ms. As the third line of evidence the identification of a line from the decay of ^{65}Mn was made based on firm coincidences with the Mn lines already identified in the first two steps.

5.3.1 ^{65}Mn half-life

The ^{65}Mn half-life was obtained by fitting a time spectrum sorted out from the aforementioned two-parameter data set. It was gated by the 363.7 keV γ-ray, the strongest transition in ^{65}Fe, and projected onto the time elapsed from the last proton pulse. The time spectrum is shown in Fig. 5.6. A portion of the spectrum, from 400 to 1200 ms, was fitted to an exponential decay plus a constant background. At 400 ms after the proton pulse the beam gate was closed and radioactive sample was left free to decay, while 1200 ms marks the shortest period set between two consecutive proton pulses. The fitted slope yields the half-life of $T_{1/2}$ = 91.9(0.9) ms, in very close agreement with the adopted half-life of 92(1) ms [84]. A similar analysis was performed on the next five strongest lines in ^{65}Fe, namely 455.6, 569.1, 683.3 (a summed doublet), 725.2 and 1002.9 keV lines. The weighted average of these five γ-rays gives $T_{1/2}$ = 92.0(1.3) ms in agreement with the former result.

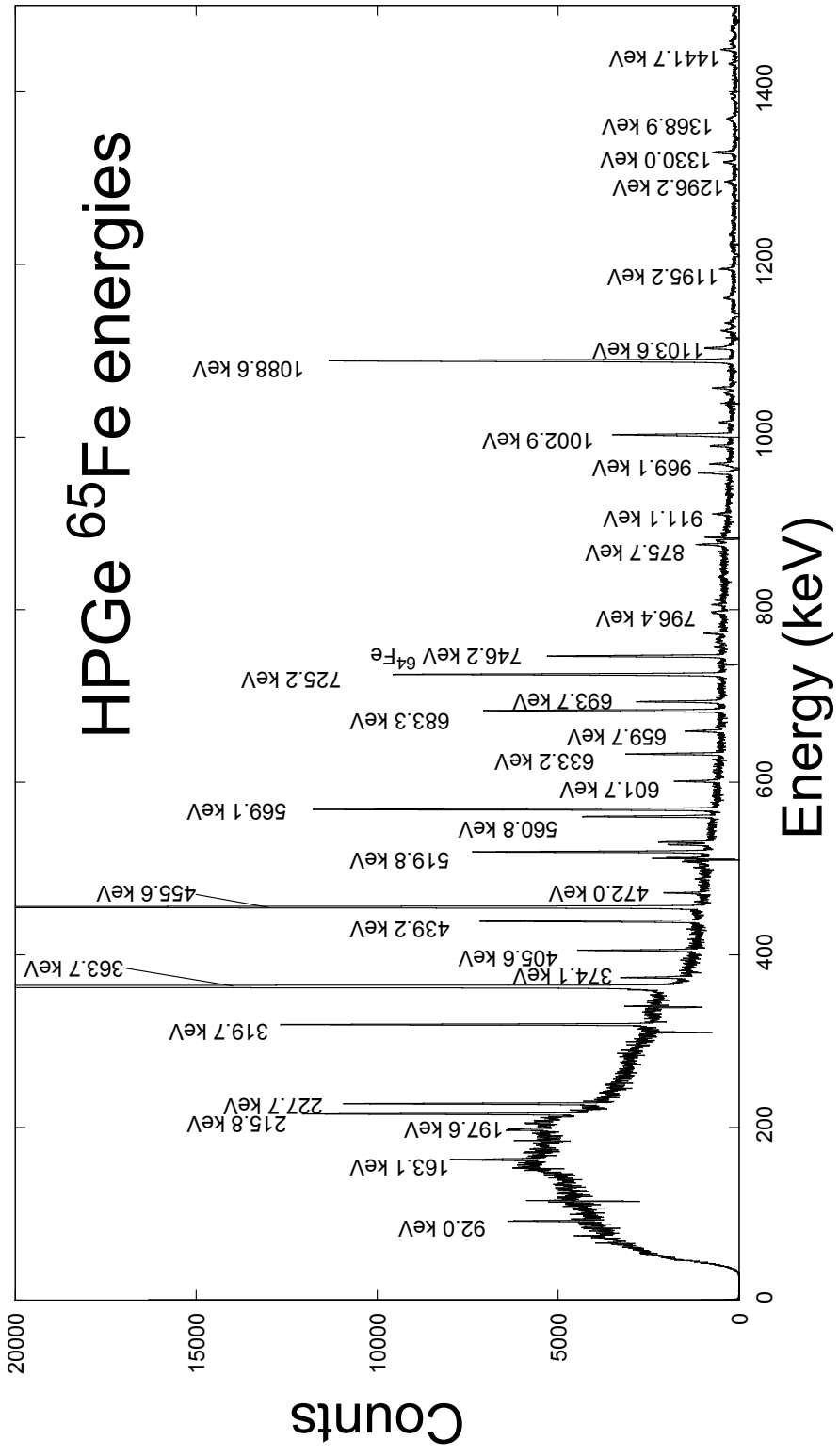

Figure 5.3: Lower energy HPGe spectrum with ^{65}Mn activity enhanced and ^{65}Fe transitions identified.

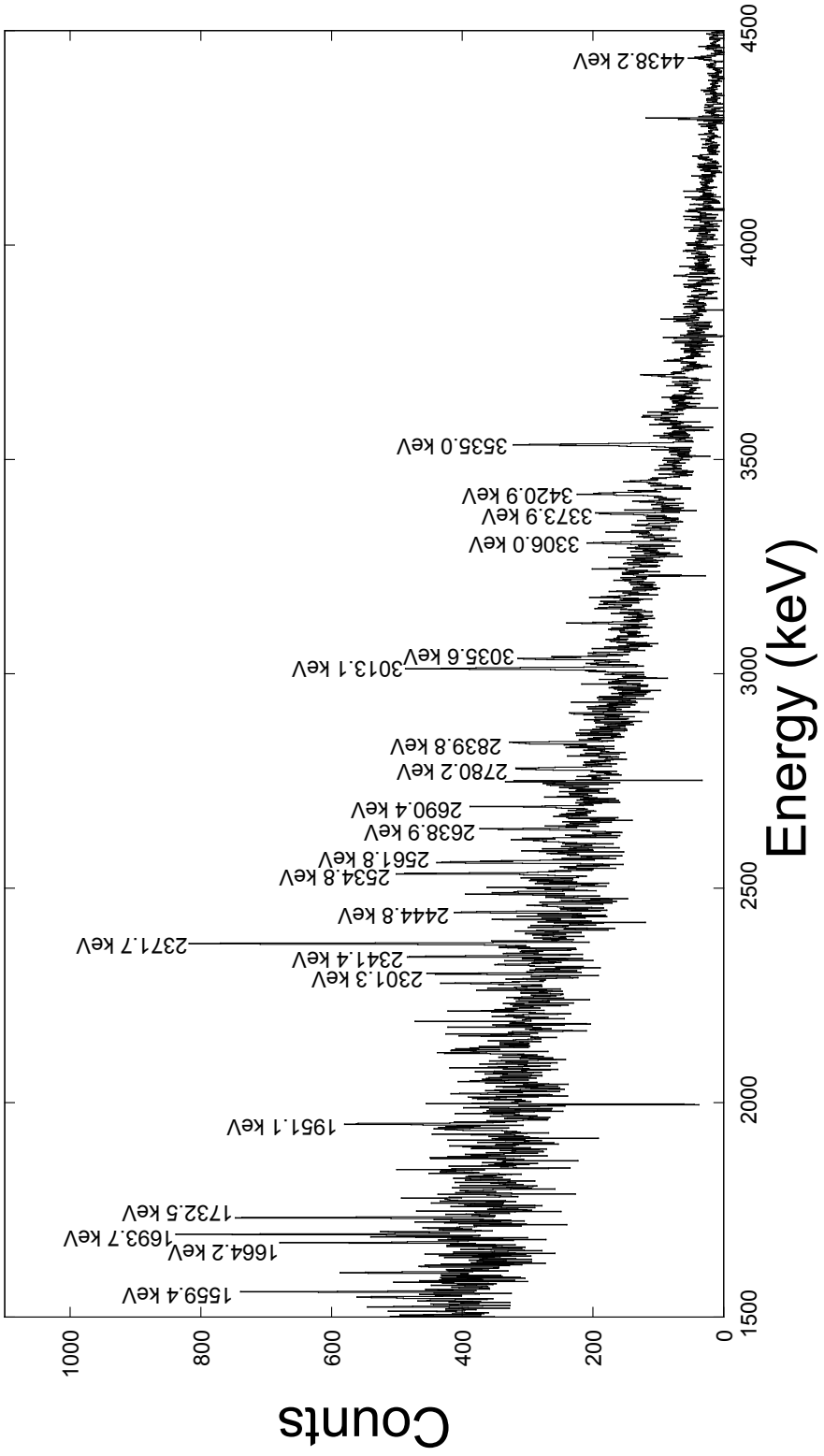

Figure 5.4: Higher energy HPGe spectrum with ^{65}Mn activity enhanced and ^{65}Fe transitions identified. This part of the spectrum has been further compressed for a clearer display.

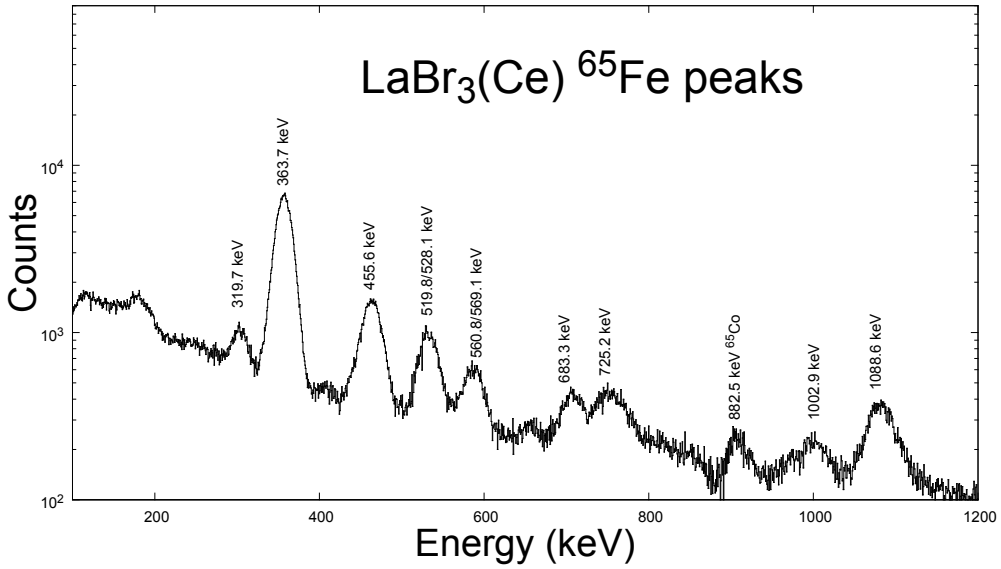

Figure 5.5: $LaBr_3(Ce)$ energy spectrum obtained in an equivalent way to the HPGe energy spectrum. Peaks are labelled by the most intense transition energies in ^{65}Fe.

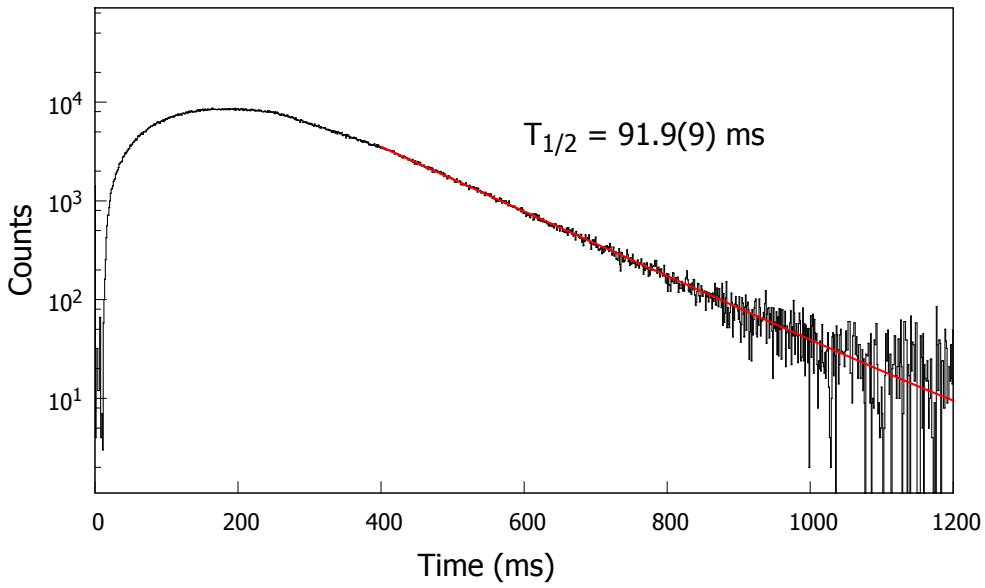

Figure 5.6: The time spectrum for the time elapsed from the last proton pulse for the Ge events gated by the 363.7 keV transition. The fit between 400 and 1200 ms gives the half-life of ^{65}Mn; see text for details.

5.3.2 $\gamma - \gamma$ coincidences

The identification of weak γ transitions in ^{65}Fe was based on the $\gamma - \gamma$ coincidence relations with the known transitions in ^{65}Fe. The $\gamma - \gamma$ coincidences were sorted out from a 3 parameter data set, which included a pair of coincident γ-rays recorded in HPGe-1 and HPGe-2 within a time resolution of ± 0.5 μs and the time elapsed from the last proton pulse. Gates were set on the full energy peaks in one of the HPGe detectors and projected onto the other HPGe and vice-versa. Fig 5.7 shows γ-rays in coincidence with the 363.7 keV line. In order to enhance the ^{65}Mn activity a gate was also set on the proton time spectrum between 10 to 450 ms.

A detailed level scheme for the β-decay of ^{65}Mn to ^{65}Fe was determined for the first time. It includes 85 transitions and 41 excited states. These are summarized in Figs. 5.8 and 5.9 and Tables. 5.1 and 5.2. We have also identified a level scheme in ^{64}Fe populated in the β-n branch, see Tab. 5.3. The relative intensities were obtained from the singles γ-ray spectra, except for the γ rays that were part of multiplets or were too weak to clearly show up in the singles spectrum. In those cases their energies and intensities were obtained from the γ-γ coincidences. There are a few high energy transitions without coincidences that define a level by themselves in ^{65}Fe. Even if they are firmly assigned to the ^{65}Mn decay, there exists the possibility, albeit minor, that these gamma-rays belong in the ^{64}Fe scheme. Without a detailed ^{64}Fe level scheme, this possibility cannot be completely excluded.

Out of 10 transitions for the decay of ^{65}Mn to ^{65}Fe identified by Gaudefroy *et al.* [87] we confirm 7 lines at the energy of 92, 363, 455, 684, 724, 1004, and 1089 keV. It is not certain whether the 214 keV line listed in Ref. [87] is our 215.8 keV transition, but we definitely did not identify transitions of the energies 1550 and 1843 keV as belonging to the decay of ^{65}Mn. Based on our $\gamma\gamma$ coincidences we confirm the very tentative and partial level scheme proposed in [87] where the energy matching of strong transitions were used.

E_γ (keV)	$E^{level}_{initial}$ (keV)	E^{level}_{final} (keV)	I^{rel}_γ	Strongest $\gamma\gamma$ coincidences (keV)
33.9(2)	397.6(2)	363.7(1)	4(1)[a]	-
92.0(1)	455.6(1)	363.7(1)	0.8(1)	228.1, 363.7, 439.5, 683.8, 1103.6
114.5(3)	683.3(1)	569.1(1)	0.2(1)[b]	205.7, 363.6, 569.3
163.1(1)	561.0(2)	455.6(1)	0.7(1)	363.7, 456.0, 528.5
197.6(3)	561.0(2)	363.7(1)	1.4(1)[b]	363.7, 528.2, 2371.7
205.3 (2)	569.1(1)	363.7(1)	0.3(1)	363.7, 455.0, 520.4, 633.3, 725.9, 1318.3
215.8(1)	609.5(3)	393.7(2)	2.9(2)	757.5, 763.4, 1123.0, 1392.5
227.7(1)	683.3(1)	455.6(1)	2.5(2)	92.8, 363.7, 374.0, 405.9, 455.8

319.7(1)	683.3(1)	363.7(1)	4.4(3)	363.9, 374.6, 405.9, 683.8, 724.6, 875.8, 1319.0
363.7(1)	363.7(1)	g.s.	100	92.4, 163.5, 197.7, 205.9, 227.9, 319.9, 374.4, 405.8, 439.3, 531.5, 659.7, 683.7, 693.9, 725.4, 875.4, 969.1, 1002.9, 1318.3, 1330.1, 1368.7, 2372.1,
374.1(1)	1057.3(1)	683.3(1)	1.0(1)	227.8, 319.6, 363.9, 455.9, 683.5, 796.7, 2341.5
405.6(1)	1088.7(1)	683.3(1)	1.8(1)	227.9, 320.0, 363.9, 455.9, 683.6
439.2(1)	894.8(1)	455.6(1)	3.5(3)	92.2, 363.5, 455.9, 472.4, 958.7
455.6(1)	455.6(1)	g.s.	24.4(1.8)	227.9, 374.1, 405.8, 439.4, 472.3, 601.9, 633.5, 683.7, 875.8, 911.0, 958.6, 1001.6, 1103.2
472.0(1)	1366.6(2)	894.8(1)	0.9(1)	92.9, 363.7, 439.4, 455.9
488.3(2)	1057.3(1)	569.1(1)	0.2(1)	569.2
501.3(5)[c]	-	-	0.2(1)	-
519.8(1)	1088.7(1)	569.1(1)	4.3(3)	205.9, 569.4
528.1(1)	1088.7(1)	561.0(2)	0.9(1)	163.6, 197.6, 363.7, 561.1
531.1(1)	894.8(1)	363.7(1)	1.1(1)	363.8, 472.0, 837.7, 958.5
560.8(1)	561.0(2)	g.s.	2.7(2)	528.4, 806.2, 811.6, 1163.2, 1559.4, 2444.8, 3535.1
569.1(1)	569.1(1)	g.s.	8.4(6)	114.4, 488.2, 520.0, 796.8, 989.7 1123.9, 1163.7, 1731.9, 1950.7, 2371.2
601.7(1)	1057.3(1)	455.6(1)	0.9(1)	92.5, 363.8, 455.9
633.2(1)	1088.7(1)	455.6(1)	2.2(2)	92.3, 363.9, 455.9
659.7(1)	1057.3(1)	397.6(1)	0.8(1)	363.9
683.3(1)[d]	683.3(1)	g.s.	3.6(3)	92.4, 228.1, 319.9, 363.7, 374.5, 405.8, 455.9, 683.5, 875.9
683.3(1)[d]	1366.6(2)	683.3(1)	2.6(2)	See above
691.5(5)[e]	1088.7(1)	397.6(1)	0.2(2)	363.5
693.7(1)	1057.3(1)	363.7(1)	2.2(2)	363.7
725.2(1)	1088.7(1)	363.7(1)	8.8(7)	363.7
757.2(2)	1366.6(2)	609.5(3)	0.2(1)	215.9
763.0(3)	1372.6(3)	609.5(3)	0.2(1)	215.8
772.6(2)[f]	1228.2(2)	455.6(1)	0.4(1)	92.3, 363.5, 455.9
796.4(4)	1853.5(4)	569.1(1)	0.9(2)	569.4
796.9(1)	1366.6(2)	1057.3(1)	0.5(1)[b]	693.9

805.9(2)	1366.6(2)	561.0(2)	0.3(1)	163.5, 197.8, 363.7, 560.1
811.6(1)	1372.6(3)	561.0(2)	0.3(1)	197.5, 561.9
837.6(5)	1732.5(4)	894.8(1)	0.6(1)[b]	439.9, 455.2
875.7(1)	1558.9(5)	683.3(1)	0.8(1)	115.6, 227.9, 319.9, 363.9, 455.9, 683.4
911.1(2)	1366.6(2)	455.6(1)	0.3(1)	92.8, 364.3, 455.9
958.5(2)	1853.5(4)	894.8(1)	0.9(1)	364.4, 439.4, 455.9, 531.5
969.1(1)	1366.6(2)	397.6(1)	0.8(1)	363.8
989.7(1)	1558.9(5)	569.1(1)	0.7(1)	205.4, 363.4, 569.3
1001.6(5)	1457.2(5)	455.6(1)	0.8(1)[b]	92.0, 363.9, 455.8
1002.9(1)	1366.6(2)	363.7(1)	4.8(4)	364.0
1051.5(5)[c]	-	-	0.2(1)	-
1057.2(1)	1057.3(1)	g.s.	0.7(1)	-
1088.6(1)	1088.7(1)	g.s.	16.9(1.3)	-
1103.2(1)	1558.9(5)	455.6(1)	1.4(1)	92.5, 363.4, 455.8
1123.0(2)	1732.5(4)	609.5(3)	0.6(1)	216.3
1124.6(5)	1693.7(1)	569.1(1)	0.2(1)[b]	569.0
1132.4(5)	1530.0(5)	397.6(2)	0.2(1)	363.5
1161.5(3)	1558.9(5)	397.6(1)	0.5(1)	364.0
1163.6(3)	1732.5(4)	569.1(1)	0.2(1)[b]	569.0
1195.2(2)	1558.9(5)	363.7(1)	0.6(1)	364.0
1296.2(2)	1693.7(1)	397.6(1)	0.6(1)	364.0
1318.7(2)	2002.0(3)	683.3(1)	0.6(1)	319.9, 363.7, 683.8
1330.0(1)	1693.7(1)	363.7(1)	1.2(1)	364.1
1366.2(4)	1366.6(2)	g.s.	0.3(1)	-
1368.9(3)	1732.5(4)	363.7(1)	0.6(1)	363.8
1392.4(4)	2002.0(3)	609.5(3)	0.2(1)	215.9
1397.8(3)	1853.5(4)	455.6(1)	0.2(1)	92.1, 364.0, 455.0
1432.8(3)	2002.0(3)	569.1(1)	0.3(1)	205.5, 363.7, 569.6
1449.1(4)	1449.1(4)	g.s.	0.4(1)	-
1472.0(6)	1472.0(6)	g.s.	0.1(1)	-
1559.4(4)	1558.9(5)	g.s.	0.1(1)	-
1674.2(7)	1674.2(7)	g.s.	0.1(1)	-
1693.7(4)	1693.7(1)	g.s.	0.3(1)	-
1732.5(4)	1732.5(4)	g.s.	0.3(1)	-
1951.1(4)	2520.2(4)	569.1(1)	0.4(1)	205.6, 363.6, 569.4
2301.3(8)	2301.3(8)	g.s.	0.1(1)	-
2341.4(7)	2341.4(7)	g.s.	0.1(1)	-
2371.7(4)	2932.6(4)	561.0(2)	0.6(1)	197.6, 363.8, 561.1

2444.8(7)	3013.5(7)	569.1(1)	0.3(1)	205.5, 363.6, 569.0
2534.8(8)	2898.5(8)	363.7(1)	0.3(1)	363.3
2561.8(7)	3245.1(7)	683.3(1)	0.4(1)	320, 364, 683
2638.9(8)	2638.9(8)	g.s.	0.1(1)	-
2690.4(8)	2690.4(8)	g.s.	0.2(1)	-
2780.2(8)	2780.2(8)	g.s.	0.2(1)	-
2839.8(8)	2839.8(8)	g.s.	0.3(1)	-
3013.1(6)	3013.5(7)	g.s.	0.5(1)	-
3035.6(5)	3399.3(5)	363.7(1)	0.3(1)	363.3, 569.3
3306.0(9)	3306.0(9)	g.s.	0.3(1)	-
3373.9(8)	3373.9(8)	g.s.	0.2(1)	-
3420.9(9)	3420.9(9)	g.s.	0.3(1)	-
3535.0(4)	4096.0(4)	561.0(2)	0.6(1)	561
4438.2(9)	4438.2(9)	g.s.	0.3(1)	-

Table 5.1: A list of γ-ray energies, relative intensities, placement and the strongest $\gamma\gamma$ coincident transitions from the β decay of ^{65}Mn. ^{a}: This value is the total intensity obtained from the time-delayed component of the 363.7 keV transition, see text for details. ^{b}: Intensity obtained from $\gamma\gamma$ coincidences spectra. ^{c}: γ-rays assigned to the ^{65}Mn decay but not placed in the level scheme. ^{d}: Doublet in ^{65}Fe, the intensity is obtained from coincidences with 374.1 and 405.6 keV transitions. ^{e}: Only seen in the delayed coincidences of the 363.7 keV transition. ^{f}:It is very unlikely that this is the same line as the 771.6(7) keV γ-ray seen in [3]; in our data it is in strong coincidences with the 455.6 keV transition.

E_{level} (keV)	β-feeding	log(ft)	$T_{1/2}$	J_π
0	< 8.8	> 6.0	0.81(5) s	$(1/2^-)$
363.7(1)	42(5)	4.63(7)	93(3) ps	$(3/2^-)$
393.7(2)			1.12(15) s	$(9/2^+)$
397.6(2)	0.1(6)		437(55) ns	$(5/2^+)$
455.6(1)	8.1(1.1)	5.33(5)	350(10) ps	$(5/2^-)$
561.0(2)	1.5(2)	6.06(8)	350(50) ps	$(3/2^+, 3/2^-, 5/2^-)$
569.1(1)	0.9(4)	6.31(5)	< 12 ps	$(1/2, 3/2)$
609.5(3)	1.0(1)	6.2(6)		$(7/2^+)$
683.3(1)	2.1(3)	5.86(8)	24(12) ps	$(3/2^+, 3/2^-, 5/2^-)$
894.8(1)	1.4(2)	5.99(8)	< 27 ps	$(7/2^-)$
1057.3(1)	2.9(2)	5.64(6)		
1088.7(1)	20.7(9)	4.78(5)		$(3/2^-, 5/2^-)$
1228.2(2)	0.2(1)	6.76(23)		
1366.6(2)	6.3(3)	5.23(5)		$(5/2^-)$

1372.6(3)	0.3(1)	6.55(15)		
1449.1(4)	0.3(1)	6.31(10)		
1457.2(5)	0.5(1)	5.59(5)		
1472.0(6)	0.1(1)	7.0(5)		
1530.0(5)	0.2(1)	6.74(22)		
1558.9(5)	2.4(1)	5.61(5)		
1674.2(7)	0.1(1)	7.0(5)		
1693.7(1)	1.3(1)	5.84(6)		
1732.5(4)	1.4(1)	5.8(6)		
1853.5(4)	1.2(1)	5.84(6)		
2002.0(3)	0.7(1)	6.04(8)		
2301.3(8)	0.1(1)	6.8(5)		
2341.4(7)	0.1(1)	6.8(5)		
2520.2(4)	0.2(1)	6.45(23)		
2638.9(8)	0.1(1)	6.7(5)		
2690.4(8)	0.1(1)	6.7(5)		
2780.2(8)	0.1(1)	6.7(5)		
2839.8(8)	0.2(1)	6.4(2)		
2898.5(8)	0.2(1)	6.4(2)		
2932.6(4)	0.4(1)	6.04(12)		
3013.5(7)	0.5(1)	5.92(10)		
3245.1(4)	0.3(1)	6.07(15)		
3306.0(9)	0.2(1)	6.23(23)		
3373.9(8)	0.1(1)	6.5(5)		
3399.3(5)	0.2(1)	6.2(23)		
3420.9(9)	0.2(1)	6.2(23)		
40960(4)	0.3(1)	5.81(15)		
4438.2(9)	0.2(1)	5.87(23)		

Table 5.2: A list of level energies, level half-lives, β-feeding, logft, and spin/parity assignments for the levels populated in the β-decay of ^{65}Mn to ^{65}Fe.

5.3.3 The exact energy of the β-decaying isomer

The 215.8 keV transition is in firm mutual coincidences with the 757.2, 763.0, 1123.0, and 1392.4 keV γ-rays (see Fig. 5.10). They all belong to the decay of ^{65}Mn. The 215.8 keV line is placed feeding the isomeric level at 402(10) keV reported by Block *et al.* [88]. Indeed if the energy of the isomer is 393.7(2) keV, then one defines a new level at 609.5 keV de-excited by the 215.8 keV transition, and then all four coincident lines de-excite levels already assigned to the level scheme based on other

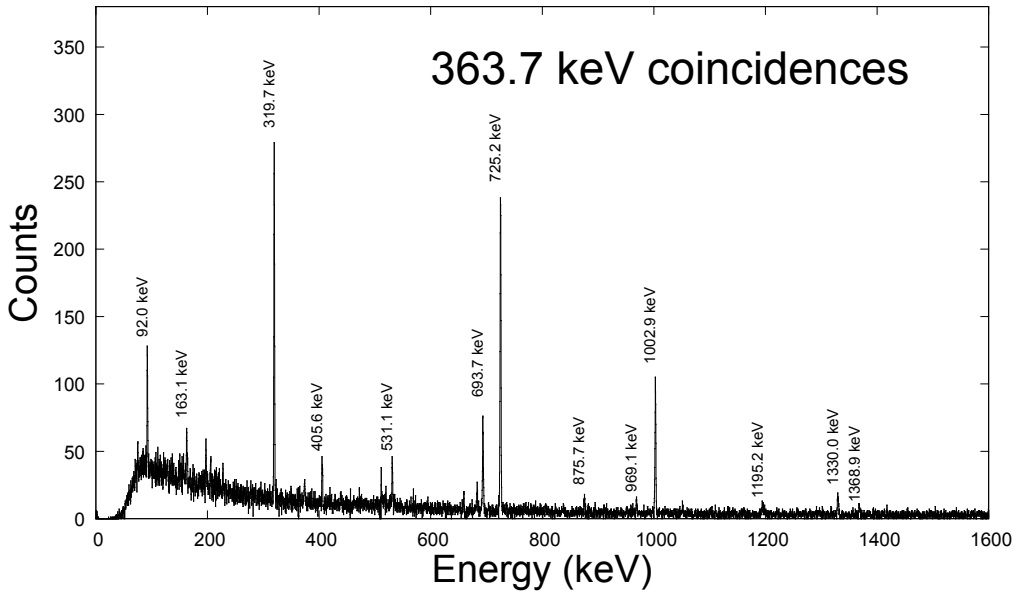

Figure 5.7: $\gamma - \gamma$ coincident spectrum gated on the intense 363.7 keV line in a HPGe detector and projected onto the second HPGe; see text for details.

$\gamma\gamma$ coincidences. These levels are at 1366.2, 1372.6, 1732.5, and 2002.0 keV. The possibility of 215.8 keV transition feeding directly the ground state was discarded, as it would involve the creation of 5 new levels instead of one. Our data precisely determine the energy of the β-decaying isomer at 393.7(2) keV.

By knowing the exact energy of the state we have looked for a ground state transition of the energy 393.7 keV. No such transition was found and an upper limit of intensity was established at 0.15 relative to 100 for the 363.7 keV transition. In the following discussion we will use the term "relative intensity" to define an intensity normalized to 100 for the 363.7 keV line. On the other hand, as absolute intensity we define the intensity per 100 β decays of ^{65}Mn expressed in %.

5.3.4 The 420 ns isomer

Using our coincidence data we have identified at the energy of 397.6 keV the 420(13) ns 396.8 keV isomer reported previously in [85]. In the analysis we have examined a four-parameter data set involving $\beta - \gamma(t)$ coincidences using β and HPGe detectors. The first two parameters were the energies of the β- and γ-rays. The third parameter was the time difference between events in the β detector (which started the time counting) and the HPGe, which provided the STOP signal. The forth parameter was the time elapsed between the γ-ray event from the last proton

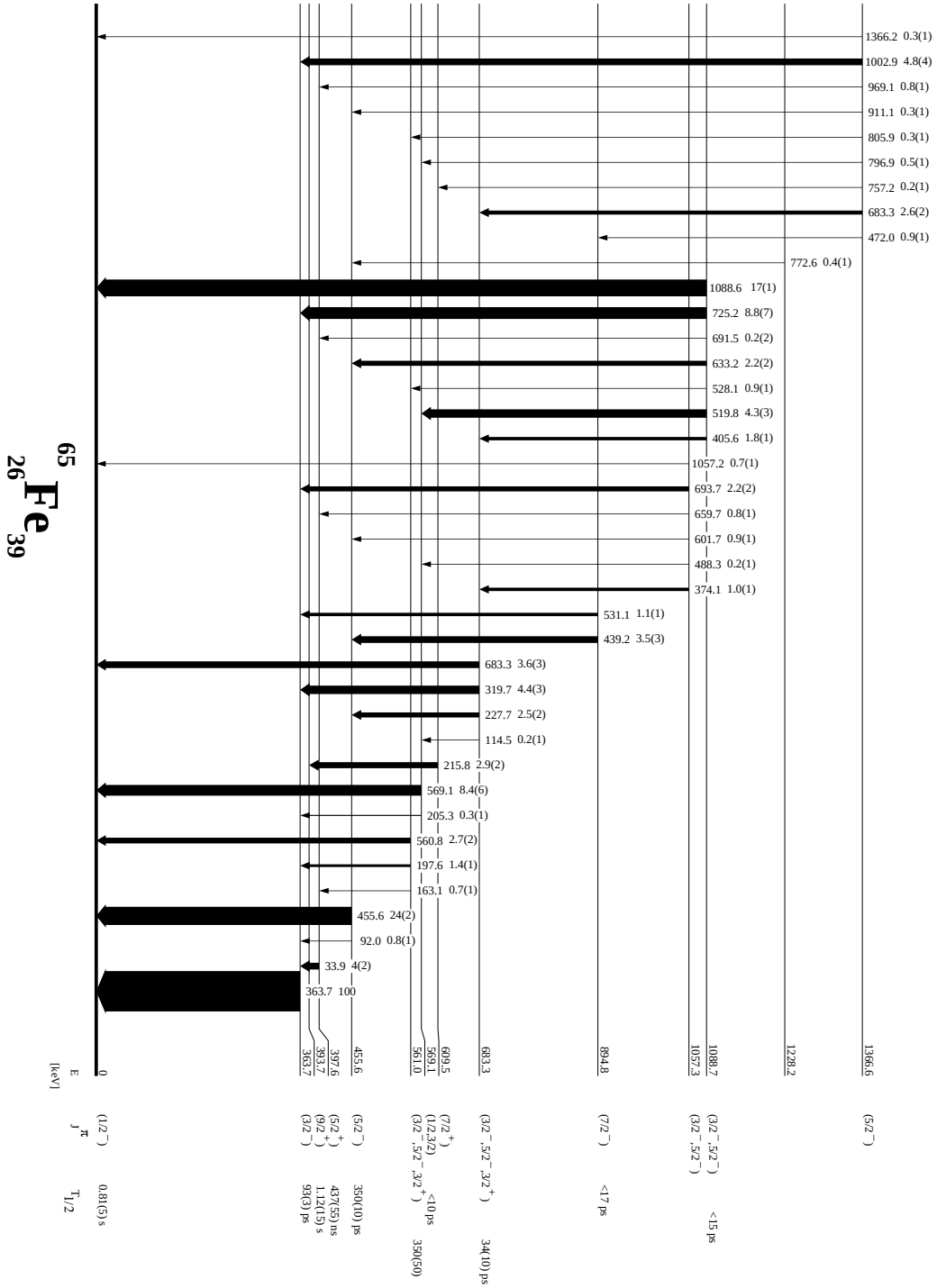

Figure 5.8: Lower energies ^{65}Fe level scheme populated in the β-decay of ^{65}Mn. Measured half lives and tentatively assigned spin-parities are shown next to each level. All results are from this work except for the half-lives of the β-decaying states.

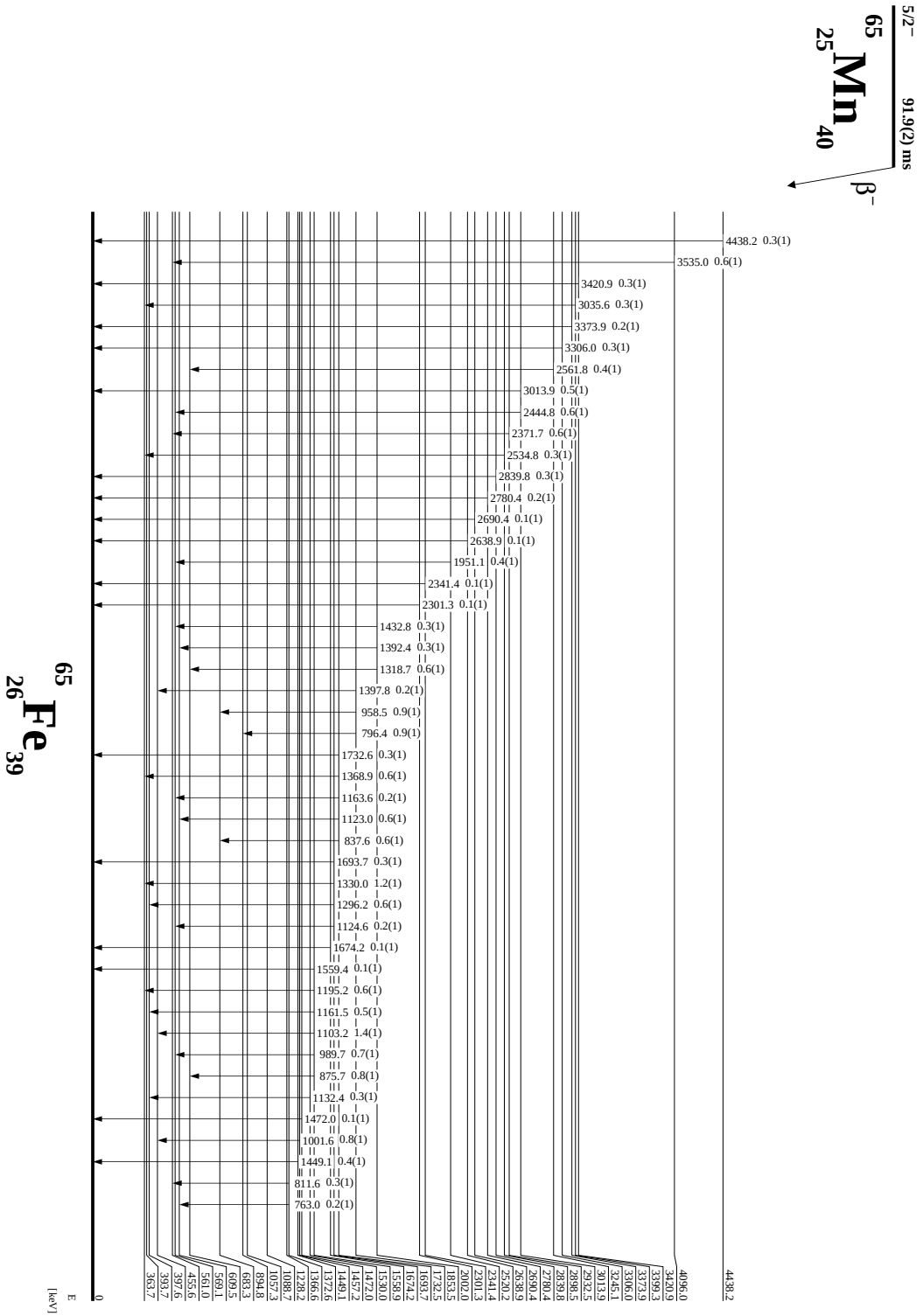

Figure 5.9: ^{65}Fe level scheme populated in the β-decay of ^{65}Mn.

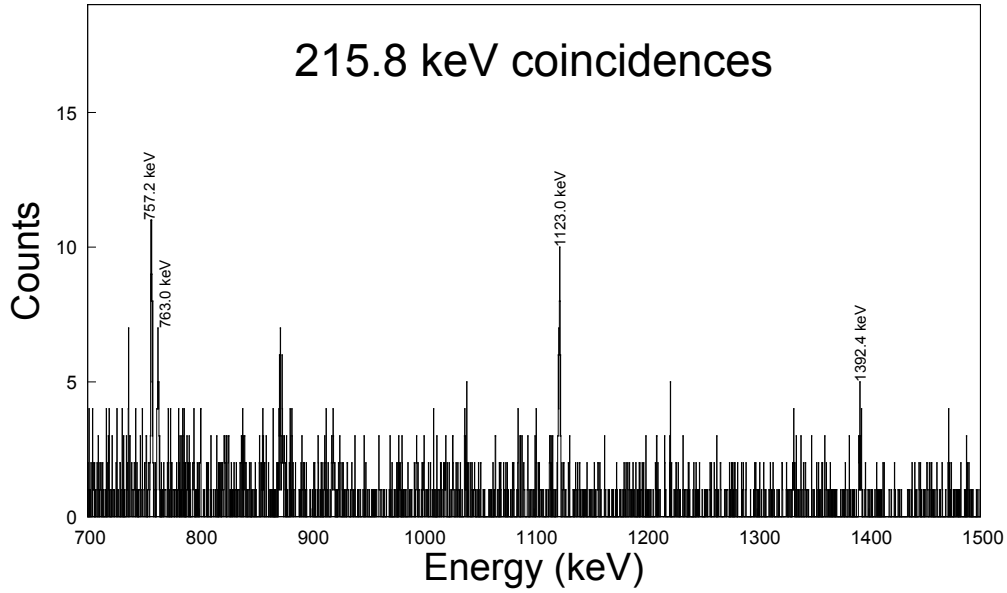

Figure 5.10: $\gamma - \gamma$ coincident spectrum gated by the 215.8 keV transition, the only γ-ray directly feeding the β-decaying isomer at 393.7 keV.

pulse, where a gate was set between 10 to 450 ms in order to enhance the ^{65}Mn activity. The $\beta\gamma$(t) time spectrum gated by the 363.7 keV transition in HPGe, shows a large prompt peak and a sloping delayed component with a half life in the $\sim$400 nanosecond range. This implies a direct 33.9 keV transition between the 397.6 and 363.7 keV levels. Indeed a 33.5 keV line feeding the 363.7 keV level was reported in [86, 85, 87]. Unfortunately, we do not observe this transition as the energy threshold on each of our HPGe detectors was above this energy.

Using the same data one can estimate the intensity of the 33.9 keV γ ray relative to the intensity of the 363.7 keV transition. Using the $\beta\gamma$(t) time spectrum we first subtract the constant background from the delayed and prompt parts. The area of the delayed component corresponds to the intensity of the 33.9 keV transition. The area was determined using the sloping part outside of the prompt area and increased to account for the delayed part under the prompt peak. The total area of the combined prompt and delayed parts represent the total intensity of the 363.7 keV line. The total intensity of the 33.9 keV transition was estimated to be 4(1) in relative units. As it is an indirect measurement, any possible conversion electron is included, independently of the multipolarity of the transition.

We have then examined a four-parameter data set involving time-delayed $\gamma - \gamma$(t) coincidences using two HPGe detectors. The four parameters were: the energies of γ-rays in the detectors, the time-difference between events in the HPGe-START

and HPGe-STOP, and the time elapsed for the coincident event and the last proton pulse. Fig. 5.11 shows the coincident HPGe spectrum gated by the 363.7 keV transition with two additional gates. One gate was set on the proton time between 10 to 450 ms to enhance the ^{65}Mn decay, while the second gate was set on the $\sim$400 ns slope part (outside of the semi-prompt region) of the $\gamma\gamma$(t) time-delayed spectrum where the 363.7 keV transition was selected in the HPGe-STOP detector. The transitions shown in the spectrum are those which are feeding the 420-ns isomer from above and have started the time measurement. The spectrum in Fig. 5.11 shows coincident transitions of energy 163.1, 659.7, 969.1, 1132.4, 1161.5, and 1296.2 keV, which feed the 397.6 keV level and are coincident to the 363.7 keV line via the 33.9 keV transition unobserved by us.

By resorting the data and constructing a time spectrum started by these γ-rays and stopped by the 363.7 keV line, one obtains a spectrum shown in the insert to Fig. 5.11. The slope in the time spectrum gives a half-life of $T_{1/2} = 437(55)$ ns in agreement with the known half-life of the isomeric state. All the coincident γ-rays feeding the isomer de-excite established levels in ^{65}Fe. From the energy relations the energy of the isomer is determined to be 397.6(2) keV, and the energy of the de-exciting transition is then 33.9(2) keV. The intensity sum of the observed γ-rays feeding the isomer is 3.9(2) in relative units, which compared to the estimated relative total intensity of the 33.9 keV transition of 4(1) implies that this isomer is weakly, if at all, directly populated in β-decay of ^{65}Mn.

No indication of any other γ-ray de-exciting this isomer was found by us. In particular no γ-ray of energy 397.6 keV that would feed the ground state was identified, neither in γ-ray singles nor in $\gamma\gamma$ coincidences. An upper limit of intensity for the 397.6 keV transition is 0.15 in relative units.

5.3.5 Absolute β and γ intensities

The $A = 65$ measurement was run for 18 hours in a saturation mode, in which the beam was deposited onto an Al foil and no old activity was removed from it. As a consequence an intensity balance was established in the $A = 65$ decay chain all the way down to the stable ^{65}Cu. An intensity balance also took place in the β_n branch along the $A = 64$ chain. The saturated mode allows to measure the absolute decay branches for the decay of ^{65}Mn using absolutely calibrated γ transitions from other members of the decay chain. We assume here that only one β-decaying state of ^{65}Mn is present in this measurement and that the ion source does not surface ionize other atoms in the β-decaying $A = 65$ chain (Fe, Co, Ni and Cu) owing to the larger ionization potential. In the following analysis we use unrestricted γ-ray spectra observed in the HPGe detectors.

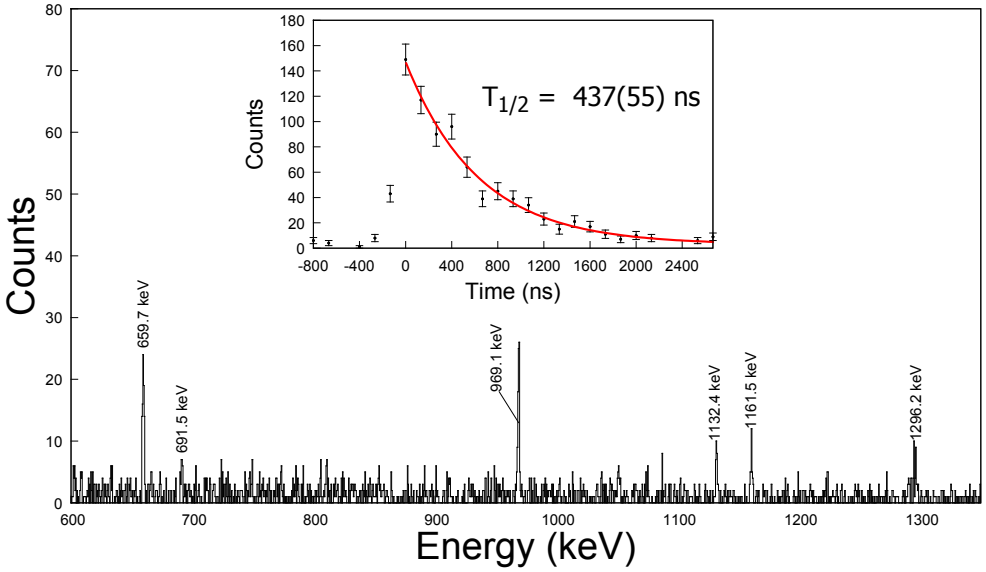

Figure 5.11: Time-delayed coincidence HPGe γ-spectrum gated by the 363.7 keV transition in ^{65}Fe. These γ rays populate the 397.6 keV isomer and are in coincidence with 363.7 keV transition through the 33.9 keV line. The insert shows the time spectrum (time differences) between the γ-rays feeding the isomer and the coincident 363.7 keV transition. The fitted slope shows a half-life of 437(55) ns, in good agreement with the known $T_{1/2} = 420(13)$ ns for the isomer; see text for details.

In order to determine the ground state β feeding and the β-delayed neutron emission probability, we divide the total intensity of the β decay of ^{65}Mn into four decay branches. These branches include: β-delayed neutron emission branch, β_n, direct β feeding to the ground state of ^{65}Fe, $\beta^{g.s.}$, β feeding to the low-spin levels in ^{65}Fe, which then directly or indirectly feed the low-spin ground state in ^{65}Fe, β_{LS}^{levels}, and the portion of the β feeding that ends up in the second β decaying state in ^{65}Fe at 393.7 keV, β_{HS}^{levels}.

Two of these branches, $\beta^{g.s.}$ and β_{LS}^{levels}, end up feeding the J^{π}=$(1/2^{-})$ g.s. in ^{65}Fe, which then follows by β decay into ^{65}Co. The absolute intensities in this β decay have been recently measured by Pauwels *et al.,* [89]. This decay has no direct β feeding to the ground state of ^{65}Co. 100% of the β intensity is carried out by three γ-rays of the energy of 882.5-, 1222.7-, and 1996.6 keV. We observe these transitions in our measurement with their relative intensities summed to I = 163.6(6.1). On the other hand, the intensity of the β_{LS}^{levels} feeding is simply the sum of intensities of γ-rays directly feeding the ground state in ^{65}Fe and is equal to 162.1(13.5) in relative units. The difference between these intensity values gives the direct g.s. feeding in ^{65}Fe, which is 1.5(14.8) in relative units.

The β_n branch feeds the ground state and the excited states in ^{64}Fe. The ground state of ^{64}Fe β decays to ^{64}Co, which then decays to ^{64}Ni. The β decay of ^{64}Co has been recently investigated by Pauwels *et al.,* [91], who precisely determined the absolute γ and β transitions in this decay. The strongest γ transition is the 1345.8 keV line, which represents 7.54% of the total decay intensity. In our HPGe γ spectrum we observe a transition at 1345.1 keV with the intensity of 1.3(0.1) relative units. This transition includes an impurity component from the decay of ^{65}Ga to ^{65}Ni with the energy of 1343.9 keV and the intensity of 0.18(0.02). The intensity was determined using the known lines in the decay of ^{65}Ga of the energy 115.1-, 152.9-, 751.7-, and 1228.6 keV and the branching ratios listed in [84]. The resultant relative intensity of the 1345.8 keV transition in ^{64}Ni is 1.1(0.1), which gives for the β_n branch the relative intensity of 14.6(2.1).

The last component to be determined is the β intensity feeding the isomeric state at 393.7 keV. We have identified only one γ-ray, which directly feeds this state. The relative intensity of this 215.8 keV transition is 2.9(0.2). In any case the feeding of this state must be very weak due to the spin/parity differences between the isomer, with the expected J^{π} = $(9/2^{+})$ and the ground state of ^{65}Mn with J^{π} = $(5/2^{-})$. We could assume that there may be a few more transitions feeding the isomer yet these lines were too weak to be observed in our measurement. Thus the total intensity might be higher by factor of 2-3 than the observed one. This way we could expect that the feeding of this state is of the order of 6.0(3.0) in relative units. Even if the feeding of this state would be twice as high, still the overall results obtained in this section would not be significantly affected.

The 393.7 keV isomer β decays to levels in ^{65}Co, which are different than those observed in the ground state decay of ^{65}Fe [89]. In the following analysis we use the absolute intensities re-evaluated by the A=65 Nuclear Data Table [84]. In our γ-ray singles spectra we observe transitions of energy 1412.7, 1642.2, 2443.7 and 2558.0, which we associate with the lines in ^{65}Co. The summed intensity of these lines is 4.5(0.3) in relative units. The total intensity for these γ-rays is 62.0(7.6) % of the isomer decay, giving the intensity of 7.3(1.0) in relative units for the population of the isomer in ^{65}Fe. Independently, we looked into the intensities from the decay of ^{65}Ni to ^{65}Cu. Using the intensities of the 366.2, and 1481.5 keV transitions (the latter corrected for a 4% impurity contribution from the 1479.0 keV line in ^{65}Cu), we obtain the total feeding intensity to the β decaying levels in ^{65}Fe as 172.1(10.1) relative units, which must be compared to the individual contributions of 163.6(6.1) and 7.3(1.0) for the ground state and isomer, respectively, giving together 170.9(6.2) in excellent agreement with the ^{65}Cu data.

Thus the total β feeding in relative units of the four components is: 14.6(2.1), 163.6(6.1) (sum of two components) and 7.3(1.0), giving a total relative intensity of 185.5(6.5), which is equal to 100% of the decay intensity. Thus we have to renormalize the relative intensities for the β and γ rays by a factor of 0.539(0.019) in order to get the absolute intensities. Then the β_n branch is 7.9(1.2) % and a direct ground state feeding is $\leq$8.8%. We note an excellent agreement with the preliminary value of <10% for the ground state β feeding reported in [87].

The absolute β-feeding to each level was calculated as the difference of γ transition absolute intensities feeding and depopulating the level. Thus for weak branches they should be taken as upper limits since only observed γ transitions were taken into account. Two of the levels, at 363.7 and 1088.7 keV, get a very strong β feeding which together amounts to more than 60%. A significant β feeding goes also to the levels at 455.6, 683.3, 1057.3, 1366.6 and 1558.9 keV. Further 21 levels are very weakly populated with the feeding at or below 0.3%. A summary of the properties of levels in ^{65}Fe is given in Table 5.2.

5.3.6 β-n branch directly feeding the g.s. of ^{64}Fe

The total β-delayed neutron emission branch in the decay of ^{65}Mn is 7.9(1.2) %. Our data show that a significant portion of the β-n feeding goes to the excited states. We observe a 746.4(1) keV transition (see Fig. 5.12) in the decay of ^{65}Mn, which was already assigned to ^{64}Fe from a reaction study of [92] and the β-decay work of [4]). Moreover, this line is in coincidences with the 1017.4 keV γ-ray (seen in [92]) and the 1105.8 and 1370.7 keV transitions both already placed in the level scheme of ^{64}Fe [18]. A fit to the time decay slope following the proton pulse, see

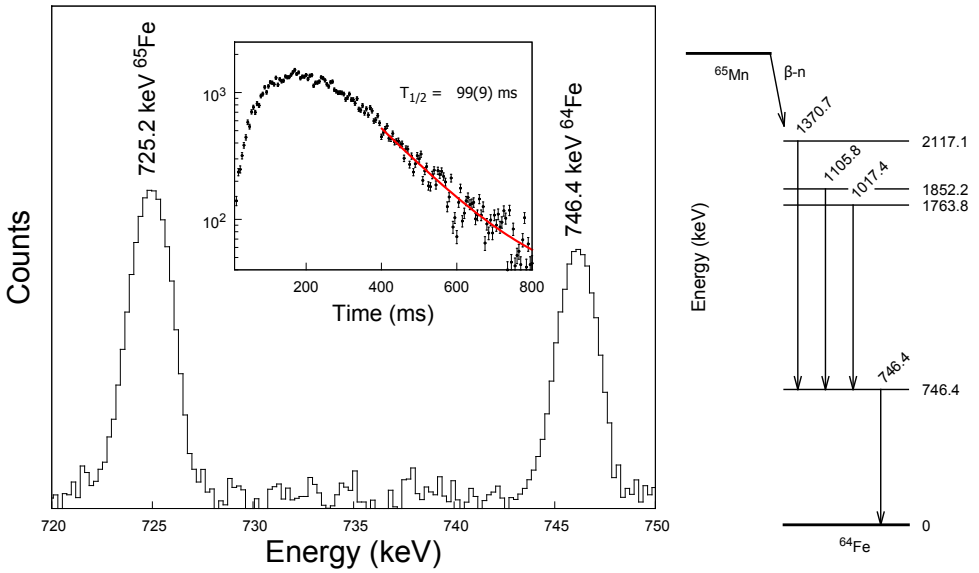

Figure 5.12: *Left:* A portion of the singles γ-ray spectrum enhancing the short-lived decay of ^{65}Mn, showing the 746.4 keV peak due to a line in ^{64}Fe from the β-n branch. *Insert:* Decay time spectrum of the 746.4 keV events after the proton pulse. Fitting the slope gives the half-life of 99(9) ms consistent with the β decay of ^{65}Mn. *Right:* A level scheme of ^{64}Fe populated in the β-n decay of ^{65}Mn.

an insert in Fig. 5.12, firmly assigns the 746.4 keV line to the β-n decay of ^{65}Mn. Table 5.3 provides a summary on the information of these transitions. The absolute intensity of the 746.4 keV transition is 2.4(0.1)%. There must be other ground state transitions as well in this β-n decay that remain unobserved by us. This leads to a conclusion that a direct β-n feeding to the g.s. of ^{64}Fe is less than 5.5%.

Our P_n value of 7.9(1.2)% contradicts the value of 21.0(5)% reported by Hannawald *et al.* [18] for the neutron delayed emission of ^{65}Mn as our result is about three times lower. Our results on the direct g.s. feeding are even more different, since in ref. [18] the entire β-n intensity of 21% was assigned to directly feed the ground state of ^{64}Fe, while in our work a significant portion goes to the excited states. Thus for the direct ground state feeding our intensity is almost four times lower.

E_γ (keV)	$E^{level}_{initial}$ (keV)	E^{level}_{final} (keV)	I^{rel}_γ	$\gamma\gamma$ coincidences (keV)
746.4(1)	746.4(1)	g. s.	4.4(2)	1017.4, 1105.8, 1370.7
1017.4(3)	1763.8(3)	746.4(1)	0.4(1)	746.4
1105.8(5)	1852.2(5)	746.4(1)	0.5(1)	746.4
1370.7(5)	2117.1(5)	746.4(1)	0.2(1)	746.4

Table 5.3: γ-rays assigned to ^{64}Fe from the β-n decay of ^{65}Mn. The intensities are normalized to the 363.7 keV intensity of 100. The 764.4(1)- and 1016.7(1) keV transitions were observed in ref. [92], where the 746.4 keV and 1763.8 keV levels were assigned spin parities of 2_1^+ and 4_1^+, respectively. The 746.7-, 1017-, 1105-, and 1370-keV transitions were observed in the β-decay of ^{64}Mn by [18].

5.4 Fast Timing measurements

Level lifetimes in ^{65}Fe have been measured with the Advanced Time-Delayed method [13, 14, 15]. The shape deconvolution technique was used for the half-lives above 80 ps when time spectra have shown a slope on the delayed side, while the centroid shift analysis was applied for shorter lifetimes. A summary of lifetime measurements is given in Table 5.4. Besides the β detectors, there were two HPGe and two $LaBr_3$(Ce) detectors in the fast timing setup. The contribution from the HPGe detectors were summed together, while those from the $LaBr_3$(Ce) detectors were analyzed separately since their time responses were different.

Our preliminary analysis of the level lifetimes in ^{65}Fe indicated that only three levels have sufficiently long lifetimes to be measurable by the deconvolution method. These levels are at 363.7, 455.6 and 561.0 keV. The lifetimes were deduced from a four parameter data set, which included the energies of the fast-response β and $LaBr_3$(Ce) γ detectors, a time difference between their signals recorded in the TAC unit with 50 ns range, and the time elapsed between the $\beta\gamma$(t) event and the last proton pulse. Fig. 5.13 shows a $LaBr_3$(Ce) energy spectrum with a gate set in the delayed part of the fast-TAC, cutting away the semi-prompt part. Under this conditions only transitions from levels with lifetimes over $\sim$ 100 ps are enhanced, which corresponds with the previously listed ones.

The first two levels are de-excited by strong γ-rays, which are well separated in the $\beta\gamma$(t) spectra where a $LaBr_3$(Ce) γ detector was used, see Fig. 5.5. We start the analysis with the 455.6-keV level, since the $\beta\gamma$ time spectrum gated by the 455.6-keV transition shows only a single time component due to the lifetime of the 455.6-keV level. On the other hand the time spectrum gated by the 363.7-keV transition includes as the main component the slope due to the lifetime of the 363.7-keV level and a smaller component due to the lifetime of the 455.6-keV level present in the spectrum due to the 92.0-keV transition connecting these levels. For the 561.0-keV level, the de-exciting 560.8-keV transition cannot be resolved in the $LaBr_3$(Ce) energy spectrum, but long-lived contributions from the higher lying levels are excluded in the analysis.

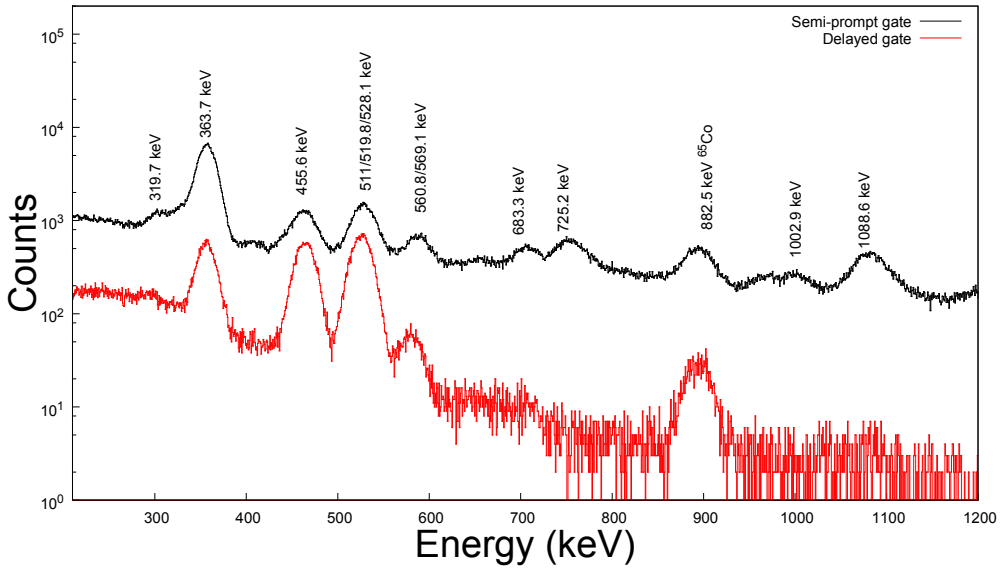

Figure 5.13: $LaBr_3(Ce)$ energy spectrum with a gate in the delayed part of the fast-TAC. This way only transitions with half lives over 100 ps are enhanced, while shorter lifetimes are suppressed.

5.4.1 Half-life of the 455.6-keV

A narrow gate was set on the 455.6-keV peak in the $LaBr_3(Ce)$ spectrum to ensure that the contribution from the 439.3-keV transition is minimized. In any case, the 894.8 keV level has a very short half-life (see results below) so that a small presence of the 439.3-keV γ-ray in the energy gate does not influence the present slope measurement. The $\beta\gamma$ time spectrum gated by the 455.6-keV transition is shown in Fig. 5.14. Fitting the slope to an exponential decay yielded the half-life of 350(10) ps. This result is the weighted average of the two lifetimes obtained independently using each of the $LaBr_3(Ce)$ detectors. The half-life value of 350 ps for the 455.6-keV level was confirmed by using the triple coincident $\beta\gamma\gamma$ data with the addition of a HPGe detector in coincidences. By gating in the HPGe detector on the γ-ray transitions feeding the 455.6-keV level from above and on the 455.6-keV transition in the $LaBr_3(Ce)$ detector one obtained time spectra with the characteristic slope of about 350 ps although with much lower statistics.

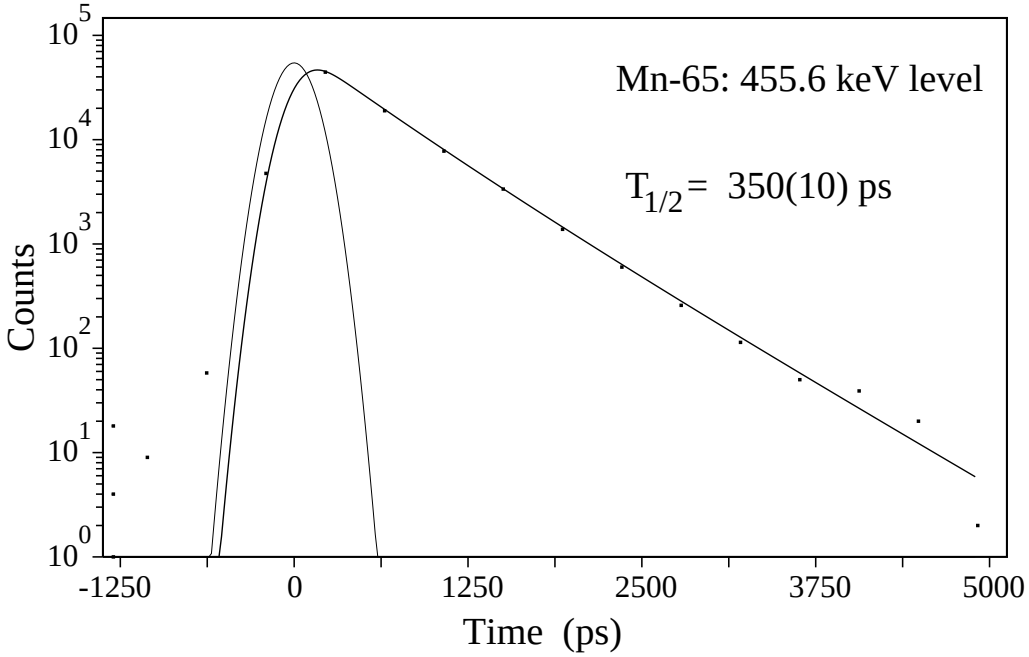

Figure 5.14: Time-delayed $\beta\gamma$(t) spectrum gated by the 455.6-keV transition. Its slope is due to the half-life of the 455.6-keV level. A fit to the exponential decay yields $T_{1/2} = 350(10)$ ps.

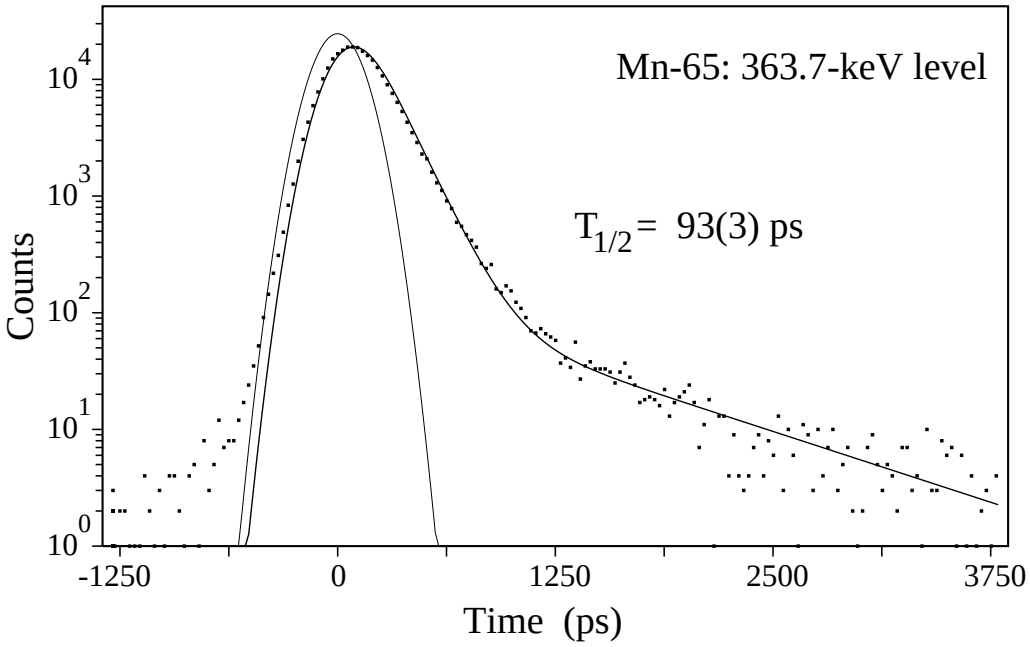

Figure 5.15: Time-delayed $\beta\gamma$(t) spectrum gated by the 363.7-keV transition. Its shorter slope is due to the 93(3) ps half-life of the 363.7-keV level in ^{65}Fe; see text for details.

5.4.2 Half-life of the 363.7-keV level

Using the same $\beta\gamma$ data set, a time spectrum was generated by gating on the 363.7-keV transition in the $LaBr_3$(Ce) detector. The spectrum, shown in Fig. 5.15, has two lifetime components. The longer one, with a half-life consistent with 350 ps is due to the level half-life of the 455.6-keV state that feeds the 363.7-keV level via the 92.0-keV line. The time distribution was fit to a prompt Gaussian plus two exponential decays. The shorter component gives 93(3) ps for the half-life of the 363.7-keV level. One should note that on a much longer scale, not relevant to this analysis, this time spectrum has also a 420 ns component due to the 397.6-keV isomer feeding the 363.7-keV level via the 33.9-keV transition. Over a few ns range, this long component provides merely a flat background contribution.

In the analysis of the fast timing triple coincident $\beta\gamma\gamma$ data, we have gated in the HPGe detector on a few transitions feeding the 363.7-keV level from above and on the 363.7-keV line in $LaBr_3$(Ce) detector. The deconvolution of the coincident $\beta\gamma$(t) time-delayed spectrum gives $T_{1/2}$ = 105(15) ps consistent with the earlier result.

We have also use the centroid shift method, the fast timing $\beta\gamma\gamma$ data and the

γ-ray cascade of two consecutive transitions of energy 725.2-363.7 keV. By gating on the 363.7-keV line in HPGe and the 725.2-keV peak in $LaBr_3$(Ce) one obtains a time spectrum, whose centroid shift defines a reference position. By reversing the gates in the HPGe and $LaBr_3$(Ce) one obtains the time spectrum, whose centroid shift represents the reference position plus an extra shift due to the mean-life of the 363.7-keV level. The difference between these centroids corrected for the time response of the $LaBr_3$(Ce) to the full energy peak events at 725.2 and 363.7 keV, yields the half-life of the 363.7-keV level as 81(16) ps in agreement with the previous results.

5.4.3 Half-life of the 561.0-keV level

In the $LaBr_3$(Ce) energy spectrum of the $\beta\gamma$ data set, the 561.0- and 569.1-keV can not resolved. Thus, the time spectrum generated by gating that peak will present a combination of the half lives of both levels (561.0- and 569.1-keV). This time spectrum shows a long slope in its delayed part. The 569.1-keV γ-ray is 3 times more intense than the 561.0-keV, but its half life is short enough to appear as a semi-prompt time distribution (as shown in the following section). Consequently the observed half life was assigned to the 561.0-keV level. Employing the deconvolution technique, a fit was performed for a two component exponential decay. The fast component (nearly semi-prompt) accounted for the 569.1-keV transition contribution while the longer one yielded the 561.0-keV level half life. The weighted average of both detectors gave $T_{1/2} = 390(30)$ ps.

None of the 561.0-keV level de-exciting transitions feeds the 455.6-keV level and the energies of their γ-rays are sufficiently apart. Despite the similarity of their half lives, the possibility that they are related was discarded in the analysis.

5.4.4 Half-life of the 569.1-keV level

The half-lives of the 569.1-, 683.3-, and 894.8-keV levels were obtained by the centroid shift method using the triple coincident fast timing $\beta\gamma\gamma$ data. For the 569.1-keV level we have used the two-γ-ray cascade of 519.8-569.1 keV transitions. The centroid of the time-delayed $\beta\gamma$(t) spectrum gated by the 519.8-keV γ ray in $Labr_3$ detector with an additional HPGe gate at 569.1 keV, gives a time reference spectrum. By reversing the gates and taking the 569.1-keV line in $LaBr_3$ and the 519.8-keV transition in HPGe, one obtains a time spectrum, whose centroid is shifted from the reference point by the mean-life of the 569.1-keV level. In all centroid-shift analysis we make standard corrections for the Compton continuum under the full-energy peaks in the LaB_3 spectrum and the energy dependent time response for the

full-energy peaks (the RD-corrections) [15]. For the first $LaBr_3$ detector the centroid shift gives the value of $T_{1/2}$ = 0.0(10.6) ps, and for the second the value of 8.7(10.4) ps, giving the average value of $T_{1/2}$ = 4.3(7.4) ps or a limit of $\leq$12 ps.

5.4.5 Half-life of the 683.3-keV level

For the 683.3- and 894.8-keV levels we do not have easily defined reference points for the centroid shift analysis. Therefore, we define an approximate prompt position at 363.7 keV. First we construct three $\beta\gamma$(t) time spectra gated by the 697.7-, 725.2-, and 1002.9-keV transitions in the HPGe detector, respectively, and by the 363.7-keV line in the $LaBr_3$(Ce). These time spectra are shifted from the prompt time position by $\Delta\tau = \tau_0 + \tau_{toplevel} + \tau_{363}$, where τ_0 is a constant shift from the prompt due to setting of the electronics, $\tau_{toplevel}$ is the mean life of the top level, which in this case is either the 1057.7-, 1088.7-, or 1366.6-keV level, respectively, while τ_{363} is the meanlife of the 363.7-keV state, which has a known value of 134.2(4.3) ps ($T_{1/2}$ = 93(3) ps) measured by us. The three time spectra for the first $LaBr_3$ detector differ by less than 3 ps from their average position, while for for the second detector they differ by less than 1.6 ps. It means the lifetimes of the top levels are the same within a few ps. Since these state do not have lifetimes manifested by slopes, and it is very unlikely that all of them have the same lifetime of tens of ps, therefore the equality of their centroids really means their lifetimes are short with $T_{1/2}$ below a few ps. Consequently, as a correction we arbitrarily assume for these levels a half-life of $T_{1/2}$ = 0(8) ps, which effectively increases the uncertainty in the lifetime determinations due to the our inability to determine the lifetimes of the "top levels" assumed here to be below a few ps.

Using the triple coincidence fast timing $\beta\gamma\gamma$ data, a gate was set on the HPGe detector on the 363.7-keV transition and a γ-ray peak was selected in the $LaBr_3$ detector at 319.7 keV. The centroid of the selected fast timing $\beta\gamma$ spectrum is equal to $\tau_0 + \tau_{683}$. The difference from the approximate prompt position at 363.7 keV in the half-life units is 31(12) ps for the first $LaBr_3$ detector and 18(12) ps for the second one. The weighted average of these results with the subtracted correction for the reference levels of 0(8) ps, gives the half-life of the 683.3-keV equal to 24(12) ps.

5.4.6 Half-life of the 894.8-keV level

In a similar way we have measured the lifetime of the 894.8-keV state. Using the fast timing $\beta\gamma\gamma$ data, a gate was set in the HPGe detector on the 455.6-keV transition and a γ-ray peak was selected in the $LaBr_3$ detector at 439.2 keV. The centroid of

the selected fast timing $\beta\gamma$ spectrum is equal to $\tau_0 + \tau_{894}$. The difference from the approximate prompt position at 363.7 keV in the half-life units is 8(18) ps for the first $LaBr_3$ detector and 16(16) ps for the second one. The weighted average of these results with the subtracted correction for the reference levels of 0(8) ps, gives the half-life of the 894.8-keV equal to 12(15) ps, thus the adopted value for the level is $T_{1/2} \leq$27 ps.

5.5 Discussion

As the starting point for the spin/parity assignments to levels in ^{65}Fe we take the assignments adopted by the evaluators in the Nuclear Data Sheets for $A = 65$ [84] for the following β-decaying states: $J^\pi = (5/2)^-$ for the ground state of ^{65}Mn and $J^\pi = (1/2)^-$ and $(9/2)^+$ for the ground state and the 393.7-keV states in ^{65}Fe, respectively. We do not adopt other assignments proposed in [84] as our new results correct them.

Ground state, $J^\pi = (1/2^-)$ The tentative spin parity assignments of $(5/2)^-$ and $(1/2)^-$ to the ground states of ^{65}Mn and ^{65}Fe would imply a very weak direct β feeding between these states as the feeding would go via a second forbidden β transition. Our limit on a direct β feeding is $\leq$8.8 %, supporting these assignments.

363.7-keV level, $J^\pi = (3/2^-)$ This state receives a very high direct β feeding with the intensity of 42(5)% and $\log ft = 4.6$, which implies an allowed β transition between the $(5/2)^-$ g.s. of ^{65}Mn and the 363.7-keV state, the same parity for the states, and the spin/parity assignments of $(3/2)^-$, $(5/2)^-$ and $(7/2)^-$.

The first excited state has a half-life of 93(3) ps and it decays to the ground state by the 363.7-keV line. If this γ ray would have an $E2$ multipolarity its $B(E2)$ value would be 62(2) W.u., thus about three times higher than the collective $B(E2; 2_1^+ \rightarrow 0_1^+)$ values in the neighboring even-even Fe isotopes. Consequently this rate is too high and the 363.7-keV transition is not an $E2$. Based on the lifetime measurement this transition could be either E1 or M1 in character, with the $B(E1)$ value of 9.3×10^{-5} W.u. or $B(M1) = 4.9\times10^{-3}$ W.u. Due to the parity considerations, this transition could be only $M1$ in character, limiting the spin/parity for the level to $(3/2)^-$. The lifetime of the level does not exclude a small $E2$ component in the transition. If we assumed a small $E2$ component in the 363.7-keV transition with $B(E2)$ of 5 W.u. then the branching ratio for $E2$ would be 8% while for $M1$ it would be 92%.

393.7-keV level, $J^\pi = (9/2^+)$ The second excited state in ^{65}Fe is a β decaying isomer with $T_{1/2} = 1.12(15)$ s. In this work we could precisely determine its excitation energy and we could then also investigate a possible γ-decay branches to the lower-lying states: the ground state and the 363.7-keV state. The isomer has a weak direct and indirect β feeding, which accounts to only 3.9(5) %, out of which 1.6% goes via a single 215.8-keV γ-ray feeding the state. There are likely a few more γ rays feeding the isomer that remain unobserved in our measurement. Direct β feeding is probably much smaller owing to the spin/parity differences between $J^\pi = (9/2^+)$ for the isomer and $J^\pi = (5/2^-)$ for the ground state of ^{65}Mn.

We do not observe any γ ray connecting the β-decaying states in ^{65}Fe. The upper limit on intensity for the 393.7-keV transition is 0.15 in relative units, while the relative intensity in the β-decay channel is 7.3(1.0). Thus using the γ branch of ≤ 0.021 one obtains for a $M4$ transition the $B(M4) \leq 3900$ W.u., which is consistent with no observation of any γ transition, since it means that the true γ branching is much lower than the measured limit. The other possible parity changing multipolarities are $E1$, $M2$ or $E3$. Yet, they have exceptionally low and unrealistic rates except perhaps for the $E3$ multipolarity

This isomer may also decay to the 363.7-keV level by a 30.0-keV transition, which would be $E3$ in character. But even with the $B(E3)$ value of $\sim$10 W.u. the total intensity of this transition would be negligible.

397.6-keV level, $J^\pi = (5/2^+)$ The 397.6-keV state is also an isomer with the half-life of 420(13) ns. It decays to the $(3/2^-)$ state by the 33.9-keV line, for which an $E1$ multipolarity was proposed by Daugas *et al.*, albeit no evidence was provided for this assignment [86]. The observed γ intensity feeding the isomer is 3.9(2) in relative units, while the total intensity of the 33.9-keV transition is 4(1). This intensity balance implies that the isomer is weakly, if at all, directly populated in the β-decay of ^{65}Mn. We do not observe any direct γ transition to the ground state at the energy 397.6 keV, for which an upper limit of intensity was established to be 0.15 in relative units. Another possible branch of decay is a 3.9-keV transition to the $(9/2^+)$ state at 393.7 keV.

The 33.9-keV transition must be a dipole either $E1$ or $M1$ in character making the spin of the 397.6-keV state either 1/2, 3/2 or 5/2. The $B(E1)$ and $B(M1)$ values would be 1.2×10^{-5} W.u. and 7.9×10^{-4}W.u., respectively. The transition cannot be $E2$ since then its $B(E2)$ value would be 64 W.u., a transition rate too collective for the case of ^{65}Fe. Moreover, its electron conversion coefficient of 29.5 would make this transition virtually undetectable in low-intensity experiments and yet the transition was previously observed.

If the unobserved 397.6-keV transition would be a dipole $E1$ or $M1$ trans-

ition then the $B(E1)$ and $B(M1)$ rates would be $\leq 6\times10^{-10}$ W.u. and $\leq 3\times10^{-8}$ W.u., respectively. These rates are too low to be realistic, therefore we reject these option. Consequently, this transition must be either $E2$ or $M2$ in character. The corresponding $B(E2)$ and $B(M2)$ rates are $\leq 3\times10^{-4}$ W.u. and $\leq 1.7\times10^{-2}$ W.u., respectively. The $B(E2)$ rate is exceptionally low, while the $B(M2)$ rate is just about the average value one could expect for this nucleus [93, 94]. Consequently, the most likely spin/parity assignment for the 397.6-keV state is $(5/2^+)$. The difference in the parity between this state and the ground state of ^{65}Mn explains very weak, if any, direct β feeding to this state.

The proposed spin/parity assignments would imply that the unobserved 3.9-keV transition is $E2$ in character. By assuming that its $B(E2)$ value is below 20 W.u. it would imply the total intensity for this transition to be less than 0.05 in relative units, thus negligible. On the other hand, if the 3.9-keV transition would be $M1$ or $E1$ in character, a significant portion de-exciting the 397.6-keV level would feed the state at 393.7-keV. That portion would be detectable via missing intensity in the 33.9-keV line. The balance of intensities feeding and de-exciting the 397.6-keV level excludes this possibility. Thus the 397.6-keV level is de-excited almost exclusively by the 33.9-keV transition, which supports the proposed spin/parity assignments to this level.

455.6-keV level, $J^\pi = (5/2^-)$ This level receives a strong β feeding with $\log ft = 5.3$ from the $(5/2^-)$ ground state in ^{65}Mn, which implies a spin/parity of $(3/2^-)$, $(5/2^-)$ or $(7/2^-)$ for the 455.6-keV state. On the other hand, this level has a relatively long half-life of 350(10) ps and is de-excited by γ-rays to the $(1/2^-)$ ground state and the $(3/2^-)$ 363.7-keV state. The 455.6-keV ground state transition can be either $M1$ with $B(M1) = 6.4(8)\times10^{-4}$W.u., or $E2$ with $B(E2) = 5.2(6)$ W.u., while the 92.0-keV transition can be $M1$ with $B(M1) = 2.5(4)\times10^{-3}$ W.u. The 92.0-keV γ ray cannot be $E2$ since then its $B(E2)$ would have an unrealistic value of 500 W.u.

The transition rates allow for a choice of only two spin/parities: $(3/2^-)$ or $(5/2^-)$. We adopt the second alternative, since it allows for a $B(E2)$ value for the ground state transition consistent with a core coupled state.

This level can also decay by a 58.0-keV transition to the $(5/2^+)$ state at 397.6 keV. Assuming a typical $B(E1)$ value of about 1×10^{-5} W.u. for this transition its total relative intensity would be only about 0.2.

561.0 keV, $J^\pi = (3/2^-, 5/2^-, 3/2^+)$ This level has a small β-feeding of 1.5% giving a $\log ft = 6.1$ and populates levels of spin $(1/2^-)$ and $(3/2^-)$ and $(5/2^+)$, but not the $9/2^+$ β-isomer nor the $(5/2^-)$ state. One of the γ transitions must be parity

changing $E1$. If the 163.1-keV line is E1 then the possible spin/parity for the 561.0-keV level is either $(3/2^-)$, $(5/2^-)$ or $(7/2^-)$. Taking the measured $T_{1/2}$ we obtain a $B(E1)$ value of 4×10^{-5} W.u., the 197.6-keV line must be M1, with a $B(M1)$ value of 2.2×10^{-3} W.u., as an $B(E2)$ rate of above 93 W.u. would be too high and unacceptable. The 560.8-keV transition could be then $M1$ ($B(M1)$ $\sim1.8\times10^{-4}$ W.u.) or $E2$ ($B(E2)$ ~1.0 W.u.), but $M3$ is firmly excluded. This scenario allows only for the spin/parity of $(3/2^-)$ and $(5/2^-)$ for the 561.0-keV state.

If the 197.6-keV line is $E1$, then the 163.1-keV γ ray could be $M1$ ($B(M1)$ $\sim1.9\times10^{-3}$ W.u.), but $E2$ is excluded. While the 560.8-keV transition could be $E1$ ($B(E1)$ $\sim3\times10^{-6}$ W.u.) but $M2$ is excluded. This scenario allows only for the spin/parity of $(3/2^+)$.

569.1 keV, $J = (1/2, 3/2)$ This level receives a very low β-feeding of 0.9% with $\log ft = 6.3$, which may indicate a forbidden transition from the parent ^{65}Mn. It de-excites to the ground state and the first excited state. With the half-life limit of $\leq$ 12 ps, the 569.1-keV ground state transition can be either $E1$ with $B(E1)$ $\geq1.8\times10^{-4}$W.u. or $M1$ with $B(M1)$ $\geq9.6\times10^{-3}$W.u. The $M2$ and $E2$ multipolarities are excluded for this transition. A similar situation is for the 205.3-keV line. Thus the spin for the 569.1-keV level can be either (1/2) or (3/2) with either parity, although a negative parity would be favoured.

Due to the very short lifetime limit and energy factors, even a moderately fast 171.5-keV transition to the $(5/2^+)$ 397.6-keV level would be undetectable in our experiment, regardless of whether it would be $M1$ or $E1$ in character.

609.5 keV, $J^\pi = (7/2^+)$ This level is the only one that is known to de-excite to the β-isomer at 393.7 keV. It has very weak β feeding if any, with the intensity of $\leq$1.0%. It is mainly γ fed from higher energy levels. The only reasonable spin/parity assignment would be $(7/2^+)$. A lower spin or negative parity would make transitions possible to other levels beside the $(9/2^+)$ isomer (the $(5/2^-)$ at 455.l keV, for example). A higher spin would cause the levels, whose transitions feed the 609.5-keV level, to directly γ feed the β-decaying isomer. We found no evidence for that.

There is no observation in singles or coincidence spectra of a 211.9-keV transition to the $(5/2^+)$ γ-ray isomer. An upper limit of intensity for this transition is 0.2 in relative units.

683.3 keV, $J^\pi = (3/2^-, 5/2^-, 3/2^+)$ The 683.3-keV level is weakly β fed. It de-excites to four levels with three of them having spin/parity $(1/2^-)$, $(3/2^-)$ and $(5/2^-)$, respectively. All of the de-exciting γ rays could be only of either $E1$ or $M1$

type, with the exception of the ground state transition which can be also $E2$ in character. This makes the possible spin/parity assignments for this level as $(3/2^-)$, $(5/2^-)$ and $(3/2^+)$.

894.8 keV, $J^\pi = (7/2^-)$ This level seems to get some β-feeding, which would imply negative parity. Moreover it feeds two excited states of spin/parity $(3/2^-)$ and $(5/2^-)$, but it does not feed the ground state, which is energetically favoured. The transition rates imply that each of the de-exciting transitions could be either $E1$ or $M1$ in character, but the 531.1-keV transition could be also of the $E2$ type with $B(E2) \geq 8$ W.u. The lack of any ground state feeding almost definitely excludes the $(1/2^-)$ and $(3/2^-)$ cases, and makes even the $(5/2^-)$ assignment unlikely. As a result the most likely spin/parity assignment for this level is $(7/2^-)$.

1057.2 keV, $J^\pi = (3/2^-, 5/2^-)$ This level has a β feeding of 2.9% and $\log ft$ =5.6, which favours negative parity for this state. It populates six states mainly of negative parity but also the $(5/2^+)$ state. As discussed before, our evidence indicates that the half-life of this state is very short in the range of a few ps, thus it was used as an internal "semi-prompt" reference. We have placed a rather arbitrary limit of $\leq$8 ps on the half-life of this level. A check on the lifetime limit is provided by the $B(E1)$ value which we expect to be in the range of about 5×10^{-5} W.u.

Indeed the half-life limit gives the 659.7-keV E1 transition a $B(E1)$ value of $\geq 2.5\times10^{-5}$ W.u. and firmly excludes this transition to be $M2$. The $E1$ nature of this γ ray feeding the $(5/2^+)$ state limits the possible spin/parity assignments to the 1057.2-keV level to $(3/2^-)$, $(5/2^-)$ and $(7/2^-)$. However, a direct feeding to the $(1/2^-)$ ground state definitely excludes the $(7/2^-)$ case. The 1057.2-keV transition could be either $M1$ ($B(M1) \geq 2.8\times10^{-4}$ W.u.) or $E2$ ($B(E2) \geq 0.42$ W.u.), but not $M3$.

The most intense transition is the 693.7-keV one feeding the $(3/2^-)$ state. This transition can be either $M1$ with $B(M1) \geq 3.1\times10^{-3}$ W.u. or $E2$ with $B(E2) \geq 11$ W.u., or a mixture of both. On the other hand the fastest transition is the 374.1-keV line, which could be either $E1$ ($B(E1) \geq 1.7\times10^{-4}$ W.u.) or $M1$ ($B(M1) \geq 1.6\times10^{-2}$ W.u.) but for sure not $E2$ in character. The transition rates for γ ray de-exciting this state are thus consistent with the proposed spin/parity assignment.

1088.7 keV, $J^\pi = (3/2^-, 5/2^-)$ This level has the second highest β feeding and the second lowest $\log ft$ value. This rules out a positive parity for this state and limits the spin/parity to $(3/2^-)$, $(5/2^-)$ and $(7/2^-)$ as the β transition is clearly allowed. In similarity to the 1057.3-keV state this level was also used as "semi-prompt" reference and a limit of $\leq$8 ps was set on its half-life. With this limit

the 1088.6-keV transition feeding the $(1/2^-)$ ground state can be either $M1$ or $E2$, with the corresponding $B(M1)$ $\geq$1.0$\times10^{-3}$ W.u. and $E2$ with $B(E2)$ $\geq$1.4 W.u., but definitely not $M3$. This limits the spin/parity assignment for this level as $3/2^-$ or $5/2^-$. All transition rates for other γ rays de-exciting this level are consistent with this assignment. The strong β-feeding to the $(3/2^-)$ levels in ^{65}Fe makes a $(3/2^-)$ the most reasonable choice for the 1088.7-keV state, but $(5/2^-)$ cannot be completely discarded.

Level (keV)	$T_{1/2}$ (ps)	E_γ (keV)	Multipolarity	B(XL) W.u.
363.7	93(3)	363.7	M1	$4.9(2)\cdot10^{-3}$
397.6	437(55) ns	33.3	E2	$9.2(71)\cdot10^{2}$
455.6	350(10)	92.0	M1	$2.6(4)\cdot10^{-3}$
		455.6	E2	5.1(6)
561.0	390(30)	163.1	M1	$6.4(8)\cdot10^{-4}$
			E1	$3.9(4)\cdot10^{-5}$
		197.6	M1	$2.2(3)\cdot10^{-3}$
			E1	$7.7(1)\cdot10^{-7}$
		561.0	M1	$1.8(2)\cdot10^{-4}$
			E2	11(1)
569.1	<12	205.3	M1	$>7.9\cdot10^{-3}$
			E1	$>1.5\cdot10^{-4}$
		569.1	M1	$>9.6\cdot10^{-3}$
			E1	$>1.8\cdot10^{-4}$
683.3	24(12)	227.7	M1	$1.8(9)\cdot10^{-2}$
			E1	$3.5(18)\cdot10^{-4}$
		319.7	M1	$1.2(6)\cdot10^{-2}$
			E1	$2.2(11)\cdot10^{-4}$
		683.3	M1	$9(5)\cdot10^{-4}$
			E1	$1.8(3)\cdot10^{-5}$
894.8	<27	439.2	M1	$>7.1\cdot10^{-3}$
			E1	$>1.4\cdot10^{-4}$
		531.1	M1	$>1.3\cdot10^{-3}$
			E1	$>2.5\cdot10^{-5}$
			E2	>7

Table 5.4: Table that summarizes the different half lives and transition rates measured in ^{65}Fe.

1366.6 keV, $J^\pi = (5/2^-)$ This level has a significant β feeding of 6.3% with a small $\log ft = 5.2$, which implies an allowed transition making the possible spin/parity assignments of $(3/2^-)$, $(5/2^-)$ and $(7/2^-)$. This state was also used as a "semi-

prompt" time reference and a limit of $\leq$8 ps was set on its half-life. The γ-rays feeding the $(5/2^+)$ and $(7/2^+)$ states are $E1$ in character with the $B(E1)$ values of $\geq 4.3\times10^{-6}$ W.u. and $\geq 2.3\times10^{-6}$ W.u., respectively, while the $M2$ character is definitely excluded. This allows only the J^π assignments of $(5/2^-)$ and $(7/2^-)$. On the other hand, the ground state 1366.2-keV transition can be either $M1$ ($B(M1)$ $\geq 3.0\times10^{-5}$ W.u.) or $E2$ ($B(E2)$ $\geq 2.7\times10^{-2}$ W.u.), but definitely not $M3$ in character. This excludes the J^π assignment of $(7/2^-)$, leaving $(5/2^-)$ as the only alternative. The absence of a transtion linking this state to the $(9/2^+)$ further supports this assignment.

5.6 Calculations

Shell model calculations were performed using the Lenzi-Nowacki-Poves-Sieja (LNPS) effective interaction [6]. This interaction works in a large shell model space, employing ^{48}Ca as a core and including pf orbitals for protons and $pfgd$ ($1p_{3/2}$, $1p_{1/2}$, $0f_{5/2}$, $0g_{9/2}$ and $1d_{5/2}$) orbitals for neutrons. The two-body matrix elements that involve the $1d_{5/2}$ orbit were calculated from the G matrix, based on the Kahana-Lee-Scott potential [95]. The monopole Hamiltonian was adjusted using the experimental B(E2) value in ^{80}Zn and the $0g_{9/2}$–$1d_{5/2}$ gap systematics for Zr isotopes (Z=40). The quadrupole-quadrupole interaction of the neutron $0g_{9/2}$ and $1d_{1/2}$ was increased by 20% to describe the observed shape evolution in the $Z = 20 - 28$, $N = 36 - 42$ mass region. For further details, refer to [6].

For the beta-decay calculations the ^{65}Mn $5/2^-$ ground state was constructed with the ingredients described above. The Gamow-Teller operator was applied in order to connect to the states in ^{65}Fe, and the $\log ft$ value was calculated. The decay pattern obtained in the calculations is plotted together with the experimental results in Fig. 5.16 for energies below 1.6 MeV. Very good agreement is obtained for the $3/2^-$ and $5/2^-$ states when compared to the experimental results, easily identifying the first $3/2^-$ and $5/2^-$ with the 363.7 and 455.6 keV levels seen in the experiment. The $\log ft$ values help identifying the assigned spins and parities. The calculated $7/2^-$ states are above 1.5 MeV with $\log ft > 6.5$. States with spin-parity $1/2^-$ were not calculated as there would not be allowed β transitions to them. Sizeable Gamow-Teller strength above 4 MeV is reproduced in the calculations for the beta-decay to the negative parity states in ^{65}Fe, corresponding to the tail of the giant resonance. For the lowest lying negative $1/2^-$ (g.s.), $3/2^-$ and $5/2^-$ states similar configurations are obtained, supporting their interpretation as the coupling of the single particle $p_{1/2}$ neutron orbit to the 0^+ and 2^+ states of the core.

The positive parity states have been also calculated for spins 3/2, 5/2, 7/2 and 9/2. They are in reasonable agreement with the experimentally measured states that

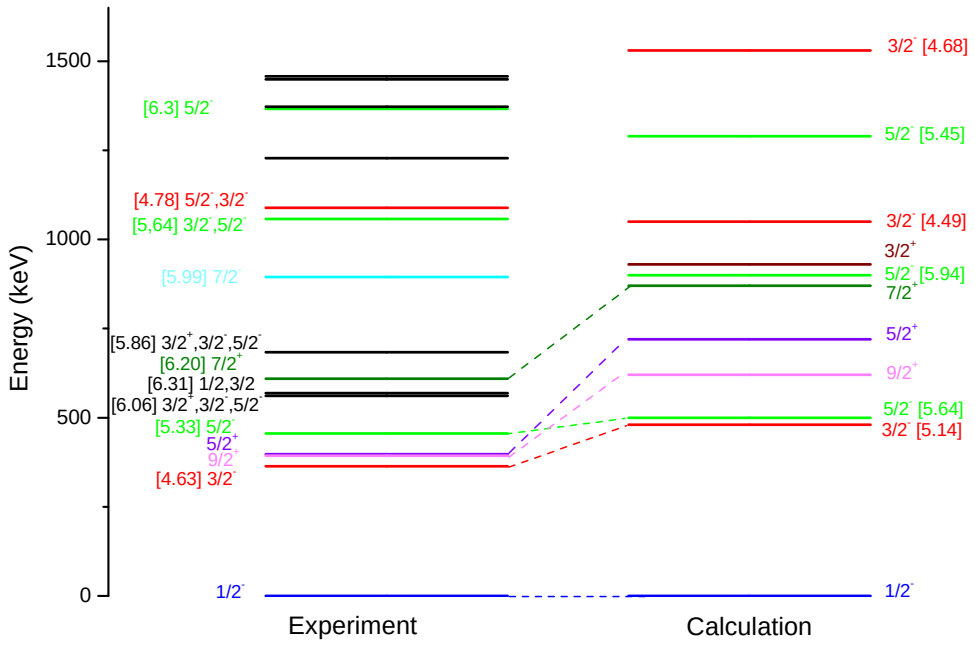

Figure 5.16: A comparison of the experimental and calculated levels (see text for details). Logft and spin/parities were calculated for the lower energy levels.

have been assigned positive parity, although they are predicted at slightly higher energies. This fact arises from the dimension limitations of the calculations, which slows down the convergence of the energy values. The calculations show a level with spin parity $3/2^+$ at 930 keV, which would be above the γ-decaying isomer (at 720 keV in the calculations). This level has not been identified in the experiment, nor their expected $3/2^+ \rightarrow 5/2^+$ and $3/2^+ \rightarrow 5/2^+$ transitions observed.

5.7 Conclusion

The ^{65}Mn half life have been precisely measured ($T_{1/2}$=91.9(9) ms), confirming previous results. The ^{65}Fe level scheme now comprehends 87 γ-transitions and 41 excited states (up to 4.4 MeV) and an upper limit for the direct β-feeding to the ground state has been given for the first time. A new value of $P_n = 7.9(1.2)\%$ was obtained, which can not agree with previous values. Moreover, it has been observed for the first time that the βn branch populates excited states in ^{64}Fe, contrary to what previously was believed.

The $9/2^+$ β-decaying isomer energy has been precisely determined at 393.7 keV. Gamma transitions populating and de-exciting the 397.6 keV isomer have been directly or indirectly observed.

Employing the ATD method, the half lives of 4 excited levels have been measured and upper limits have been set for two more. The measured transition rates allowed to make spin/parity assignments to the low energy levels. The proposed assignment suggests that some of the first excited states arise from the coupling of the unpaired neutron with the collective 2^+ and 4^+ states. During the analysis the $1/2^-$ (ground state), $3/2^-$, $5/2^-$ and $7/2^-$ were identified, not so a $9/2^-$ spin state. The arrangement of these levels have been corroborated by shell model calculations using the LNPS effective interaction.

Positive parity states have also been observed at low energies ($9/2^+$ at 393.7 keV, $5/2^+$ at 397.6 keV and $7/2^+$ at 609.5 keV), observation supported by the calculations. They show the importance of the positive parity orbitals across the N = 40 subshell gap.

5.A ^{65}Co preliminary results

In order to study the direct β-feeding of ^{65}Fe, its decay to ^{65}Co was analysed. For internal coherence, the intensities shown in table 5.5 were used in the calculations.

E_γ (keV)	$E^{level}_{initial}$ (keV)	E^{level}_{final} (keV)	I^{rel}_γ
127.4(1)	1222.9	1095.5	2.1(2)
212.7(1)	1095.5	882.8	13(1)
340.2(1)	1222.9	882.8	51(4)
736.4(1)	1959.3	1222.9	26(2)
773.7(1)	1996.4	1222.9	4.1(3)
863.9(1)	1959.3	1095.5	1.4(1)
882.8(1)	882.8	g.s.	100
901.0(1)*	1959.3	1095.5	0.9(1)
960.5(2)	2183.5	1222.9	16(1)
1076.3(1)	1959.3	882.8	11(1)
1088.4(1)	2183.5	1095.5	3.0(2)
1113.5(3)	1996.4	882.8	14(1)
1222.8(1)	1222.9	g.s.	20(1)
1996.4(1)	1996.4	g.s.	38(3)

Table 5.5: A list of γ-ray energies, relative intensities and placement from the β decay of ^{65}Fe. *: This transition was not placed in the previous level scheme [89].

While inspecting the ^{65}Co peaks in β-$LaBr_3$(Ce) coincidences it was observed a delayed component in the 882.5-keV peak (see Fig. 5.13). The time response for this response in the fast-TAC (see Fig. 5.17) shows a semi-prompt component ($\sim$ 90% of the counts) and a delayed one ($\sim$ 10% of the counts). The presence of a delayed component and a semi-prompt one indicates that most likely the observed lifetime is due the transition of a higher energy level populating the 882.5-keV level and that the half life of this level is much shorter.

The time distribution was fit two a double exponential decay using the deconvolution technique and yielded a preliminary value of $T_{1/2}$ = 1.3(1) ns. So far this lifetime cannot unambiguously be assigned to any of the ^{65}Co excited levels.

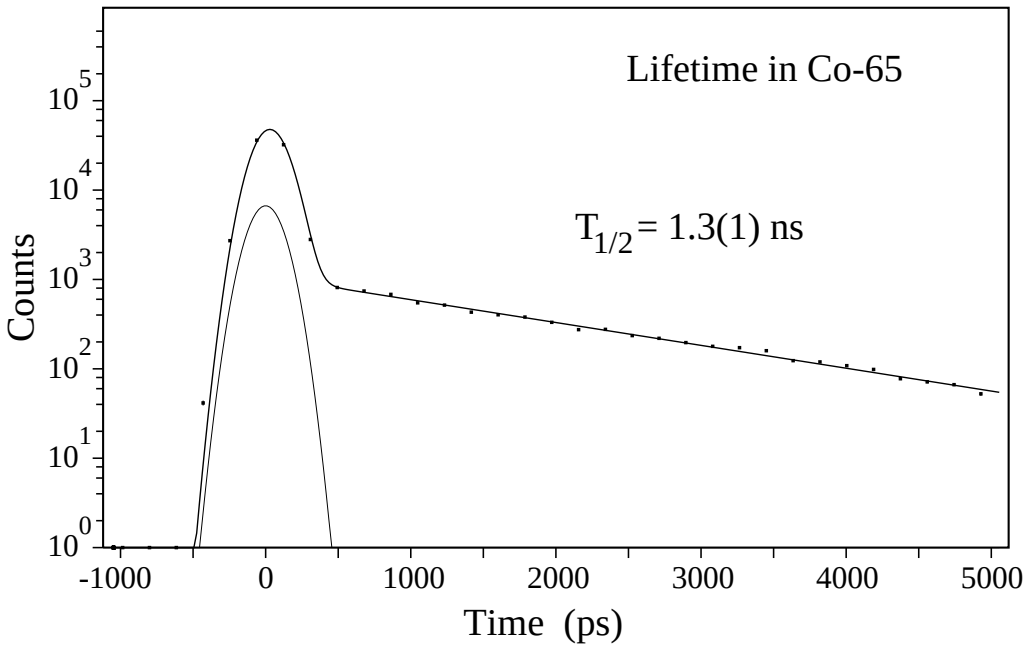

Figure 5.17: Time-delayed $\beta\gamma$(t) spectrum gated by the 882.5-keV transition in ^{65}Co.

Chapter 6

Mn-63

6.1 Experimental results

The experiment IS474 ran mass $A = 63$ for around $\sim$ 19 hours. The production yield was much higher than for masses 65 and 66 (as expected for an isotope closer to the Valley of Stability), so there was abundant statistic to perform the analysis. The ^{63}Mn production yield at ISOLDE facility is so high that the beam gate was left open only for 40 ms after the proton impact in the target, time enough to build up sufficient ^{63}Mn activity to collect the desired amount of data. This had the advantage of preventing any significant amount of ^{63}Ga ions arriving to the experimental chamber, so the amount of this contaminant during the analysis was negligible. On the other hand, mass $A = 66$ was run before masses 65 and 63 and ^{66}Ga has a $T_{1/2} \approx 9.5$ hours, so a significant amount of it was still present.

6.1.1 ^{63}Mn half life

The ^{63}Mn β-decay half life has been measured a number of times. The accepted value by the evaluators was measured by Hannawald and collaborators [4], $T_{1/2}$=275(4) ms. Other values, obtained at the same time, but with worse precision, gave slightly different values: 322(23) ms [96], 322(23) ms [31], 250(40) ms [97].

As explained previously, the beam gate was left open for 40 ms after the proton impact on the target, thus leaving ample time for the ^{63}Mn to decay before the next proton cycle at 1200 ms. By selecting the 357.3 keV gamma (the most intense in the ^{63}Mn β-decay) and projecting on to the time since last proton impact, the ^{63}Mn half life was measured (see Fig. 6.1).

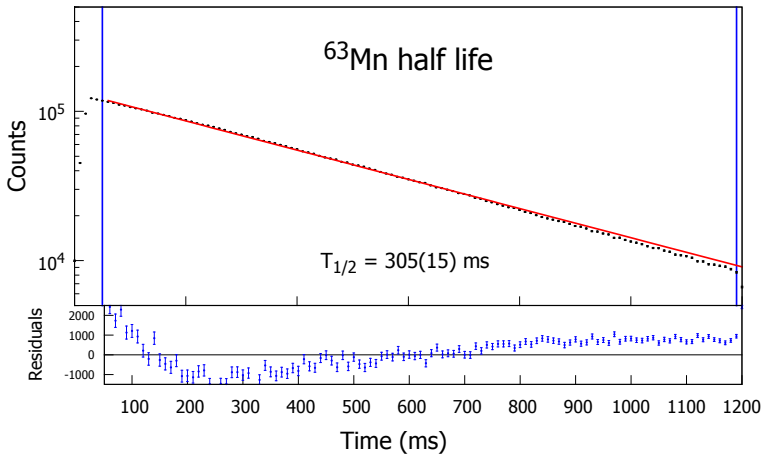

Figure 6.1: ^{63}Mn β-decay half life fitted to an exponential decay. The spectrum was obtained by gating 357.3 keV transition in ^{63}Fe.

Usually the fitting range would be selected since the closing of the beam gate (40 ms) to the end of the first proton cycle (1200 ms) in order to maximize the available statistics, but the result should be independent of the region fitted. That was not the case for ^{63}Mn. The value varied slightly depending on the time-range selected. The half life was as high as 320(2) ms for the earlier part of the decay while it went down to 290(1) ms for the later one. Any contribution from other half lives would show the opposite behaviour, a shorter half life at the beginning and a longer one at the end, so this possibility was ruled out.

Another possible explanation would be an ion leaking due to some malfunction of the beam gate. If this leaking is larger at the beginning (because there is a larger amount of Mn ions at the target) but grows smaller as time goes (because the beam gates slowly closes or just because the Mn ions have decayed away and there are less) could explain why longer half lives are observed just after the beam gate is closed.

To corroborate this possibility we tried to fit the observed release of ^{65}Mn from the target and compare it to the tabulated release parameters (see table 3.1). To do this, it was needed a high amount of statistics and a beam gate opened for long enough to observe the release. Only during masses $A = 65,\ 66$ was the beam gate opened long enough to appreciate the release, and production yield was considerably higher for $A = 65$ than for $A = 66$, so this analysis was performed on the lighter isotope. Due to the high number of parameters (three exponentials and weighting and normalization factors) no reliable fit was obtained. Regardless of this, when the tabulated Mn release parameters are plotted over the measured release (see Fig. 3.4 and Sec. 3.1.3 for further details), it is obvious that the recorded release is much

slower. This could be an indication of the hypothetical ion leaking.

As no concluding explanation has been obtained for the dependence of the ^{63}Mn half life with the fitting range, the presented value is an average of the results obtained by fitting the different regions, $T_{1/2}$=305(15) ms. The error takes into account the time dependence of the fit. This result was verified by fitting ^{63}Mn activity with gates in other gammas, as 451.1 or 1132.5 keV, in ^{63}Fe.

6.1.2 ^{63}Fe levels and transitions

The only previous information about the populated levels of the ^{63}Mn β-decay into ^{63}Fe was reported by Bosch *et al.* [97], who observed the first gamma assigned to this decay. They created ^{63}Mn isotopes in a multinucleon transfer reaction and observed a 356(10) keV line in its decay.

Later, H. Mach and the Fast Timing Collaboration performed a test at ISOLDE for the IS474 experiment [19]. During this brief test several gammas were observed, the half lives of the first two excited states were measured and tentative spin parities were assigned. Transitions and levels seen in both the test and the experiment are indicated in Tables 6.1 and 6.2. The order of transitions 424.5 and 658.6 keV has been inverted, line 1542.6 keV was not observed and, in this work, we ruled out the possibility that the 681.6 keV transition is a doublet.

The IS474 experiment was considerable longer than the brief test, so much higher statistics were achieved. Figs. 6.3, 6.4 and 6.5 shows both HPGe energy spectra added. A time gate was set to enhance the ^{63}Mn decay, but due to the specific half lives of the $A = 63$ isotopic chain, the spectrum could not be completely cleared. Peaks were identified via its parent half life and coincidences with other known gammas (with a $\pm \sim 0.5\ \mu s$ time gate).

Table 6.1 lists the gammas assigned to the ^{63}Mn decay. Their relative intensities have been normalized to 100 for the 357.3 keV transition. Several gammas with weak intensity (all of them add up to 2.4 in relative units) belonged to the ^{63}Mn decay, but their lack of coincidences made impossible to place them in either the β or β-n branch, so they are listed but not placed in the level scheme.

$Energy_\gamma$ (keV)	$Energy_{level}$ (keV)	I_γ	Multipolarity
93.8(1)†	451.1(1)	16(1)	M1
206.3(1)	681.3(1)	5(4)	
226.1(1)	1132.6(1)	0.5(1)	
230.1(1)†	681.3(1)	1(1)	
268.3(1)†	625.6(1)	1.2(1)	
289.9(1)	1534.3(2)	0.1(1)	

323.9(1)†	681.3(1)	1.6(1)	
357.3(1)†	357.3(1)	100(7)	M1
401.6(1)	1534.3(2)	0.4(1)	
424.5(1)†	1534.3(2)	2.7(2)	
451.1(1)†,*	451.1(1)	16.1(1)	E2
451.1(1)*	1132.6(1)	1.2(3)	
455.4(1)†	906.6(1)	1.6(1)	
460.8(1)	1142.0(1)	0.5(1)	
463.1(1)	820.4(1)	0.1(1)	
507.0(1)†,*	1132.6(1)	9.1(7)	
549.2(1)†	906.6(1)	1.3(1)	
563.2(1)	1244.5(1)	0.1(1)	
625.6(1)†,*	625.6(1)	14(1)	
627.9(2)*	1534.3(2)	2(2)	
658.6(1)†	1109.8(2)	3.7(3)	
681.6(1)†	1132.6(1)	3.5(3)	
727.0(1)	1178.1(1)	0.4(1)	
750.3(2)*	1431.6(2)	0.5(1)	
752.4(1)*	1628.0(2)	0.8(1)	
769.5(1)#	1244.5(1)	0.7(1)	
775.4(1)†	1132.6(1)	11(1)	
784.6(1)	1142.0(1)	0.2(1)	
820.8(1)†	1178.1(1)	1.7(1)	
831.4(2)	1737.7(1)	0.2(1)	
849.7(1)	1756.0(3)	0.1(1)	
853.1(1)	1534.3(2)	3.3(2)	
877.2(1)	β-n	0.9(1)	
906.7(1)*	906.6(1)	1.8(1)	
908.7(1)†,*	1534.3(2)	1.4(1)	
918.4(1)	1369.4(2)	0.4(1)	
932.1(1)	1289.4(1)	0.2(1)	
942.1(1)	2185.8(3)	0.3(1)	
945.5(1)	2055.3(2)	0.1(1)	
1012.1(1)	1369.4(2)	0.5(1)	
1060.2(1)	1511.3(1)	0.4(1)	
1083.0(1)†	1534.3(2)	0.6(1)	
1128.1(1)	2034.7(1)	1.3(1)	
1132.5(1)†	1132.6(1)	33(2)	
1152.8(1)	2330.7(3)	0.2(1)	
1176.9(1)†	1534.3(2)	4.9(4)	
1183.7(1)	1808.9(2)	0.2(1)	

1286.6(3)	1737.7(1)	0.1(1)	
1304.6(1)	1756.0(3)	0.2(1)	
1357.8(1)	1808.9(2)	0.6(1)	
1369.3(1)	1369.4(2)	1.9(1)	
1380.3(1)	1737.7(1)	0.2(1)	
1393.7(1)	1844.8(1)	0.2(1)	
1398.7(1)	1756.0(3)	0.7(1)	
1409.2(1)	2034.7(1)	0.2(1)	
1451.5(1)	1808.9(2)	0.8(1)	
1471.9(1)	1829.3(1)	0.2(1)	
1534.0(1)	1534.3(2)	0.4(1)	
1580.1(2)#	2055.3(2)	0.1(1)	
1604.3(1)	2055.3(2)	0.2(1)	
1677.3(1)	2034.7(1)	0.4(1)	
1735.1(1)	2185.8(3)	0.4(1)	
1808.9(1)	1808.9(2)	1.1(1)	
1828.3(3)	2185.8(3)	0.2(1)	
1855.6(1)#	2330.7(3)	0.6(1)	
1879.4(1)	2330.7(3)	0.4(1)	
1959.0(1)	Unplaced	0.1(1)	
2140.8(1)	Unplaced	0.1(1)	
2185.2(7)	2185.8(3)	0.3(1)	
2205.6(1)	2831.2(2)	0.3(1)	
2235.0(1)	Unplaced	0.2(1)	
2243.2(2)	Unplaced	0.1(1)	
2386.3(3)	2837.7(3)	0.2(1)	
2474.0(2)	2831.2(2)	0.4(1)	
2480.5(2)	2837.7(3)	0.3(1)	
2526.6(2)	Unplaced	0.2(1)	
2606.3(3)	3057.4(3)	0.3(1)	
2703.1(2)	3328.7(2)	0.3(1)	
2729.4(2)	Unplaced	0.1(1)	
2735.0(2)	Unplaced	0.1(1)	
2775.4(1)	Unplaced	0.6(1)	
2817.9(2)	Unplaced	0.2(1)	
2841.0(2)	Unplaced	0.2(1)	
3057.4(2)	Unplaced	0.2(1)	
3112.3(3)	3563.5(3)	0.3(1)	
3656.3(2)	Unplaced	0.2(1)	
3903.2(3)	Unplaced	0.1(1)	

Table 6.1: Summary of the observed transitions in the ^{63}Mn decay. †: Gammas already observed in [19]. $^{\#}$: No coincidences observed, placed above the 475.0 keV level because they fit with previously established levels. *: Intensity obtained in coincidences, see text for details.

Transition 451.1 keV is assigned as a doublet because it had clear coincidences with the 206.3 and 323.9 keV lines, while neither of these had coincidences with 93.8 keV. The relative intensity was obtained by the ratio of the areas for 451.1 and 853.1 keV in the 323.9 keV coincidences energy spectrum. The peak of 507.0 keV transition was to close to the annihilation peak 511 keV, so its intensity was obtained in coincidences as well. The full-energy peaks of pairs 625.6-627.9, 750.3-752.4 and 906.7-908.7 keV could not be completely separated, so their intensities were obtained in coincidences. The possibility that the 681.6 keV could be a doublet and also de-excited the 681.3 keV level to the ground state was studied. None of the gammas populating the 681.3 keV level shows significant coincidences with the 681.6 keV transition. 853.1 keV (the most intense of such gammas) would place an upper limit of 0.1 for the intensity of this hypothetical transition. For this reason, and the fact that the energies do not match exactly, it was decided to rule out the possibility of a doublet in the 681.6 keV peak with a significant intensity.

1580.1 and 1855.6 keV transitions showed no coincidences. They were tentatively placed above the 475.0 keV level (to see how this level was established see Sec. 6.1.3) because their energy fitted with previous independently established levels. The 289.9 and 942.1 keV transitions were clearly in coincidences with the 769.5 keV gamma, but were not in coincidences with anything else. Placing the 769.5 kev transition above the 475.0 keV level made it fit with the 1244.5 keV level. Intensity-wise, 289.9 and 942.1 keV were placed above the 769.5 keV transition, and they fitted with the 1534.3 and 2055.3 keV levels respectively. In this arrangement, 289.9 and 942.1 keV transitions should have coincidences with the 563.2 keV gamma (decays from the same level as the now placed 769.5 keV), but their weak intensity makes this coincidences to be in the noise level.

Table 6.2 summarizes the populated levels in the ^{63}Mn β-decay. The β-feeding has been calculated as the difference between the transitions populating and de-exciting one level. The normalization factor for the absolute intensities is 174(8), as the sum of all the gammas feeding the ground state and the 475.0 keV level. For this calculation and the $\log(ft)$ values the direct ground state feeding has been considered negligible (see Sec. 6.1.4). For the mass difference a $Q_\beta = 8748.6(5.5)$ keV [98] value was used in the calculations.

Level (keV)	β-feeding	$\log(ft)$	$T_{1/2}$	J^P

0	$< 7\,\%$	> 5.7	305(15) ms	$(1/2^-)$
357.3(1)†	34(4)	5,0(1)	125(20) ps	$(3/2^-)$
451.1(1)†	9(1)	5.5(1)	805(30) ps	$(5/2^-)$
475.0(1)$^+$				
625.6(1)†	2.3(7)	6.1(1)		
681.3(1)†	1.1(3)	6.4(1)		
820.4(1)	0.1(1)	7.4(5)		
906.6(1)†	0.5(2)	6.6(2)		
1109.8(2)	2.5(2)	5.9(1)		
1132.6(1)†	33(2)	4.8(1)		
1142.0(1)	0.4(1)	6.7(1)		
1178.1(1)†	1.1(1)	6.2(1)		
1244.5(1)	0.1(1)	7.3(5)		
1289.4(1)	0.1(1)	7.2(5)		
1369.4(2)	1.6(1)	6,0(1)		
1431.6(2)	0.3(1)	6.7(2)		
1511.3(1)	0.2(1)	6.9(2)		
1534.3(2)†	8.9(3)	5.2(1)		
1737.7(1)	0.3(1)	6.6(1)		
1756.0(3)	0.6(1)	6.3(1)		
1808.9(2)	1.5(1)	5.9(1)		
1829.3(1)	0.1(1)	7.1(5)		
1844.8(1)	0.1(1)	7.1(5)		
2034.7(1)	1.1(1)	6,0(1)		
2055.3(2)	0.2(1)	6.7(2)		
2185.8(3)	0.5(1)	6.3(1)		
2330.7(3)	0.3(1)	6.5(2)		
2831.2(2)	0.4(1)	6.2(1)		
2837.7(3)	0.3(1)	6.3(2)		
3057.4(3)	0.2(1)	6.4(2)		
3328.7(2)	0.2(1)	6.3(2)		
3563.5(3)	0.2(1)	6.2(2)		

Table 6.2: Summary of the ^{63}Fe populated levels in the ^{63}Mn β-decay. †: Levels already observed in [19]. $^+$: No gamma is observed to de-excite this level, see Sec. 6.1.3 for details.

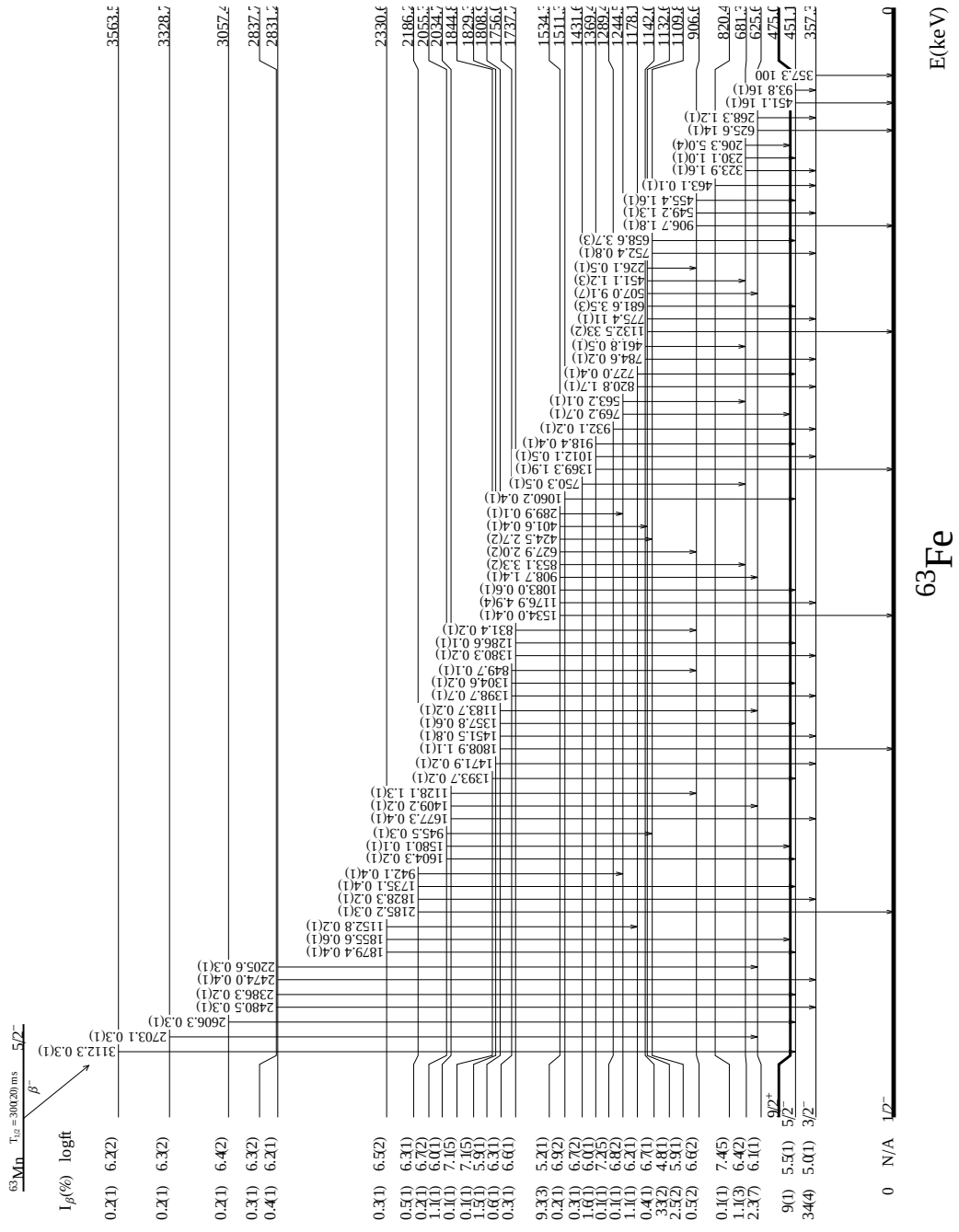

Figure 6.2: ^{63}Fe level scheme populated in the β-decay of ^{63}Mn from this work.

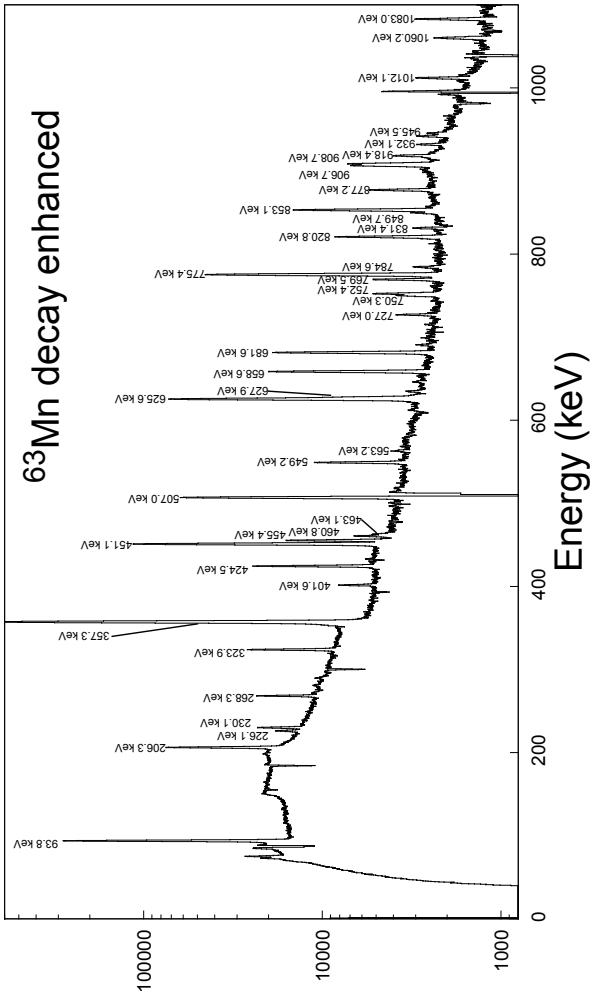

Figure 6.3: Energy spectra of both HPGe detectors added with the ^{63}Mn activity enhanced. Peaks assigned to the ^{63}Mn are identified.

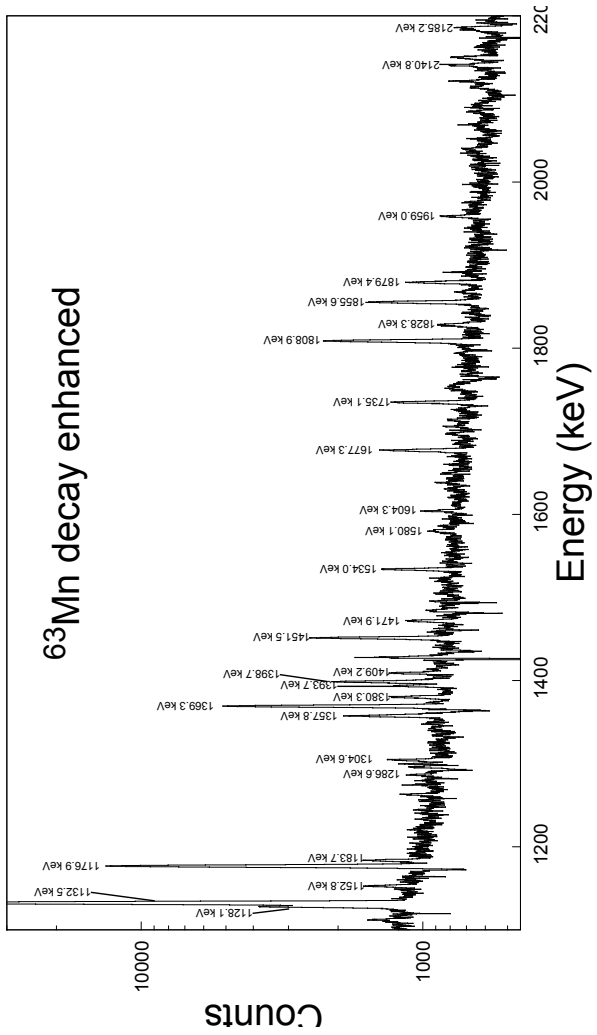

Figure 6.4: Energy spectra of both HPGe detectors added with the ^{63}Mn activity enhanced. Peaks assigned to the ^{63}Mn are identified.

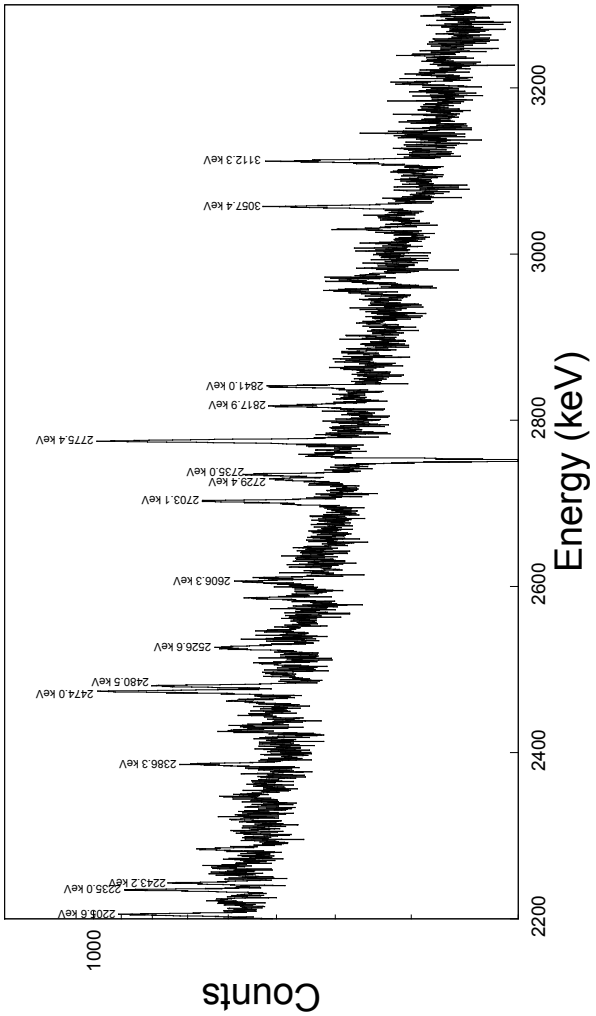

Figure 6.5: Energy spectra of both HPGe detectors added with the ^{63}Mn activity enhanced. Peaks assigned to the ^{63}Mn are identified.

6.1.3 475.0 keV isomer

The 206.3 keV γ-ray had very clear coincidences with 451.1 (it is a doublet), 461.8, 563.2, 750.3 and 853.1 keV transitions, but no with 93.8 or 357.3 keV lines within the $\pm 0.5 \mu s$ time gate. This placed the gamma de-exciting the 681.3 keV level to a new 475.0 keV level which has no observed gammas de-populating it.

This level at 475.0 keV could only de-excite via gamma to the 451.1, 357.3 keV and ground sate, via a 23.9, 117.7 or 475.0 keV transitions, respectively. In total this level is fed by 6.4 units of relative intensity (disregarding any hypothetical direct β-feeding), which, even shared about these three transition, would be clearly noticeable in the HPGe energy spectra. None of this three peaks are observed in the HPGe ungated energy spectrum. The 23.9 keV is certainly below the CFD threshold, but the other two, if existed, should be observed. Table 6.3 shows the total conversion coefficients α_T of this three transitions as a function of their possible multipolarities. 475.0 keV would have very low conversion coefficient, even as an M4, so this does not explain why it is not observed. 117.7 keV have a significant α_T, but only the ones for multipolarities E4 and M4 would explain why it is not observed. 23.9 keV is absolutely converted, which would make a direct observation unachievable. As mentioned before, the CFD threshold would render its observation impossible in any case, but the coefficient can play an important role in the calculation of a hypothetical half life.

Energy (keV)	$\alpha_T(E1)$	$\alpha_T(E2)$	$\alpha_T(E3)$	$\alpha_T(E4)$
475.0(1)	4.52(7)E-04	1.60(23)E-03	5.03(7)E-03	1.52(22)E-02
117.7(1)	2.58(4)E-02	2.63(4)E-01	2.27(4)E+00	1.91(3)E+01
23.9(1)	3.14(6)E+00	1.05(22)E+02	3.79(10)E+03	1.77(6)E+05
Energy (keV)	$\alpha_T(M1)$	$\alpha_T(M2)$	$\alpha_T(M3)$	$\alpha_T(M4)$
475.0(1)	7.58(11)E-04	2.50(4)E-03	7.73(11)E-03	2.37(4)E-02
117.7(1)	2.29(4)E-02	2.09(3)E-01	1.84(3)E+00	1.64(25)E+01
23.9(1)	1.93(4)E+00	7.83(17)E+01	2.60(7)E+03	9.50(3)E+04

Table 6.3: Total conversion coefficients α_T of the possible transitions depopulating the 475.0 keV level as a function of their multipolarity. Data obtained from evaluation [99].

Even if unseen in the energy spectra, these transitions could show themselves as a delayed component in the lines de-exciting the levels they would populate. If all the intensity coming into the 475.0 keV level de-excites though the 23.9 keV, it means that approximately $\sim 1/5$ of the 451.1 keV transition counts should be delayed. Left plot in Fig. 6.6 shows the slow-TAC (β-HPGe) spectrum gated in the 451.1 keV, with a compression of 2.4 ns/channel. The peak on the left side are

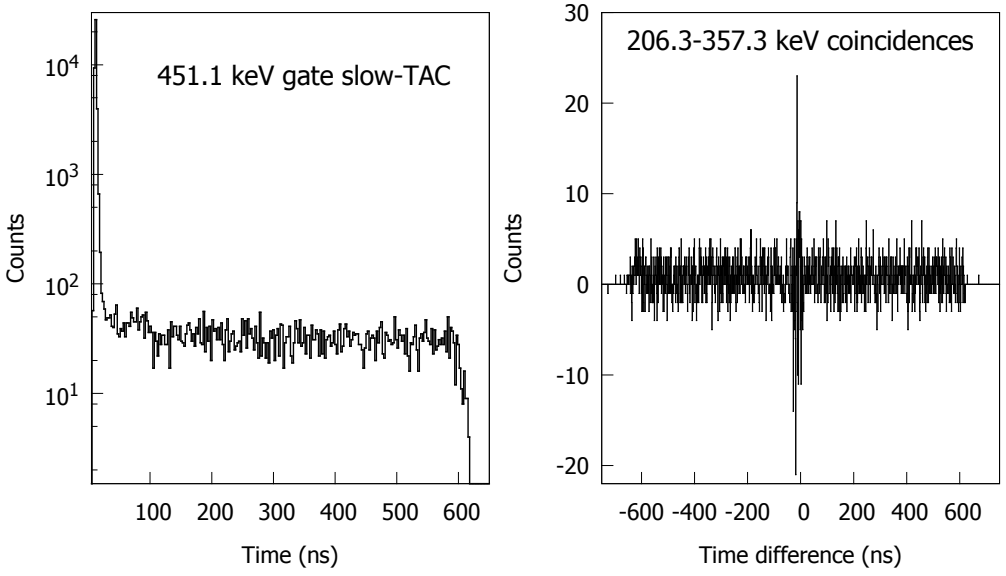

Figure 6.6: *Left:* slow-TAC spectra with a gate in the 451.1 keV transition. *Right:* time difference between coincidences of transitions 206.3 and 357.6 keV. See the text for details.

prompt transitions (in this contest means transition with lifetimes below 1 ns) while the flat plateau are random coincidences. A delayed feeding of the 451.1 keV would show itself as a slope between the prompt peak and the random plateau, which clearly is not.

A similar approach was followed for the 357.3 keV level. If this level is fed from the 475.0 keV level through the unseen 117.7 keV transition, transition 206.3 and 357.3 keV should be in coincidences and their time difference should show a delayed component (see Sec. 5.3.4 for an example of such a case). Right plot in Fig. 6.6 shows the time difference made with the PIXIE clock while gating 206.3 and 357.3 keV full-energy peaks in the HPGe-HPGe coincidences spectra with a ± 8 μs time window. The resulting spectrum should show a decaying slope from zero (if the 475.0 keV has a half life in the ns-μs range) or a prompt peak (if such half life is in the ps range or below). What is shown is a random distribution with a net area of zero. This is a clear indication that there is no coincidences between 206.3 and 357.3 keV below the ms range.

The lack of fast coincidences (in the ps or ns range) and unobserved 475.0 keV transition to the ground state rules out the possibility that this level has negative parity or a positive parity with low spin, as $1/2^+$ or $3/2^+$.

Table 6.4 shows the partial half lives of these transitions for different multi-

polarities assuming a higher spin positive parity for the 475.0 keV level. It can be discarded the possibility that this level has a spin-parity of $5/2^+$. In this case the level would have a half life in the picoseconds range, while 117.7 keV would compete with the 23.9 keV transition. The lack of fast coincidences between 206.3 and 357.3 keV gamma rays shows that this is not the case. The absence of fast coincidences between 206.3 and 93.8 keV transitions also rules out the possibility of the level having spin $7/2^+$.

475.0 keV J^π	E_{Level}	J^π	E_γ	Multipolarity	τ_γ (s)
$9/2^+$	0	$1/2^-$	475.0	M4	4E5
	357.3	$3/2^-$	117.7	E3	5
	451.1	$5/2^-$	23.9	M2	2E-2
$7/2^+$	0	$1/2^-$	475.0	E3	8E-4
	357.3	$3/2^-$	117.7	M2	6E-4
	451.1	$5/2^-$	23.9	E1	7E-12
$5/2^+$	0	$1/2^-$	475.0	M2	8E-7
	357.3	$3/2^-$	117.7	E1	3E-13
	451.1	$5/2^-$	23.9	E1	7E-12

Table 6.4: Partial half lives of the hypothetical transitions de-exciting the 475.0 keV level as a function of its possible spin-parities. 1 W.u. is assumed for the electric transitions and 0.1 W.u. for the magnetic ones.

In this scenario the most likely spin-parity configuration is $9/2^+$, a neutron promoted to the $g_{9/2}$ orbital. In this case there are two possibilities. On one hand the level decays through gamma transition M2 to level 451.1 keV with a lifetime in the order of milliseconds (this would be out of the coincidences gate range, thus explaining why no delayed component is observed). On the other hand this level is an isomer that de-excites through β-decay to ^{63}Co, with a half life in the order of a few seconds (to compete with the ^{63}Fe ground state) and possibly populates high spin or positive parity states, similarly to ^{65m}Fe (see Sec. 5.3.3).

6.1.4 Ground state feeding

To estimate the direct ground state β feeding in the ^{63}Mn decay, the daughter decays in the isotopic chain were studied. In order to avoid half lives corrections, the comparison of different isotopes intensities was performed without setting any gate in the time since last proton cycle.

There is scarce information on the ^{63}Fe β decay to ^{63}Co. Runte *et al.* published a study [76] where they assigned 80% of the β decay feeding directly to the

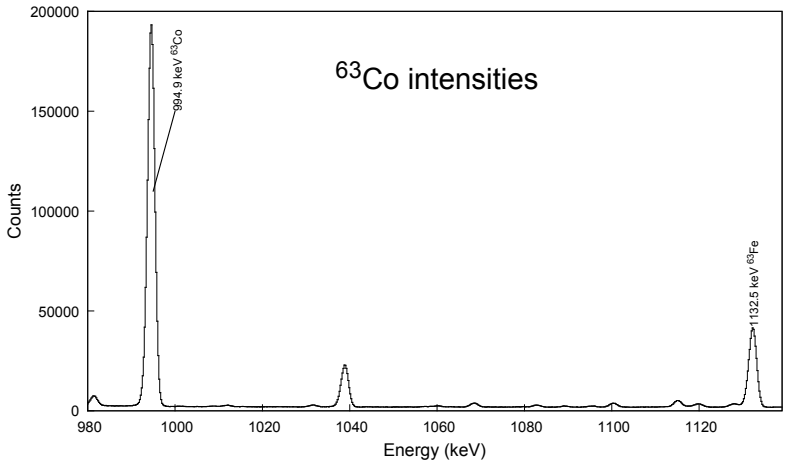

Figure 6.7: Comparison of the 994.9 keV full-energy peak in ^{63}Co with 1132.5 keV in ^{63}Fe (absolute intensity 19(1)%).

ground state. They gave no error, but the evaluators estimated them to be $\sim 34\%$ [100]. The only significant γ transitions would be 994.9 and 1427.1 keV, with absolute intensities of 14(19)% and 4.6(63)% respectively. Even with the large errors suggested by the evaluators, the intensities we observe for these peaks are not in agreement with the reported values. See Fig 6.7 for a comparison of 994.4 keV in ^{63}Co and 1132.5 keV in ^{63}Fe. Coincidences and half life did not show any sign that this peak could be a doublet. Because of these discrepancies with the intensities, it was decided not to use ^{63}Co transitions.

The ^{63}Co decay into ^{63}Ni was studied by Jongsma and collaborators [101] and its transition intensities given with high precision. The 87.1, 155.6, 981.7 and 1069.1 keV (absolute intensities add up 53.8%) in ^{63}Ni were compared to 357.3 and 451.1 keV in ^{63}Fe (absolute intensities add up 66.8% normalized using only the transitions directly populating the ground state). The ratio of their areas showed no missing intensity in the ^{63}Fe transitions, so an upper limit was set of $< 7\%$ for the direct ground state β-feeding and assumed negligible for following calculations. This result could be further improved if the ^{63}Ni total intensities were measured with the IS474 data for internal coherence.

The ^{63}Ni to ^{63}Cu decay has a very small $Q_\beta = 66.945(5)$ keV, so no excited level are populated. As there are no observable transitions, the direct ground state feeding value obtained could not be verified with the grand-daughter decay.

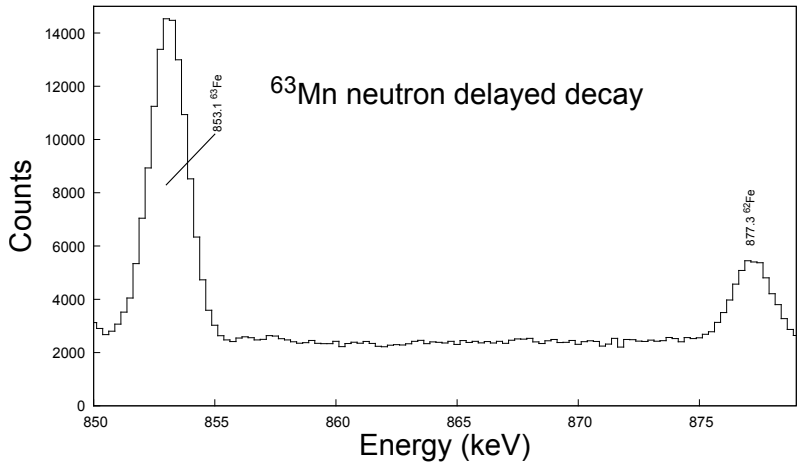

Figure 6.8: 877.3 keV transition in the ^{63}Mn decay neutron delayed branch.

6.1.5 Neutron delayed emission branch

The 877.3 keV transition was observed in the ^{63}Mn decay, with no coincidences with other gammas. This transition was already assigned to the ^{62}Mn β-decay into ^{62}Fe [102], so its observation was interpreted as a β-n branch from ^{63}Mn populating excited states in ^{62}Fe (see Fig. 6.8). A relative intensity of 0.9(1) (normalized to 100 for 357.3 keV) was observed.

As there exists the possibility that the β-n branch directly populates the ^{62}Fe ground state, in order to measure the P_n value the ^{62}Co decay into ^{62}Ni was analysed. Gammas 1172.9 and 2301.9 kev in ^{62}Ni (total intensities add up 97.9% [103]) were compared to 357.3 and 451.1 keV in ^{63}Fe (total intensities add up 66.8% assuming 100% β decay). The ratio of intensities showed that $P_n = 2.0(2)\%$ decays through a β-n branch.

By comparing the ^{62}Ni gammas with the intensity observed for 877.3 keV, there was clearly a large quantity of missing intensity. This difference was attributed to direct β-n ground state feeding, with 24(3)% going though the excited state and the rest directly to the ground or unobserved transitions.

The ^{62}Fe decay into ^{62}Co was not used for this calculations because the only gamma assigned to this decay is at 506.1 keV [104], which could not be separated from the 511 keV annihilation peak.

No other gammas could be firmly assigned to the β-n decay, but it cannot be excluded that some of the unplaced transitions in the ^{63}Mn decay belongs to this branch.

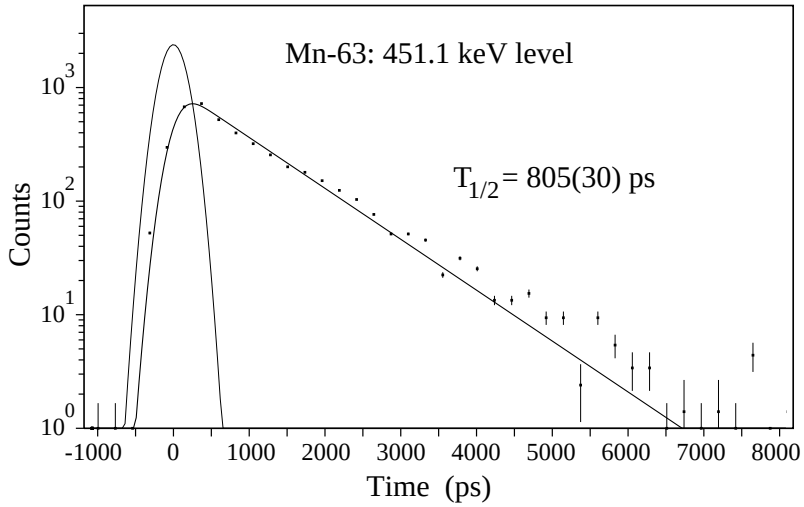

Figure 6.9: Half life of the 451.1 keV obtained using the convolution technique. The spectrum was generated by gating the 357.3 full-energy peak in the HPGe detector and the 93.8 keV in the $LaBr_3$(Ce) crystal.

6.2 Half lives

Half lives in the hundred picoseconds range were measured using the Deconvolution Technique [13]. Not other half lives were observed in this range, but it is not discarded that in future analysis faster half lives can be measured using the Centroid Shift Technique.

6.2.1 451.1 keV level

When gating on the 93.8 or 451.1 keV peaks in the $LaBr_3$(Ce) crystal (both depopulate the same level) their times distributions presented a clear, long slope in the delayed part (see Fig. 6.9). Using the deconvolution technique the slope was fitted, obtaining results in good agreement between the two transitions and both detectors.

Triple coincidences (93.8 keV transition in the $LaBr_3$(Ce) crystal and 357.3 full-energy peak in the HPGe detector) produced a much cleaner spectra, with an improved peak-to-background ratio, at the cost on much lower statistics. The fit of the slope yielded values slightly lower than the $\beta - \gamma$ did, but within the error bar.

The final result is the weighted average of the different results, giving $T_{1/2} =$ 805(30) ps for the 451.1 keV level. This result is in very good agreement with the one published previous value ($T_{1/2} = 780$ ps) obtained by the Fast Timing Collaboration [19].

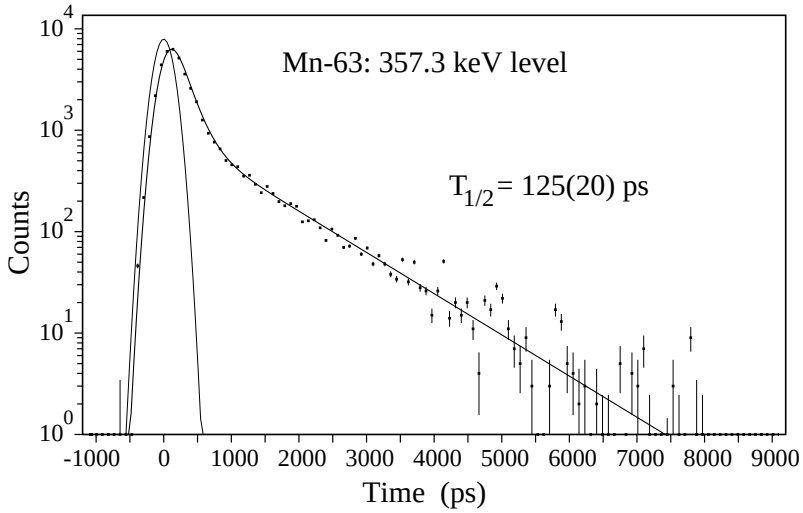

Figure 6.10: Fit of the 357.3 keV level half life. The time spectra was generated in triple coincidences $\beta - \gamma - \gamma$, selecting the 357.3 keV peak in the $LaBr_3$(Ce) crystal but leaving the HPGe ungated.

6.2.2 357.3 keV level

The time distribution of the 357.3 keV gamma also showed a slope on its delayed part, but much shorter than in the previous case. This level is fed by several gammas, all coming from levels with no apparent half life, with the exception of the 93.8 keV transition. When 357.3 keV is selected in the $LaBr_3$(Ce) crystal without selecting a specific gamma cascade, its time distribution presents the half lives of both levels, 357.3 and 451.1 keV (see Fig. 6.10). The fit to its time distribution was made a double exponential decay, with the half life of the 451.1 keV level fixed.

This fit was repeated without the contribution of the 451.1 keV level half life. The 357.3 keV peak was selected in the $LaBr_3$(Ce) crystal, while all the gammas feeding this level, except the 93.8 keV, were selected in the HPGe detector. The resulting time spectra were added together to increase statistics and the fit was done to a single exponential using the deconvolution technique. The result was slightly longer and with larger error bars than in the previous result, but still in good agreement.

The final result, a weighted average between both methods and the two detectors, is $T_{1/2} = 125(20)$ ps. This result also confirms the previously measured value by H. Mach and the Fast Timing Collaboration ($T_{1/2} = 110$ ps) [19].

6.3 Discussion

The observed transitions in the ^{63}Mn decays allows us to assign possible spin-parity configurations to some of the lower energy levels in ^{63}Fe. The multipolarity of some of this transitions based in the measured half lives is discussed as well.

Ground state level It is expected that the ground state spin-parity configuration is determined by the fp shell, so the possible spins are $1/2^-$, $3/2^-$ and $5/2^-$. The lack of direct β-feeding indicates a forbidden transition. The ground state of ^{63}Mn is tentatively assigned $5/2^-$ based in systematic [100], so $1/2^-$ is the most likely configuration for the ^{63}Fe ground state. This result is interpreted as the coupling of the unpaired neutron with the 0^+ state of the even-even core, resulting $|0^+ \otimes 1/2^-\rangle = 1/2^-$.

357.3 keV level Following the previous reasoning, the first two excited states are expected to be the coupling of the 2_1^+ of the even-even core with the unpaired neutron, resulting in $|2^+ \otimes 1/2^-\rangle = 3/2^-,\ 5/2^-$. If this first level is the $5/2^-$, its de-excitation to the ground state would be an E2 with B(E2)=49(8) W.u., an unreasonable value, twice the value for ^{64}Fe and thrice of the ^{62}Fe. On the other hand, if this transition has a multipolarity M1, its value is $B\,(M1) = 3.9(6) \cdot 10^{-3}$ W.u., is in good agreement with the results obtained for similar levels in ^{65}Fe. The strong β-feeding and low $\log(ft)$ suggest an allowed β-transition, supporting a spin assignment of $3/2^-$.

451.1 keV level This leaves the 451.1 keV level as a candidate to be the first $5/2^-$. The 93.8 keV transition to the first excited state would have multipolarity M1 with $B\,(M1) = 17(1) \cdot 10^{-3}$ *W.u.* and the 451.1 keV gamma to the ground sate $B\,(E2) = 1.2(1)$ *W.u.* In the ^{65}Fe case, the E2 transition was clearly favoured over the M1, while in this case both transition have similar intensities, despite the energy factor. This level is also strongly populated in β-decay, but not as much as the 357.3 keV, which suggests that the ^{63}Mn decay favours the population of levels with spin $3/2^-$ over the ones with spin $5/2^-$.

475.0 keV level This level was discussed in Sec. 6.1.3 and it is a firm candidate to be the $9/2^+$ isomer state already observed in other odd neutron-rich Fe nuclides.

625.6 keV level This level populates the ground state and the first excited, but there is no gamma observed to the 451.1 keV level. If this level had $3/2^-$ spin, a

174.5 keV line with an intensity near ~ 0.5 (to have a similar B(M1) value as the other two) should be observed. That intensity is well within the system efficiency limit, so we can safely discard $3/2^-$ spin. That only leaves an assignment of $1/2^-$ for the level and multipolarity M1 for the 625.6 and 268.3 keV transitions.

681.1 keV level This level clearly favours the transition to the $9/2^+$ isomer state over their transitions to the $3/2^-$ and $5/2^-$ levels. This suggests a positive parity, with most likely spins of $5/2^+$ or $7/2^+$.

906.7 keV level This level populates the g.s., 357.3 and 451.1 keV levels with a similar intensity. This suggest a negative parity state of either $1/2^-$, $3/2^-$ or $5/2^-$. In principle it could also have a spin-parity of $3/2^+$ and the three transitions have E1 multipolarity, but there are no observed gamma to the positive parity states at 475.0 or 681.3 keV, so this option seems much less likely.

1132.6 keV level This level has the lowest $\log(ft)$ value, so an allowed transition is expected and in principle spins $3/2^-$, $5/2^-$ and $7/2^-$ could be assigned. Its strong transition to the $1/2^-$ ground state rules out the possibility of a $7/2^-$ spin. In lower energy levels it was clear that the ^{63}Mn decay favours populating $3/2^-$ states over $5/2^-$ (a similar trend was observed as well in the ^{65}Mn decay), so spin $3/2^-$ seems more likely than $5/2^-$. Without a half life to calculate the transition rates, neither of the spins can be discarded.

6.4 Conclusions

The ^{63}Fe proposed level scheme confirm the results from the Fast Timing Collaboration test. It also expand it for a total of 73 γ transitions and 31 levels. Additionally 13 γ-rays have been assigned to the ^{63}Mn decay, but were not placed in the level scheme. An upper limit of $< 7\%$, compatible with zero, has been set for the direct β-feeding to the ground state. For the first time a neutron delayed emission branch has been observed and a value of $P_n = 2.0(2)\%$ was measured. In a very similar way to the ^{65}Mn βn decay, the ^{63}Mn βn decay populates excited states in ^{62}Fe.

The observed level at 475.0 keV is proposed as the $9/2^+$ β-decaying isomer. If confirmed, the systematic of the $9/2^+$ states in odd-Fe isotopes would describe a perfect decreasing parabola, with its minimum at ^{65}Fe and then increasing again for ^{67}Fe. This would be a determinant verification of the developing importance of the $g_{9/2}$ orbital as neutrons are added.

By making use of the deconvolution technique the half lives of the first two excited states were measured. Making use of this result the spin-parity sequence could be set. It follows the same order as in ^{65}Fe, $1/2^-$ $3/2^-$ $5/2^-$. No suitable candidate has been found so far for $7/2^-$ or $9/2^-$ states.

Chapter 7

^{66}Fe analysis

In the last years the structure of the ^{66}Fe isotope has been the subject of a number of studies, both theoretical and experimental, as it is an interesting nucleus which can give valuable information on the collectivity of the region below ^{68}Ni.

The low energy ^{66}Fe level scheme populated in the ^{66}Mn β-decay has been constructed. It adds several new transitions and levels up to 3.6 MeV. The direct β-feeding to the ground state and the P_n value has been calculated as well. The half life of the E_1^+ has been measured and the result is in good agreement with the previous result. Some level lifetimes limits were set as well.

With the LNPS interaction the ^{66}Mn β-decay and ^{66}Fe excitation structure has been calculated. By comparing the theoretical predictions with the measured level scheme the spin-parity of some levels was tentative assigned.

7.1 Previous available information on ^{66}Fe

Prior to this study, the half life of the ^{66}Mn β^--decay into ^{66}Fe had been measured a number of times, with an adopted value, as a the weighted average of several different measurements, of $T_{1/2}$=65(2) ms [84].

The first gamma and the 2_1^+ level were identified at 573.4 keV for the first time by Hannawald and collaborators [4]. In that study they also observed a gamma of 840.5 keV in coincidence with 573.4 keV and tentatively assigned the 1414 keV level a spin-parity of 4^+.

In a one- and two-proton knockout from cobalt and nickel experiment Adrich *et al.* [12] observed a gamma of 832.5(60) keV depopulating a level at 1407 keV in ^{66}Fe, which was assigned $J^\pi = 4^+$. They also observed transitions of 957(10)

and 1310(15) keV, but were not placed in the level scheme, nor a multipolarity was assigned.

Fioretto and collaborators [22] populated excited ^{66}Fe levels in a ^{64}Ni $+^{238}$ U reaction at $E_{lab} = 400$ MeV. The $2^+ \rightarrow 0^+$ 574 keV transition, $4^+ \rightarrow 2^+$ 834 keV transition and $6^+ \rightarrow 4^+$ 957 keV transition were observed.

The 2_1^+ half life was measured for the first time by Rother *et al.* [21] using the recoil distance Doppler-shift technique applied to projectile Coulomb excitation reactions. They obtained a value of $\tau = 39.4(40)$ with $B(E2) = 332(34)\ e^2fm^4$, corroborating the enhanced collectivity of the neutron rich iron nuclei.

Recently Liddick *et al.* published an in-depth ^{66}Mn β-decay study [20]. The low-energy levels scheme of ^{66}Fe was constructed up to 3.3 MeV, proposing 17 gammas and 9 levels. They also measured a β-delayed neutron emission branch value of $P_n = 4(1)\%$.

7.2 Experimental results

In the IS474 experiment $A = 66$ data was collected for $\approx$ 30 hours. RILIS laser selectively ionized Mn atoms and then mass 66 was selected in the General Purpose Separator (GPS). Ga atoms were surface-ionized too due to its low ionization potential. The GPS resolving power is not enough to resolve the ^{66}Mn to ^{66}Ga mass ratio, so it was present as a contaminant during the whole experiment. The ^{66}Ga are much closer to the Valley of Stability than the ^{66}Mn are, so its production yield is much higher. Fig. 7.1 shows the high abundance of ^{66}Ga in the deposition point during the experiment, roughly $\sim$ 30 times the number of ^{66}Mn ions. The long half life of ^{66}Ga ($T_{1/2} = 9.49(3)$ h) allowed to subtract its peaks from the ^{66}Mn decay, which was enhanced by selecting a time window of 10 to 600 ms after proton impact.

Fig. 7.2 shows an HPGe energy spectrum with enhanced ^{66}Mn decay with the gammas in ^{66}Fe identified. The subtraction was calculated to hinder the abundant ^{66}Ga. This caused some decay products of the neutron rich chain to be oversubtracted, creating negative peaks. ^{66}Fe also presented some high energy intense transitions. The first and second escape peaks of these gammas were observed.

The small volume of the $LaBr_3$(Ce) crystals chosen to maximize their timing properties hindered their efficiency at higher energies, loosing a great portion of the ^{66}Mn decay (see Fig. 7.3 for an example of a $LaBr_3$(Ce) energy spectrum). Moreover, the XP20D0 PMT coupled to the $LaBr_3$(Ce) crystals have great timing properties, at the cost of high non-linearity for higher energies [105]. The high non-linearity of the PMT can be observed in the increasing width of the spectrum bins in Fig. 7.3. Peaks over 2 MeV have an apparent great energy resolution, due to their high

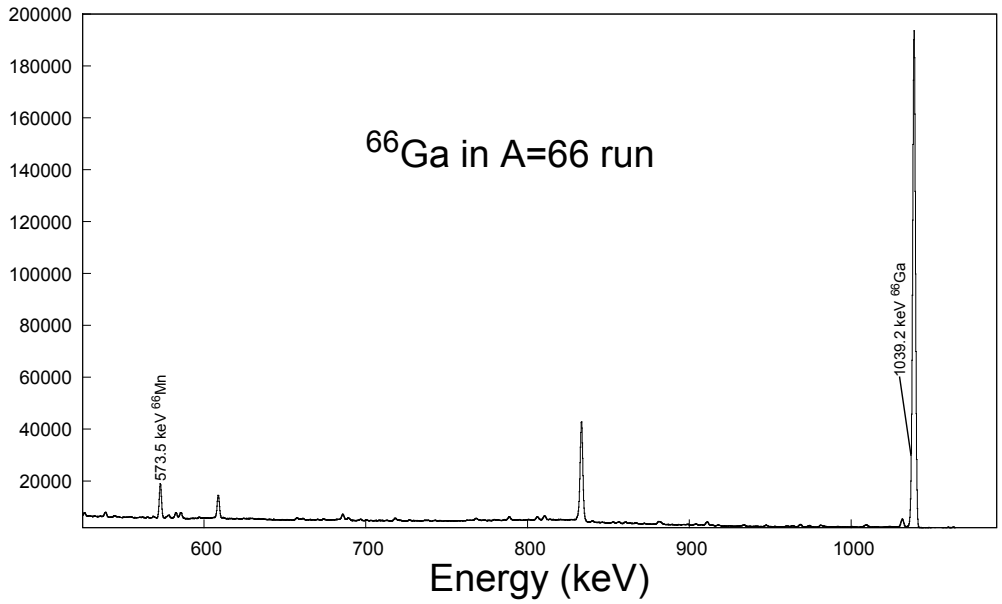

Figure 7.1: HPGe singles energy spectrum with no time gates set. The most intense gamma following the decay of ^{66}Mn (573.5 keV 33% total intensity) and ^{66}Ga (1039.2 keV 37% total intensity [84]) have been identified.

compression, but they were hard to identified.

7.2.1 ^{66}Mn half life

In order to maximize the amount of ^{66}Mn ions arriving to the experimental area, the ISOLDE beam gate was set to close 400 ms after the protons impact on the target. Due to its short half life $T_{1/2}$ = 65(2) ms, over 90% of the ^{66}Mn ions that have arrived to the experimental setup have already decayed when the beam gate is closed. For this reason only a small fraction of the total statistics could be used to measure the ^{66}Mn half life. In this condition the result heavily depended on the fitting range, but always yielded a result between 50 to 100 ms, so the half life could be unambiguously distinguished from the other isotopes in the decay chain. Fig. 7.4 shows an example of one of the fits performed.

7.2.2 ^{66}Fe half life

A fit was done to improve the ^{66}Fe half life tabulated value precision ($T_{1/2}$=440(60) ms [84]). A gate in the 470.8 keV gamma in ^{66}Co was set and then projected on to the proton impact time. To let most of the ^{66}Mn decay away and maximize the

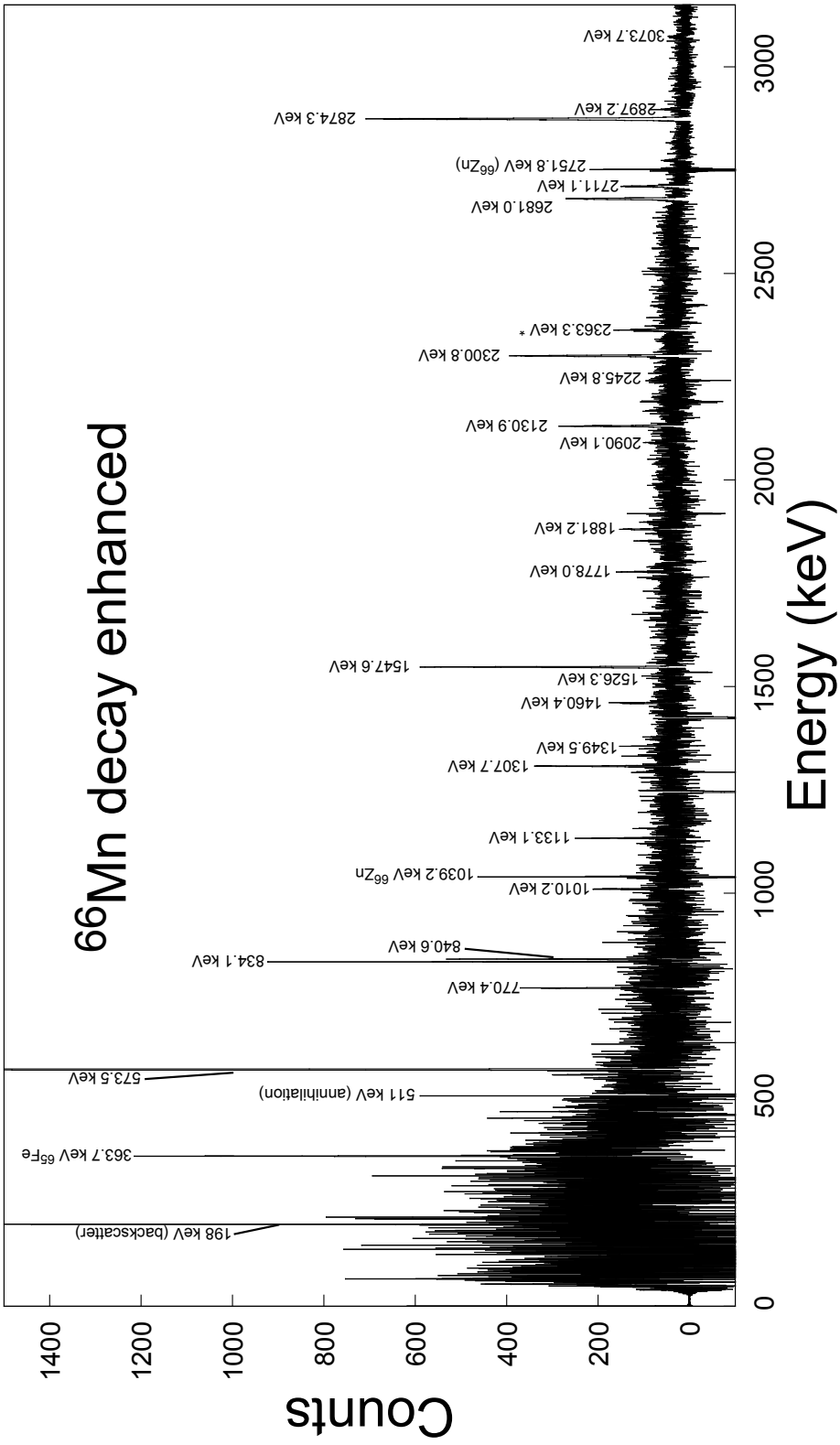

Figure 7.2: HPGe energy spectrum with the ^{66}Mn activity enhanced and the ^{66}Fe transitions identified. Long lived contaminants were subtracted.*: The 2363.3 keV peak is the first scape from 2874.3 keV in ^{66}Fe.

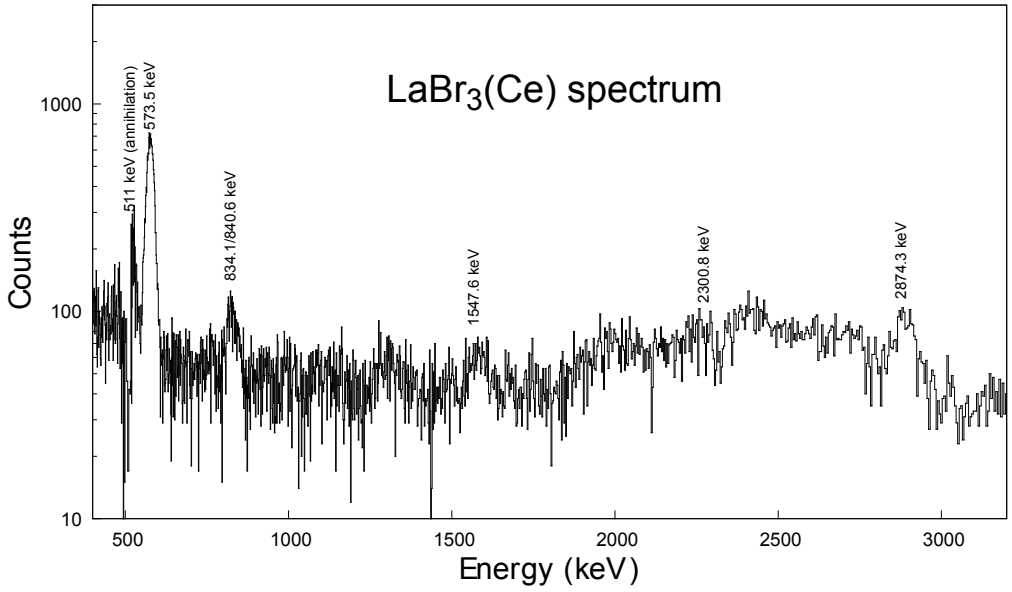

Figure 7.3: $LaBr_3(Ce)$ energy spectrum taken in $\beta - \gamma - \gamma$ coincidences with the ^{66}Mn decay enhanced and the most intense ^{66}Fe transitions identified. Long lived contaminants were subtracted, thus the negative and strange shape of the 511 kev peak. The spectra has been linialized for representation.

time range, the fitting limits were set to the second proton cycle (specifically from 1.25 to 2.39 seconds).

The fit was done two a double exponential decay, fixing the ^{66}Mn half life. The shorter half life did not affected the final value, as the remaining ^{66}Mn proportion in the fitting range was negligible. The same way the ^{66}Mn half life did, the result greatly depended on the fitting range, but the value always oscillated between 700 to 1000 ms (see Fig. 7.5). These results are far from the evaluated values and the newly measured $T_{1/2}$=351(6) ms by Liddick *et al.* [106].

7.2.3 ^{66}Fe level scheme

The assignment of gammas to the ^{66}Fe was based on their parent decay half life and their coincidence relation with previously assigned gammas. Fig. 7.6 shows the HPGe-HPGe coincidences gated on the 573.5 keV gamma. Most of the gammas observed on the ^{66}Mn decay were in coincidence with this gamma. Only 1881.2, 2874.3 and 3284.7 keV were not in coincidence, and thus were placed in the scheme due to its mother half life. Some high energy gammas with not enough statistics to be observed in $\gamma - \gamma$ coincidences but with a parent short half life were assigned to

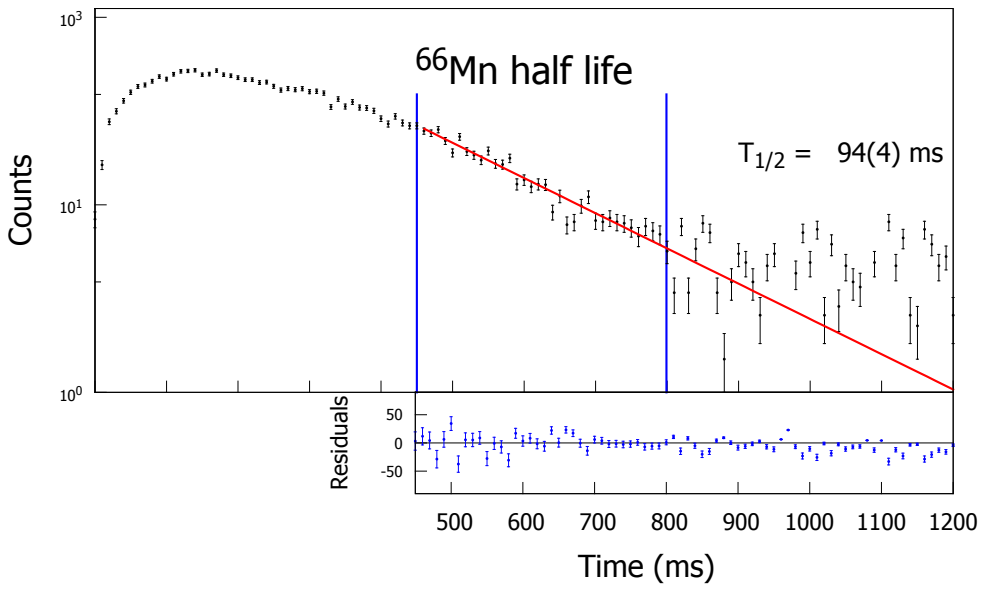

Figure 7.4: Fit to a exponential decay plus a constant background of ^{66}Mn half life through a gate in 574.5 keV gamma in ^{66}Fe. The blue markers represent the fitting limits, after the beam gate closure and before the number of counts becomes so low as to make Poison distribution dominant.

the ^{66}Mn decay but not placed in ^{66}Fe level scheme.

The level scheme now comprehends 16 levels and 24 gammas (see Fig. 7.7 and Tab. 7.1 for details). The relative intensity of the transition was obtained from the singles spectra and normalized to 100 units for 573.5 keV. Those gammas which could not be unambiguously separated had their intensity obtained from $\gamma-\gamma$ coincidences (see footnotes on Tab. 7.1). The total intensity is expressed as the % of ^{66}Mn β-decays for which the gamma is observed (to 100% β^- decays, taking into account the direct ground state feeding but not the β-n branch).

E_γ (keV)	E_{parent} (keV)	E_{final} (keV)	I_γ	Main coincidences (keV)
573.4 (1)	100 (7)	573.5 (1)	g.s.	770.7 834.1 840.9 1010.7 1133.3 1307.7 1349.4 1460.1 1547.8 1778.1 2090.2 2131.2 2246.0 2300.5 2681.1 2711.2 2897.0 3074.2
770.4 (1)	3.1 (2)	2891.4 (2)	2121.0 (1)	573.8 1547.9
834.1 (1)*	8.8 (7)	1407.5 (1)	573.5 (1)	573.7 1156.3
840.6 (1)	6.2 (5)	1414.0 (1)	573.5 (1)	573.8 1460.5

1010.2 (2)	1.8 (2)	2891.4 (2)	1881.1 (1)	573.9 1307.3 1881.7
1133.1 (2)	3.0 (2)	3254.4 (2)	2121.0 (1)	574.0 1547.9
1156.2 (3)	0.8 (1)	2563.7 (3)	1407.5 (1)	573.7 833.9
1307.7 (1)	6.1 (5)	1881.1 (1)	573.5 (1)	573.9 1010.7
1349.5 (2)	0.6 (1)	3470.6 (4)	2121.0 (1)	574.0 1547.9
1460.4 (2)	2.8 (2)	2874.3 (1)	1414.0 (1)	573.6 840.7
1526.3 (3)*	1,0 (1)	3647.2 (4)	212100 (1)	573.8 1547.3
1547.6 (1)	13.0 (1)	2121.0 (1)	573.5 (1)	573.7 770.3 1133.5 1350.0
1778.0 (1)	3.5 (3)	2351.5 (2)	573.5 (1)	573.8
1881.2 (1)	3.6 (3)	1881.1 (1)	g.s.	1010.6
2090.1 (2)	1.6 (2)	2663.5 (1)	573.5 (1)	573.8
2130.9 (1)	8.4 (7)	2704.3 (1)	573.5 (1)	573.6
2245.8 (2)*	2.5 (7)	2819.3 (2)	573.5 (1)	573.5
2300.8 (1)	17.0 (1)	2874.3 (1)	573.5 (1)	573.3
2681.0 (2)	12.8 1,0	3254.4 (2)	573.5 (1)	573.7
2711.1 (2)	5.3 (5)	3284.6 (3)	573.5 (1)	573.9
2874.3 (1)	45(4)	2874.3 (1)	g.s.	-
2897.2 (4)	2.8 (3)	3470.6 (4)	573.5 (1)	573.6
3073.7 (5)	2.2 (2)	3647.2 (4)	573.5 (1)	574.0
3284.7 (2)	7.0 (1)	3284.6 (3)	g.s.	-
4230.9 (4)†	1.5 (2)	-	-	-
5105.9 (3)†	0.4 (1)	-	-	-

Table 7.1: Summary of the observed gammas in the β-decay of ^{66}Mn to ^{66}Fe. *: Intensity obtained from $\gamma - \gamma$ coincidences. †: Gammas assigned to the ^{66}Mn decay but not placed in the level scheme.

Energy	Beta-feeding	Log(ft)	$T_1/2$	J_π
g.s.	49 (14)	5.1 (1)		0^+
573.5 (1)	3.1 (2.6)	6.2 (5)	35(9)	2^+
1407.5 (1)	2.6 (2)	6.19 (5)	< 15	4^+
1414.0 (1)	1.1 (2)	6.57 (5)		0^+
1881.1 (1)	2.6 (2)	6.11 (5)		(2^+)
2121.0 (1)	1.8 (4)	6.15 (8)	< 30	$(0,3)^+$
2351.5 (2)	1.2 (1)	6.36 (5)		(3^+)
2563.7 (3)	(3) (1)	7.0 (2)		
2663.5 (1)	(5) (1)	6.6 (1)		
2704.3 (1)	2.7 (2)	5.93 (4)		
2819.3 (2)	0.8 (2)	6.4 (1)		

2874.3 (1)	21 (1)	4.94 (3)	17(9)	1^+
2891.4 (2)	1.6 (1)	6.14 (4)		
3254.4 (2)	5.2 (4)	5.54 (4)		
3284.6 (3)	4.0 (3)	5.65 (3)		
3470.6 (4)	1.1 (1)	6.19 (5)		
3647.2 (4)	1 (1)	6.33 0.8		

Table 7.2: Summary of the levels populated in the β-decay of ^{66}Mn to ^{66}Fe.

The β-feeding to the levels was calculated as the difference of the γ transitions feeding and de-populating a specific level. They should be taken as upper limits since only observed transitions were taken into account. With a large mass difference ($Q_\beta = 13.32$ MeV [98]) several unobserved high energy transitions can be expected. See Tab. 7.2 for a list of levels, their calculated Log(ft) and β-feeding.

Relative intensities verification

To verify the measured relative intensities, they were calculated again in the 573.5 keV coincidences spectra and normalized to an intensity of 13.2 for the 1547.6 keV gamma. As can be seen in table 7.3, all the intensities are within the error bars, thus confirming the results obtained in singles.

7.2.4 β ground state feeding

The experiment was run in saturation, so data on the whole $A = 66$ decay chain was collected. The ^{66}Fe β-decay was studied recently [106], so the absolute intensities of its transitions are known. The total intensities of 470.7 keV (15(3)%) and 806.8 keV (5(2)%) most intense gammas in ^{66}Co[1] were compared to the intensity obtained for 573.5 keV gamma in ^{66}Fe (64(5)% if no direct β-feeding to the ground state is assumed). The excess of intensity in the ^{66}Co transitions indicated a direct ^{66}Mn β-feeding to the ^{66}Fe ground state of 46(12)%. The main source of error in this value are the uncertainties of the ^{66}Co total intensities.

In order to verify this result, the ^{66}Co decay in to ^{66}Ni was analysed. The reported total intensities from [107] for the transitions in the ^{66}Co to ^{66}Ni are not in agreement with our results by a factor of 5-7. One possible explanation is that the cited work did not account for any possible direct ground state β-feeding. At

[1]Transition 881.5 (8(3)%) keV was not used because of 881.8 keV gamma in ^{65}Co, present due to the β-n decay branch.

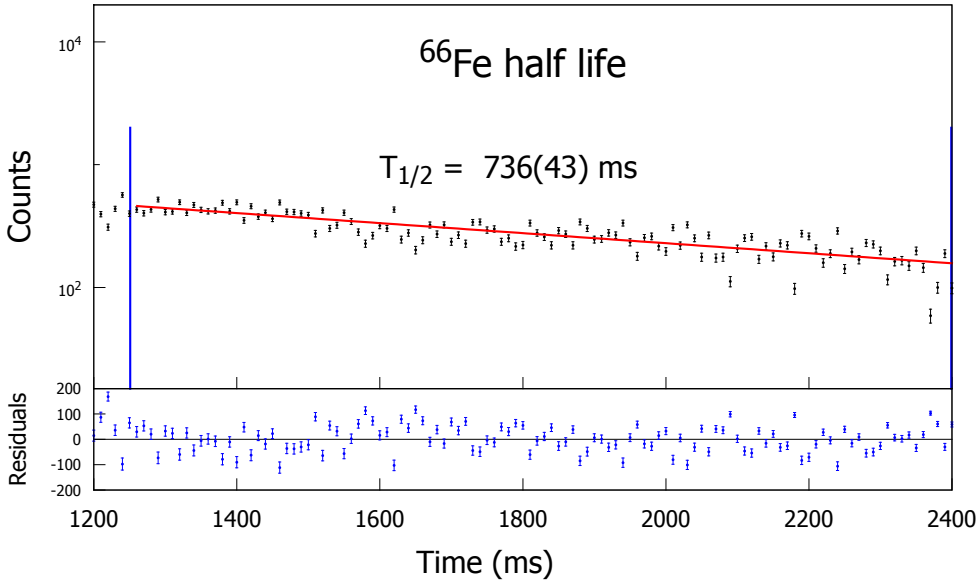

Figure 7.5: Fit to a double exponential decay of the ^{66}Mn and ^{66}Fe half life through a gate in 470.8 keV gamma in ^{66}Co. The blue markers represent the fitting range, which have been limited to 1.25 to 2.39 seconds. The ^{66}Mn half life was fixed, even if its contribution was negligible as it had already decayed in the fitted time range.

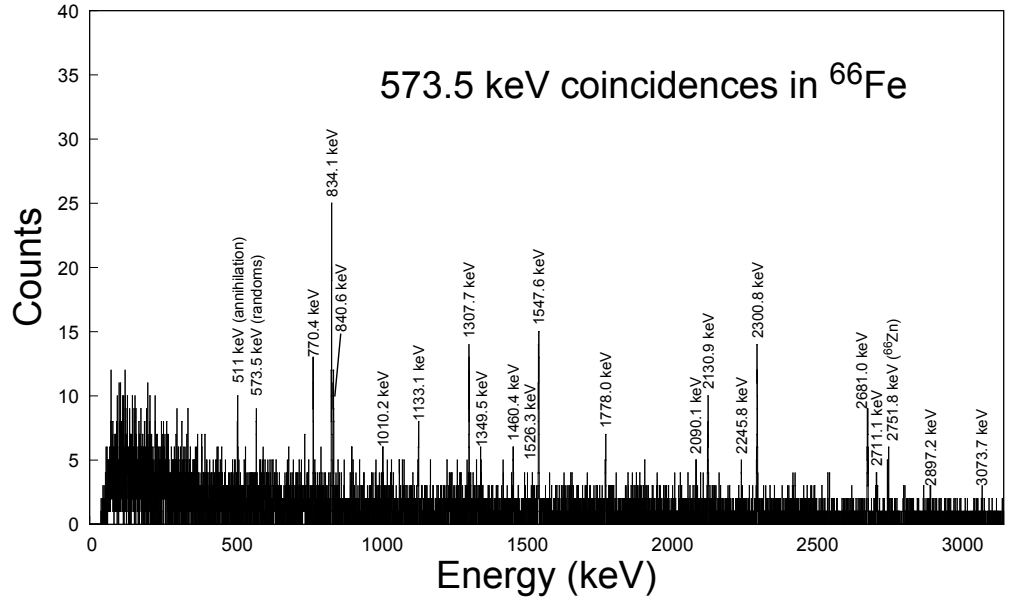

Figure 7.6: HPGe-HPGe energy spectra with the 573.5 keV gamma in ^{66}Fe gated. 511 and 2751.8 keV (from ^{66}Ga decay) are still partly visible after subtraction, while a fraction of them is oversubtracted. The net area of these two peaks is zero.

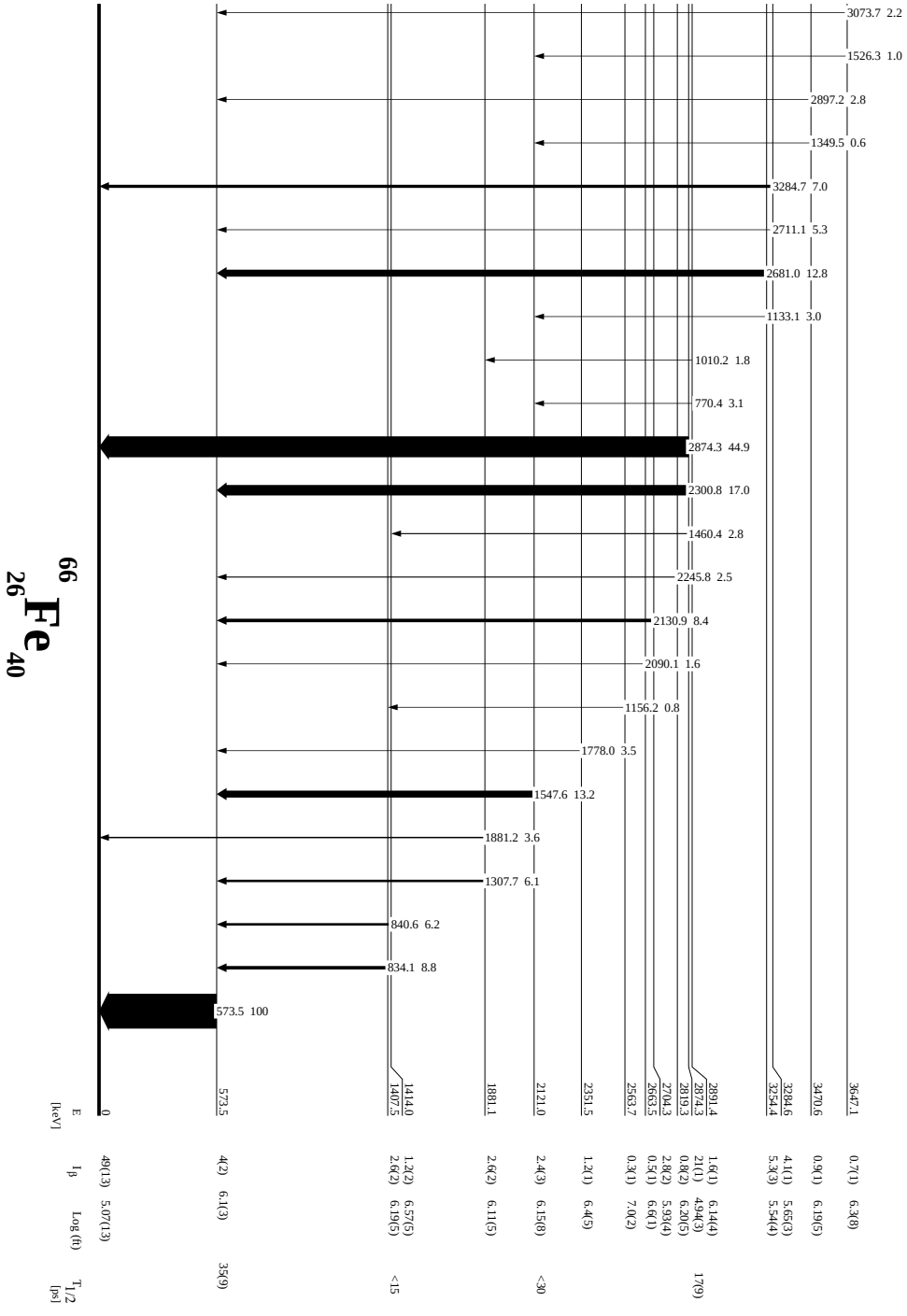

Figure 7.7: ^{66}Fe level scheme populated in the β-decay of ^{66}Mn from this work.

Transition (keV)	$I_{coincidences}$	$I_{singles}$
833.9 (1)	10 (1)	8.8 (7)
840.6 (2)	5 (1)	6.2 (5)
1307.7 (1)	7 (1)	6.1 (5)
1547.6 (2)	13 (1)	13 (1)
1778.4 (3)	4 (1)	3.5 (3)
2090.5 (4)	2 (1)	1.6 (2)
2131.0 (2)	10 (1)	8.4 (7)
2300.6 (2)	18 (2)	17 (1)
2681.0 (2)	14 (2)	12 (1)
2711.4 (5)	6 (2)	5.3 (5)
2904.2 (7)	3 (1)	2.8 (3)
3074 (1)	2 (1)	2.2 (2)

Table 7.3: Relative intensities obtained in HPGe-HPGe coincidences with a gate in the 573.5 keV peak. The intensities have been normalised to 13(1) for the 1547.6 keV transition.

the time of the cited work ^{66}Co ground state was tentatively assigned (3^+) spin [108], but a more recent publications assign it (1^+) [106], which would imply high direct β-feeding to the ^{66}Ni ground state and the big difference in the observed total intensities.

7.2.5 Delayed neutron emission branch

A small β-n branch was observed in the ^{66}Mn decay. Fig. 7.8 shows the 363.6, 455.4 and 560.7 keV already assigned in the ^{65}Mn β^--decay to ^{65}Fe (see table 5.1). The small energy differences are within the error bars. As the level population is different for the β-n branch than that of the β-branch, in order to get a P_n value the ^{65}Fe decay to ^{65}Co was analysed.

For internal coherence, the ^{65}Co intensities measured in this experiment were used (see Sec. 5.3.5). The 882.1 keV in ^{65}Co could not be used because of 881.5 keV in ^{66}Co. Instead, transitions 1222.9 (13(1)% absolute intensity) and 1996.6 keV (23(2)%) were used. Their ratio to 573.5 keV in ^{66}Fe (33(2)% taking into account the ^{66}Fe ground state direct β-feeding) yielded a value of $P_n = 3.9(8)\%$.

This value was further confirmed with the intensity of the 1481.8 keV gamma in ^{65}Cu (absolute intensity 23.6(2)%). Using only this gamma a $P_n = 3.7(8)\%$ value was obtained, in good agreement with previous result.

To present a final result, a weighted average was made with all three gammas

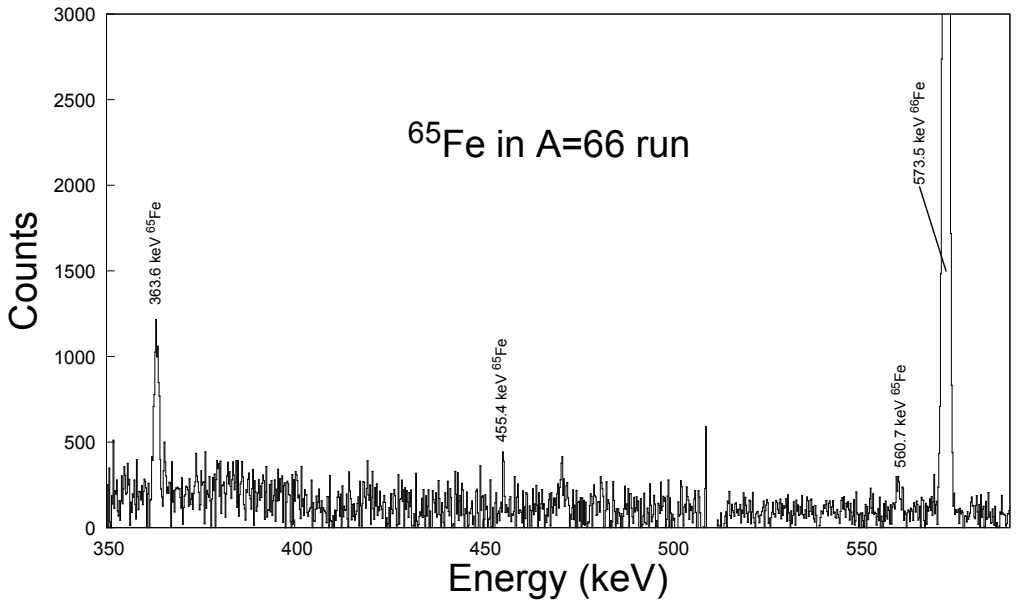

Figure 7.8: HPGe singles energy spectrum with a time gate that enhances ^{66}Mn activity. The 363.6, 455.4 and 560.7 keV transitions were already observed in the ^{65}Mn β^--decay to ^{66}Fe. In this case they have been assigned to the ^{66}Mn $\beta - n$ branch.

(both from ^{65}Co and ^{65}Cu), yielding $P_n = 3.8(7)\%$ for the neutron delayed branch of the ^{66}Mn decay.

Table 7.4 shows the populated levels in the ^{66}Mn β-n decay to ^{65}Fe. The gamma relative intensities have been normalized to 100 units for 573.5 keV. The βn-feeding of the levels has been normalized to add up 100% for the whole β-n branch. The direct feeding to the ground state was calculated as the excess of intensity in the observed ^{65}Co transitions.

E_{level} (keV)	βn-feeding	Transition (keV)	Intensity
g.s.	33(12)	-	-
363.6(1)	51(4)	363.6(1)	5.2(3)
455.4(2)	6.6(9)	455.4(2)	0.7(1)
560.7(2)	9(1)	560.7(2)	1.0(1)

Table 7.4: Summary of the levels populated in the βn-decay of ^{66}Mn to ^{65}Fe and their observed transitions.

7.3 Timing analysis

Level lifetimes in ^{66}Fe have been measured with the ATD method, making use of the centroid shift technique. First every time spectrum was analysed using the deconvolution technique [13], but no level presented half life long enough to appear as a slope in their time distribution. Tab. 7.5 summarizes the obtained half lives and their transition rates.

Energy	$T_1/2$	E2 (W.u.)	M1 (W.u.)
573,5(1)	35(9)	15(3)	
834,1(1)	< 15	> 6	
1547,6(1)	< 30	$> 0,13$	
1460,4(2)	17(9)		$1,8(9) \cdot 10^{-}5$
2300,8(1)			$2,8(15) \cdot 10^{-}5$
2874,3(1)			$3,8(20) \cdot 10^{-}5$

Table 7.5: Summary of the transition rates obtained in the timing analysis.

7.3.1 Absolute prompt reference in $A = 66$ run

The centroid shift technique requires an absolute prompt reference to shift the measured time centroid to the *prompt curve*. As there was no suitable candidate for it in the ^{66}Mn decay, it was decided to use another transition from a different nucleus within the decay chain.

The most intense gamma in the ^{66}Ga decay to ^{66}Zn is the 1039.2 keV transition, which de-excites the 2_1^+ 1039.2 keV state. This state has a $T_{1/2} = 1.68(3)$ ps, which has been obtained as the weighted average of over 10 different experiments [84]. This combination of a short and precise half life with high intensity makes this gamma a perfect candidate for the absolute prompt reference calibration. The shift for $LaBr_3$(Ce)-1 was 628.1(8) channels, while for $LaBr_3$(Ce)-2 the shift was 627.1(7) channels.

To verify the result, this analysis was repeated in $\beta - \gamma - \gamma$ coincidences. Selecting 833.5 keV in the HPGe and 1039.2 keV in the $LaBr_3$(Ce) the shift was 627.6(14) channels for detector 1 and 627.9(15) channels for detector 2. These values are in good agreement with the $\beta - \gamma$ results, verifying the absolute prompt calibration.

It must be noted that this 1039.2 keV level is also populated in the ^{66}Cu decay to ^{66}Zn. Obviously it will present the same level half life regardless of the parent

decay, but the β-walk can be very different for the two decays modes, thus giving an overall different time response. This contribution has been neglected as the total production of ^{66}Ga is around 30 times bigger than the neutron rich side of the isobar chain (see Fig. 7.1).

7.3.2 $\beta - \gamma$ half lives

As the production yield for ^{66}Mn was very low, the amount of data was not enough to perform a reliable $\beta - \gamma - \gamma$ analysis so it was performed in β-$LaBr_3$(Ce) coincidences. Gates were set on the observable peaks in the $LaBr_3$(Ce) spectra (see Fig. 7.3) and projected on to the TAC. The results were corrected by the Compton event contributions and then shifted to the *prompt curve* using the absolute prompt calibration 1039.2 keV gamma in ^{66}Zn (see previous section).

Tab. 7.6 shows the half lives obtained in the $\beta - \gamma$ coincidences analysis for the ^{66}Fe. The energy difference of the 834.1 and 840.6 keV transitions is below the resolution of the $LaBr_3$(Ce) crystals, so they could not be separated. Thus, the time response obtained by gating in the the 834.1/840.6 keV peak is a combination of their two half lives together.

Level (keV)	Gamma (keV)	$T_{1/2}$ (ps)
573.5	573.5	35(9)
1407.5/1414.0	834.1/840.6	< 12
2121.0	1547.6	< 30
2874.3	2300.8	< 30
	2874.3	17(9)

Table 7.6: Table that summarizes the different half lives measured in $\beta - \gamma$ coincidences in ^{66}Fe.

7.3.3 $\beta - \gamma - \gamma$ half lives

Even if the low statistics did not allow obtaining precise values, it served as a check of the $\beta - \gamma$ results. Tab. 7.7 shows the time response of gammas with the 573.5 keV gamma gated in the HPGe detectors. These results were obtained shifting the centroids using the 1039.2 keV gamma from the ^{66}Ga decay. Once again the 834.1 and 840.6 keV gammas could not be separated, so the result is the combination of both time responses.

Level (keV)	Gamma (keV) $LaBr_3$(Ce)	$T_{1/2}$ (ps)
1407.5/1414.0	834.1/840.6	< 16

52121.0	1547.6	26(20)
2874.3	2300.8	< 18

Table 7.7: Half lives obtained by gating the 573.5 keV gamma in the HPGe detectors.

7.3.4 Centroid shift check

Gamma in $LaBr_3$	Gamma in HPGe	Time response
574.5	834.1	$T_1 = \tau_{573.5} + \tau_{1407.5}$
574.5	840.6	$T_2 = \tau_{573.5} + \tau_{1414.0}$

Table 7.8: Different $\beta - \gamma - \gamma$ coincidence combinations performed with the time responses they produced.

Setting gates as described in table 7.8 and making use of Eq. 7.1 the relative lifetime difference of levels 1407.5 and 1414.0 keV was verified. Expressions in Tab. 7.8 assumes that the Compton contribution and the detector time response have been corrected.

$$T_1 - T_2 = \tau_{1407.5} - \tau_{1414.0} =< 40\ ps \tag{7.1}$$

Eq. 7.1 suggest that the 1407.5 keV level half life is longer than that of the 1414.0 keV level. In $\beta - \gamma$ coincidences an upper limit of $T_{1/2} < 15$ ps was obtained for the combined half lives of 1407.5 and 1414.0 keV levels, so it is assumed that the main contribution to this time difference is from the 1407.5 keV half life and the lifetime of 1414.0 kev level is even shorter.

7.4 Calculations

To help characterize the ^{66}Fe nuclear structure shell model calculations were performed using the Lenzi-Nowacki-Poves-Sieja (LNPS) effective interaction [6]. The calculation uses ^{40}Ca as a core, but also blocks the $\nu 0f_{7/2}$ and $\nu 1p_{3/2}$ orbitals. This leaves 8 neutrons in the $0f_{5/2}$, $1p_{1/2}$, $0g_{9/2}$ and $1d_{5/2}$ orbitals and 6 protons in the $0f_{7/2}$, $1p_{3/2}$, $0f_{5/2}$ and $1p_{1/2}$ orbitals.

There are two sets of independent calculations. A first one sets the ^{66}Mn ground state as a 1^+ and calculates the energy levels and their log(ft). The second

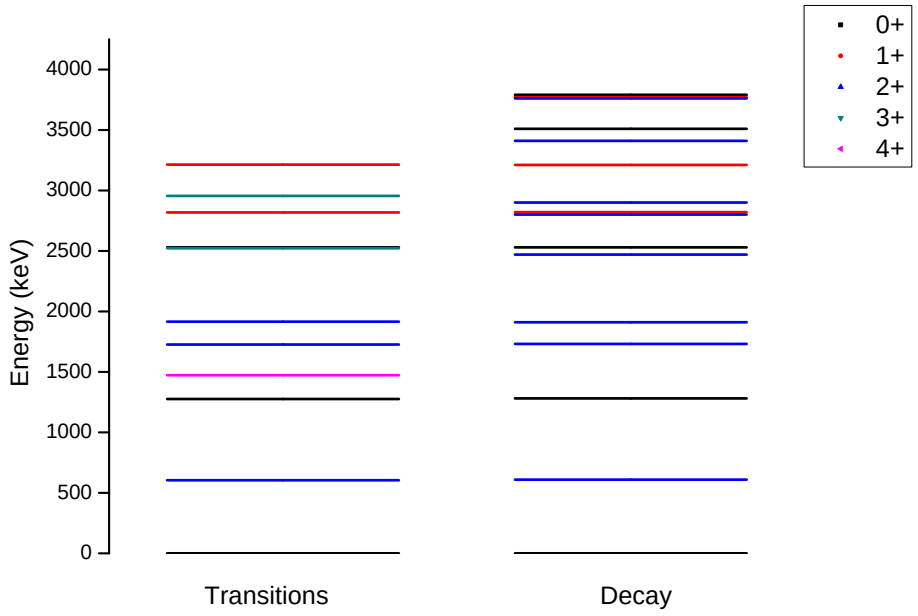

Figure 7.9: Comparison of the resulting levels from the decay calculations and the transition calculations. In the transitions the 3^+ and 4^+ state which are not populated in the β-decay appear. In the decay calculation there are more 2^+ states. Energies are very similar, but not exact.

one calculates the ^{66}Fe level energy (as particle binding energy), the level particle occupation and the transition rates of the gammas between these levels.

Fig. 7.9 shows a comparison of the two sets of levels obtained in the different calculations. The energies are very similar but not exactly equal, so when the two were available, the β-decay level energy was chosen. In the β-decay calculation only appear the populated levels, so there is no negative parity or levels with a spin higher than 2, but on the other hand it has levels up to 4 MeV. In the structure excitation calculation positive parity levels with spin up to 4^+ were calculated. All the 0^+, 1^+ and 2^+ obtained in the structure excitation of the nucleus appear as well in the decay calculation.

Table 7.9 shows the obtained levels in both calculations, their log(ft) and their dominant and average particle occupation for the $\nu(0f_{5/2},\ 1p_{1/2},\ 0g_{9/2},\ 1d_{5/2})$ and $\pi(0f_{7/2},\ 1p_{3/2},\ 0f_{5/2},\ 1p_{1/2})$ orbitals. From the calculation it is obvious that the proton orbitals play a minor role in the ^{66}Fe level structure, as there is almost no proton excitation in any of the calculated levels. The excited levels are mainly

explained by the occupation of the $0f_{5/2}$, $1p_{1/2}$ and $0g_{9/2}$ orbitals while the $1d_{5/2}$ orbital remains empty for the studied energy range.

E (keV)	J^π	log(ft)	Avg. neutron $f_{5/2}\ p_{1/2}\ g_{9/2}\ d_{5/2}$	Avg. proton $f_{7/2}\ p_{3/2}\ f_{5/2}\ p_{1/2}$	Prob.	Neutron	Proton
0	0^+	5.03	3.9 1.0 2.8 0.3	5.4 0.3 0.3 0.0	0.17	4 2/0 2/4 0	6 0 0 0
610	2^+	5.49	3.7 0.8 3.1 0.4	5.4 0.3 0.3 0.0	0.13	4 0/2 4/2 0	6 0 0 0
1280	0^+	5.4	4.0 1.2 2.4 0.4	5.4 0.3 0.2 0.0	0.23	4 2 2 0	6 0 0 0
1472	4^+		3.6 0.6 3.3 0.5	5.3 0.4 0.3 0.0	0.18	4 0 4 0	6 0 0 0
1730	2^+	> 7	4.0 1.3 2.3 0.4	5.5 0.3 0.2 0.0	0.27	4 2 2 0	6 0 0 0
1910	2^+	6.9	4.1 1.2 2.4 0.2	5.4 0.3 0.3 0.0	0.17	4/5 2/1 2 0	6 0 0 0
2470	2^+	6.35					
2522	3^+		4.0 1.2 2.5 0.3	5.4 0.3 0.3 0.0	0.16	5/4 1/2 2 0	6 0 0 0
2530	0^+	5.28	5.3 1.7 0.8 0.1	5.7 0.1 0.1 0.0	0.53	6 2 0 0	6 0 0 0
2800	2^+	5.39					
2820	1^+	6.6	3.5 0.8 3.2 0.5	5.4 0.3 0.3 0.0	0.12	4/3 0/1 4 0	6 0 0 0
2900	2^+	6.26					
2955	3^+		4.0 1.1 2.6 0.3	5.4 0.3 0.3 0.0	0.27	5 1 2 0	6 0 0 0
3210	1^+	6.6	3.2 0.9 3.4 0.5	5.3 0.4 0.3 0.0	0.2	3 1 4 0	6 0 0 0
3410	2^+	6.74					
3510	0^+	4.42					
3760	2^+	5.15					
3770	1^+	6.6					
3790	0^+	6					

Table 7.9: Calculated ^{66}Fe level structure for the $\nu(0f_{5/2},\ 1p_{1/2},\ 0g_{9/2},\ 1d_{5/2})$ and $\pi(0f_{7/2},\ 1p_{3/2},\ 0f_{5/2},\ 1p_{1/2})$. The *Avg.* columns are the average particle occupation for the calculated orbitals. *Prob.* column indicates the weight of the dominant configuration in the average occupation. *Neutron* column stands for the dominant neutron configuration and *Proton* column for the dominant proton configuration. When there are two numbers in one orbital it is because two different occupations were equally probable.

Table 7.10 shows the transition rates for the calculated M1 and E2 transitions. The transition energy has been calculated as the difference of the energy levels. When possible, more than one multipolarity has been calculated and the δ mixing ratio is expressed next to the E2 component.

E_i (keV)	E_γ (keV)	E_f (keV)	Multipolarity	$B(\downarrow;^M_E\lambda)$ (e^2fm^4/μ_N^2)	δ^2
610	610	0	E2	291.1	
1280	670	610	E2	5.7	
1472	862	610	E2	430.4	
1730	258	1472	E2	12.5	
	450	1280	E2	221.0	
	1120	610	E2	29.1	

	1730	0	E2	1.9	
1910	180	1730	E2	115,0	
	438	1472	E2	4,0	
	630	1280	E2	1.0	
	1300	610	E2	54.2	
	1910	0	E2	8.4	
2522	612	1910	E2	387,0	0.19
			M1	0.1	
	792	1730	E2	1.6	0.01
			M1	0.0	
	1050	1472	E2	23.2	0.03
			M1	0.1	
	1912	610	E2	12.2	0.1
			M1	0.0	
2530	620	1910	E2	1.5	
	800	1730	E2	3.5	
	1920	610	E2	0.2	
2820	290	2530	E2	0,0	
	298	2522	E2	3.4	
	910	1910	E2	47.2	0.02
			M1	0.1	
	1090	1730	E2	27.2	0.06
			M1	0.0	
	1540	1280	M1	0.1	
	2210	610	E2	0.1	0.0
			M1	0.2	
	2820	0	M1	0.2	
2955	135	2820	E2	1.6	
	433	2522	E2	5.9	
	1045	1910	E2	3.7	0.02
			M1	0.0	
	1225	1730	E2	7.4	0.21
			M1	0.0	
	1483	1472	E2	2.3	0.1
			M1	0.0	
	2345	610	E2	2.5	0.17
			M1	0.0	
3210	255	2955	E2	19.8	
	390	2820	E2	4.2	
	410	2800	E2	4.2	
	680	2530	M1	0.0	

688	2522	E2	2.6	
1300	1910	E2	2.6	0.04
		M1	0.0	
1480	1730	E2	5.2	0.02
		M1	0.0	
1930	1280	M1	0.1	
2600	610	E2	2.0	0.01
2600	610	M1	0.1	
3210	0	M1	0.1	

Table 7.10: Calculated M1 and E2 reduced transition probabilities. The level energy has been taken from the β-decay calculation when possible and the transition as the level energy difference. If possible, both M1 and E2 multipolarities were calculated for the same transition and their δ mixing ratio is showed next to them.

7.5 Discussion

Using the experimental and theoretical information obtained on the nucleus we can have a good insight of the ^{66}Fe nuclear structure.

Ground state, $J^\pi = 0^+$ As expected for an even-even nuclei, the assigned spin-parity for the ground state is 0^+. A high direct β-feeding to the ground state was observed in the experiment. This would corroborate the tentative assignment of 1^+ for the ^{66}Mn ground state, which was assigned based on systematics. According to the calculations this level is a mix configuration of 2 holes 2 particles (2h2p) and 4h4p. This result corroborates the deformation of the nuclei, as the excitation of 3 neutrons on average to the $0g_{9/2}$ orbital indicates that the intruder configuration drops below the normal one. Proton orbitals does not seem to play such crucial role, as none is promoted above the $f_{7/2}$ in the most dominant configurations and only 0.3 particles on average are excited to the $p_{5/2}$ and $f_{5/2}$ orbitals.

573.5 keV, $J^\pi = 2^+$ The 2_1^+ was obtained at 610 keV in the calculations, in good agreement with the experiment. Its configuration is the same as that of the ground state, a mix of 2p2h and 4p4h. The level half life $T_{1/2}$=35(9) ps, which yields B(E2)=234(54) e^2fm^4, is in agreement with the calculated transition rate of B(E2)=291 e^2fm^4. The calculation suggests that it should have log(ft)=5.5, indicating a certain amount of direct β-feeding, but the experiment shows that the level is weakly populated in β-decay in spite of the decay being allowed.

2874.3 keV, $J^\pi = (1^+)$ This level has a direct β-feeding of 21(1)% and the lowest log(ft) of the present scheme, which suggests a low spin. Its clear transition to the 0^+ ground state rules out the possibility that the 2874.3 keV itself has a 0^+ spin as well. As 2^+ it should populate both the 0_2^+ and the 4^+ levels around 1.4 MeV (see following sections) with similar intensity, while it only clearly populates one of them. If 1^+ spin-parity is assigned, it would only populate the 0^+ level, while there would be no observable transition to the 4^+. In the calculations the 1_1^+ state is at 2.82 MeV and it is depopulated by 3 M1 transitions (the E2 transitions are clearly to weak to be observed) whose transition rates follow the ratio 3:3:1 (from lower final level to higher), see Tab. 7.10. In the experiment, if the 2874.3, 2300.8 and 1460.4 kev transitions are assigned as M1 (assuming the 2874.3 keV has 1^+ spin) their transition rate ratios would be 2.1(14):1.6(10):1, in agreement with the calculated 1_1^+. These transition rates would be of the order of 10^{-5} W.u. for M1 and $10^{-2} - 10^{-3}$ W.u. for E2 multipolarity, so the half life does not rule out neither the 1^+ or 2^+ assignment for the level.

1407.5 keV, $J^\pi = (4^+)$ This level populates the 2_1^+ but not the 0^+ ground state and is not populated by the the 1_1^+ at 2874.3 keV, which suggests a spin of 3^+ or higher. Reaction experiments tentatively assigns spin 4^+ to a level at 1407(6) keV. Our calculations suggests that the 4_1^+ state is around 1.4 MeV, while the 3_1^+ is over 2.5 MeV, so we confirm the previous assignment of 4_1^+ for this level. Its β-feeding may be explained by high energy gammas not observed in the experiment, as if this assignment is correct, it would be a forbidden β-decay.

1414.0 keV, $J^\pi = (0^+)$ This level populates the 2_1^+ and is populated by 1_1^+ level, so a spin of 3 or lower is expected. A spin of 1^+ or 2^+ would strongly populate the 0^+ ground state, so they can be discarded. Once again the calculation does not obtain a level with spin 3^+ until 2.5 MeV, so 0^+ is the most likely spin. Calculations gives 0_2^+ at 1280 keV, in agreement with the experiment, but predicts a log(ft) of 5.4 while in the experiment log(ft)=6.57(5) was observed. The calculation also predicts a 2h2p, similar to the ground state, so its lack of direct β feeding remains unexplained.

1881.1 keV, $J^\pi = (2^+)$ Calculations predicts the second and third 2^+ states at 1.7 and 1.9 MeV respectively. The 1881.1 keV level has two transitions to the 0_1^+ ground state and the 2_1^+ state, but there is no observed transitions to the 1407.5 and 1414.0 keV levels. If 2^+ spin is assgined to this level, the unobserved transitions would be E2 and their intensity would be less than 0.1 due to the energy factor of the transition rates, below the observation limit for this mass. If a 2^+ spin was assigned to this level, it should be populated from the 1_1^+ at 28754.3 kev by a M1

transition of 993.2 keV with a relative intensity of 2, which should be observed in this experiment[2]. Regardless, it can not be tell if this is the 2_2^+ or the 2_3^+ level, because according to the calculation, the 2_2^+ level should not be β populated, so there is a chance that it is not seen in the experiment.

2121.0 keV, $J^\pi = (3^+)$ This level only feeds the 2_1^+ state and is fed by several higher energy levels. The calculation predicts 2^+ states at 1.9 MeV and 2.47 MeV and a 3^+ at 2.52 MeV. If spin of 2^+ is assigned to this level, an intense transition of 2121.0 keV to the ground state should be observed. On the other hand, if we assume that this level has a 3^+ spin, only a transition of 714 keV to the 1407.5 keV 4_1^+ with a relative intensity of 1 would be missing. With a similar argument, 0^+ spin can be assigned to this level. It would explain why it does not populate the ground state or the 0_2^+ and the 4_1^+, while the transition from the 1^+ would have a relative intensity below 0.5, which explains why is not observed. The experimental counterargument for this assignment are the three level above 3 MeV that populates this level and the 2_1^+ but not the ground state, which would be difficult to explain if this level has a spin-parity of 0^+. The calculation predicts the 0_3^+ at 2.5 MeV, which seems a rather large energy difference.

7.6 Conclusions

The ^{66}Fe level scheme constructed confirms most of the γ transitions previously observed and expand it to include a total of 24 γ-rays and 16 excited levels, plus two other high energy gammas assigned to the ^{66}Mn decay but unplaced on the level scheme. The observed direct β-feeding to the ground state (46(12)%) is in good agreement with recently reported works. An improved value of $P_n = 3.8(7)\%$ has been given for the neutron delayed emission branch. Moreover, the populated excited states in ^{65}Fe have been clearly observed.

Employing the centroid shift technique, from the ATD $\beta\gamma\gamma$(t) method, the half lives of two levels (including the 2_1^+ state) haven measured and two more upper limits have been set. The obtained value $B(E2; 2_1^+ \rightarrow 0_1^+) = 15(3)$ W.u. is in agreement with previously reported works and it indicates a high collectivity in the nucleus, but also points that the onset of collectivity may be ^{64}Fe and not ^{66}Fe, as was proposed.

Extensive shell model calculations using the LNPS effective interaction have been performed, proving information on the ^{66}Mn β-decay and ^{66}Fe excited level

[2]For example 1010.2 keV gamma in ^{66}Fe was observed with a relative intensity of 1.8

configuration. These calculations confirm the multinucleon-multihole character of the 2_1^+ state.

Making use of this calculation and the measured transition rates a spin-parity has been proposed for several levels. We confirm the confirm the previous tentative identification of the 4_1^+ state and propose the assignment of the 1_1^+ at 2874.3 keV.

Half life in ^{66}Ni

The $2_1^+ \rightarrow 0_1^+$ transition 1426 kev ($T_{1/2}$=0.8 ps) in the ^{66}Co decay to ^{66}Ni was inspected as a candidate for the absolute prompt reference calibration. However, the $\beta - \gamma$ time distribution of this gamma presented a clear slope suggesting a 200 ps half life.

The ^{66}Co β^--decay mainly populates the 2672 keV level ($I_\beta = 69(5)\%$) which is only de-excited by one gamma of 1246 keV to the the 1426 keV level and this one to the ground state [107]. Setting a gate on 1246 keV in β-$LaBr_3$(Ce) coincidences and projecting on the TAC revealed the same half life (see Fig. 7.10). This slope was not present in the Compton background inspected next to each peaks (1246 and 1426 keV).

As 1246 keV is above in the level scheme, the half life was assigned to the 2672 keV level and the slope observed in the 1426 keV transition was a contribution from the feeding 1246 keV gamma (the direct β-feeding for the higher energy level is three times bigger). Thus, the half life has been measured twice, directly in the 1246 keV gamma and then carried into the 1426 keV transition. Both detectors and gammas give results in good agreement, with an average of $T_{1/2} = 170(7)$ ps.

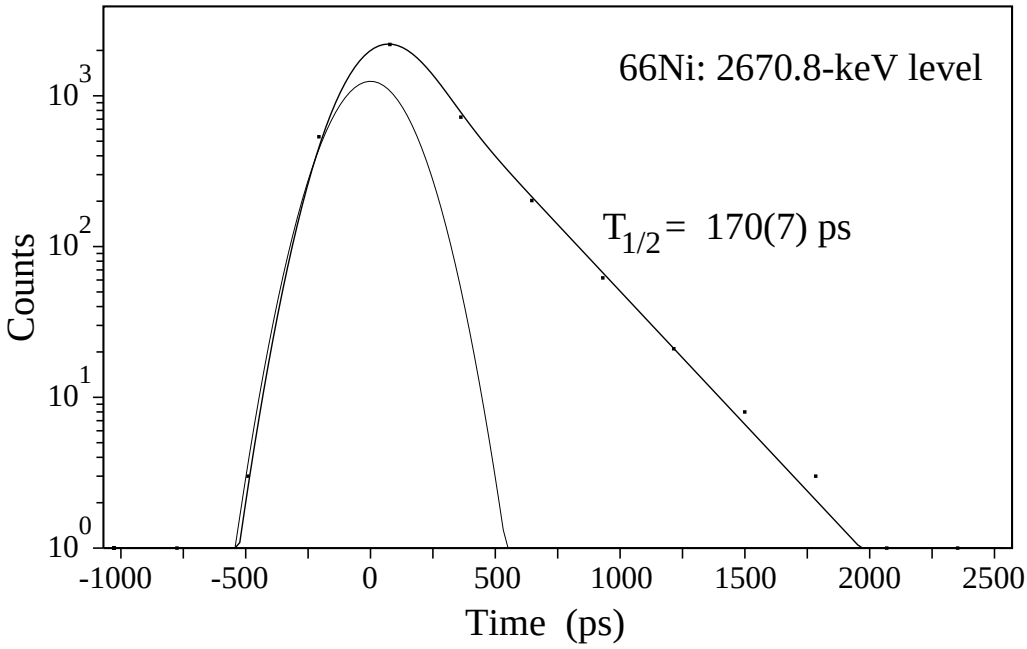

Figure 7.10: Fit to the 2672 keV level half life in ^{66}Co. The fit was done to a double exponential decay to account for the significant Compton background contribution, as the data was taken from β-$LaBr_3$(Ce) coincidences.

Chapter 8

Conclusions and future work

Conclusions

The data analysed in this thesis was obtained in an experiment performed by the Fast Timing Collaboration. In this experiment $^{59-66}$Mn ions were produced at ISOLDE, CERN, in order to study their β-decay and explore the region below ^{68}Ni using the ATD $\beta\gamma\gamma$(t) method. In particular this thesis presents the results obtained so far in ^{63}Fe, ^{65}Fe and ^{66}Fe isotopes, populated in the decay of their Mn isobars. These nuclei has been studied by means of $\gamma\gamma$ coincidences with two HPGe detectors and, by using the deconvolution and centroid shift techniques, some of their lower energy half lives have been measured with fast $LaBr_3$(Ce) crystals. The results obtained in the analysis of the ^{65}Fe have been submitted to the *Physical Review C* journal for publication. The articles on the other two nuclides are in preparation.

The most relevant result of this thesis are:

Level schemes For the first time the level of the ^{65}Fe has been constructed. It consists of 87 γ-transitions and 41 excited states (up to 4.4 MeV). The partial ^{63}Fe level scheme published by the Fast Timing Collaboration was verified and expanded to a total of 73 γ transitions and 31 levels. The recently published ^{66}Fe has been completed with new transitions and levels up to 24 γ-rays and 16 excited levels.

Direct β-feeding to the ground state For the first time upper limits have been set for the ground state feeding of ^{63}Fe and ^{65}Fe ($< 7\%$ and $< 8.8\%$, respectively), both of them compatible with zero. On the other hand the ^{66}Fe ground state feeding was confirmed with a value as high as 46(12)%.

Neutron delayed emission A βn branch was seen in the three isotopes, with values $P_n(^{63}Mn) = 2.0(2)\%$, $P_n(^{65}Mn) = 7.9(1.2)\%$ and $P_n(^{66}Mn) = 3.8(7)\%$. In the three cases the βn-decay populated excited levels, but a big portion of the intensity was not observed. It was assigned to unobserved γ-rays rather than a direct ground state feeding, as it would violate the decay selection rules for the assigned spin-parities.

$9/2^+$ state For the first time the β-decaying isomer energy in ^{65}Fe was precisely measured at 393.7 keV. A firm candidate for such state was found in ^{63}Fe at 475.0 keV. If confirmed, the energy evolution of the $9/2^+$ states would follow a perfect parabola in the neutron-rich odd-isotopes from A=57 to A=65.

Level lifetimes Using the ATD$\beta\gamma\gamma$(t) method 6 half lives were measured in ^{65}Fe, 2 in ^{63}Fe and 4 in ^{66}Fe. The first B(E2) for the odd nuclei gave 1.3(1) and 5.1(6) W.u. for ^{63}Fe and ^{65}Fe respectively, while the B(M1) where in the 10^{-3} W.u. order. For the even ^{66}Fe the 2_1^+ half life yielded a transition rate of $B(E2; 2_1^+ \rightarrow 0_1^+) = 15(3)$ W.u. It indicates a high collectivity for this nucleus, but also points that the onset of collectivity may be ^{64}Fe (with a higher $B(E2; 2_1^+ \rightarrow 0_1^+)$ value) and not ^{66}Fe, as was initially proposed.

Shell model calculations Shell model calculations using the LNPS effective interaction were performed. For A=65 the ^{65}Mn β-decay into ^{65}Fe was calculated, obtaining excited levels in the Fe isotope with spin-parity assignation, in very good agreement with the experimental results. In the ^{66}Fe case the same decay calculations were performed and, in addition, ^{66}Fe particle excitation and occupation were calculated as well, with good agreement between calculations and experiment. This particle occupation confirmed the importance of the $g_{9/2}$ orbit, with between 2 and 4 particles occupying this orbital in the ground state. The multiparticle-multihole character of the 2_1^+ state was confirmed.

Future work

The analysis of the IS474 experiment is still ongoing and many new results are still expected, as we have only started to scratch the surface of the immense amount of data obtained. Following the publication of this thesis, this is the expected roadmap:

- **^{66}Fe results publication:** some of the results obtained in this thesis about the ^{66}Fe nucleus have already been published, but our study confirms and deep-

ens in them. Furthermore, we have state-of-the art shell model calculations which puts us one step ahead in order to understand the nuclear structure of the ^{66}Fe nucleus.

- **^{63}Fe analysis:** we believe that more half lives could be obtained using the centroid shift technique in this nucleus, which surely will help to assign more spin-parities to higher energy levels. By further analysing the A=63 isotopic chain we hope to find a high-spin structure populated by the $9/2^+$ isomer and, in this way, unambiguously assign the 475.0 keV level as a β-decaying isomer.

- **Analysis of other masses:** the IS474 experiment collected data on the decay of Mn isotopes with masses from 59 to 66. The analysis of the the mores stable isotopes would yield valuable information which would help to study the systematics of Fe isotopes.

- **Analysis further in the isotopic chains:** as mentioned before and shown in some of the appendixes, much information can be obtained by analysing the decay products of Fe. The level schemes of many of these nuclei are poorly studied and some level lifetimes have been already observed. This information would be most helpful in our effort mapping the region below ^{68}Ni.

- **Study of heavier n-rich Fe isotopes:** the IS474 collaboration still has beam-time available and it is planned to use to study the ^{67}Fe nucleus. This isotope is one neutron over the studied N=40 sub-shell gap, so it would yield valuable information on the $g_{9/2}$ orbital evolution.

Bibliography

[1] Takaharu Otsuka, Toshio Suzuki, Rintaro Fujimoto, Hubert Grawe, and Yoshinori Akaishi. Evolution of nuclear shells due to the tensor force. *Phys. Rev. Lett.*, 95:232502, Nov 2005.

[2] K. Kaneko, Y. Sun, M. Hasegawa, and T. Mizusaki. Shell model study of single-particle and collective structure in neutron-rich cr isotopes. *Phys. Rev. C*, 78:064312, Dec 2008.

[3] S. Lunardi, S. M. Lenzi, F. Della Vedova, E. Farnea, A. Gadea, N. Mărginean, D. Bazzacco, S. Beghini, P. G. Bizzeti, A. M. Bizzeti-Sona, D. Bucurescu, L. Corradi, A. N. Deacon, G. de Angelis, E. Fioretto, S. J. Freeman, M. Ionescu-Bujor, A. Iordachescu, P. Mason, D. Mengoni, G. Montagnoli, D. R. Napoli, F. Nowacki, R. Orlandi, G. Pollarolo, F. Recchia, F. Scarlassara, J. F. Smith, A. M. Stefanini, S. Szilner, C. A. Ur, J. J. Valiente-Dobón, and B. J. Varley. Spectroscopy of neutron-rich fe isotopes populated in the ^{64}Ni+^{238}U reaction. *Phys. Rev. C*, 76:034303, Sep 2007.

[4] M. Hannawald, T. Kautzsch, A. Wöhr, W. B. Walters, K.-L. Kratz, V. N. Fedoseyev, V. I. Mishin, W. Böhmer, B. Pfeiffer, V. Sebastian, Y. Jading, U. Köster, J. Lettry, H. L. Ravn, and the ISOLDE Collaboration. Decay of neutron-rich mn nuclides and deformation of heavy fe isotopes. *Phys. Rev. Lett.*, 82:1391–1394, Feb 1999.

[5] E. Caurier, F. Nowacki, and A. Poves. Large-scale shell model calculations for exotic nuclei. *The European Physical Journal A - Hadrons and Nuclei*, 15(1-2):145–150, 2002.

[6] S. M. Lenzi, F. Nowacki, A. Poves, and K. Sieja. Island of inversion around 64cr. *Phys. Rev. C*, 82:054301, 2010.

[7] R. Broda, B. Fornal, W. Królas, T. Pawat, D. Bazzacco, S. Lunardi, C. Rossi-Alvarez, R. Menegazzo, G. de Angelis, P. Bednarczyk, J. Rico, D. De Acuña, P. J. Daly, R. H. Mayer, M. Sferrazza, H. Grawe, K. H. Maier, and R. Schubart.

$n = 40$ neutron subshell closure in the ^{68}Ni nucleus. *Phys. Rev. Lett.*, 74:868–871, Feb 1995.

[8] O. Sorlin, S. Leenhardt, C. Donzaud, J. Duprat, F. Azaiez, F. Nowacki, H. Grawe, Zs. Dombrádi, F. Amorini, A. Astier, D. Baiborodin, M. Belleguic, C. Borcea, C. Bourgeois, D. M. Cullen, Z. Dlouhy, E. Dragulescu, M. Górska, S. Grévy, D. Guillemaud-Mueller, G. Hagemann, B. Herskind, J. Kiener, R. Lemmon, M. Lewitowicz, S. M. Lukyanov, P. Mayet, F. de Oliveira Santos, D. Pantalica, Yu.-E. Penionzhkevich, F. Pougheon, A. Poves, N. Redon, M. G. Saint-Laurent, J. A. Scarpaci, G. Sletten, M. Stanoiu, O. Tarasov, and Ch. Theisen. $^{68}_{28}ni_{40}$: Magicity versus superfluidity. *Phys. Rev. Lett.*, 88:092501, Feb 2002.

[9] C. Guénaut, G. Audi, D. Beck, K. Blaum, G. Bollen, P. Delahaye, F. Herfurth, A. Kellerbauer, H.-J. Kluge, J. Libert, D. Lunney, S. Schwarz, L. Schweikhard, and C. Yazidjian. High-precision mass measurements of nickel, copper, and gallium isotopes and the purported shell closure at $n = 40$. *Phys. Rev. C*, 75:044303, Apr 2007.

[10] A. Gade, R. V. F. Janssens, T. Baugher, D. Bazin, B. A. Brown, M. P. Carpenter, C. J. Chiara, A. N. Deacon, S. J. Freeman, G. F. Grinyer, C. R. Hoffman, B. P. Kay, F. G. Kondev, T. Lauritsen, S. McDaniel, K. Meierbachtol, A. Ratkiewicz, S. R. Stroberg, K. A. Walsh, D. Weisshaar, R. Winkler, and S. Zhu. Collectivity at $n = 40$ in neutron-rich ^{64}Cr. *Phys. Rev. C*, 81:051304, May 2010.

[11] A.O. Macchiavelli. Selected aspects of the structure of exotic nuclei and new opportunities with gretina. *Acta Physica Polonica B*, 44(3):359, 2013.

[12] P. Adrich, A. M. Amthor, D. Bazin, M. D. Bowen, B. A. Brown, C. M. Campbell, J. M. Cook, A. Gade, D. Galaviz, T. Glasmacher, S. McDaniel, D. Miller, A. Obertelli, Y. Shimbara, K. P. Siwek, J. A. Tostevin, and D. Weisshaar. In-beam γ-ray spectroscopy and inclusive two-proton knockout cross section measurements at n$\approx$40. *Phys. Rev. C*, 77:054306, May 2008.

[13] H. Mach, R.L. Gill, and M. Moszyński. A method for picosecond lifetime measurements for neutron-rich nuclei: (1) outline of the method. *Nuclear Instruments and Methods in Physics Research Section A: Accelerators, Spectrometers, Detectors and Associated Equipment*, 280(1):49 – 72, 1989.

[14] M. Moszyński and H. Mach. A method for picosecond lifetime measurements for neutron-rich nuclei: (2) timing study with scintillation counters. *Nuclear Instruments and Methods in Physics Research Section A: Accelerators, Spectrometers, Detectors and Associated Equipment*, 277(23):407 – 417, 1989.

[15] H. Mach, F.K. Wohn, G. Molnár, K. Sistemich, John C. Hill, M. Moszyński, R.L. Gill, W. Krips, and D.S. Brenner. Retardation of b(e2; $0^+ \rightarrow 2^+$) rates in 90-96sr and strong subshell closure effects in the a 100 region. *Nuclear Physics A*, 523(2):197 – 227, 1991.

[16] XIA LLC. Xia instruments that advance the art. , 2013. [Online; accessed January-2013].

[17] H. Mach and B. Fogelberg. Fast timing studies of the neutron-rich singly-magic n = 82 nuclei. *Phys.Scr.*, T56:270, 1995.

[18] M. W. Hannawald. *Kernspektroskopie an $N \approx 40$ und $N \approx 82$ Nukliden*. PhD thesis, Univ.Johannes Gutenberg, Mainz, 2000.

[19] H. Mach, A-M. Baluyut, E. Ruchowska, U. Köster, L.M. Fraile, R. Boutami, H. Bradley, N. Braun, C. Fransen, J. Jolie, J. Nyberg, and V. Ugryumov. Structure of heavy fe nuclei at the point of transition at n $\sim$ 37. *Acta Physica Polonica B*, 40(3):477–480, 2009.

[20] S. N. Liddick, B. Abromeit, A. Ayres, A. Bey, C. R. Bingham, B. A. Brown, L. Cartegni, H. L. Crawford, I. G. Darby, R. Grzywacz, S. Ilyushkin, M. Hjorth-Jensen, N. Larson, M. Madurga, D. Miller, S. Padgett, S. V. Paulauskas, M. M. Rajabali, K. Rykaczewski, and S. Suchyta. Low-energy level schemes of $^{\mathbf{66,68}}$fe and inferred proton and neutron excitations across $\mathbf{Z = 28}$ and $\mathbf{N = 40}$. *Phys. Rev. C*, 87:014325, Jan 2013.

[21] W. Rother, A. Dewald, H. Iwasaki, S. M. Lenzi, K. Starosta, D. Bazin, T. Baugher, B. A. Brown, H. L. Crawford, C. Fransen, A. Gade, T. N. Ginter, T. Glasmacher, G. F. Grinyer, M. Hackstein, G. Ilie, J. Jolie, S. McDaniel, D. Miller, P. Petkov, Th. Pissulla, A. Ratkiewicz, C. A. Ur, P. Voss, K. A. Walsh, D. Weisshaar, and K.-O. Zell. Enhanced quadrupole collectivity at $n = 40$: The case of neutron-rich fe isotopes. *Phys. Rev. Lett.*, 106:022502, Jan 2011.

[22] E Fioretto, D Bazzacco, S Beghini, L Corradi, G de Angelis, E Farnea, A Gadea, S M Lenzi, S Lunardi, P Mason, D Mengoni, G Montagnoli, D R Napoli, E Sahin, F Scarlassara, R Silvestri, A M Stefanini, C A Ur, J J Valiente-Dobón, G Pollarolo, S Szilner, N Marginean, the PRISMA, and CLARA collaborations. Spectroscopic studies with the prisma-clara set-up. *Journal of Physics: Conference Series*, 205(1):012038, 2010.

[23] D. E. Alburger, C. Chasman, K. W. Jones, J. W. Olness, and R. A. Ristinen. Parity of be^{11}. *Phys. Rev.*, 136:B916–B919, Nov 1964.

[24] C. Thibault, R. Klapisch, C. Rigaud, A. M. Poskanzer, R. Prieels, L. Lessard, and W. Reisdorf. Direct measurement of the masses of ^{11}Li and $^{26-32}$Na with an on-line mass spectrometer. *Phys. Rev. C*, 12:644–657, Aug 1975.

[25] J. Dobaczewski, I. Hamamoto, W. Nazarewicz, and J. A. Sheikh. Nuclear shell structure at particle drip lines. *Phys. Rev. Lett.*, 72:981–984, Feb 1994.

[26] S. G. Nilsson. Binding states of individual nucleons in strongly deformed nuclei. *Mat. Fys. Med. Dan. Vid. Selsk.*, 29(16), 1955.

[27] E. Browne. Nuclear data sheets for a = 90. *Nuclear Data Sheets*, 82(3):379 – 546, 1997.

[28] C. J. Lister, M. Campbell, A. A. Chishti, W. Gelletly, L. Goettig, R. Moscrop, B. J. Varley, A. N. James, T. Morrison, H. G. Price, J. Simpson, K. Connel, and O. Skeppstedt. Gamma radiation from the N=Z nucleus $^{80}_{40}$zr$_{40}$. *Phys. Rev. Lett.*, 59:1270–1273, Sep 1987.

[29] K. Langanke, J. Terasaki, F. Nowacki, D. J. Dean, and W. Nazarewicz. How magic is the magic ^{68}Ni nucleus? *Phys. Rev. C*, 67:044314, Apr 2003.

[30] B. Pritychenko, J. Choquette, M. Horoi, B. Karamy, and B. Singh. An update of the b(e2) evaluation for transitions in even-even nuclei near. *Atomic Data and Nuclear Data Tables*, 98(4):798 – 811, 2012.

[31] O. Sorlin, C. Donzaud, L. Axelsson, M. Belleguic, R. Béraud, C. Borcea, G. Canchel, E. Chabanat, J.M. Daugas, A. Emsallem, D. Guillemaud-Mueller, K.-L. Kratz, S. Leenhardt, M. Lewitowicz, C. Longour, M.J. Lopez, F. de Oliveira Santos, L. Petizon, B. Pfeiffer, F. Pougheon, M.G. Saint-Laurent, and J.E. Sauvestre. Beta decay half-lives of neutron rich ti–co isotopes around n=40. *Nuclear Physics A*, 660(1):3 – 19, 1999.

[32] A. M. Nathan, J. W. Olness, E. K. Warburton, and J. B. McGrory. Yrast decay schemes from heavy-ion + ^{48}Ca fusion-evaporation reactions. iii. ^{57,58}Fe, ^{54,55}Cr, and ^{57,58}Mn. *Phys. Rev. C*, 17:1008–1025, Mar 1978.

[33] E. K. Warburton, J. W. Olness, A. M. Nathan, J. J. Kolata, and J. B. McGrory. Yrast decay schemes from heavy-ion + ^{48}Ca fusion-evaporation reactions. ii. $^{59-60}$Fe and $^{59-60}$Co. *Phys. Rev. C*, 16:1027–1039, Sep 1977.

[34] R. Grzywacz, R. Béraud, C. Borcea, A. Emsallem, M. Glogowski, H. Grawe, D. Guillemaud-Mueller, M. Hjorth-Jensen, M. Houry, M. Lewitowicz, A. C. Mueller, A. Nowak, A. Płochocki, M. Pfützner, K. Rykaczewski, M. G. Saint-Laurent, J. E. Sauvestre, M. Schaefer, O. Sorlin, J. Szerypo, W. Trinder,

S. Viteritti, and J. Winfield. New island of μs isomers in neutron-rich nuclei around the $z = 28$ and $n = 40$ shell closures. *Phys. Rev. Lett.*, 81:766–769, Jul 1998.

[35] R. Ferrer, M. Block, C. Bachelet, B. R. Barquest, G. Bollen, C. M. Campbell, M. Facina, C. M. Folden, C. Guénaut, A. A. Kwiatkowski, D. L. Lincoln, D. J. Morrissey, G. K. Pang, A. M. Prinke, R. Ringle, J. Savory, P. Schury, and S. Schwarz. Penning trap mass spectrometry of neutron-rich fe and co isotopes around $n = 40$ with the lebit mass spectrometer. *Phys. Rev. C*, 81:044318, Apr 2010.

[36] D. Kameda, T. Kubo, T. Ohnishi, K. Kusaka, A. Yoshida, K. Yoshida, M. Ohtake, N. Fukuda, H. Takeda, K. Tanaka, N. Inabe, Y. Yanagisawa, Y. Gono, H. Watanabe, H. Otsu, H. Baba, T. Ichihara, Y. Yamaguchi, M. Takechi, S. Nishimura, H. Ueno, A. Yoshimi, H. Sakurai, T. Motobayashi, T. Nakao, Y. Mizoi, M. Matsushita, K. Ieki, N. Kobayashi, K. Tanaka, Y. Kawada, N. Tanaka, S. Deguchi, Y. Satou, Y. Kondo, T. Nakamura, K. Yoshinaga, C. Ishii, H. Yoshii, Y. Miyashita, N. Uematsu, Y. Shiraki, T. Sumikama, J. Chiba, E. Ideguchi, A. Saito, T. Yamaguchi, I. Hachiuma, T. Suzuki, T. Moriguchi, A. Ozawa, T. Ohtsubo, M. A. Famiano, H. Geissel, A. S. Nettleton, O. B. Tarasov, D. Bazin, B. M. Sherrill, S. L. Manikonda, and J. A. Nolen. Observation of new microsecond isomers among fission products from in-flight fission of 345 mev/nucleon ^{238}u. *Phys. Rev. C*, 86:054319, Nov 2012.

[37] J. M. Daugas, I. Matea, J.-P. Delaroche, M. Pfützner, M. Sawicka, F. Becker, G. Bélier, C. R. Bingham, R. Borcea, E. Bouchez, A. Buta, E. Dragulescu, G. Georgiev, J. Giovinazzo, M. Girod, H. Grawe, R. Grzywacz, F. Hammache, F. Ibrahim, M. Lewitowicz, J. Libert, P. Mayet, V. Méot, F. Negoita, F. de Oliveira Santos, O. Perru, O. Roig, K. Rykaczewski, M. G. Saint-Laurent, J. E. Sauvestre, O. Sorlin, M. Stanoiu, I. Stefan, Ch. Stodel, Ch. Theisen, D. Verney, and J. Żylicz. β-decay measurements for $n > 40$ mn nuclei and inference of collectivity for neutron-rich fe isotopes. *Phys. Rev. C*, 83:054312, May 2011.

[38] J. Ljungvall, A. Görgen, A. Obertelli, W. Korten, E. Clément, G. de France, A. Bürger, J.-P. Delaroche, A. Dewald, A. Gadea, L. Gaudefroy, M. Girod, M. Hackstein, J. Libert, D. Mengoni, F. Nowacki, T. Pissulla, A. Poves, F. Recchia, M. Rejmund, W. Rother, E. Sahin, C. Schmitt, A. Shrivastava, K. Sieja, J. J. Valiente-Dobón, K. O. Zell, and M. Zielińska. Onset of collectivity in neutron-rich fe isotopes: Toward a new island of inversion? *Phys. Rev. C*, 81:061301, Jun 2010.

[39] A. J. Aas. *Lifetime measurements in nuclei with different shapes*. PhD thesis, University of Oslo, Norway, 1999.

[40] L.M Fraile. *Correlaciones octupolares en los nucleos Ra-229 y Ra-231*. PhD thesis, Universidad de Salamanca, Spain, 2000.

[41] Henryk Mach and LuisMario Fraile. Fast life-time measurements on fission products. *Hyperfine Interactions*, pages 1–10, 2012.

[42] Erich Kugler. The isolde facility. *Hyperfine Interactions*, 129:23–42, 2000.

[43] A.Lombardi and M.Vretenar. Linac 2. *50th anniversary of the CERN Proton Synchrotron*, pages 15–20, 2012.

[44] D. Warner. Accelerating structures of the cern new 50 mev linac. In *Linear Accelerator Conference*, 1979.

[45] D.J. Warner and M. Weiss. Beam optics in the cern new 50 mev linac. In *Linear Accelerator Conference*, 1979.

[46] K. Hanke, J. Sanchez-Conejo, and R. Scrivens. Dispersion matching of a space charge dominated beam at injection into the cern ps booster. In *Particle Accelerator Conference, 2005. PAC 2005. Proceedings of the*, pages 3283 – 3285, may 2005.

[47] Maurizio Vretenar. A high-intensity h^- linac at cern based on lep-2 cavities. Technical Report physics/0008142. CERN-NEUTRINO-FACTORY-NOTE-40. CERN-NUFACT-NOTE-40. CERN-PS-2000-059-RF, CERN, Geneva, Sep 2000.

[48] Klaus Hanke. Ps booster energy upgrade feasibility study first report. Technical Report 1082646-0003, CERN, Geneva, Sep 2010.

[49] C.E. Hill C. Metzger K. Schindl H. SchGnauer D.J. Simon B.W. Allardyce, R. Billinge. Isolde: A new client for the cern ps booster. In *European Particle Accelerator Conference EPAC90*, page 583, 1990.

[50] B. Jonson and K. Riisager. The isolde facility. 5(7):9742, 2010.

[51] M. Oinonen, Y. Jading, U. Köster, J. Lettry, H. Ravn, J. Äystö, P. Dendooven, J. Huikari, A. Jokinen, P.O. Lipas, A. Nieminen, K. Peräjärvi, T. Siiskonen, P. Baumann, A. Huck, A. Knipper, M. Ramdhane, G. Walter, F. Didierjean, V.N. Fedoseyev, V.I. Mishin, M. Koizumi, W. Liu, E. Roeckl, and V. Sebastian. Laser ionization in beta decay studies of zn and mn nuclei. *Hyperfine Interactions*, 127:431–436, 2000.

[52] J. Lettry, R. Catherall, P. Drumm, P. Van Duppen, A.H.M. Evensen, G.J. Focker, A. Jokinen, O.C. Jonsson, E. Kugler, and H. Ravn. Pulse shape of the isolde radioactive ion beams. *Nuclear Instruments and Methods in Physics Research Section B: Beam Interactions with Materials and Atoms*, 126(14):130 – 134, 1997. ¡ce:title¿International Conference on Electromagnetic Isotope Separators and Techniques Related to Their Applications¡/ce:title¿.

[53] U. Köster, V.N. Fedoseyev, A.N. Andreyev, U.C. Bergmann, R. Catherall, J. Cederkall, M. Dietrich, H. De Witte, D.V. Fedorov, L. Fraile, S. Franchoo, H. Fynbo, U. Georg, T. Giles, M. Gorska, M. Hannawald, M. Huyse, A. Joinet, O.C. Jonsson, K.L. Kratz, K. Kruglov, Ch. Lau, J. Lettry, V.I. Mishin, M. Oinonen, K. Partes, K. Peräjärvi, B. Pfeiffer, H.L. Ravn, M.D. Seliverstov, P. Thirolf, K. Van de Vel, P. Van Duppen, J. Van Roosbroeck, and L. Weissman. On-line yields obtained with the isolde rilis. *Nuclear Instruments and Methods in Physics Research Section B: Beam Interactions with Materials and Atoms*, 204(0):347 – 352, 2003. 14th International Conference on Electromagnetic Isotope Separators and Techniques Related to their Applications.

[54] U.C. Bergmann, G. Aubäck, R. Catherall, J. Cederkall, C.Aa. Diget, L. Fraile, S. Franchoo, H. Fynbo, H. Gausemel, U. Georg, T. Giles, H. Jeppesen, O.C. Jonsson, U. Köster, J. Lettry, T. Nilsson, K. Peäjärvi, H. Ravn, K. Riisager, L. Weissman, and J.Äystä. Production yields of noble-gas isotopes from isolde ucx/graphite targets. *Nuclear Instruments and Methods in Physics Research Section B: Beam Interactions with Materials and Atoms*, 204(0):220 – 224, 2003. 14th International Conference on Electromagnetic Isotope Separators and Techniques Related to their Applications.

[55] Manuela Turrion and Urszula Herman-Izycka. ISOLDE yields. , 2013. [Online; accessed Feb-2013].

[56] A.H. Sullivan. *Radiation safety considerations for the new ISOLDE facility using the PS Booster beam*, 1990. CERN RCP/90/XV/68.

[57] V.I. Mishin, V.N. Fedoseyev, H.-J. Kluge, V.S. Letokhov, H.L. Ravn, F. Scheerer, Y. Shirakabe, S. Sundell, and O. Tengblad. Chemically selective laser ion-source for the cern-isolde on-line mass separator facility. *Nuclear Instruments and Methods in Physics Research Section B: Beam Interactions with Materials and Atoms*, 73(4):550 – 560, 1993.

[58] V.N. Fedosseev, B.A. Marsh, D.V. Fedorov, U. Köster, and E. Tengborn. Ionization scheme development at the isolde rilis. *Hyperfine Interactions*, 162:15–27, 2005.

[59] V.N. Fedoseyev, G. Huber, U. Köster, J. Lettry, V.I. Mishin, H. Ravn, and V. Sebastian. The isolde laser ion source for exotic nuclei. *Hyperfine Interactions*, 127:409–416, 2000.

[60] V.N. Fedosseev, D.V. Fedorov, R. Horn, G. Huber, U. Köster, J. Lassen, V.I. Mishin, M.D. Seliverstov, L. Weissman, and K. Wendt. Atomic spectroscopy studies of short-lived isotopes and nuclear isomer separation with the isolde rilis. *Nuclear Instruments and Methods in Physics Research Section B: Beam Interactions with Materials and Atoms*, 204(0):353 – 358, 2003. 14th International Conference on Electromagnetic Isotope Separators and Techniques Related to their Applications.

[61] V.N. Fedoseyev, K. Bätzner, R. Catherall, A.H.M. Evensen, D. Forkel-Wirth, O.C. Jonsson, E. Kugler, J. Lettry, V.I. Mishin, H.L. Ravn, and G. Weyer. Chemically selective laser ion source of manganese. *Nuclear Instruments and Methods in Physics Research Section B: Beam Interactions with Materials and Atoms*, 126(14):88 – 91, 1997. International Conference on Electromagnetic Isotope Separators and Techniques Related to Their Applications.

[62] RILIS-ISOLDE. R I L I S Elements. , 2013. [Online; accessed January-2013].

[63] J.H.M. Neijzen and A. Danszelmann. Dye laser study of the np 2p12,32 rydberg series in neutral gallium and indium atoms. *Physica B+C*, 114(2):241 – 250, 1982.

[64] ISOLDE collaboration. The beamgate system. , 2001. [Online; accessed January-2013].

[65] ISOLDE collaboration. ISOLDE. , 2013. [Online; accessed January-2013].

[66] Nuclear Enterprises, Unc., San Carlos, CA 94070, USA. *Scintillator for the Physical Sciences, brochure No.126P.*

[67] Eljen Technologies, TX 79556 USA. *EJ-232 PLASTIC SCINTILLATOR.*

[68] M. Moszyński, M. Gierlik, M. Kapusta, A. Nassalski, T. Szczesniak, Ch. Fontaine, and P. Lavoute. New photonis xp20d0 photomultiplier for fast timing in nuclear medicine. *Nuclear Instruments and Methods in Physics Research Section A: Accelerators, Spectrometers, Detectors and Associated Equipment*, 567(1):31 – 35, 2006. Proceedings of the 4th International Conference on New Developments in Photodetection BEAUNE 2005.

[69] E. V. D. van Loef, P. Dorenbos, C. W. E. van Eijk, K. Krämer, and H. U. Güdel. High-energy-resolution scintillator: Ce[sup 3+] activated labr[sub 3]. *Applied Physics Letters*, 79(10):1573–1575, 2001.

[70] Gem series coaxial hpge detector product configuration guide. , 2010. [Online; accessed February-2013].

[71] Gmx series coaxial hpge detector product configuration guide. , 2010. [Online; accessed February-2013].

[72] L.C. Mihailescu, C. Borcea, and A.J.M. Plompen. Data acquisition with a fast digitizer for large volume hpge detectors. *Nuclear Instruments and Methods in Physics Research Section A: Accelerators, Spectrometers, Detectors and Associated Equipment*, 578(1):298 – 305, 2007.

[73] U.S. Department of Energy. *Standard NIM instrumentation system*, May 1990.

[74] XIA. *User's Manual Digital Gamma Finder (DGF) Pixie-4*, 2.20 edition, January 2011.

[75] L.M. Fraile, H. Mach, V. Vedia, B. Olaizola, V. Paziy, E. Picado, and J.M. Udias. Fast timing study of a cebr3 crystal: Time resolution below 120 ps at 60co energies. *Nuclear Instruments and Methods in Physics Research Section A: Accelerators, Spectrometers, Detectors and Associated Equipment*, 701(0):235 – 242, 2013.

[76] E. Runte, K.L. Gippert, W.D. Schmidt-Ott, P. Tidemand-Petersson, L. Ziegeler, R. Kirchner, O. Klepper, P.O. Larsson, E. Roeckl, D. Schardt, N. Kaffrell, P. Peuser, M. Bernas, P. Dessagne, M. Langevin, and K. Rykaczewski. Decay studies of neutron-rich isotopes of manganese, iron, cobalt, nickel, copper and zinc. *Nuclear Physics A*, 441(2):237 – 260, 1985.

[77] B. Pritychenko, E. BÄ›tÃ¡k, M.A. Kellett, B. Singh, and J. Totans. The nuclear science references (nsr) database and web retrieval system. *Nuclear Instruments and Methods in Physics Research Section A: Accelerators, Spectrometers, Detectors and Associated Equipment*, 640(1):213 – 218, 2011.

[78] Victor Delgado Martinez, Raúl T. Mainardi, Raúl A. Barrea, Carmen Martínez Hidalgo, Pedro A. Derosa, and Marisa Marco Arboli. Parametric equation for the efficiency curve of germanium detectors. *X-Ray Spectrometry*, 27(5):321–324, 1998.

[79] Ayman Ibrahim Hawari and Ronald F. Fleming. High accuracy determination of the shape of the efficiency curve of the hpge detector in the energy range 900 to 1300 kev. *Nuclear Instruments and Methods in Physics Research Section A: Accelerators, Spectrometers, Detectors and Associated Equipment*, 353(13):106 – 108, 1994.

[80] L. Moens and J. Hoste. Calculation of the peak efficiency of high-purity germanium detectors. *The International Journal of Applied Radiation and Isotopes*, 34(8):1085 – 1095, 1983.

[81] S. Hurtado, M. Garcia-Leon, and R. Garcia-Tenorio. Geant4 code for simulation of a germanium gamma ray detector and its application to effciency calibration. *Nuclear Instruments and Methods in Physics Research Section A: Accelerators, Spectrometes, Detectors and Associated Equipment*, 518(3):764, 2004.

[82] AMETC. 462 time calibrator. Technical report, ORTEC, 2013.

[83] S. RAMAN, C.W. NESTOR JR., and P. TIKKANEN. Transition probability from the ground to the first-excited 2+ state of even-even nuclides. *Atomic Data and Nuclear Data Tables*, 78(1):1 – 128, 2001.

[84] E. Browne and J.K. Tuli. Nuclear data sheets for a = 65. *Nuclear Data Sheets*, 111(9):2425 – 2553, 2010.

[85] J. M. Daugas, T. Faul, H. Grawe, M. Pfützner, R. Grzywacz, M. Lewitowicz, N. L. Achouri, J. C. Angélique, D. Baiborodin, R. Bentida, R. Béraud, C. Borcea, C. R. Bingham, W. N. Catford, A. Emsallem, G. de France, K. L. Grzywacz, R. C. Lemmon, M. J. Lopez Jimenez, F. de Oliveira Santos, P. H. Regan, K. Rykaczewski, J. E. Sauvestre, M. Sawicka, M. Stanoiu, K. Sieja, and F. Nowacki. Low-lying isomeric levels in ^{75}Cu. *Phys. Rev. C*, 81:034304, Mar 2010.

[86] J. M. Daugas, M. Sawicka, M. Pfützner, I. Matea, H. Grawe, R. Grzywacz, N. L. Achouri, J. C. Angélique, D. Baiborodin, F. Becker, G. Bélier, R. Bentida, R. Béraud, C. Bingham, C. Borcea, R. Borcea, E. Bouchez, A. Buta, W. N. Catford, E. Dragulescu, A. Emsallem, G. de France, J. Giovinazzo, M. Girod, H. Goutte, G. Gorgiev, K. L. Grzywacz-Jones, F. Hammache, F. Ibrahim, R. C. Lemmon, M. Lewitowicz, M. J. Lopez-Jimenez, P. Mayet, V. Méot, F. Negoita, F. de Oliveira-Santos, O. Perru, P. H. Regan, O. Roig, K. Rykaczewski, M. G. Saint-Laurent, J. E. Sauvestre, G. Sletten, O. Sorlin, M. Stanoiu, I. Stefan, C. Stodel, C. Theisen, D. Verney, and J. Zylicz. Isomeric island in the vicinity of [sup 66]fe. *AIP Conference Proceedings*, 831(1):427–429, 2006.

[87] L. Gaudefroy. *Etude de la fermeture de couche N=28 autour du noyau 46 18Ar28 par réaction de transfert d'un neutron : application à l'astrophysique et Spectroscopie beta de noyaux riches en neutrons autour de N=32/34 et N=40.* PhD thesis, UNIVERSITÉ DE PARIS XI U.F.R. SCIENTIFIQUE D'ORSAY, 2005.

[88] M. Block, C. Bachelet, G. Bollen, M. Facina, C. M. Folden, C. Guénaut, A. A. Kwiatkowski, D. J. Morrissey, G. K. Pang, A. Prinke, R. Ringle, J. Savory, P. Schury, and S. Schwarz. Discovery of a nuclear isomer in ^{65}Fe with penningtrap mass spectrometry. *Phys. Rev. Lett.*, 100:132501, Apr 2008.

[89] D. Pauwels, O. Ivanov, N. Bree, J. Büscher, T. E. Cocolios, M. Huyse, Yu. Kudryavtsev, R. Raabe, M. Sawicka, J. Van de Walle, P. Van Duppen, A. Korgul, I. Stefanescu, A. A. Hecht, N. Hoteling, A. Wöhr, W. B. Walters, R. Broda, B. Fornal, W. Krolas, T. Pawlat, J. Wrzesinski, M. P. Carpenter, R. V. F. Janssens, T. Lauritsen, D. Seweryniak, S. Zhu, J. R. Stone, and X. Wang. Structure of ^{65,67}Co studied through the β decay of ^{65,67}Fe and a deep-inelastic reaction. *Phys. Rev. C*, 79:044309, Apr 2009.

[90] V. N. Fedosseev, L.-E. Berg, D. V. Fedorov, D. Fink, O. J. Launila, R. Losito, B. A. Marsh, R. E. Rossel, S. Rothe, M. D. Seliverstov, A. M. Sjödin, and K. D. A. Wendt. Upgrade of the resonance ionization laser ion source at isolde on-line isotope separation facility: New lasers and new ion beams. *Review of Scientific Instruments*, 83(2):02A903, 2012.

[91] D. Pauwels, D. Radulov, W. B. Walters, I. G. Darby, H. De Witte, J. Diriken, D. V. Fedorov, V. N. Fedosseev, L. M. Fraile, M. Huyse, U. Köster, B. A. Marsh, L. Popescu, M. D. Seliverstov, A. M. Sjödin, P. Van den Bergh, J. Van de Walle, P. Van Duppen, M. Venhart, and K. Wimmer. Gamow-teller decay population of ^{64}ni levels in the decay of 1^+ ^{64}co. *Phys. Rev. C*, 86:064318, Dec 2012.

[92] N. Hoteling, W. B. Walters, R. V. F. Janssens, R. Broda, M. P. Carpenter, B. Fornal, A. A. Hecht, M. Hjorth-Jensen, W. Królas, T. Lauritsen, T. Pawłat, D. Seweryniak, X. Wang, A. Wöhr, J. Wrzesiński, and S. Zhu. Yrast structure of ^{64}Fe. *Phys. Rev. C*, 74:064313, Dec 2006.

[93] P.M. Endt. Strengths of gamma-ray transitions in a = 45–90 nuclei. *Atomic Data and Nuclear Data Tables*, 23(6):547 – 585, 1979.

[94] P.M. Endt. Strengths of gamma-ray transitions in a = 91–150 nuclei. *Atomic Data and Nuclear Data Tables*, 26(1):47 – 91, 1981.

[95] S. Kahana, H. C. Lee, and C. K. Scott. Effect of woods-saxon wave functions on the calculation of $a = 18,\ 206,\ 210$ spectra with a realistic interaction. *Phys. Rev.*, 180:956–966, Apr 1969.

[96] S. Leenhardt, F. Azaiez, O. Sorlin, M. Belleguic, C. Bourgeois, C. Donzaud, J. Duprat, S. Grévy, D. Guillemaud-Mueller, A.C. Mueller, F. Pougheon, I. Deloncle, J. Kiener, M.G. Porquet, J.M. Daugas, M. Lewitowicz, F. de Oli-

veira, M.G. Saint-Laurent, J. Winfield, J.C. Angélique, N. Orr, A. Gillibert, F. Marie, C. Borcea, Yu-E. Penionzhkevich, Yu. Sobolev, R. Béraud, G. Canchel, E. Chabanat, A. Emsalem, C. Longour, and J.E. Sauvestre. Subshell closure study at n=40 by coulomb excitation and beta-decay. *Nuclear Physics A*, 654(1, Supplement 1):683c – 686c, 1999.

[97] U. Bosch, W.-D. Schmidt-Ott, P. Tidemand-Petersson, E. Runte, W. Hillebrandt, M. Lechle, F.-K. Thielemann, R. Kirchner, O. Klepper, E. Roeckl, K. Rykaczewski, D. Schardt, N. Kaffrell, M. Bernas, Ph. Dessagne, and W. Kurcewicz. Beta-decay half-lives of new neutron-rich chromium-to-nickel isotopes and their consequences for the astrophysical r-process. *Physics Letters B*, 164(1–3):22 – 26, 1985.

[98] S. Naimi, G. Audi, D. Beck, K. Blaum, Ch. Böhm, Ch. Borgmann, M. Breitenfeldt, S. George, F. Herfurth, A. Herlert, A. Kellerbauer, M. Kowalska, D. Lunney, E. Minaya Ramirez, D. Neidherr, M. Rosenbusch, L. Schweikhard, R. N. Wolf, and K. Zuber. Surveying the $n = 40$ island of inversion with new manganese masses. *Phys. Rev. C*, 86:014325, Jul 2012.

[99] T. Kibédi, T.W. Burrows, M.B. Trzhaskovskaya, P.M. Davidson, and C.W. Nestor Jr. Evaluation of theoretical conversion coefficients using bricc. *Nuclear Instruments and Methods in Physics Research Section A: Accelerators, Spectrometers, Detectors and Associated Equipment*, 589(2):202 – 229, 2008.

[100] BAI ERJUN and HUO JUNDE. Nuclear data sheets for a = 63. *Nuclear Data Sheets*, 92(1):147 – 251, 2001.

[101] H. W. Jongsma, R. Kamermans, and H. Verheul. The decay of ^{63}co. *Z. Phys.*, 251:425, 1972.

[102] E. Runte, W.-D. Schmidt-Ott, P. Tidemand-Petersson, R. Kirchner, O. Klepper, W. Kurcewicz, E. Roeckl, N. Kaffrell, P. Peuser, K. Rykaczewski, M. Bernas, P. Dessagne, and M. Langevin. Decay studies of neutron-rich products from 76ge induced multinucleon transfer reactions including the new isotopes 62mn, 63fe and 71, 72, 73cu. *Nuclear Physics A*, 399(1):163 – 180, 1983.

[103] Alan L. Nichols, Balraj Singh, and Jagdish K. Tuli. Nuclear data sheets for a = 62. *Nuclear Data Sheets*, 113(4):973 – 1114, 2012.

[104] E. M. Franz, S. Katcoff, H. A. Smith, and T. E. Ward. Decay of the new isotope ^{62}Fe. *Phys. Rev. C*, 12:616–618, Aug 1975.

[105] L.M. Fraile, H. Mach, V. Vedia, B. Olaizola, V. Paziy, E. Picado, and J.M. Udías. Fast timing study of a cebr3 crystal: Time resolution below 120 ps at 60co energies. *Nuclear Instruments and Methods in Physics Research Section A: Accelerators, Spectrometers, Detectors and Associated Equipment*, 701(0):235 – 242, 2013.

[106] S. N. Liddick, B. Abromeit, A. Ayres, A. Bey, C. R. Bingham, M. Bolla, L. Cartegni, H. L. Crawford, I. G. Darby, R. Grzywacz, S. Ilyushkin, N. Larson, M. Madurga, D. Miller, S. Padgett, S. Paulauskas, M. M. Rajabali, K. Rykaczewski, and S. Suchyta. Low-energy structure of $^{66}_{27}\mathrm{co}_{39}$ and $^{68}_{27}\mathrm{co}_{41}$ populated through β decay. *Phys. Rev. C*, 85:014328, Jan 2012.

[107] W. F. Mueller, B. Bruyneel, S. Franchoo, M. Huyse, J. Kurpeta, K. Kruglov, Y. Kudryavtsev, N. V. S. V. Prasad, R. Raabe, I. Reusen, P. Van Duppen, J. Van Roosbroeck, L. Vermeeren, L. Weissman, Z. Janas, M. Karny, T. Kszczot, A. Płochocki, K.-L. Kratz, B. Pfeiffer, H. Grawe, U. Köster, P. Thirolf, and W. B. Walters. β decay of ^{66}Co, ^{68}Co, and ^{70}Co. *Phys. Rev. C*, 61:054308, Apr 2000.

[108] U. Bosch, W.-D. Schmidt-Ott, E. Runte, P. Tidemand-Petersson, P. Koschel, F. Meissner, R. Kirchner, O. Klepper, E. Roeckl, K. Rykaczewski, and D. Schardt. Beta- and gamma-decay studies of neutron-rich chromium, manganese, cobalt and nickel isotopes including the new isotopes 60cr and 60gmn. *Nuclear Physics A*, 477(1):89 – 104, 1988.